THE UNIVERSITY *of* EDINBURGH

ON THE PATH INTEGRATION SYSTEM OF INSECTS: THERE AND BACK AGAIN

IOANNIS PISOKAS

Doctor of Philosophy
School of Informatics
University of Edinburgh

2023

Ioannis Pisokas:
On the path integration system of insects:
There and back again
Doctor of Philosophy, 2023

SUPERVISORS:
Barbara Webb
Stanley Heinze

LAY SUMMARY

Many animals can return to their nest even when no landmarks exist to assist them. This is a critical capability for animals living in habitats with no vegetation, mountains or other features.

Some insects can do this with a remarkable level of accuracy. For instance, ants living in the salt pans of North Africa can return to their nest after travelling hundreds of metres away from it. They do this by using the light from the sun as a compass and estimating the distance they walked by counting their steps. But how do the neurons in their brains perform the necessary computations? This is the core question of this thesis.

In the first part of this thesis, I investigate the internal sun compass that insects are known to have. I compare the internal compasses of two different insects, flies and locusts, to determine how they changed during evolution. In the second part of the thesis, I try to understand how insects remember the direction of their nest and how far they have travelled from it. This is vital information to remember to be able to return to their nest after a long foraging trip.

The reason for pursuing this research is to understand how brains function and to use what we learn to build better navigation systems for humans and robots.

ABSTRACT

Navigation is an essential capability of animate organisms and robots. Among animate organisms of particular interest are insects because they are capable of a variety of navigation competencies solving challenging problems with limited resources, thereby providing inspiration for robot navigation.

Ants, bees and other insects are able to return to their nest using a navigation strategy known as path integration. During path integration, the animal maintains a running estimate of the distance and direction to its nest as it travels. This estimate, known as the 'home vector', enables the animal to return to its nest.

Path integration was the technique used by sea navigators to cross the open seas in the past. To perform path integration, both sailors and insects need access to two pieces of information, their direction and their speed of motion over time. Neurons encoding the heading and speed have been found to converge on a highly conserved region of the insect brain, the central complex. It is, therefore, believed that the central complex is key to the computations pertaining to path integration.

However, several questions remain about the exact structure of the neuronal circuit that tracks the animal's heading, how it differs between insect species, and how the speed and direction are integrated into a home vector and maintained in memory. In this thesis, I have combined behavioural, anatomical, and physiological data with computational modelling and agent simulations to tackle these questions.

Analysis of the internal compass circuit of two insect species with highly divergent ecologies, the fruit fly *Drosophila melanogaster* and the desert locust *Schistocerca gregaria*, revealed that despite 400 million years of evolutionary divergence, both species share a fundamentally common internal compass circuit that keeps track of the animal's heading. However, subtle differences in the neuronal morphologies result in distinct circuit dynamics adapted to the ecology of each species, thereby providing insights into how neural circuits evolved to accommodate species-specific behaviours.

The fast-moving insects need to update their home vector memory continuously as they move, yet they can remember it for several hours. This conjunction of fast updating and long persistence of the home vector does not directly map to current short, mid, and long-term memory accounts. An extensive literature review revealed a lack of available memory models that could support the home vector memory requirements.

A comparison of existing behavioural data with the homing behaviour of simulated robot agents illustrated that the prevalent hypothesis, which posits that the neural substrate of the path integration memory is a bump attractor network, is contradicted by behavioural evidence.

An investigation of the type of memory utilised during path integration revealed that cold-induced anaesthesia disrupts the ability of ants to return to their nest, but it does not eliminate their ability to move in the correct homing direction. Using computational modelling and simulated agents, I argue that the best explanation for this phenomenon is not two separate memories differently affected by temperature but a shared memory that encodes both the direction and distance.

The results presented in this thesis shed some more light on the labyrinth that researchers of animal navigation have been exploring in their attempts to unravel a few more rounds of Ariadne's thread back to its origin. The findings provide valuable insights into the path integration system of insects and inspiration for future memory research, advancing path integration techniques in robotics, and developing novel neuromorphic solutions to computational problems.

PUBLICATIONS

Some of the thesis content has been published in the papers listed below. While these papers contain authors other than Ioannis Pisokas, he is the leading author of all the publications associated with this thesis.

Pisokas, I. (2021). Reverse engineering and robotics as tools for analyzing neural circuits. *Frontiers in Neurorobotics*, 14:122.

Pisokas, I., Heinze, S., and Webb, B. (2020). The head direction circuit of two insect species. *eLife*, 9:e53985.

Pisokas, I. and Hennig, M. (2022). Can the insect path integration memory be a bump attractor? *In review*.

Pisokas, I., Rössler, W., Webb, B., Zeil, J., and Narendra, A. (2022). Anesthesia disrupts distance, but not direction, of path integration memory. *Current Biology*, 32(2):445–452.

ACKNOWLEDGEMENTS

It has been a privilege to be given the opportunity to spend several years studying a topic of great interest to me. This would have been impossible without the support of the Principal's Career Development scholarship. I would like to thank my supervisors, Barbara Webb and Stanley Heinze, for the great amount of time and effort they put into supporting me and giving me the freedom to work on the problems I found most interesting. I am also very grateful to the fantastic collaborators that I have been fortunate to work with: Ajay Narendra, Wolfgang Rössler, Jochen Zeil, Matthias Hennig, Michael Mangan, and Antoine Wystrach.

The fantastic people around me hugely enhanced my experience. I am grateful to Mark van Rossum, Matt Nolan, and Rüdiger Wehner for the inspiring discussions. I am also grateful to my fantastic friends Nina Kudryashova, Philippa Shoemark, Roman Goulard, Jan Stankiewicz, Melanie Stefan, Povilas Karvelis, and my sister Eleni Pisoka for the countless hours of proofreading. Finally, I am very grateful to my family for being supportive in all my endeavours, small and big.

DECLARATION

I declare that this thesis was composed by myself, that the work contained herein is my own except where explicitly stated otherwise in the text, and that this work has not been submitted for any other degree or professional qualification except as specified.

Edinburgh, 2023

Ioannis Pisokas,
23rd January 2023

CONTENTS

ACRONYMS

ANN	artificial neural network
CaMKII	Ca^{2+}/calmodulin-dependent protein kinase II
CBL	lower division of the central body, also known as EB
CBU	upper division of the central body, also known as FB
CX	central complex
DGPS	differential global positioning system
EB	ellipsoid body, also known as CBL
EC	entorhinal cortex
FB	fan-shaped body, also known as CBU
FWHM	full width at half maximum
GPS	global positioning system
LA	lateral amygdala
LIDAR	light detection and ranging
NMDA	N-methyl-d-aspartic acid
NO	noduli
PB	protocerebral bridge
SLAM	simultaneous localisation and mapping
SONAR	sound navigation and ranging

1

INTRODUCTION

1.1 GENERAL INTRODUCTION

Navigation is an essential capability that evolved in animals over millennia and was refined by humans over the last thousands of years, allowing navigators to cross vast distances on the land, sea, and even in space. Most recently, navigation has become essential in the context of mobile robots, self-driving cars, and unmanned aerial vehicles moving autonomously from one place to another.

The term navigation refers to a range of skills, including determining one's location and moving purposefully from one place to another. Throughout evolution, multiple animal species had to tackle similar navigation problems in different ecological settings. These opportunities lead to a variety of solutions stipulated by the available resources and constraints in each case. Since the ability to navigate is a problem shared by animals and robots, studying animal navigation may be a fruitful endeavour both for understanding how nervous systems solve the navigation problem and learning how to build better navigation systems for autonomous vehicles.

Of particular interest in this thesis is insect navigation. Many insect species solve challenging navigation problems despite having low-resolution sensing and simple nervous systems compared to vertebrates (Haberkern and Jayaraman, 2016). Among the navigation competencies of insects, path integration is of particular interest. Recent work has provided novel insight into the underlying neuronal substrate of insect path integration, including the discovery of neural activity that tracks the head direction of the animal and evidence for neuronal circuits that could support the animal's ability to track its displacement from a starting location. This thesis pertains to two general questions. Firstly, what is the underlying neuronal circuit structure that tracks the head direction of insects? Secondly, how do insects maintain an estimate of their displacement from their nest in memory?

In the subsequent sections of this chapter, I discuss the main topics with which this thesis is concerned as well as some methodological issues. I conclude the chapter with an outline of the contributions of the presented work to the current state of our body of understanding.

1.2 ROBOT NAVIGATION

A plethora of navigation competencies has been explored in robotics research, some requiring a map while others not. However, robot navigation research has mostly focused on map-based navigation since this is seemingly one of the most advanced forms of navigation we are familiar with, and it is a long tradition in artificial intelligence first to attempt to imitate the most advanced of man's skills (e.g. logical reasoning, and chess-playing).

A map can be metric, detailing the geometrical relationships between places, or topological, encoding only the topological relations between places. In both cases, the map may be pre-supplied or constructed by the robot, for instance, using simultaneous localisation and mapping (SLAM) (Thrun et al., 2005).

Determining an agent's location in space (localisation) is necessary for autonomous map construction and for planning a course of action to reach other places. Therefore, robot navigation research has explored the use of relevant sensory modalities for identifying the agent's location. The types of sensors available to the robotic platform stipulate the localisation methods that can be employed. For instance, Ultrasonic SONAR and LIDAR sensors provide information about proximity to the nearest surfaces around the robot and have been used for identifying places based on the geometrical signature of the surrounding space (Drumheller, 1987; Bosse and Zlot, 2009).

An alternative to these RADAR-type sensors is computer vision. Computer vision does not provide direct distance measurements but offers luminosity and chromatic detail. The use of computer vision in mobile robots has been historically limited due to its high computational requirements (Pisokas, 2006; Davison et al., 2007; Lemaire et al., 2007). However, the increased availability of computing power and developments in deep neural networks have made computer vision a viable sensory modality for mobile robots (Sünderhauf et al., 2015; Weyand et al., 2016; Lopez-Antequera et al., 2017; Zhang et al., 2021).

RADAR-type sensors and computer vision can be utilised for place recognition; an alternative to place recognition is the use of triangulation to calculate an agent's location in relation to fixed beacons in the environment. The global positioning system (GPS) is one such modality that provides an estimate of the robot's current location in geodesic coordinates (Bonnifait et al., 2001; He et al., 2002).

The mentioned localisation methods provide a location fix with reference to external entities (allocentric localisation). Another localisation approach is to track the robot's relative displacement from its previous position. To estimate the relative displacement of an agent, two pieces of information are required, the direction and distance it

travels at each time interval. Various sensors have been explored for measuring the distance an agent has travelled. Some utilise proprioceptive cues (e.g. wheel encoder odometry, von der Hardt et al. 1996), while others use exteroceptive cues (e.g. visual odometry or the Doppler effect, Nistér et al. 2004; Lee and Song 2004; Pisokas 2005). To track the agent's bearing, the relative rotation from its previous heading can be estimated using proprioceptive cues (e.g. wheel encoders, inertial measurement units, Barshan and Durrant-Whyte 1995; von der Hardt et al. 1996; Fuke and Krotkov 1996) or exteroceptive cues (e.g. optic flow, Nistér et al. 2004). Alternatively, the agent's bearing can be estimated in reference to allothetic cues (e.g. magnetic compass, celestial compass, sun compass, von der Hardt et al. 1996; Lambrinos et al. 2000). Travel distance sensors, together with heading change or allothetic compass sensors, can be used to update an agent's position estimate over time using a process known as dead reckoning in robotics and path integration in biology.

Dead reckoning is the method used by sea navigators in the past to cross the open seas. However, in robotics, dead reckoning has been historically considered unreliable, and its use has been limited to relatively short distances due to the incremental nature of position estimation and the associated error accumulation over time. This error accumulation in robot dead reckoning is primarily due to the common use of proprioceptive motion sensors (e.g. wheel encoder based odometry).

Due to uncertainty in a robot's position, probabilistic approaches in SLAM have been developed. Rather than maintaining a single position estimate, these maintain a probability distribution estimate of the agent's position over the map, typically using extended Kalman filters (Thrun et al., 2001) or particle filters (Gustafsson et al., 2002) to update their estimates. Other lines of research have taken a bio-inspired approach to navigation and developed models of animal navigation systems such as the place cells system of rodents (Milford et al., 2004) and the path integration system of insects (Stone et al., 2017).

1.3 INSECT NAVIGATION

Navigation is essential for animate organisms; it is required for foraging, finding cover, mating, and migration. Animals have different constraints than robots due to the underlying implementation substrate, available sensory modalities, computational capabilities, and locomotive apparatus. In addition, the ecological situation of each species may mandate particular sensing, locomotion, control, and survivability constraints. For instance, a walking ant can count its steps to estimate its displacement while a flying bee cannot; instead, it uses optic flow (Wittlinger et al., 2006; Srinivasan et al., 1996).

The available sensory, computational, and locomotory resources and constraints also determine the navigational approaches that the organism could potentially employ. For example, a biological equivalent of GPS or topographical surveying equipment does not exist, limiting the ability of animals to create metric maps with accurate distance measurements. However, a wide range of alternative navigation techniques have evolved in animals but have not been sufficiently explored in robotics research.

The navigation competencies of the simplest animals involve a more substantial stochastic element than is typically tolerable in robotics. For example, the 'run' and 'tumble' gradient ascent behaviour exhibited by *Escherichia coli* is an effective navigation method for specific tasks enabling bacteria to thrive for millennia, but still is not an approach often used in robot navigation. On the other hand, goal-directed navigation involving map use, planning, and shortcut finding that the most complex animals utilise, has been of more interest in robotics.

The navigation capabilities of insects lie between those of the simplest and the most complex animal species. Insects are known to employ visual beacon aiming, visual homing, route following, and path integration (Collett and Rees, 1997; Collett, 1996; Collett et al., 1992; Wehner et al., 1996; Collett and Collett, 2002; Wehner, 2003; Zeil, 2012). These capabilities are not as stochastic as the behaviours of the simplest animals and are necessary components for more complex navigation competencies. Notably, the current consensus is that insects do not use cognitive maps (Gould, 1986; Wehner and Menzel, 1990; Wehner and Wehner, 1990; Collett and Collett, 2006; Collett et al., 2013; Webb, 2019), yet, several insect species can travel distances tens of thousands of times their body length and then return successfully to their nest in the absence of familiar visual cues (Müller and Wehner, 1988). They achieve this by using path integration. On the other hand, our robot dead reckoning implementations are far from attaining comparable performance. This suggests that remains a lot to learn about its biological implementation.

To path integrate, the animal needs to have access to its current heading, its current speed (or equivalently the distance it travels per time interval), and must possess a mechanism to integrate its velocity vector over time to calculate the overall displacement from its starting location (Heinze et al., 2018). The overall displacement estimate is known as the 'home vector'[1] (Müller and Wehner, 1988). The home vector must be maintained in memory until the insect needs to return to its starting location, for instance, its nest. How the computations pertaining to path integration are accomplished in the insect brain has remained unknown. Path integration is one of the most primitive navigation behaviours present in a wide range of animal species permeating

1 The home vector is a vector pointing from the animal's current location to its origin, e.g. home. The home vector can be instead pointing from the origin to the current location, but regardless, it encodes the spatial relation of these two places.

all strata of life, from insects (Müller and Wehner, 1988) to birds (Mittelstaedt and Mittelstaedt, 1982; Saint Paul, 1982) and mammals (Mittelstaedt and Mittelstaedt, 1980; Etienne and Jeffery, 2004). The computation pertaining to path integration is fundamentally vector arithmetic, thus understanding the neuronal substrate of path integration will reveal not only the neural mechanism itself but also the neural basis for important and more generally applicable mathematical computations.

Insects are an ideal organism for studying path integration because they have relatively small brains, and current technology allows single-neuron imaging resolution of their brains, enabling us to study the underlying neuronal circuitry in unprecedented detail (Haberkern and Jayaraman, 2016). Therefore, it is imaginable that we may succeed in unravelling the neuronal circuit responsible for performing the necessary computations for path integration.

1.4 BIOROBOTICS AND NEUROSCIENCE

Biorobotics is the discipline at the cross-section of biology and robotics. Practitioners of bio-robotics have a two-fold purpose: to understand how biological organisms solve problems and get inspiration from biology to solve problems in robotics. The first purpose — understanding — is served by a biomimetic approach which intends to replicate how animals solve a problem using the technological domain of robotics as the implementation platform. The immediate goal of the biomimetic approach is to understand how animals solve problems rather than designing better robots. This is an exemplification of the learning by construction approach.

The second purpose of bio-robotics practitioners — inspiration from biological organisms — has the immediate goal of solving robotics problems rather than replicating nature. This approach has historically guided a range of disciplines such as cybernetics, artificial intelligence, and materials science. Regardless of their immediate goals, both approaches can help us learn how to build better robots in the long term and should be equally explored.

In this thesis, I use simulated robot agents to replicate animal behaviour and test hypotheses about the underlying neural substrate. This method is in contrast to widely used alternatives that study neuronal circuits as mere signal processors, measuring the activity of neurons in brain slices, or *in vivo* while an animal is presented with stimuli. On the contrary, real brains are embodied and inseparable from the organism's body. Real organisms are situated in their environment; their actions have consequences resulting in altered sensory stimuli that guide their behaviour. Action, computation, sensing, and environment are interdependent. A dramatic methodological reductionism approach that considers neurons as isolated closed systems may

not produce an understanding of the interplay between sensing, computation, action, and environment; an understanding of the 'whole'.

Robotics enables us to build artificial brains embodied in bodies that move around. As the bodies move in their environment, their situation changes, as do the stimuli that reach their artificial brains[2]. Building something helps us understand it better; if we want to understand animals, we should build artificial animals, not computers[3].

Once a hypothetical neural solution is implemented as part of a robot agent and tested in scenarios resembling those where the animals are situated, its limitations become apparent. In this thesis, I use simulated agents to test hypotheses about the insect path integration system and study the relevant neuronal circuits as part of a behaving agent[4].

We live in a unique era in history; we can combine behavioural experiments, neuroanatomy, electrophysiology, live animal neural imaging, computational modelling, and robotics into a scientific framework for hypothesis formulation, testing, and prediction making. All of these methods can guide each other in an interdependent multidisciplinary ecosystem.

1.5 CONTRIBUTIONS

The wide variety of ecological domains and behaviour of insects, including ants foraging a few hundreds of metres from their nest (Huber and Knaden, 2015), honey bees travelling to flower patches several kilometres away (von Frisch, 1967), locusts and butterflies migrating over hundreds of kilometres (Homberg, 2015; Heinze et al., 2013), impose different demands on sensing, locomotion, and neural control. Yet, in Part i of this thesis, I report that comparisons of the homologous head direction tracking circuits of two evolutionary distant species revealed that the major features of the circuit have been conserved (Pisokas et al. 2020 and Chapter 3). However, I also demonstrate that even subtle differences in the neuronal projection patterns between the species can have significant effects on the dynamical response of the homologous neuronal circuits. Notably, I observe that the effects of these identified differences are consistent with the behavioural ecology of the two species. I, therefore, find a direct correspondence between circuit adaptations, behavioural capabilities, and the

2 I am still using a reductionist approach, but not as dramatic as studying individual neurons. Instead, I utilise reductionism at the functional block level or behavioural competence level.

3 The word 'computers' is used here to refer to models of neurons and neuronal circuits studied as computational units in isolation.

4 The use of simulated agents is not the ultimate objective; using real robots would be preferable, but limited time and other resource constraints dictated a first approximation using simulated agents. Nevertheless, this is still a more revealing approach than studying neurons or groups of neurons in isolation.

ecological needs of each species (Chapter 3). These findings illustrate the potential fruitfulness of a comparative approach to neuroscience.

Then in Part ii, I report investigations on how path integrating insects might maintain a memory of their distance and direction from their nest (home vector). These investigations begin with an extensive literature review of memory mechanisms, put in the context of insect path integration (Chapter 4). I then show that the often voiced hypothesis that the underlying memory substrate of path integration might be a bump attractor network is contradicted by evidence (Chapter 5).

Finally, I conclude the investigations included in this thesis by reporting on the findings of a set of experiments using anaesthesia to manipulate the insect's home vector memory in order to shed light on its characteristics (Pisokas et al. 2022 and Chapter 6). This study revealed that the distance component of the home vector memory is affected by cold-induced anaesthesia, but the direction component is preserved. It also revealed that the two home vector memory components, direction and distance, may counterintuitively be encoded not separately but combined, sharing a common memory substrate.

The body of work presented in this thesis advances our current understanding of the neural substrate of path integration and hints at the possible existence of a different kind of memory than previously reported; a memory kind that would satisfy the particular ecological needs of path integrating insects.

BIBLIOGRAPHY

Barshan, B. and Durrant-Whyte, H. F. (1995). Inertial navigation systems for mobile robots. *IEEE transactions on robotics and automation*, 11(3):328–342.

Bonnifait, P., Bouron, P., Crubillé, P., and Meizel, D. (2001). Data fusion of four ABS sensors and GPS for an enhanced localization of car-like vehicles. In *IEEE International Conference on Robotics and Automation*, volume 2, pages 1597–1602. IEEE.

Bosse, M. and Zlot, R. (2009). Keypoint design and evaluation for place recognition in 2D lidar maps. *Robotics and Autonomous Systems*, 57(12):1211–1224.

Collett, M., Chittka, L., and Collett, T. S. (2013). Spatial memory in insect navigation. *Current Biology*, 23(17):R789–R800.

Collett, M. and Collett, T. S. (2006). Insect navigation: no map at the end of the trail? *Current biology*, 16(2):R48–R51.

Collett, T. S. (1996). Insect navigation en route to the goal: multiple strategies for the use of landmarks. *Journal of Experimental Biology*, 199(1):227–235.

Collett, T. S. and Collett, M. (2002). Memory use in insect visual navigation. *Nature Reviews Neuroscience*, 3(7):542–552.

Collett, T. S., Dillmann, E., Giger, A., and Wehner, R. (1992). Visual landmarks and route following in desert ants. *Journal of Comparative Physiology A*, 170(4):435–442.

Collett, T. S. and Rees, J. A. (1997). View-based navigation in hymenoptera: multiple strategies of landmark guidance in the approach to a feeder. *Journal of Comparative Physiology A*, 181(1):47–58.

Davison, A. J., Reid, I. D., Molton, N. D., and Stasse, O. (2007). Monoslam: Real-time single camera slam. *IEEE transactions on pattern analysis and machine intelligence*, 29(6):1052–1067.

Drumheller, M. (1987). Mobile robot localization using sonar. *IEEE transactions on pattern analysis and machine intelligence*, (2):325–332.

Etienne, A. S. and Jeffery, K. J. (2004). Path integration in mammals. *Hippocampus*, 14(2):180–192.

Fuke, Y. and Krotkov, E. (1996). Dead reckoning for a lunar rover on uneven terrain. In *Proceedings of IEEE International Conference on Robotics and Automation*, volume 1, pages 411–416. IEEE.

Gould, J. L. (1986). The locale map of honey bees: do insects have cognitive maps? *Science*, 232(4752):861–863.

Gustafsson, F., Gunnarsson, F., Bergman, N., Forssell, U., Jansson, J., Karlsson, R., and Nordlund, P.-J. (2002). Particle filters for positioning, navigation, and tracking. *IEEE Transactions on signal processing*, 50(2):425–437.

Haberkern, H. and Jayaraman, V. (2016). Studying small brains to understand the building blocks of cognition. *Current Opinion in Neurobiology*, 37:59–65.

He, B., Wang, D., Pham, M., and Yu, T. (2002). GPS/encoder based precise navigation for a 4WS mobile robot. In *7th International Conference on Control, Automation, Robotics and Vision*, volume 3, pages 1256–1261. IEEE.

Heinze, S., Florman, J., Asokaraj, S., El Jundi, B., and Reppert, S. M. (2013). Anatomical basis of sun compass navigation II: The neuronal composition of the central complex of the monarch butterfly. *Journal of Comparative Neurology*, 521(2):267–298.

Heinze, S., Narendra, A., and Cheung, A. (2018). Principles of insect path integration. *Current Biology*, 28(17):R1043–R1058.

Homberg, U. (2015). Sky compass orientation in desert locusts—evidence from field and laboratory studies. *Frontiers in Behavioral Neuroscience*, 9:346.

Huber, R. and Knaden, M. (2015). Egocentric and geocentric navigation during extremely long foraging paths of desert ants. *Journal of Comparative Physiology A: Neuroethology, Sensory, Neural, and Behavioral Physiology*, 201(6):609–616.

Lambrinos, D., Möller, R., Labhart, T., Pfeifer, R., and Wehner, R. (2000). A mobile robot employing insect strategies for navigation. *Robotics and Autonomous Systems*, 30(1):39–64.

Lee, S. and Song, J.-B. (2004). Robust mobile robot localization using optical flow sensors and encoders. In *IEEE International Conference on Robotics and Automation*, pages 1039–1044. IEEE.

Lemaire, T., Berger, C., Jung, I.-K., and Lacroix, S. (2007). Vision-based slam: Stereo and monocular approaches. *International Journal of Computer Vision*, 74(3):343–364.

Lopez-Antequera, M., Gomez-Ojeda, R., Petkov, N., and Gonzalez-Jimenez, J. (2017). Appearance-invariant place recognition by discriminatively training a convolutional neural network. *Pattern Recognition Letters*, 92:89–95.

Milford, M. J., Wyeth, G. F., and Prasser, D. (2004). RatSLAM: a hippocampal model for simultaneous localization and mapping. In *IEEE International Conference on Robotics and Automation*, volume 1, pages 403–408. IEEE.

Mittelstaedt, H. and Mittelstaedt, M. L. (1982). Homing by path integration. In *Avian navigation*, pages 290–297. Springer.

Mittelstaedt, M. L. and Mittelstaedt, H. (1980). Homing by path integration in a mammal. *Die Naturwissenschaften*, 67(11):566–567.

Müller, M. and Wehner, R. (1988). Path integration in desert ants, *Cataglyphis fortis*. *Proceedings of the National Academy of Sciences*, 85(14):5287–5290.

Nistér, D., Naroditsky, O., and Bergen, J. (2004). Visual odometry. In *2004 IEEE Computer Society Conference on Computer Vision and Pattern Recognition*, volume 1.

Pisokas, I., Heinze, S., and Webb, B. (2020). The head direction circuit of two insect species. *eLife*, 9:e53985.

Pisokas, I., Rössler, W., Webb, B., Zeil, J., and Narendra, A. (2022). Anesthesia disrupts distance, but not direction, of path integration memory. *Current Biology*, 32(2):445–452.

Pisokas, J. (2005). Frequency shift for position estimation in mobile robots. In *2005 IEEE International Conference on Systems, Man and Cybernetics*, volume 4, pages 3516–3521.

Pisokas, J. (2006). Global navigation through local reference frames. In Nolfi, S., Baldassarre, G., Calabretta, R., Hallam, J. C. T., Marocco, D., Meyer, J.-A., Miglino,

O., and Parisi, D., editors, *International Conference on Simulation of Adaptive Behavior: From Animals to Animats 9*, volume 4095 LNAI, pages 274–285. Springer Berlin Heidelberg.

Saint Paul, U. v. (1982). Do geese use path integration for walking home? In *Avian navigation*, pages 298–307. Springer.

Srinivasan, M., Zhang, S., Lehrer, M., and Collett, T. S. (1996). Honeybee navigation en route to the goal: visual flight control and odometry. *Journal of experimental biology*, 199(1):237–244.

Stone, T., Webb, B., Adden, A., Weddig, N. B., Honkanen, A., Templin, R., Wcislo, W., Scimeca, L., Warrant, E., and Heinze, S. (2017). An anatomically constrained model for path integration in the bee brain. *Current Biology*, 27(20):3069–3085.

Sünderhauf, N., Shirazi, S., Dayoub, F., Upcroft, B., and Milford, M. (2015). On the performance of ConvNet features for place recognition. In *2015 IEEE/RSJ International Conference on Intelligent Robots and Systems (IROS)*, pages 4297–4304. IEEE.

Thrun, S., Burgard, W., and Fox, D. (2005). *Probabilistic robotics*. Intelligent Robotics and Autonomous Agents series. The MIT Press Cambridge, MA, USA.

Thrun, S., Fox, D., Burgard, W., and Dellaert, F. (2001). Robust monte carlo localization for mobile robots. *Artificial Intelligence*, 128(1):99–141.

von der Hardt, H.-J., Wolf, D., and Husson, R. (1996). The dead reckoning localization system of the wheeled mobile robot ROMANE. In *1996 IEEE/SICE/RSJ International Conference on Multisensor Fusion and Integration for Intelligent Systems (Cat. No. 96TH8242)*, pages 603–610. IEEE.

von Frisch, K. (1967). *The dance language and orientation of bees*. Harvard University Press.

Webb, B. (2019). The internal maps of insects. *Journal of Experimental Biology*, 222(Suppl 1):jeb188094.

Wehner, R. (2003). Desert ant navigation: How miniature brains solve complex tasks. *Journal of Comparative Physiology A*, 189(8):579–588.

Wehner, R. and Menzel, R. (1990). Do insects have cognitive maps? *Annual Review of Neuroscience*, 13(1):403–414.

Wehner, R., Michel, B., and Antonsen, P. (1996). Visual navigation in insects: coupling of egocentric and geocentric information. *Journal of Experimental Biology*, 199(1):129–140.

Wehner, R. and Wehner, S. (1990). Insect navigation: Use of maps or ariadne's thread? *Ethology Ecology and Evolution*, 2(1):27–48.

Weyand, T., Kostrikov, I., and Philbin, J. (2016). PlaNet - photo geolocation with convolutional neural networks. In Leibe, B., Matas, J., Sebe, N., and Welling, M., editors, *European Conference on Computer Vision*, pages 37–55. Springer.

Wittlinger, M., Wehner, R., and Wolf, H. (2006). The ant odometer: Stepping on stilts and stumps. *Science*, 312(5782).

Zeil, J. (2012). Visual homing: an insect perspective. *Current opinion in neurobiology*, 22(2):285–293.

Zhang, X., Wang, L., and Su, Y. (2021). Visual place recognition: A survey from deep learning perspective. *Pattern Recognition*, 113:107760.

2

BACKGROUND

2.1 NAVIGATION IN INSECTS

Insects possess a variety of navigation competencies, including pheromone trail following (Morgan, 2009), visual beacon aiming (Collett and Rees, 1997; Collett and Collett, 2002), visual homing (Collett, 1996), route following (Collett et al., 1992; Wehner et al., 1996; Wehner, 2003), and path integration (Müller and Wehner, 1988). When the habitat contains sufficiently unique visual features, ants and bees can use them, but they resort to path integration when the visual information is insufficient (Wehner et al., 1996; Wehner, 2003). Evidence for the use of path integration comes from displacement experiments illustrating that animals captured while away from their nest and displaced to an unfamiliar location, once released, walk in a direction parallel to the direction they would have walked from the capture point for returning to their nest (Müller and Wehner, 1988). Further evidence for path integration is that honey bees appear to communicate to their nest mates the direction and distance to food sources via their waggle dance (von Frisch, 1967).

Interestingly, regardless of the error accumulation that has limited the use of path integration in robotics, insects can travel distances thousands of times larger than their body length and yet successfully return to their nest using path integration (Müller and Wehner, 1988). Understanding how insects perform path integration has potentially two major benefits, first will help us understand how the encoding, computation, and memory demands of path integration are solved by brains and second will help us build improved robot navigation systems, especially for navigating in non-structured and dynamically changing environments where navigation based on place recognition is impossible.

2.1.1 *Path Integration*

When a solitary foraging ant of the species *Cataglyphis fortis* embarks in search of food, it follows a circuitous path but then returns to its nest walking in an approximately straight line (Müller and Wehner, 1988). This ability is not unique to ants and was observed at least as early as the time of Charles Darwin, who ascribed it to some form

of unconscious dead-reckoning[1] in his attempt to explain the anecdotally reported ability of native Siberians to navigate (Darwin, 1873). Dead reckoning, known as path integration in biology, has also been described in other animals, including birds (Mittelstaedt and Mittelstaedt, 1982; Saint Paul, 1982) and mammals (Mittelstaedt and Mittelstaedt, 1980; Etienne and Jeffery, 2004).

2.1.2 *Path Integration Memory*

Path integrating insects maintain an estimate of the direction and distance to a reference point, which can be their nest or another salient place such as a feeding location (Collett, 2019). This estimate is commonly known as the 'home vector' (Heinze et al., 2018; Collett, 2019). The home vector memory is updated continuously as the insect moves (Menzel and Muller, 1996; Wehner, 2003), yet the home vector's latest state has to be remembered long enough for the animal to be able to return to its nest, even if its journey is interrupted for some time.

Ants can be captured at any moment during their voyage, and then once displaced and released in an unfamiliar location, they immediately run towards the location they expect to find their nest, according to their home vector memory (Müller and Wehner, 1988; Menzel and Muller, 1996; Collett, 2019). This suggests an instantaneous home vector memory updating mechanism that does not need a memory consolidation period before becoming available (Menzel and Muller, 1996; Müller, 2013; Tomchik and Davis, 2013). Furthermore, foraging ants were shown to reset their home vector memory to a zero vector length state once entering their nest (Knaden and Wehner, 2005) and have been observed to remerge from their nest for foraging again within a few minutes (Personal observation, also personal communication Barbara Webb). These findings suggest a memory mechanism capable of quick updating.

On the other hand, the home vector memory has to be maintained until the insect needs it to return to its nest (Schmid-Hempel, 1984; Cheng et al., 2005; Muser et al., 2005). *Cataglyphis* ants prevented from returning to their nest can still use their home vector when released tens of hours later (Ziegler and Wehner, 1997; Cheng et al., 2005). This observation suggests that the path integrator uses a persistent type of memory for maintaining the home vector. The conjunction of fast updating and long persistence does not directly map to existing accounts of short, mid, and long-term memory Pisokas et al. (2022).

1 Charles Darwin used the term dead-reckoning, alluding to the process used by sea navigators of that time who used a magnetic compass and vector addition on a map.

2.1.3 *Models of Path Integration*

Several researchers attempted to create mathematical models of the path integration behaviour exhibited by various animals (Mittelstaedt, 1985; Müller and Wehner, 1988; Benhamou et al., 1990; Gallistel, 1990). These models describe the observed path of the animal at a behavioural level without implying that the animal's brain actually performs these exact mathematical computations. Some authors have occasionally explicitly stated this distinction (for instance Benhamou and Séguinot, 1995).

Attempts to develop neurally plausible path integration models started with Hartmann and Wehner (1995) and Wittmann and Schwegler (1995). Hartmann and Wehner (1995) used what they called 'neural chains' to encode the direction and distance of the agent to the nest. These were chains or rings of neurons with the number of subsequent active neurons encoding the distance or direction to the origin (the nest). The state of the neural chains was updated as the agent moved. For returning to its nest, turning commands were produced by computing the overlap between the estimated agent's heading and a current sky-compass heading. As the agent approached its nest, the distance estimate stored in the neural chain was reduced, with zero indicating arrival at the nest.

Wittmann and Schwegler (1995) proposed a model based on a 'sinusoidal array' to represent the home vector as a sinusoidal wave (phasor), with the peak of the waveform indicating the direction to the nest and the amplitude of the waveform encoding the distance to the nest. The current movement of the agent was also encoded as a sinusoid wave. The sinusoidal array was updated by the element-wise addition of new sinusoidal waves representing the agent's motion. To return to its nest, the agent compared the encoded home vector with its sky-compass heading and moved until its home vector length became zero (i.e. until the amplitude of the sinusoid wave stored in the sinusoidal array became zero). A similar model utilising an encoding of the distance to the nest along different directions but without imposing a sinusoidal constraint was presented by Kim and Hallam (2000); Kim and Lee (2011).

Another neurally plausible model was proposed by Bernardet et al. (2008), who used population coding to represent the animal's heading direction. In this case, the home vector was discretised in 36 directions around the agent, with each direction encoded by a group of 1000 neurons. The number of active neurons in each of these groups represented the distance the agent had travelled in the corresponding direction. Goldschmidt et al. (2015, 2017) used rings of neurons to represent the home vector of a simulated six-legged robot and stored 'global vector' memories for later use in goal-directed navigation.

Maurer (1998) took another approach and used backpropagation to train an artificial neural network (ANN) with two hidden layers to predict the direction and distance to the nest. In this case, the agent was assumed to be moving in fixed steps along one of three directions (forward, left, or right). After training the artificial neural network, during an outward excursion from the nest, the only input to the network was the agent's direction of motion during each step. After each step, the neural network's output encoded the current distance and direction to the nest. However, no mechanism was provided for enabling the agent to return to its nest.

Taking a different approach, Vickerstaff and Di Paolo (2005) used a genetic algorithm to evolve path integration models. This approach had the potential to generate speculative yet biologically plausible neural architectures that could support the path integration computation. The model constraints were encoded by the objective function, the encoding of the input signals, and the neuron model. The authors observed that their most robust and compatible with insect behaviour model resembled an instantiation of the Cartesian bi-component model proposed by Mittelstaedt (1985). Following the same approach, Haferlach et al. (2007) used a genetic algorithm to evolve models of path integration but imposed stricter constraints on the network connectivity while providing two types of neurons to the genetic algorithm, a perceptron with a sigmoid activation function and an integrating neuron with a fixed time constant. After receiving criticism from Vickerstaff and Di Paolo (2008), the authors altered their model (Wessnitzer et al., 2008) to use the compass input processing stage that was proposed by Sakura et al. (2008), which resulted in a more biologically plausible model.

The models mentioned until this point were testing hypotheses derived from behavioural observations rather than trying to model specific neural circuits. As the involvement of the central complex in navigation became more widely recognised (Vitzthum et al., 2002; Strauss, 2002), it opened the door for concrete attempts in modelling the specific neural substrate involved in path integration. It is worth mentioning that some of the artificially evolved architectures (Wittmann and Schwegler, 1995; Wessnitzer et al., 2008) already had similarities with the neuronal projection patterns reported by researchers studying the neuroanatomy of the central complex of the insect brain (for instance Heinze and Homberg, 2007). Subsequently, models of path integration that were deliberately based on neuroanatomical evidence followed. Arena et al. (2013) presented a spatial memory model based on speculative connectivity of the ring neurons in the ellipsoid body of *Drosophila melanogaster*. However, the authors did not present a method for this spatial memory to be utilised for returning to the nest. Stone et al. (2017) combined the results of Haferlach et al. (2007) with anatomical and electrophysiological findings to propose a model grounded on the neuroanatom-

ical evidence of the sweat bee's central complex. More recently, derivatives of Stone et al. (2017) have proposed modifications supporting behavioural evidence and new connectomic results (Le Moël et al., 2019; Hulse et al., 2021).

At the same time, attempts to model the path integration circuit have also taken place in the mammalian literature. Such path integration models include those of McNaughton et al. (1996), Samsonovich and McNaughton (1997), Fuhs and Touretzky (2006), McNaughton et al. (2006), Burgess et al. (2007), and Burgess (2008). However, these models involve neural substrates available in mammals but not insects; in particular, the place cells in the hippocampus (O'Keefe and Dostrovsky, 1971), and grid cells in the medial entorhinal cortex (Hafting et al., 2005) of rodents.

2.2 THE CENTRAL COMPLEX

The central complex (CX) is a brain region conserved across insect species that has been implicated in a variety of navigation behaviours. Studies indicate that the central complex is involved in the processing of polarised light (Heinze and Homberg, 2007), spatial representation of visual cues (Liu et al., 2006), visual spatial memory (Neuser et al., 2008), place learning (Ofstad et al., 2011), orientation control for walking and flying (Triphan et al., 2010; Seelig and Jayaraman, 2015; Cope et al., 2017), as well as various forms of arousal (Ueno et al., 2012). Several behavioural studies attest to this as well as other roles of the central complex in insect behaviour while neurophysiological studies have provided us with the neural circuit substrate that supports those functionalities (Wolff et al., 2015; Wolff and Rubin, 2018; Hulse et al., 2021). Webb and Wystrach (2016) discuss the computations afforded by the neural circuitry, while Stone et al. (2017) proposed a computational model of a subset of the neural circuitry illustrating that it can support the computations needed for path integration.

2.2.1 *Central Complex Anatomy*

The central complex is located in the centre of the insect brain and consists of: the 'central body', the 'protocerebral bridge', and — in pterygote insects — the two 'noduli' (Pfeiffer and Homberg, 2014). The central body is subdivided into the 'upper central body' (CBU) and 'lower central body' (CBL). It is worth mentioning that in the *Drosophila* fruit fly literature the same subdivisions are referred to as 'fan-shaped body' (FB) and 'ellipsoid body' (EB), respectively.

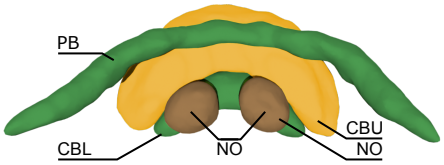

Figure 2.1: Central complex anatomy. The central complex is anatomically divided into the 'protocerebral bridge' (PB), 'upper central body' (CBU), 'lower central body' (CBL), and the two 'noduli' (NO). In the *Drosophila* fruit fly the CBU and CBL are referred to as 'fan-shaped body' (FB) and 'ellipsoid body' (EB), respectively. This pseudo-colour image of the *Cataglyphis nodus* ant's CX was created and adapted from `insectbraindb.org`. The original data are from Habenstein et al. (2020).

Table 2.1: Nomenclature of central complex anatomy.

Drosophila	Other species
Protocerebral bridge (PB)	Protocerebral bridge (PB)
Fan-shaped body (FB)	Upper central body (CBU)
Ellipsoid body (EB)	Lower central body (CBL)
Noduli (NO)	Noduli (NO)

The protocerebral bridge (PB) is a neuropil divided in 16 or 18 glomeruli[2], commonly referred to as 'columns', 'slices' or 'segments'. These are arranged the one next to the other, forming a shape reminiscent of a moustache handlebar spanning the middle line of the brain; half of the glomeruli are located in each hemisphere (Figure 2.1). In some species, the protocerebral bridge appears to be a single continuous structure, while in others appears to be two structures connected by a commissure (Pfeiffer and Homberg, 2014; Honkanen et al., 2019).

The upper central body (CBU) neuropil is neuroanatomically organised in 8 'columns' (left-right axis), in horizontal 'layers' (ventral to dorsal axis), and in 'shells' (anterior-posterior axis) (Wolff et al., 2015; Wolff and Rubin, 2018; Hulse et al., 2021).

The lower central body (CBL) neuropil is neuroanatomically organised in 'columns' (or 16 'wedges' and 8 'tiles' in *Drosophila*), in horizontal 'layers' (or 'rings' in *Drosophila*), and in 3 'shells' (anterior-posterior axis). Wedges are further subdivided in 'demi-wedges' due to some neurons arborising only in half of the wedge's width (Wolff et al., 2015; Pfeiffer and Homberg, 2014).

Finally, the two noduli (NO) consist of three subunits (NO_1, NO_2 and NO_3) each subdivided in compartments and no columnar organisation is discerned (Wolff et al., 2015). Further details about the anatomy and connectivity of the central complex will be discussed in Chapter 3.

2 The number of the glomeruli is dependent on the species. Wolff et al. (2015) reported the identification of 18 glomeruli in *Drosophila* while previous publications had reported or assumed only 16 glomeruli.

2.3 RECENT DEVELOPMENTS

As the research presented in this thesis was done over several years, in this section, I mention some of the most recent relevant research developments. After the publication of Pisokas et al. (2020) more anatomical detail became available about *Drosophila* (Turner-Evans et al., 2020; Hardcastle et al., 2021), especially with the publication of the *Drosophila* hemibrain connectome (Hulse et al., 2021). In addition, progress has been made in other species, including the publication of the projectome of the bumblebee (Sayre et al., 2021). Some conceptual models of path integration specific to *Drosophila melanogaster* that derive from Stone et al. (2017) and are adapted to new evidence were presented in Hulse et al. (2021). Finally, the central complex circuitry was treated in the context of performing transformations between frames of reference by Lyu et al. (2022); Lu et al. (2022).

BIBLIOGRAPHY

Arena, P., Maceo, S., Patane, L., and Strauss, R. (2013). A spiking network for spatial memory formation: Towards a fly-inspired ellipsoid body model. In *Proceedings of the International Joint Conference on Neural Networks*, pages 1–6. IEEE.

Benhamou, S., Sauvé, J.-P., and Bovet, P. (1990). Spatial memory in large scale movements: Efficiency and limitation of the egocentric coding process. *Journal of Theoretical Biology*, 145(1):1–12.

Benhamou, S. and Séguinot, V. (1995). How to find one's way in the labyrinth of path integration models. *Journal of Theoretical Biology*, 174(4):463–466.

Bernardet, U., Bermúdez i Badia, S., and Verschure, P. F. M. J. (2008). A model for the neuronal substrate of dead reckoning and memory in arthropods: a comparative computational and behavioral study. *Theory in Biosciences*, 127(2):163–175.

Burgess, N. (2008). Grid cells and theta as oscillatory interference: Theory and predictions. *Hippocampus*, 18(12):1157–1174.

Burgess, N., Barry, C., and O'Keefe, J. (2007). An oscillatory interference model of grid cell firing. *Hippocampus*, 17(9):801–812.

Cheng, K., Narendra, A., and Wehner, R. (2005). Behavioral ecology of odometric memories in desert ants: Acquisition, retention, and integration. *Behavioral Ecology*, 17(2):227–235.

Collett, T. S. (1996). Insect navigation en route to the goal: multiple strategies for the use of landmarks. *Journal of Experimental Biology*, 199(1):227–235.

Collett, T. S. (2019). Path integration: how details of the honeybee waggle dance and the foraging strategies of desert ants might help in understanding its mechanisms. *Journal of Experimental Biology*, 222(11):jeb205187.

Collett, T. S. and Collett, M. (2002). Memory use in insect visual navigation. *Nature Reviews Neuroscience*, 3(7):542–552.

Collett, T. S., Dillmann, E., Giger, A., and Wehner, R. (1992). Visual landmarks and route following in desert ants. *Journal of Comparative Physiology A*, 170(4):435–442.

Collett, T. S. and Rees, J. A. (1997). View-based navigation in hymenoptera: multiple strategies of landmark guidance in the approach to a feeder. *Journal of Comparative Physiology A*, 181(1):47–58.

Cope, A. J., Sabo, C., Vasilaki, E., Barron, A. B., and Marshall, J. A. R. (2017). A computational model of the integration of landmarks and motion in the insect central complex. *PLoS ONE*, 12(2):e0172325.

Darwin, C. (1873). Origin of certain instincts. *Nature*, 7(179):417–418.

Etienne, A. S. and Jeffery, K. J. (2004). Path integration in mammals. *Hippocampus*, 14(2):180–192.

Fuhs, M. C. and Touretzky, D. S. (2006). A spin glass model of path integration in rat medial entorhinal cortex. *Journal of Neuroscience*, 26(16):4266–4276.

Gallistel, C. R. (1990). *The organization of learning*. Cambridge, Mass. : MIT Press.

Goldschmidt, D., Dasgupta, S., Wörgötter, F., and Manoonpong, P. (2015). A neural path integration mechanism for adaptive vector navigation in autonomous agents. In *International Joint Conference on Neural Networks*, pages 1–8. IEEE.

Goldschmidt, D., Manoonpong, P., and Dasgupta, S. (2017). A neurocomputational model of goal-directed navigation in insect-inspired artificial agents. *Frontiers in Neurorobotics*, 11:1–17.

Habenstein, J., Amini, E., Grübel, K., el Jundi, B., and Rössler, W. (2020). The brain of *Cataglyphis* ants: Neuronal organization and visual projections. *Journal of Comparative Neurology*, 528(18):3479–3506.

Haferlach, T., Wessnitzer, J., Mangan, M., and Webb, B. (2007). Evolving a neural model of insect path integration. *Adaptive Behavior*, 15(3):273–287.

Hafting, T., Fyhn, M., Molden, S., Moser, M.-B., and Moser, E. I. (2005). Microstructure of a spatial map in the entorhinal cortex. *Nature*, 436(7052):801.

Hardcastle, B. J., Omoto, J. J., Kandimalla, P., Nguyen, B.-C. M., Keleş, M. F., Boyd, N. K., Hartenstein, V., and Frye, M. A. (2021). A visual pathway for skylight polarization processing in *Drosophila*. *eLife*, 10:e63225.

Hartmann, G. and Wehner, R. (1995). The ant's path integration system: a neural architecture. *Biological Cybernetics*, 73(6):483–497.

Heinze, S. and Homberg, U. (2007). Maplike representation of celestial e-vector orientations in the brain of an insect. *Science*, 315(5814):995–997.

Heinze, S., Narendra, A., and Cheung, A. (2018). Principles of insect path integration. *Current Biology*, 28(17):R1043–R1058.

Honkanen, A., Adden, A., da Silva Freitas, J., and Heinze, S. (2019). The insect central complex and the neural basis of navigational strategies. *The Journal of Experimental Biology*, 222(Suppl 1):jeb188854.

Hulse, B. K., Haberkern, H., Franconville, R., Turner-Evans, D. B., Takemura, S.-y., Wolff, T., Noorman, M., Dreher, M., Dan, C., Parekh, R., et al. (2021). A connectome of the drosophila central complex reveals network motifs suitable for flexible navigation and context-dependent action selection. *eLife*, 10:e66039.

Kim, D. and Hallam, J. C. T. (2000). Neural network approach to path integration for homing navigation. In Meyer, A., Berthoz, A., Floreano, D., Roitblat, H., and Wilson, S. W., editors, *From Animals to Animats 6*, pages 228–235. MIT Press.

Kim, D. and Lee, J. (2011). Path integration mechanism with coarse coding of neurons. *Neural Processing Letters*, 34(3):277–291.

Knaden, M. and Wehner, R. (2005). Ant navigation: resetting the path integrator. *Journal of Experimental Biology*, 209(1):26–31.

Le Moël, F., Stone, T., Lihoreau, M., Wystrach, A., and Webb, B. (2019). The central complex as a potential substrate for vector based navigation. *Frontiers in psychology*, 10:690.

Liu, G., Seiler, H., Wen, A., Zars, T., Ito, K., Wolf, R., Heisenberg, M., and Liu, L. (2006). Distinct memory traces for two visual features in the *Drosophila* brain. *Nature*, 439(7076):551–556.

Lu, J., Behbahani, A. H., Hamburg, L., Westeinde, E. A., Dawson, P. M., Lyu, C., Maimon, G., Dickinson, M. H., Druckmann, S., and Wilson, R. I. (2022). Transforming representations of movement from body-to world-centric space. *Nature*, 601(7891):98–104.

Lyu, C., Abbott, L. F., and Maimon, G. (2022). Building an allocentric travelling direction signal via vector computation. *Nature*, 601(7891):92–97.

Maurer, R. (1998). A connectionist model of path integration with and without a representation of distance to the starting point. *Psychobiology*, 26(1):21–35.

McNaughton, B. L., Barnes, C., Gerrard, J. L., Gothard, K., Jung, M. W., Knierim, J. J., Kudrimoti, H., Qin, Y., Skaggs, W. E., Suster, M., and Weaver, K. L. (1996). Deciphering the hippocampal polyglot: the hippocampus as a path integration system. *Journal of experimental biology*, 199(1):173–185.

McNaughton, B. L., Battaglia, F. P., Jensen, O., Moser, E. I., and Moser, M.-B. (2006). Path integration and the neural basis of the 'cognitive map'. *Nature Reviews Neuroscience*, 7(8):663–678.

Menzel, R. and Muller, U. (1996). Learning and memory in honeybees: From behavior to neural substrates. *Annual Review of Neuroscience*, 19:379–404.

Mittelstaedt, H. (1985). Analytical cybernetics of spider navigation. In Barth, F. G., editor, *Neurobiology of Arachnids*, pages 298–316. Springer Berlin Heidelberg.

Mittelstaedt, H. and Mittelstaedt, M. L. (1982). Homing by path integration. In *Avian navigation*, pages 290–297. Springer.

Mittelstaedt, M. L. and Mittelstaedt, H. (1980). Homing by path integration in a mammal. *Die Naturwissenschaften*, 67(11):566–567.

Morgan, E. D. (2009). Trail pheromones of ants. *Physiological Entomology*, 34(1):1–17.

Müller, M. and Wehner, R. (1988). Path integration in desert ants, *Cataglyphis fortis*. *Proceedings of the National Academy of Sciences*, 85(14):5287–5290.

Müller, U. (2013). Memory phases and signaling cascades in honeybees. In Menzel, R. and Benjamin, P. R., editors, *Handbook of Behavioral Neuroscience*, volume 22, chapter 31, pages 433–441. Elsevier.

Muser, B., Sommer, S., Wolf, H., and Wehner, R. (2005). Foraging ecology of the thermophilic Australian desert ant, *Melophorus bagoti*. *Australian Journal of Zoology*, 53(5):301–311.

Neuser, K., Triphan, T., Mronz, M., Poeck, B., and Strauss, R. (2008). Analysis of a spatial orientation memory in *Drosophila*. *Nature*, 453(7199):1244–1247.

Ofstad, T. A., Zuker, C. S., and Reiser, M. B. (2011). Visual place learning in *Drosophila melanogaster*. *Nature*, 474(7350):204–209.

O'Keefe, J. and Dostrovsky, J. (1971). The hippocampus as a spatial map. preliminary evidence from unit activity in the freely-moving rat. *Brain Research*, 34(1):171–175.

Pfeiffer, K. and Homberg, U. (2014). Organization and functional roles of the central complex in the insect brain. *Annual Review of Entomology*, 59(1):165–184.

Pisokas, I., Heinze, S., and Webb, B. (2020). The head direction circuit of two insect species. *eLife*, 9:e53985.

Pisokas, I., Rössler, W., Webb, B., Zeil, J., and Narendra, A. (2022). Anesthesia disrupts distance, but not direction, of path integration memory. *Current Biology*, 32(2):445–

452.

Saint Paul, U. v. (1982). Do geese use path integration for walking home? In *Avian navigation*, pages 298–307. Springer.

Sakura, M., Lambrinos, D., and Labhart, T. (2008). Polarized skylight navigation in insects: model and electrophysiology of e-vector coding by neurons in the central complex. *Journal of neurophysiology*, 99(2):667–682.

Samsonovich, A. and McNaughton, B. L. (1997). Path integration and cognitive mapping in a continuous attractor neural network model. *Journal of Neuroscience*, 17(15):5900–5920.

Sayre, M. E., Templin, R., Chavez, J., Kempenaers, J., and Heinze, S. (2021). A projectome of the bumblebee central complex. *eLife*, 10:e68911.

Schmid-Hempel, P. (1984). Individually different foraging methods in the desert ant *Cataglyphis bicolor* (Hymenoptera, Formicidae). *Behavioral Ecology and Sociobiology*, 14(4):263–271.

Seelig, J. D. and Jayaraman, V. (2015). Neural dynamics for landmark orientation and angular path integration. *Nature*, 521(7551):186–191.

Stone, T., Webb, B., Adden, A., Weddig, N. B., Honkanen, A., Templin, R., Wcislo, W., Scimeca, L., Warrant, E., and Heinze, S. (2017). An anatomically constrained model for path integration in the bee brain. *Current Biology*, 27(20):3069–3085.

Strauss, R. (2002). The central complex and the genetic dissection of locomotor behaviour. *Current Opinion in Neurobiology*, 12(6):633–638.

Tomchik, S. M. and Davis, R. L. (2013). *Drosophila* memory research through four eras: Genetic, molecular biology, neuroanatomy, and systems neuroscience. In Menzel, R. and Benjamin, P. R., editors, *Handbook of Behavioral Neuroscience*, volume 22, chapter 27, pages 359–377. Elsevier.

Triphan, T., Poeck, B., Neuser, K., and Strauss, R. (2010). Visual targeting of motor actions in climbing *Drosophila*. *Current Biology*, 20(7):663–668.

Turner-Evans, D. B., Jensen, K. T., Ali, S., Paterson, T., Sheridan, A., Ray, R. P., Wolff, T., Lauritzen, J. S., Rubin, G. M., Bock, D. D., and Jayaraman, V. (2020). The neuroanatomical ultrastructure and function of a biological ring attractor. *Neuron*, 108(1):145–163.

Ueno, T., Tomita, J., Tanimoto, H., Endo, K., Ito, K., Kume, S., and Kume, K. (2012). Identification of a dopamine pathway that regulates sleep and arousal in *Drosophila*. *Nature neuroscience*, 15(11):1516–1523.

Vickerstaff, R. J. and Di Paolo, E. A. (2005). Evolving neural models of path integration. *Journal of Experimental Biology*, 208(17):3349–3366.

Vickerstaff, R. J. and Di Paolo, E. A. (2008). Regarding compass response functions for modeling path integration: Comment on "evolving a neural model of insect path integration". *Adaptive Behavior*, 16(4):275–276.

Vitzthum, H., Müller, M., and Homberg, U. (2002). Neurons of the central complex of the locust *Schistocerca gregaria* are sensitive to polarized light. *Journal of Neuroscience*, 22(3):1114–1125.

von Frisch, K. (1967). *The dance language and orientation of bees*. Harvard University Press.

Webb, B. and Wystrach, A. (2016). Neural mechanisms of insect navigation. *Current Opinion in Insect Science*, 15:27–39.

Wehner, R. (2003). Desert ant navigation: How miniature brains solve complex tasks. *Journal of Comparative Physiology A*, 189(8):579–588.

Wehner, R., Michel, B., and Antonsen, P. (1996). Visual navigation in insects: coupling of egocentric and geocentric information. *Journal of Experimental Biology*, 199(1):129–140.

Wessnitzer, J., Haferlach, T., Mangan, M., and Webb, B. (2008). Path integration using a model of e-vector orientation coding in the insect brain: reply to Vickerstaff and Di Paolo. *Adaptive Behavior*, 16(4):277–280.

Wittmann, T. and Schwegler, H. (1995). Path integration — a network model. *Biological Cybernetics*, 73(6):569–575.

Wolff, T., Iyer, N. A., and Rubin, G. M. (2015). Neuroarchitecture and neuroanatomy of the *Drosophila* central complex: A GAL4-based dissection of protocerebral bridge neurons and circuits. *Journal of Comparative Neurology*, 523(7):997–1037.

Wolff, T. and Rubin, G. M. (2018). Neuroarchitecture of the *Drosophila* central complex: A catalog of nodulus and asymmetrical body neurons and a revision of the protocerebral bridge catalog. *Journal of Comparative Neurology*, 526(16):2585–2611.

Ziegler, P. E. and Wehner, R. (1997). Time-courses of memory decay in vector-based and landmark-based systems of navigation in desert ants, *Cataglyphis fortis*. *Journal of Comparative Physiology A*, 181(1):13–20.

Part I

HEAD DIRECTION TRACKING

Two pieces of information are required for performing path integration, the direction and speed of travel at each instant in time. A home vector linking the current location with the origin of the voyage can be calculated by integrating those two pieces of information as velocity vectors over time.

Part i of this thesis is concerned with the first piece of required information, the animal's direction of travel. It consists of one study investigating the effective neuronal circuit underlying the head direction tracking system of two insect species.

A comparison of the dynamical response properties of the two head direction tracking circuits reveals adaptations supporting the behavioural ecology of each species, and the circuit features responsible for these differences are identified.

The chapter contained in this part was published in the journal eLife in 2020 (Pisokas et al., 2020). The paper was co-authored by myself, Stanley Heinze, and Barbara Webb. As the lead author, I was responsible for the conceptualisation, modelling, analysis, validation, visualisations, methodology, writing of the original draft, reviewing, and editing.

Pisokas, I., Heinze, S., and Webb, B. (2020). The head direction circuit of two insect species. *eLife*, 9:e53985.

3

THE HEAD DIRECTION CIRCUIT OF TWO INSECT SPECIES

Recent studies of the Central Complex in the brain of the fruit fly have identified neurons with activity that tracks the animal's heading direction. These neurons are part of a neuronal circuit with dynamics resembling those of a ring attractor. The homologous circuit in other insects has similar topographic structure but with significant structural and connectivity differences. We model the connectivity patterns of two insect species to investigate the effect of these differences on the dynamics of the circuit. We illustrate that the circuit found in locusts can also operate as a ring attractor but differences in the inhibition pattern enable the fruit fly circuit to respond faster to heading changes while additional recurrent connections render the locust circuit more tolerant to noise. Our findings demonstrate that subtle differences in neuronal projection patterns can have a significant effect on circuit performance and illustrate the need for a comparative approach in neuroscience.

3.1 INTRODUCTION

For a variety of behaviours that relocate an insect in its environment, it is important for the animal to be able to keep track of its heading relative to salient external objects. This external reference object could be a nearby target, a distant landmark or even a celestial beacon. In insects, the discovery of a neuronal circuit with activity that tracks heading direction provides a potential basis for an internal compass mechanism (Zhang, 1996; Homberg, 2004; Heinze and Reppert, 2012). Such an internal compass can mediate a simple navigation competence such as maintaining a straight course (Dacke et al., 2003; Mouritsen and Frost, 2002) or reorienting to a target after distractions (Neuser et al., 2008), but is also essential for the more complex navigational process of path integration (or dead reckoning) which enables central-place foragers to return directly to their nest after long and convoluted outward paths (Darwin, 1873; von Frisch, 1967; Mittelstaedt, 1985; Müller and Wehner, 1988). While the neural basis underlying these navigation strategies is not known in detail, a brain region called the central complex (CX) is implicated in many navigation-related processes.

The CX of the insect brain is an unpaired, midline-spanning set of neuropils that consist of the protocerebral bridge (PB), the ellipsoid body (also called lower division of the central body), the fan-shaped body (also called upper division of the central

body) and the paired noduli. These neuropils and their characteristic internal organisation in vertical slices combined with horizontal layers are highly conserved across insect species. This regular neuroarchitecture is generated by sets of columnar cells, innervating individual slices, as well as large tangential neurons, innervating entire layers. The structured projection patterns of columnar cells result in the PB being organised in 16 or 18 contiguous glomeruli and the ellipsoid body (EB) in eight adjoined tiles.

Crucially, the CX is of key importance for the computations required to derive a heading signal (Pfeiffer and Homberg, 2014; Triphan et al., 2010; Neuser et al., 2008; Ofstad et al., 2011; Homberg, 2004; Homberg et al., 2011). In locusts (*Schistocerca gregaria*), intracellular recordings have revealed a neuronal layout that topographically maps the animal's orientation relative to simulated skylight cues, including polarised light and point sources of light (Heinze and Homberg, 2007; el Jundi et al., 2014; Pegel et al., 2019). Calcium imaging of columnar neurons connecting the EB and the PB (E-PG neurons) in the fruit fly *Drosophila melanogaster* revealed that the E-PG neuronal ensemble maintains localised spiking activity — commonly called an activity 'bump' — that moves from one group of neurons to the next as the animal rotates with respect to its surrounding (Seelig and Jayaraman, 2015; Giraldo et al., 2018). This has been confirmed for restrained flies walking on an air-supported rotating ball (Seelig and Jayaraman, 2015) as well as tethered flies flying in a virtual reality environment (Kim et al., 2017). Notably, the heading signal (the activity 'bump') is maintained even when the visual stimulus is removed, and it moves relative to the (no longer visible) cue as the animal walks in darkness (Seelig and Jayaraman, 2015). The underlying circuit therefore combines idiothetic and allothetic information into a coherent heading signal. Overall, this neuronal activity appears to constitute an internal encoding of heading in the insect's CX, which closely resembles the hypothetical ring attractor (Amari, 1977) proposed by Skaggs et al. (1995) to account for the rat 'head direction' cells (Taube et al., 1990; Blair and Sharp, 1995; Redish et al., 1996; Stackman and Taube, 1998; Goodridge et al., 1998; Goodridge and Touretzky, 2000; Sharp et al., 2001; Taube and Bassett, 2003; Stratton et al., 2010). That is, the activity has the following key properties associated with ring attractors: input to the circuit results in a single localised 'bump' of activity — centred in one subset of the neurons — while other neuronal units are silenced; the activity 'bump' can move around the attractor space, which forms a ring, in a manner that consistently tracks some property of the input; and the 'bump' of activity is maintained for some time after all input is removed. These properties can be obtained, in computational neural models, by utilising opposing excitatory and inhibitory connections with excitatory lateral connections to neighbouring neuronal units and inhibitory ones affecting neurons on the opposite side of the ring.

In recent years, several computational models of the fly's CX heading tracking circuit have been presented. Some of these models are abstract while others attempt to ascribe particular roles to neurons (Cope et al., 2017; Kakaria and de Bivort, 2017; Su et al., 2017; Kim et al., 2017). Cope et al. (2017) proposed a ring attractor model that is inspired by the rat 'head direction' cell model of Skaggs et al. (1995). Kakaria and de Bivort (2017) presented a spiking neuronal model consisting of the four types of CX neurons shown to play a role in heading encoding: E-PG, P-EN, P-EG, and Delta7 neurons. Their model demonstrated that this neuron set is sufficient for exhibiting ring attractor behaviour. In contrast, Su et al. (2017) implemented a spiking neuronal model consisting of the E-PG, P-EN, and P-EG neurons with inhibition provided by a group of R ring neurons. In both neurobiological studies and computational models, the key neurons variously involved in the hypothetical ring attractor circuit are the E-PG, P-EN, P-EG, Delta7 and R ring neurons (Wolff and Rubin, 2018; Wolff et al., 2015; Kakaria and de Bivort, 2017; Su et al., 2017; Green et al., 2017; Kim et al., 2017). The E-PG, P-EN and P-EG neurons have been postulated to be excitatory while Delta7 or R ring neurons are conjectured to be mediating the inhibition (Kakaria and de Bivort, 2017; Su et al., 2017). The E-PG and P-EN neurons are postulated to form synapses in the PB and in the EB forming a recurrent circuit. The ring attractor state is set by a mapping of the azimuthal position of visual cues to E-PG neurons around the ring which are assumed to receive the positional input to this circuit. Furthermore, P-EN neurons shift the heading signal around the ring attractor when stimulated, in a fashion similar to the left-right rotation neurons proposed by Skaggs et al. (1995) (Turner-Evans et al., 2017; Green et al., 2017). In principle, two main types of ring attractor implementation exist: one with local excitation and global, uniform, inhibition and another one characterised by sinusoidally modulated inhibition across the ring attractor. Kim et al. (2017) have experimentally explored the type of ring attractor that could underlie the head direction circuit of the fruit fly and concluded that the observed dynamics of E-PG neurons can best be modelled using a ring attractor with local excitation and uniform global inhibition.

The above outlined overall circuit depends critically on the detailed anatomical connections between cell types of the CX, so that the implementation of a specific type of ring attractor imposes additional constraints on the neuronal connection patterns and individual morphologies. Although the CX is highly conserved on a broad level, details at the level of single neurons vary between insect species. Yet, conclusions about the function of the circuit are usually drawn from *Drosophila* data and applied to insects in general. Given numerous differences in the CX neuroarchitecture between insects, we asked whether a ring attractor circuit is also plausible when taking into account anatomical data from another model species, the desert locust.

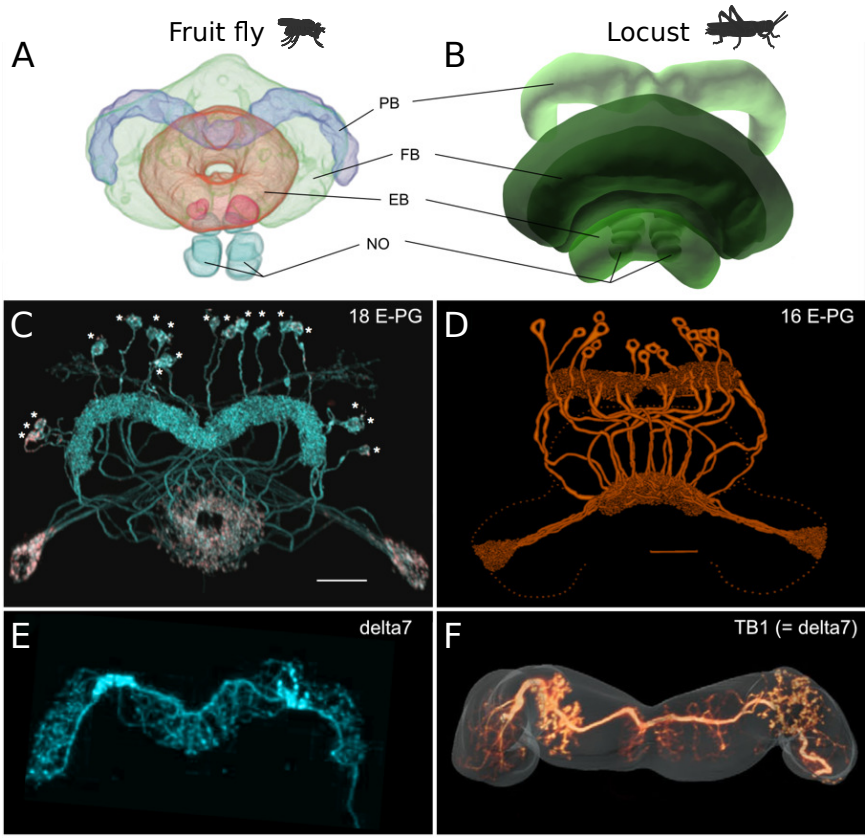

Figure 3.1: Anatomical differences between two species. There are three apparent differences between the CX of the fruit fly (*Drosophila melanogaster*) and the desert locust (*Schistocerca gregaria*). (**A**, **B**) The ellipsoid body in the fruit fly has a toroidal shape while in the locust is crescent-shaped so its two ends are separate. (**C**, **D**) The protocerebral bridge consists of 18 glomeruli and 18 corresponding E-PG and P-EG neurons in the fruit fly (see Table 3.3) while in the locust there are 16 glomeruli and neurons innervating them. (**E**, **F**) The Delta7 neurons in the fruit fly have postsynaptic domains along the whole length of their neurite while in the desert locust only in specific sections with gaps in between.

Three main differences are evident when comparing the CX of the fruit fly and the locust (Figure 3.1). First, as in most insects except *Drosophila*, the EB of the locust is not closed around the edges, but is crescent-shaped, preventing the E-PG neurons from forming a physical ring. Second, the *Drosophila* PB consists of nine glomeruli per hemisphere, and accordingly 18 groups of E-PG neurons. In locusts, there are eight glomeruli per hemisphere and 16 groups of neurons. Third, a key part of the proposed ring attractor circuit, the Delta7 neurons (TB1 neurons in the locust) differ strikingly in their arborization pattern across the width of the PB. Whereas these cells possess two columnar output sites located eight glomeruli apart in all species, their dendrites have an approximately uniform density across the PB glomeruli in *Drosophila*. This differs substantially from the dendritic distribution in the desert locust, in which the postsynaptic domains of the eight Delta7 neurons are restricted to particular glomeruli of the PB, avoiding the regions around the output branches. This pattern is conserved in other species as well, such as in the Monarch butterfly (*Danaus plexippus*), the sweat bee (*Megalopta genalis*), as well as in two species of dung beetles (*Scarabaeus lamarcki* and *Scarabaeus satyrus*) (Heinze and Homberg, 2007; Heinze et al., 2013; Stone et al., 2017; el Jundi et al., 2018). Given these three differences of the *Drosophila* CX from other insects, we explored the functional consequences of each difference and how these might relate to the behavioural characteristics of each insect.

To explore this question, we used the anatomical projection patterns of the main CX neuron types in flies and locusts and derived the effective neuronal circuits by simplifying anatomical redundancy. Both resulting circuits indeed have the structural topology of a ring attractor. Despite significant anatomical differences the homologous circuits in the fruit fly and the locust are structurally similar but not identical. Their differences have significant functional effect in the ability of the two circuits to track fast rotational movements and to maintain a stable heading signal. Our results highlight that even seemingly small differences in the distribution of dendritic fibres can affect the behavioural repertoire of an animal. These differences, emerging from morphologically distinct single neurons, highlight the importance of a comparative approach to neuroscience. Rather than assuming results from model species are generalisable, we gain deeper insight into function by discovering which elements are actually shared across species and what are the consequences of observed variation.

3.2 RESULTS

3.2.1 *The effective circuit*

The neuronal projection data of the fruit fly and the desert locust were encoded in connectivity matrices and used for the simulations we report here (Wolff et al., 2015; Wolff and Rubin, 2018; Heinze and Homberg, 2007, 2008, 2009; Heinze et al., 2009). While some simplifications could not be avoided, we have exclusively used projection patterns grounded in anatomical data for each species to construct the connectivity matrices. To facilitate conceptual understanding, we visualised the connectivity matrices as directed graphs and analysed the effective connectivity of the neuronal components of the CX for both species.

3.2.1.1 *Inhibitory circuit*

First, we focus on the inhibitory portion of the circuit. Study of the actual neuronal anatomy of Delta7 neurons in the PB shows that, in both species, each Delta7 neuron has presynaptic terminal domains in two or three glomeruli along the PB (Heinze and Homberg, 2007; Wolff and Rubin, 2018). These presynaptic terminal domains are separated by seven glomeruli (Figures 3.2A and 3.2D). In *Drosophila*, the Delta7 neurons have postsynaptic terminals across all remaining glomeruli of the PB (Wolff and Rubin, 2018; Franconville et al., 2018) while in locusts the Delta7 neurons have postsynaptic terminal domains only in specific glomeruli (Heinze and Homberg, 2007; Beetz et al., 2015; von Hadeln et al., 2020).

There are eight types of Delta7 neurons in the PB, each having the same pattern of synaptic terminals shifted by one glomerulus (Figures 3.2A and 3.2D). Within each glomerulus, the Delta7 neuron with presynaptic terminals is assumed to form synapses with all other Delta7 neurons that have postsynaptic terminals in the same glomerulus. Since each Delta7 neuron is presynaptic to the same Delta7 neurons in two or three glomeruli along the PB, we reduce these two or three synaptic domains to one single equivalent synapse between each pair of Delta7 neurons in order to draw a simplified equivalent circuit (Figures 3.2B and 3.2E). In order to highlight the main functional differences, we redrew these neuronal circuits in a network graph form which revealed an eight-fold radial symmetry in both species, regardless of the different neuronal anatomies and the anatomical presence of nine PB glomeruli in flies.

The network graph form of the circuit further makes evident a global, uniform, inhibition pattern in the case of the fruit fly versus a local inhibition pattern in the case of the locust (Figures 3.2C and 3.2F). That is, in fruit flies each Delta7 neuron forms

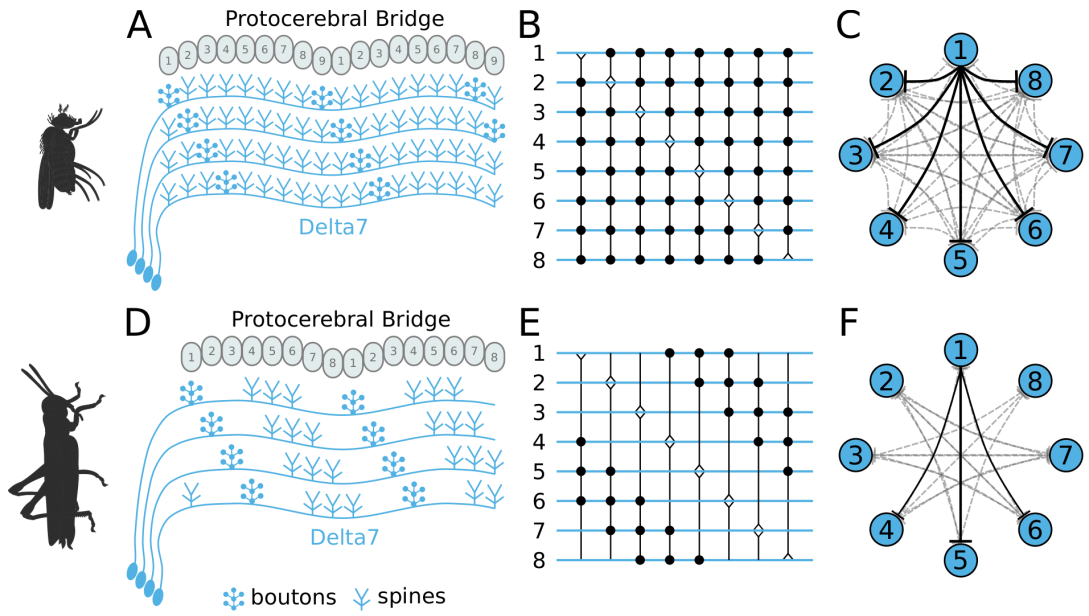

Figure 3.2: Effective connectivity of the inhibitory (Delta7) neurons. On the top row is the fruit fly circuit, on the bottom row is the locust circuit. In **A** and **D**, four examples of how the eight types of Delta7 neurons innervate the PB are illustrated. In both species, presynaptic domains are separated by seven glomeruli. (**B** and **E**) Effective connectivity. Each horizontal blue line represents one Delta7 neuron. Vertical lines represent axons, with triangles indicating outputs from Delta7 neurons and filled circles representing inhibitory synapses between axons and other Delta7 neurons. (**C** and **F**) Alternative depiction of the circuit in graph form with blue circles representing Delta7 neurons and lines representing inhibitory synapses between pairs of neurons. Each Delta7 neuron inhibits all other Delta7s in the fruit fly (**C**), but only more distant Delta7s in the locust (**F**).

synapses and inhibits all other Delta7 neurons. In contrast, in the locust each Delta7 neuron only inhibits a subset of Delta7 neurons with weakening synaptic strengths towards its nearest neighbours (Heinze and Homberg, 2007). The effective global inhibition pattern found in the fruit fly fits the observation of Kim et al. (2017) that calcium dynamics better matched a ring attractor with global inhibition in this species.

3.2.1.2 *Excitatory circuit*

We next focused on the excitatory portion of the hypothetical ring attractor circuit. For deriving the effective circuit of the excitatory portion of the network, it was necessary to employ an unconventional numbering scheme for the PB glomeruli; that is, in both hemispheres, glomeruli are numbered incrementally from left to right, 1–9 for the fruit fly (Figure 3.3) and 1–8 for the locust (Figure 3.4). EB tiles were numbered 1 to 8 for both species. For brevity, throughout this text, we denote a tile numbered '1' as T1 and a glomerulus numbered '1' as G1. Neurons are numbered by the glomerulus they

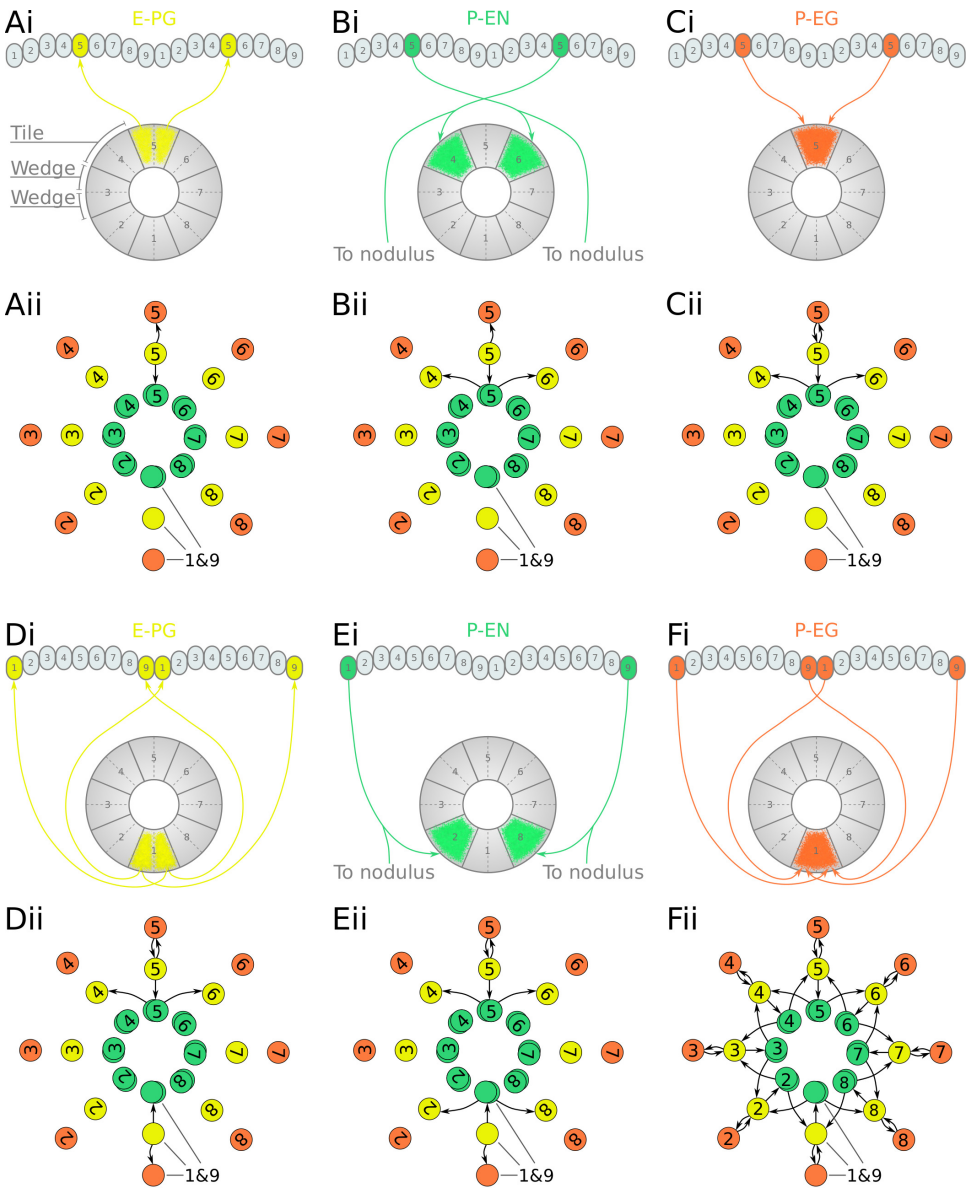

Figure 3.3: Projection patterns of the excitatory portion of the fruit fly circuit. (**Ai–Fi**) Examples of E-PG (combined E-PG and E-PG$_T$, see Table 3.3), P-EN and P-EG neurons with their synaptic domains and projection patterns. (**Aii–Cii**) Step by step derivation of the effective circuit as a directed graph network (see main text for a complete description). Each coloured disc represents a group of neurons with arrows representing excitatory synaptic connections. Pairs of E-PG and P-EG neurons can be considered to act as single units connecting the respective tile to equally numbered PB glomeruli in both hemispheres, while P-EN neurons are shown overlapped because each receives input only from its contralateral nodulus. (**Dii–Eii**) The connectivity also allows neurons innervating glomeruli 1 and 9 to act as a single unit. (**Fii**) Depiction of the complete effective connectivity of the excitatory circuit, which has an eight-fold radial symmetry.

innervate, using a numerical subscript, e.g. P-EN$_1$ for the P-EN neurons innervating glomeruli G1.

In accordance with calcium imaging (Turner-Evans et al., 2017; Green et al., 2017), simulating the fruit fly and locust circuits confirmed that there are two activity 'bumps' along the PB. The choice of unconventional numbering scheme for the PB glomeruli has as an effect that both activity 'bumps' are centred around neurons innervating identically numbered glomeruli (Supplementary Figure 3.18). We use this symmetry to simplify the circuit and derive the effective connectivity.

First, we analyse and derive the effective circuit of the fruit fly. Under our numbering scheme, each E-PG neuron has synaptic domains in identically numbered EB tiles and PB glomeruli (e.g. Figure 3.3Ai). That is, E-PG$_5$ neurons have synaptic domains in tile T5 and glomeruli G5 in both hemispheres of the PB. Since activity is symmetrical in both PB hemispheres, the pair of E-PG$_5$ neurons forms a single functional unit, as illustrated in the equivalent circuit (Figure 3.3Aii), with single synaptic connections shown to the corresponding P-EN$_5$ and P-EG$_5$ neurons. P-EN neurons, however, connect corresponding glomeruli from each PB hemisphere to two tiles, one shifted to the left and one to the right, for example, P-EN$_5$ would connect glomeruli G5 to tiles T4 and T6 (Figure 3.3Bi). P-EN neurons are indicated as two overlapped discs in the equivalent circuit (Figure 3.3Bii) because even though each pair receives common input in the glomeruli they also receive differential angular velocity input, depending on the hemisphere they innervate. The pair of P-EN$_5$ neurons forms synapses with E-PG$_4$ neurons in T4 and E-PG$_6$ neurons in T6, respectively. A third class of cells, P-EG neurons, innervate equally numbered glomeruli and tiles, following the same pattern as the E-PG neurons but with their presynaptic and postsynaptic terminals on opposite ends (Figure 3.3Ci), and are thus illustrated as single functional units in the equivalent circuit (Figure 3.3Cii). Following the synaptic connections forward around the circuit (Supplementary Figure 3.19), E-PG$_4$ and E-PG$_6$ neurons innervate glomeruli G4 and G6 respectively, forming synapses with P-EN and P-EG neurons in these glomeruli; P-EG$_6$ make reciprocal connections to E-PG$_6$; and the paired P-EN$_6$ neurons make connections back to T5 and onward to T7, etc. Thus the connectivity pattern shown in Figure 3.3Cii is repeated all the way around the circuit. Crucially, tile T1 is innervated by both E-PG$_1$ and E-PG$_9$ which also innervate glomeruli G1 and G9, respectively (Figure 3.3Di). These neurons can also be treated as one unit, E-PG$_{1\&9}$, in the effective circuit (Figure 3.3Dii) because they receive common synaptic input. Since there are no P-EN neurons innervating the innermost glomeruli (G9 in the left and G1 in the right hemisphere), P-EN$_1$ and P-EN$_9$ consist a pair of neurons in the equivalent circuit, making onward connections to tiles T2 and T8, and thus E-PG$_2$ and E-PG$_8$, respectively (Figure 3.3Ei and 3.3Eii). Therefore, the effective circuit of the fruit fly has an eight-fold radial symmetry despite the nine PB glomeruli (illustrated in Figure 3.3Fii).

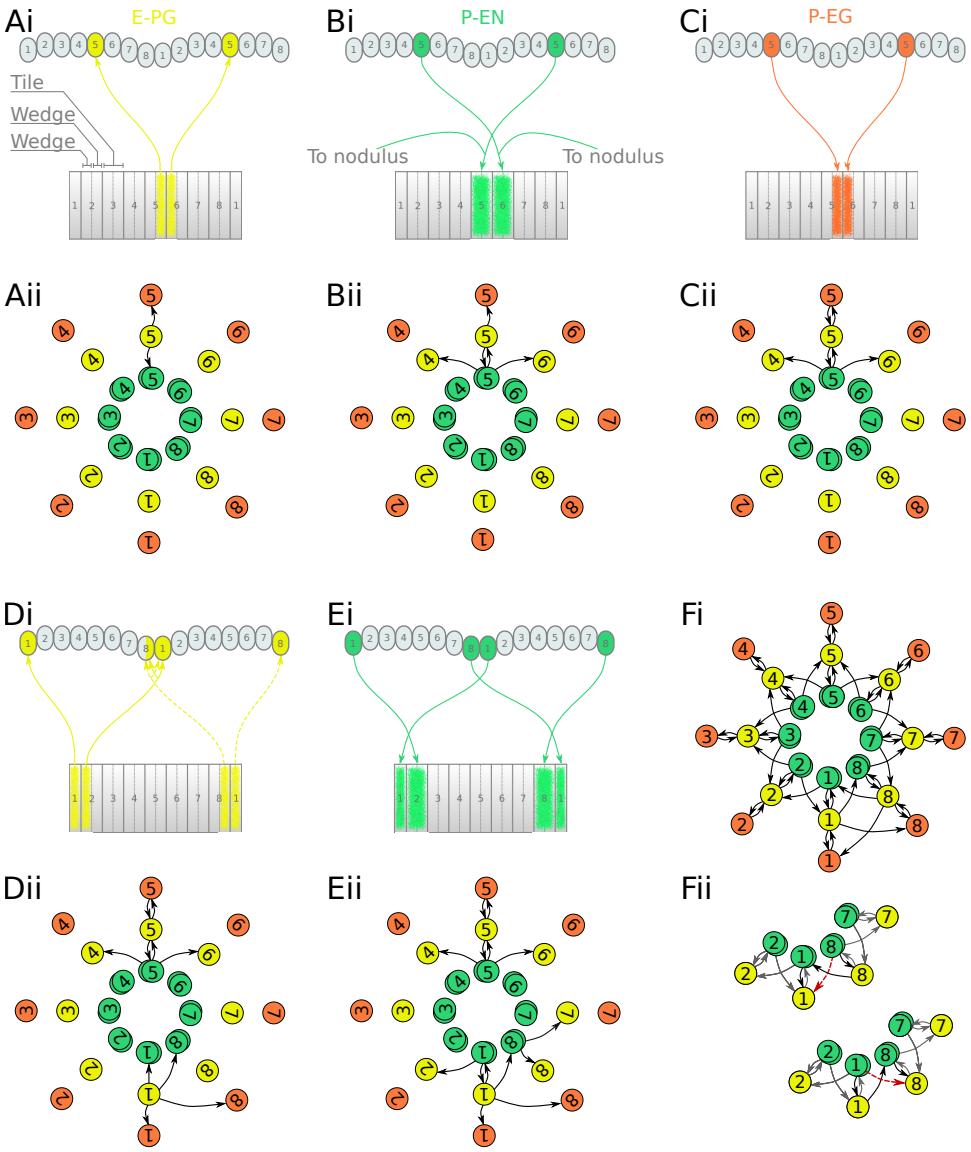

Figure 3.4: Projection patterns of the excitatory portion of the locust circuit. (**Ai–Ei**) Examples of E-PG, P-EN and P-EG neurons with their synaptic domains and projection patterns. (**Aii–Eii**) Step by step derivation of the effective circuit (see main text for a complete description). Each coloured disc represents a group of neurons with arrows representing excitatory synaptic connections. Pairs of E-PG and P-EG neurons can be considered to act as single units connecting the respective tile to equally numbered PB glomeruli in both hemispheres, while P-EN neurons are shown overlapped because each receives input only from its contralateral nodulus. Note that the numbering of the EB slices is conceptual and arbitrary, chosen to assist description of the circuit organisation; what matters for the connectivity is the overlap of the synaptic domains in the EB and not the particular numbering choice. (**Fi**) The complete effective connectivity of the locust excitatory circuit closely resembles that of the fruit fly. (**Fii**) Between octants 1 and 8, the locust circuit obtains functional connectivity from P-EN$_8$ to 'neighbouring' E-PG$_1$ (red dashed arrow) via three actual connections: P-EN$_8$ to E-PG$_8$ to P-EN$_1$ to E-PG$_1$ (black arrows); and equivalently for P-EN$_1$ to E-PG$_8$.

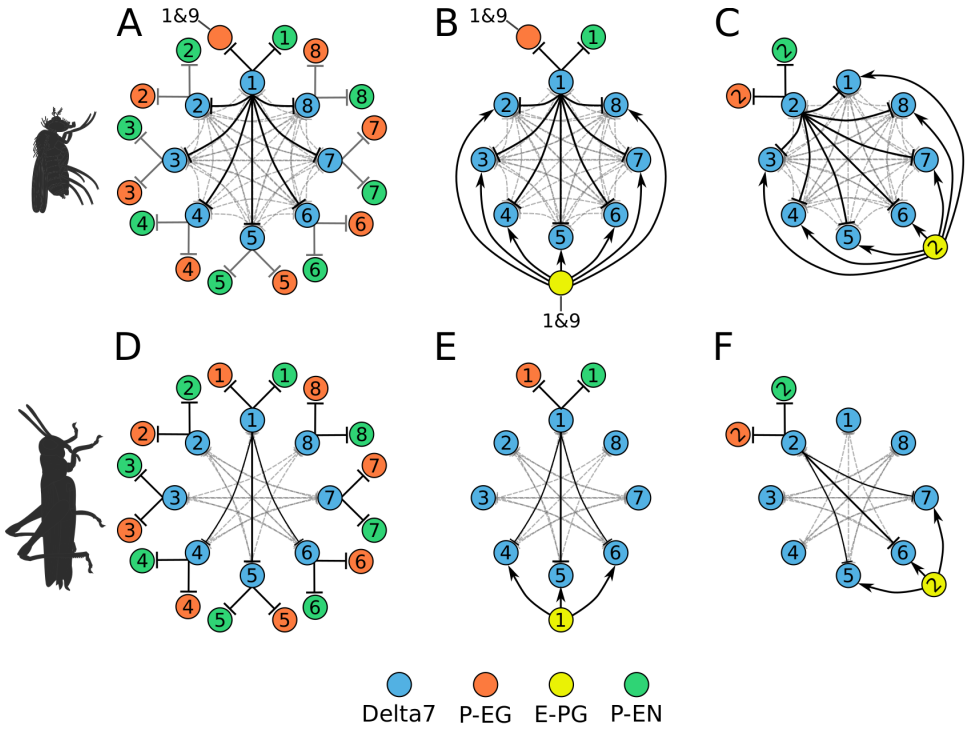

Figure 3.5: Combined excitatory and inhibitory portion of the ring attractors. Explanatory drawings of the connectivity of the inhibitory portion with the excitatory portion of the circuit for the fruit fly (**A**–**C**) and the locust (**D**–**F**). Each coloured disc represents one or more neurons with lines representing synaptic connections. The connectivity of E-PG neurons is shown for two neurons only (**B**,**C** and **E**,**F**). In this conceptual effective connectivity drawing, E-PG neurons appear to be located on the one side of the ring making synapses around the ring. However, anatomically each E-PG neuron innervates one glomerulus where it makes all its synapses with postsynaptic Delta7 neurons that run along the PB.

We follow a similar procedure to derive the effective circuit in the locust (Figure 3.4). Here, E-PG neurons from the two corresponding PB glomeruli, one in each hemisphere, have synaptic domains in two neighbouring EB wedges (half tiles), for example E-PG$_5$ innervates two wedges in tiles T5 and T6 and glomeruli G5 of the PB (Figure 3.4Ai and Supplementary Figure 3.21). Note that in the equivalent circuit (Figure 3.4Aii) we label these neurons by the relevant glomeruli number '5' and can still treat them as a single unit connecting (as for the fruit fly) to the P-EN$_5$ and P-EG$_5$. P-EN neurons connect PB glomeruli to tiles shifted by one wedge to the left and right, for example glomeruli G5 with tiles T5 and T6 (Figure 3.4Bi). This is a shift of half tile while in the fruit fly we see a whole tile shift. As a consequence, P-EN$_5$ neurons effectively make reciprocal connections back to E-PG$_5$, which does not occur in the fruit fly. However, similar to the fruit fly, the P-EN$_5$ neurons also make onward connections to E-PG$_6$ and E-PG$_4$ (note that following the same labelling system as above, the E-PG$_4$ innervates neighbouring wedges in T4 and T5) (Figure 3.4Bii). Finally, P-EG neurons

follow a similar pattern to E-PG neurons (Figure 3.4Ci), innervating equally numbered glomeruli and two wedges in neighbouring tiles, e.g. P-EG_5 connects G5 to T5 and T6, which can be shown as a single unit making a reciprocal connection to E-PG neurons with the same number. Tracing this connectivity pattern forward as before, the connections are repeated around the circuit. The circuit forms a closed ring because the pair of E-PG neurons innervating the medial glomeruli (glomerulus G8 in the left and G1 in the right hemisphere) have arborizations that cross the borders of these two glomeruli (Heinze and Homberg, 2009, Figure 1) hence forming synapses with both P-EN_1 and P-EN_8 neurons in the two medial glomeruli (Figures 3.4Di and 3.4Ei). This evolutionary adaptation results in a closed ring without the need for an extra pair of neurons connecting the two edges of the EB. The crossing of glomeruli borders is characteristically evident in these two medial glomeruli resulting in a modified connectivity pattern between octants 1 and 8 of the circuit (Figure 3.4Fi). Even though this pattern might at first appear to break the structural radial symmetry in effect it provides a functional continuity of left-right activity 'bump' shifting all around the ring as illustrated in Figure 3.4Fii. Figure 3.4Fii shows in detail the specific portion of Figure 3.4Fi, illustrating how the connectivity we found in the animal effectively functions equivalently to the other P-EN to E-PG connections around the ring. The dashed red arrows show the effective connections closing the ring.

In spite of the EB in the locust not being torus-shaped but rather having a crescent shape, the effective circuit still forms a closed ring with an eight-fold structure almost identical to that of the fruit fly (Figure 3.4Fi). This is a consequence of the combination of E-PG neurons selectively cross-innervating the two medial glomeruli and the P-EN neurons forming reciprocal connections back to the E-PG neurons in the same octant. Both of these features are missing in the fruit fly. We thus observe the existence of two different solutions to the same problem, in the fruit fly the torus-shaped EB anatomically facilitates closing the ring while in the locust, which has an EB with open ends, adaptations in the neuronal projection patterns result again in a closed ring.

3.2.1.3 *Overall circuit*

The similarity between the effective circuits of the locust and the fruit fly is striking. Despite the fact that locusts have eight PB glomeruli while fruit flies have nine, both circuits form closed rings organised in eight octants with the functional role of each neuron class appearing to be identical. The E-PG neurons were presynaptic to both P-EG and P-EN neurons, with P-EG neurons forming recurrent synapses back to E-PG neurons. P-EN neurons were presynaptic to E-PG neurons with a shift of one octant to the left or right. Overall, two of the main anatomical differences between the two species (eight versus nine PB glomeruli and ring-shaped versus crescent-shaped EB)

had no fundamental effect on the principal structure of the CX heading direction circuit.

During our analysis of the anatomical data in locusts and flies, we observed that the order of E-PG neuronal projections in the EB differs between the two species (Heinze and Homberg, 2008; Williams, 1975; Wolff et al., 2015; Wolff and Rubin, 2018). Spanning the EB clockwise starting from tile 1, the fruit fly wedges connect first to the right PB hemisphere, then to the left and so on, while in the locust they connect first to the left, then to the right and so on. However, despite this seemingly major difference in projection patterns the effective circuit is preserved between the two species.

The excitatory portions of the circuits differed in that the locust P-EN neurons make synapses back to E-PG neurons in the same octant while in the fruit fly they do not (Compare Figure 3.3F with Figure 3.4F). This difference resulted from the P-EN synaptic domains being shifted by half-tile in the locust instead of the whole tile shift seen in the fruit fly (Figures 3.3B and 3.4B). Consequently, the middle portion of neighbouring P-EN synaptic domains overlap in the EB and feed back to E-PG neurons in the same octant of the ring. This specialisation of the locust together with the cross-innervation of the two medial glomeruli by E-PG neurons enable the closing of the ring in the locust.

When we combined the inhibitory and the excitatory sub-circuits into a complete model (Figure 3.5), the E-PG neurons became presynaptically connected to the Delta7 neurons, in line with Franconville et al. (2018); Turner-Evans et al. (2019). Additionally, each Delta7 neuron inhibits the P-EN and P-EG neurons in the same octant, as well as all other Delta7 neurons (for the fruit fly) or a subset (for the locust), as described above. This difference results in two different types of ring attractor topology; one with global inhibition in the fruit fly and another with local inhibition in the locust.

3.2.2 *Predicted synaptic strengths*

We next focused on whether and how the two circuits could operate as ring attractors. To this end, we implemented computational models of the two circuits using neuronal projection patterns derived from the anatomical data and investigated what synaptic connectivity strengths would be required for the circuits to produce ring attractor dynamics. The results constitute a prediction for the synaptic efficacies we expect to be observed in insects when such measurements become available.

We used spiking Leaky Integrate and Fire neuron models following the same approach as Kakaria and de Bivort (2017) and we ran an optimisation algorithm to find regularities in the synaptic efficacy patterns that resulted in functional ring attractors (see section Methods and Materials). A functional ring attractor should

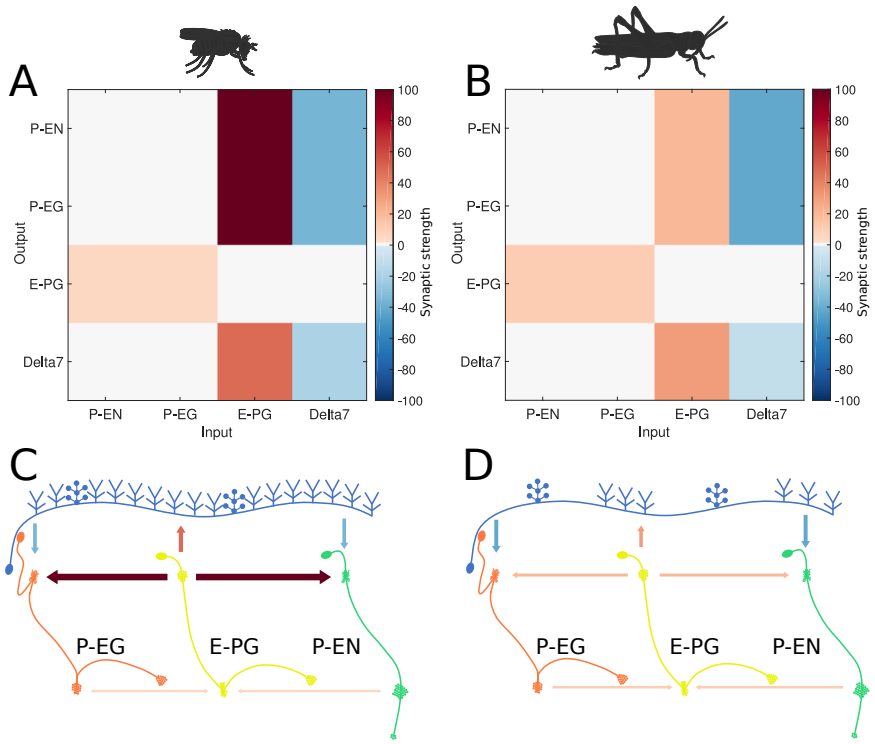

Figure 3.6: Relative synaptic strengths. Graphical depiction of the synaptic strengths between classes of neurons. (**A**,**C**) For the fruit fly ring attractor circuit. (**B**,**D**) For the desert locust ring attractor circuit. Synaptic strengths are denoted by colour in panels **A** and **B**. In panels **C** and **D**, synaptic strengths between neurons are indicated by arrow colour and thickness in scale. Note that in the locust the synaptic strengths shown for Delta7 neurons are the peak values of the Gaussian distributed strengths shown in Supplementary Figure 3.17.

maintain a 'bump' of activity along the neurons of the ring, with characteristics defined in section Methods and Materials. A k-means algorithm was used to identify the clusters around which solutions were found. These clusters were ordered by the number of instances found by repetitive runs of the optimiser. Although the absolute synaptic strengths are arbitrary, as they depend on unknown biophysical properties of the involved neurons, a pattern emerged in the relative synaptic strengths between the different synapses (Figure 3.6). The most frequent synaptic strengths patterns were comparably consistent for the fruit fly and the locust. In both species, among the excitatory synapses, the P-EN to E-PG and P-EG to E-PG synaptic strengths were the weakest, while the synaptic strengths from E-PG to P-EG and P-EN neurons were the strongest. The inhibitory synaptic strengths from Delta7 to P-EN and P-EG were stronger in the locust than in the fruit fly, which was consistent with the fly neurons receiving input from more Delta7 neurons.

3.2.3 *Predicted neuronal activity*

Whereas our simulations confirmed that both the fruit fly and the locust circuit can operate as ring attractors, there were clear differences in the spiking activity and dynamics of the two circuits (Figure 3.7). One major difference was that Delta7 neurons exhibited distinct firing patterns in the two species. In the locust, there was a strong heading-dependent modulation in the firing of Delta7 neurons, in line with the heading signal (activity 'bump') location. Those Delta7 neurons corresponding to the current heading signal location remained silent. In contrast, in the fruit fly the firing of action potentials was only minimally modulated across the Delta7 population (Figure 3.7A and Table 3.1). This difference reflected the utilisation of local inhibition in the case of the locust versus the global inhibition in the fruit fly. Electrophysiologists have indeed reported this pronounced firing rate variation in the locust (Heinze and Homberg, 2007; Heinze et al., 2009; Bockhorst and Homberg, 2015; Pegel et al., 2018). It will be interesting to see if the fruit fly neurons indeed show a lower modulation as predicted by our model.

When comparing the head-direction tuning widths between the two species, we noted that in locusts all cell types are consistently tuned more narrowly (ca. 20%, Table 3.2). Within both species, the activity 'bump' is wider for E-PG neurons than for the other excitatory neuron classes (Table 3.1), a difference that is more pronounced in the fruit fly. The tuning of the Delta7 neurons is the widest across cell types in both species (approx. 96° in the locust, Table 3.2). In the fruit fly, the activity is approximately even across all Delta7 neurons (ca. 10% modulation).

In our models, we employed one neuron for each connection, whereas in the actual animals there are multiple copies of each neuron. While definite numbers of neurons will have to await electron microscopy data, there are likely at least two copies of E-PG, P-EG and P-EN neurons in each columnar module, and three to four copies of Delta7 cells (Williams, 1975; Heinze and Homberg, 2008; Beetz et al., 2015; Wolff et al., 2015; Wolff and Rubin, 2018). If we were to replace each modelled neuron by a bundle of neurons, the action potential firing rates shown in Table 3.1 would be divided among the neurons in each bundle. The peak firing rate of each neuron would be in the range of 40–90 impulses/s which is similar to the range of the rates recorded electrophysiologically in the locust (Heinze and Homberg, 2009). The objective function did not explicitly constrain the firing rates of the neurons but the synergy of biophysical parameters, circuit structure and performance requirements produced working circuits that operate in firing rates similar to those recorded electrophysiologically (see section Discussion).

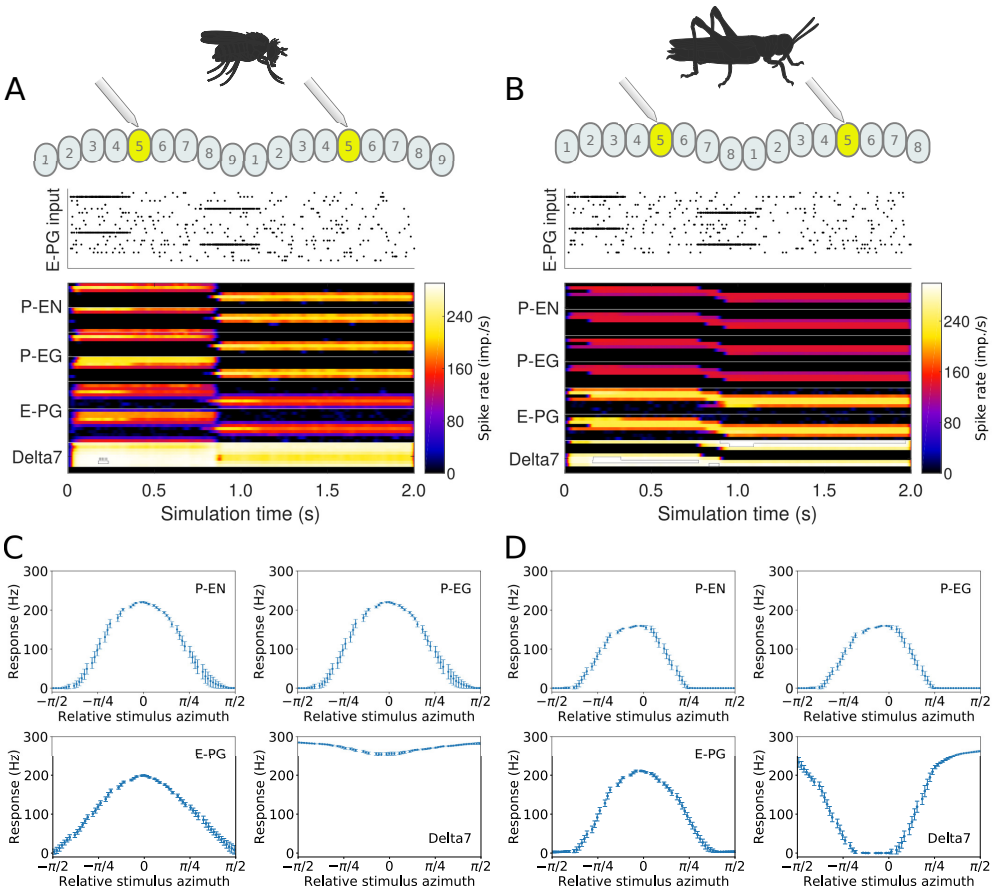

Figure 3.7: Response to abrupt stimulus changes and tuning curves of neurons. (**A** and **B**) The raster plots of the stimuli used to drive the ring attractor during the simulation are shown on top and the spiking rate activity of each neuron at the bottom. In the beginning of the simulation the stimulus spiking activity sets the ring attractor to an initial attractor state. A 'darkness' period of no stimulus follows. Then a second stimulus corresponding to a sudden change of heading by 120° is provided. In the lower parts of **A** and **B**, the spiking activity of each neuron, filtered along the time axis by a Gaussian low-pass filter with window of 120 ms and $\sigma = 24$ ms, is shown colour coded. The order of recorded neurons is the same as shown in the connectivity matrices (Supplementary Figure 3.17). (**A**) Response of the fruit fly ring attractor to sudden change of heading. (**B**) Response of the locust ring attractor to sudden change of heading. Even though the activity 'bump' in the locust model tends to start transitioning sooner, the fruit fly model completes the transition faster. (**C** and **D**) Response of individual neuron types to different stimuli azimuths (n = 40 trials in each condition). The mean and standard deviation are indicated by the error bars at the sampled azimuth points. Peak activity has been shifted to 0°. (**C**) Tuning curves for the fruit fly and (**D**) tuning curves for the locust.

The steady state peak spiking rate for each group of neurons differs between the fruit fly and the locust circuits. On average, the locust neurons showed ca. 25% higher peak firing rates compared to the fruit fly neurons while the Delta7 neurons have the

Table 3.1: Characteristics of the activity 'bump'. The full width at half maximum (FWHM), the peak impulse rate of the activity 'bump' formed across each family of neurons and the amplitude of the activity 'bump' measured as the range of firing rates are shown. Measurements were made 10 s after the stimulus was removed. Numbers are given as median and standard deviation. The activity of Delta7 neurons in *Drosophila* is approximately even, hence the corresponding FWHM measurement is not meaningful and marked as 'N/A'.

Neuron Class	*Drosophila*			Locust		
	FWHM (°)	Peak (imp./s)	Amplitude (imp./s)	FWHM (°)	Peak (imp./s)	Amplitude (imp./s)
E-PG	88.3 ±0.3	161.0 ±0.2	160.1 ±0.3	68.3 ±0.1	192.6 ±0.1	192.0 ±0.2
P-EN	80.4 ±0.4	190.1 ±0.2	190.1 ±0.2	63.1 ±0.3	153.5 ±0.1	153.5 ±0.1
P-EG	71.0 ±0.2	190.1 ±0.2	190.1 ±0.2	63.1 ±0.3	153.5 ±0.1	153.5 ±0.1
Delta7	N/A	274.7 ±0.1	27.1 ±0.2	101.1 ±0.2	266.6 ±0.2	266.6 ±0.2

Table 3.2: Characteristics of the neuron tuning curves. The full width at half maximum (FWHM), the peak impulse rate of each family of neurons and the activity amplitude measured as the range of firing rates are shown. Numbers are given as median and standard deviation. The activity of Delta7 neurons in *Drosophila* is approximately even, hence the corresponding FWHM measurement is not meaningful and marked as 'N/A'.

Neuron Class	*Drosophila*			Locust		
	FWHM (°)	Peak (imp./s)	Amplitude (imp./s)	FWHM (°)	Peak (imp./s)	Amplitude (imp./s)
E-PG	94.7 ±4.0	208.4 ±2.3	208.2 ±2.2	73.4 ±2.6	220.8 ±1.4	220.8 ±1.4
P-EN	74.6 ±3.8	230.3 ±2.3	230.3 ±2.3	58.9 ±3.1	163.6 ±0.9	163.6 ±0.9
P-EG	74.6 ±3.8	230.3 ±2.3	230.3 ±2.3	58.9 ±3.1	163.6 ±0.9	163.6 ±0.9
Delta7	N/A	289.9 ±1.8	58.1 ±4.2	96.0 ±3.2	265.4 ±2.9	265.4 ±2.9

highest spiking rate in both species. Electrophysiology studies will clarify if this is the case.

The tuning curves of the P-EN and P-EG neurons have the same statistics because in our models we assumed that all neurons have the same biophysical properties and since both these types of neurons receive the same inputs their responses are identical.

3.2.4 *Connectivity differences affect response dynamics*

Despite the substantial similarity in functional structure of the two circuits, the subtle differences in connectivity affected the dynamics of the circuit behaviour. This became apparent when we compared the response of both circuits to sudden changes of heading (Figure 3.7). At a qualitative level, the fruit fly heading signal (the 'bump') could jump abruptly from one state to another, whereas the locust circuit exhibited a gradual transition. The results obtained with our spiking neuron models were corroborated by rate-based implementations of the models (Supplementary Figure 3.22), confirming that the observed difference in response dynamics is not a consequence of neuron model choice but rather due to the differences in connectivity.

To explore whether this difference in movement dynamics of the heading signal could be a result of the different inhibition patterns produced by the Delta7 neurons, we replaced the global Delta7 connectivity pattern in the fruit fly model with the connectivity pattern of the locust Delta7 neurons, effectively swapping the fruit fly version of these cells with the locust version. Both the Delta7 to Delta7 and the E-PG to Delta7 connections were replaced with that of the locust. The data generated by this hybrid-species model revealed that changing the global inhibition to local inhibition was sufficient to produce the gradual 'bump' transition we observed in the locust circuit (Figure 3.8).

3.2.4.1 *Quantification of the ring attractor responsiveness*

Having shown that small changes in the morphology of the Delta7 cells affect the dynamics of the heading signal in a qualitative way, we next quantified the maximal rate of change each ring attractor circuit could attain. To this end, we measured the time it took for the heading signal to transition from one stable location to a new one, in response to different angular heading changes of the stimulus. This was carried out for all three models: the fruit fly model, the locust model, and the hybrid-species model. The fruit fly ring attractor circuit stabilised to the new heading in approximately half the time it takes for the locust circuit to stabilise, across different magnitudes of angular heading change (Figure 3.8A). The hybrid-species circuit had a similar response time to the locust circuit. This confirmed that the pattern of inhibition in the network is the main contributor to the observed effect.

To calculate the maximal rate of angular change each circuit can possibly track we divided the angular heading change by the time required for the heading signal to transition. When moving gradually, the heading signal transitions along the shortest path around the ring attractor. Therefore, in the calculation of the angular change rate,

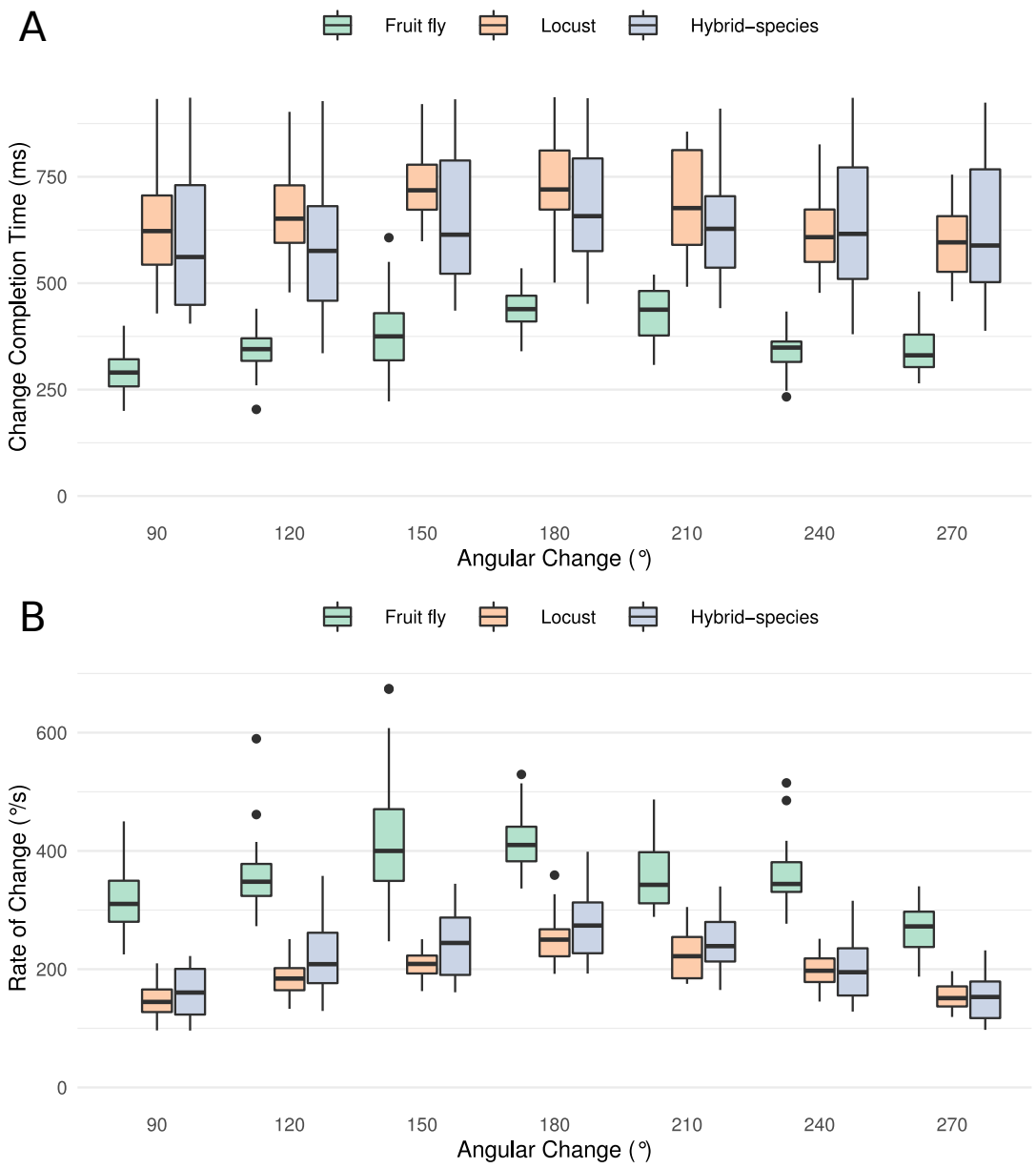

Figure 3.8: Transition time and rate of the heading signal. (**A**) Time required from the onset of the stimulus until the heading signal settles to its new state. The abscissa (horizontal axis) displays the azimuthal difference between initial and target azimuth. (**B**) The maximum rate of angular change each model can attain computed as the ratio of shortest angular change of stimulus divided by transition duration. The values for different magnitudes of heading change are depicted as medians. The boxes indicate the 25^{th} and 75^{th} percentiles while the whiskers indicate the minimum and maximum value in the data after removal of the outliers (black dots). 'Hybrid-species' is the combination of the fruit fly model with the locust inhibition pattern.

the numerator was the shortest angular distance between the two azimuths, calculated as

$$angle = \begin{cases} angle, & \text{if } angle \leq 180^\circ \\ 360^\circ - angle, & \text{if } angle > 180^\circ \end{cases} \tag{3.1}$$

The resulting angular rate of change values revealed that the circuit found in the fruit fly is significantly faster than the locust circuit and the hybrid-species circuit with localised inhibition (Figure 3.8B). The rate of change was maximal for angular displacement of 180°, because this is the maximum azimuth distance the bump has to travel, as for all other angular displacements there is a shorter path.

3.2.4.2 *Effects of varying the uniformity of inhibition*

The above results strongly suggested that the different pattern of inhibition is instrumental to generating the different dynamics in the two circuits. Up to this point, we have examined two extreme cases of inhibitory synaptic patterns, that of the global, uniform, inhibition found in *Drosophila* and the localised inhibition found in the locust. However, in principle, there could be any degree of uniformity of the inhibition between these two extremes. So far, the locust inhibition has been modelled as a summation of two Gaussian functions that approximates the synaptic density across the PB glomeruli, as derived from estimates of dendritic density along the PB in dye-filled Delta7 neurons (Heinze and Homberg, 2007; Beetz et al., 2015; von Hadeln et al., 2020). In the fruit fly, the synaptic distribution of Delta7 neurons has been modelled as uniform across the PB glomeruli, although there might be subtle synaptic density variation along their length. To account for this possibility, we explored a range of synaptic terminal domains distributions. As no measurements of synaptic strengths exist for either animal, we asked what effect varying the synaptic terminal distribution would have on the ring attractor behaviour. We thus modelled the inhibitory synaptic strength across the PB using two Gaussian functions, with peaks separated by 7 or 8 glomeruli, and varied their width (standard deviation σ, see also section Methods and Materials). This would not only give us the effect of different inhibitory synaptic domain widths but also predict the plausible range of widths that the actual animals must have in order to exhibit the observed dynamics.

Modelling these variations showed that the transition mode of the heading signal depended on both the extent of the inhibitory synaptic domain width and the angular heading change of the stimulus. This sets limits on the plausible standard deviation (σ) range that the synaptic strength distribution must obey in the actual animals (Figure 3.9). We observed that for both circuits there was a range of low σ values, corresponding to more localised inhibition, which produce gradual transitions ('locust-like'). As σ was increased, the inhibitory pattern became more uniform or global, and

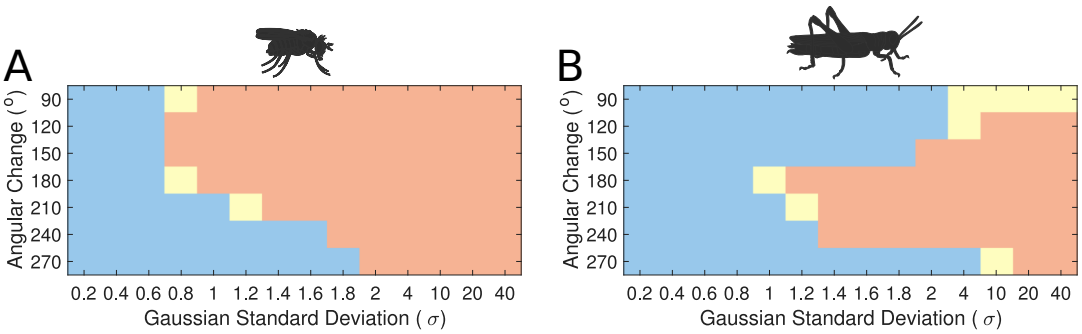

Figure 3.9: Transition regime as function of inhibitory uniformity. Heading signal transition regime for (**A**) the fruit fly ring attractor circuit and (**B**) the desert locust ring attractor circuit. Blue denotes gradual transition of the heading signal, orange denotes abrupt transition (jump), and yellow marks trials that were producing both gradual and abrupt transitions (for definitions see section Methods and Materials).

both circuits transitioned to abrupt jumps ('fly-like'). Based on density estimates of dendrites in the PB, we approximated the inhibitory synaptic distribution with a value of $\sigma = 0.8$ for the locust model, yielding a gradual activity transition regime across the whole range of angular changes. These results suggested that the pattern of inhibition is indeed key to the circuit dynamics in response to rapid heading changes.

However, the morphology of the Delta7 neurons is not the only difference between the ring attractors in the two species, hence the recorded response patterns are not identical for the two species (Figure 3.9). There is also anatomical difference in the presence of the P-EN to E-PG feedback loops only in the locust and consequently the synaptic efficacies differ between the two models. We investigate the effect of this anatomical difference in the subsequent section.

3.2.5 *Attractor states distribution*

We next investigated the attractor basin of each model. The finite size of the two circuits renders them discrete approximations of ring attractors (Brody et al., 2003). As a consequence, in the absence of input, the activity 'bump' will tend to settle to one of a discrete set of states (note this does not prevent a continuous encoding of heading while a heading stimulus is provided, which could be decoded by downstream neuronal circuits). We tested this by stimulating the E-PG neurons at varying azimuthal locations around the circuits, then removing the input stimulus and examining the position of the activity 'bump' after 3 s. Both the fruit fly and locust circuits had discrete attractor states where the heading signal eventually settled once the stimulus was removed. Typically, the heading signal moved to the nearest attractor state. When a stimulus was applied equidistantly between two attractor states then, once the

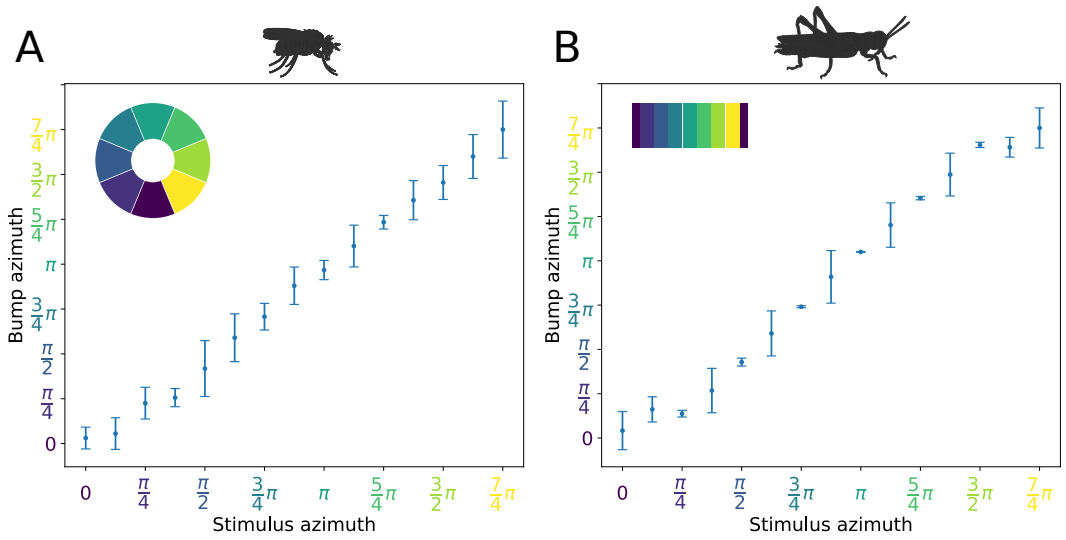

Figure 3.10: Distribution of activity 'bump' locations. The distribution of azimuthal location of the heading signal 3 s after stimulus removal is plotted. On the abscissa (horizontal axis), the azimuth where the stimulus is applied is shown. On the ordinate (vertical axis), the mean location and standard deviation of the activity 'bump' azimuth, 3 s after the stimulus is removed, are shown. (**A**) for the fruit fly and (**B**) for the locust. Inset images depict the corresponding EB tiles in colour. Smaller standard deviation corresponds to the 'bump' settling more frequently to the same azimuth. This is the case when the stimulus is applied near an attractor state. Applying the stimulus equidistantly from two attractor states results in a movement of the 'bump' to either of them and hence the increased standard deviation. In the locust when stimulating the ring attractor at one of the attractor states the 'bump' tends to settle at it, indicated by the reduced standard deviation at these locations. In the fruit fly, the activity 'bump' is prone to noise and not as stable, thus the standard deviation is not as modulated. This means that the locust attractor states are more stable resulting to the smaller dispersion of 'bump' location.

stimulus was removed, the activity 'bump' moved to one of the two attractor states stochastically due to the presence of noise in the system (Figure 3.10). These attractor states were more stable and clearly delineated in the locust while in the fruit fly there was a wider distribution of 'bump' locations, indicating that the locust ring attractor is more robust to drift and noise (Figure 3.10).

3.2.6 *Stability characteristics of the ring attractors*

3.2.6.1 *The locust head direction circuit is more robust to noise*

An important aspect of a ring attractor is its stability characteristics. The differences in the distribution of activity 'bump' locations reported in the previous section hinted that the locust ring attractor is more robust to noise. To quantify this property of the two ring attractors, we measured the effect of different levels of structural (synaptic)

noise to the circuit stability. The ring attractor of the locust was significantly more tolerant to structural noise than the fruit fly circuit (Figure 3.11A).

However, these two ring attractors differ in several respects. To identify the reason for the reduced sensitivity of the locust model to synaptic noise we compared the locust with the hybrid-species model. These two models differ in that reciprocal connections between P-EN and E-PG neurons are present only in the locust model (Figures 3.3 and 3.4). If these reciprocal connections are responsible for the increased robustness of the circuit, we would expect the locust model to be more robust to synaptic noise than the hybrid-species model. This is exactly what we found (Figure 3.11A), thus we inferred that these reciprocal connections, between P-EN and E-PG neurons, provide the increased robustness to the locust model. This circuit specialisation might have important repercussions to the behavioural repertoire of the species, enabling locusts to maintain their heading for longer stretches of time than fruit flies, an important competence for a migratory species such as the locust.

3.2.6.2 *P-EG neurons stabilise the head direction circuit*

In our models, we included the P-EG neurons connecting the PB glomeruli with EB tiles. Unlike the P-ENs, these neurons have the same connectivity pattern as the E-PG neurons but with presynaptic and postsynaptic terminals on opposite ends. What is the effect of the P-EG neurons in the circuit? Effectively, the P-EG neurons form secondary positive feedback loops within each octant of the circuit that, we hypothesised, help the heading signal to be maintained stably in the current position, even when lacking external input. Therefore, we expected the circuit to function as a ring attractor without these connections, but to be more vulnerable to drift if the neuronal connection weights are not perfectly balanced. The recurrent P-EG to E-PG loops should counteract this tendency to drift.

We tested this hypothesis by measuring the effect of imposing imbalance in the connectivity strengths of P-EN to E-PG neurons between the two hemispheres. We did this for both the full fruit fly and locust circuits as well as two altered circuits with the P-EG neurons removed. The synaptic strengths for the four circuits were optimised separately, since completely removing the P-EG neurons without appropriate synaptic strength adjustment breaks the ring attractor. We measured the percentage of simulation runs that resulted in a stable heading signal being maintained for at least 3 s. The presence of the P-EG neurons substantially increased the robustness of both species models to the effects of synaptic strength imbalance in the P-EN to E-PG synapses, as a stable heading signal was observed over a far wider range of synaptic efficacy changes (Figures 3.11B and 3.11C). The P-EG neurons therefore contribute significantly to the tolerance of the ring attractors to synaptic strength asymmetries.

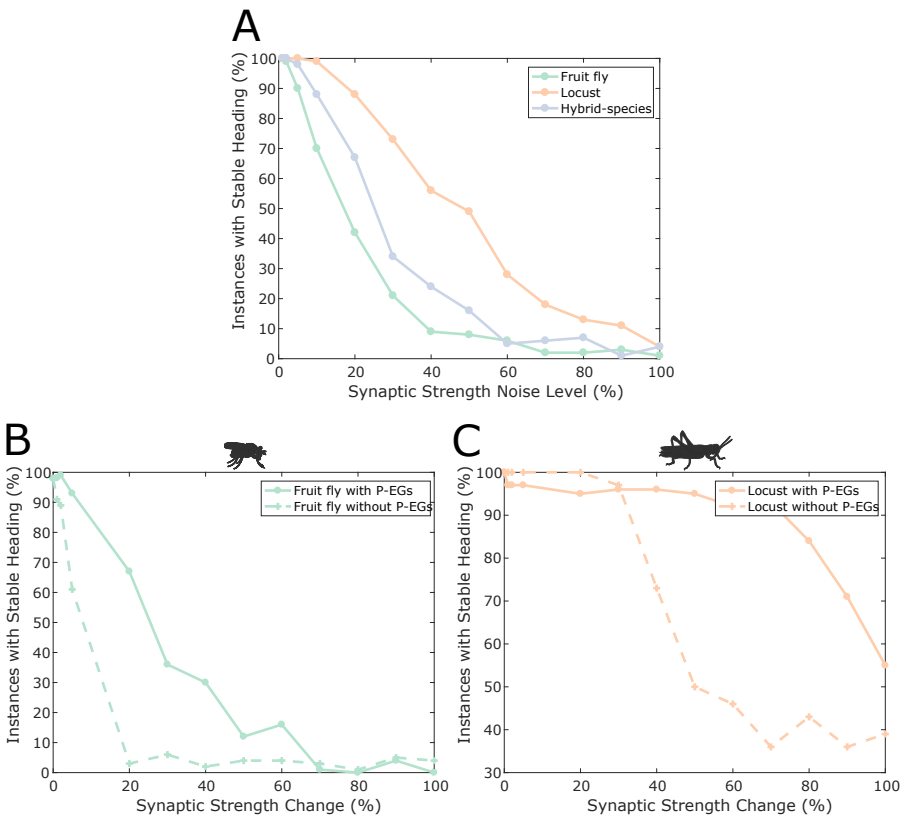

Figure 3.11: Effect of synaptic efficacy heterogeneity on ring attractor stability. (**A**) Stability of the ring attractor heading signal for the fruit fly, locust and hybrid-species (fruit fly with localised inhibition) model as a function of heterogeneity in the synaptic efficacies across all synapse types (modelled as additive white Gaussian noise). (**B**, **C**) Stability of the ring attractor heading signal as a function of structural asymmetry introduced by deviating synaptic efficacies between P-EN and E-PG neurons when the circuit includes the P-EG neurons versus when they are removed. In all three plots, the percentage of trials that result in a stable activity 'bump' is shown. On the horizontal axis the absolute value of percentile synaptic strength change is shown. Number of trials n = 100 for each level of noise. With P-EG neurons both ring attractors are more tolerant to such structural asymmetries. The locust ring attractor is more robust to both types of structural noise.

3.2.6.3 *Effect of inhibition to stability*

It is interesting to note that even though in the locust model the reciprocal connections between E-PG and P-EG neurons were weaker than in the fruit fly model, the presence of the extra reciprocal connections between P-EN and E-PG neurons in the locust resulted in a more stable ring attractor than that in the fruit fly, which possesses only one but stronger recurrency loop. Finally, the hybrid-species model was more robust than the fruit fly one (Figure 3.11A). The fruit fly and the hybrid-species models differed in the width of their inhibitory synaptic domains and in their synaptic strengths. Although their difference in robustness was smaller than the previously

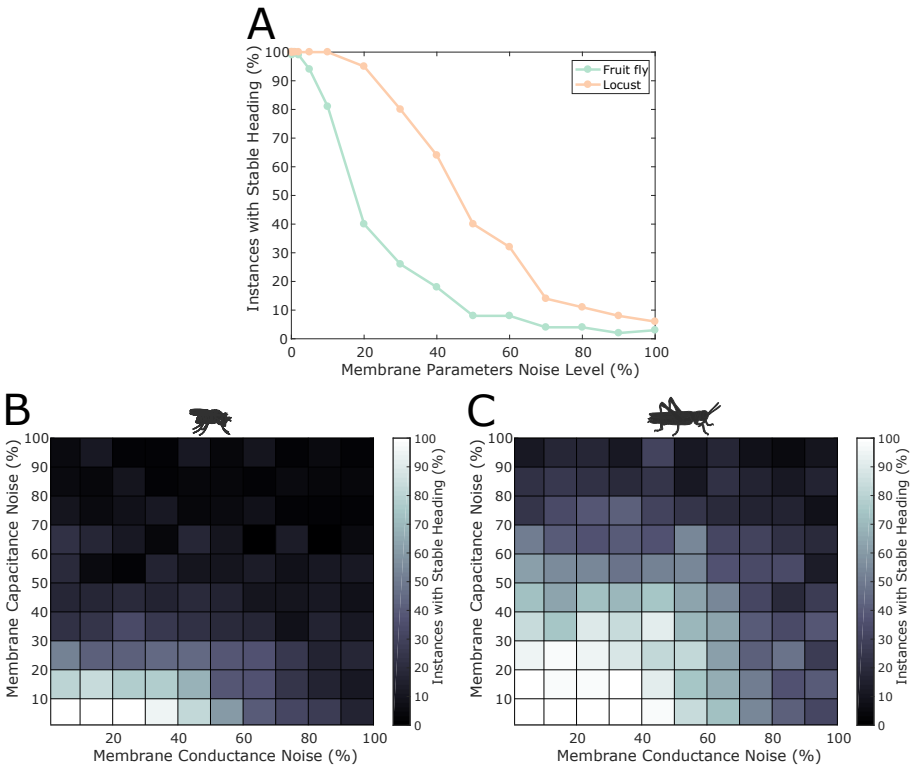

Figure 3.12: Effect of membrane parameter heterogeneity on ring attractor stability. (**A**) Stability of the ring attractor heading signal for the fruit fly and the locust model when the membrane properties are heterogeneous across the neuronal population. (**B**, **C**) Stability of the ring attractor heading signal when the level of noise on conductance and capacitance is varied independently. In all three plots, the percentage of trials that result in a stable activity 'bump' as a function of heterogeneity in cell membrane properties is shown (number of trials n = 50 for each condition). The locust ring attractor is more robust to white Gaussian noise in both conductance and capacitance. In both cases, the activity 'bump' is more tolerant to conductance variation than capacitance.

examined ones, we can see an effect of the inhibitory pattern on the stability of the circuit.

3.2.6.4 *Effect of neuronal heterogeneity*

Until this point, we have assumed that all neurons have identical properties. We now relax this assumption by making the membrane properties of the neurons heterogeneous. We tested the effect of neuronal heterogeneity to the stability of the ring attractors. Overall, the stability of the ring attractors deteriorated with increased deviation from the nominal values of membrane properties (Figure 3.12), but the locust model was more robust to these membrane property variations. Importantly, the distinct heading signal transition regimes (gradual transition in the locust model versus

jump in the fruit fly model) were preserved regardless of heterogeneous membrane properties across the neuronal population (Supplementary Figure 3.23).

3.2.7 *Response to proprioceptive stimuli*

Mechanistically, Turner-Evans *et al.* showed that the activity of P-EN neurons in one hemisphere of the brain increases when the animal turns contralaterally, both with and without visual input (Turner-Evans et al., 2017). The increase in activity is related to the angular velocity the fly experiences (Turner-Evans et al., 2017). Whereas the origin of the angular velocity information in darkness is not known, efference copies of motor commands or proprioceptive inputs are the most likely sources of information about the fly's rotational velocity. To test whether our models reproduce this behaviour, we artificially stimulated the P-EN neurons in one hemisphere of the PB, mimicking an angular velocity signal caused by turning of the animal, and observed the effect on the heading signal (Figure 3.13).

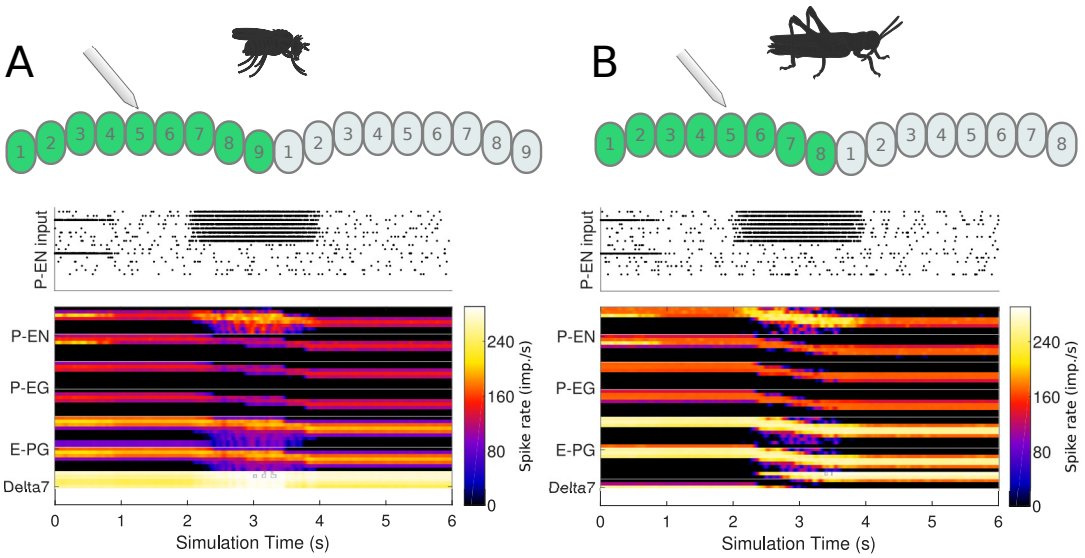

Figure 3.13: Response to uni-hemispheric stimulation. Upper plots show the P-EN stimulation protocol and corresponding induced P-EN activity; lower plots show the response of the ring attractor for (**A**) the fruit fly circuit and (**B**) the locust circuit. The initial bilateral stimulation initialises a persistent activity 'bump', which moves around the circuit in response to stimulation of P-ENs in all the columns in one hemisphere only.

Both the locust and the fruit fly model reproduced the response dynamics reported by Turner-Evans et al. (2017). Exploration of the response of the circuit to different stimulation strengths showed that the rate by which the heading signal shifts around the ring attractor increases exponentially with increase of uni-hemispheric stimulation strength (Figure 3.14). While this general relationship was consistent between the two

species, the increase was much steeper in the fly. Additionally, the required stimulus for initiating 'bump' shifting was lower in the fruit fly. Both of these aspects concur with the faster response rate of the fruit fly model to positional stimuli and support their ability to track fast body saccades even when only angular velocity input is available.

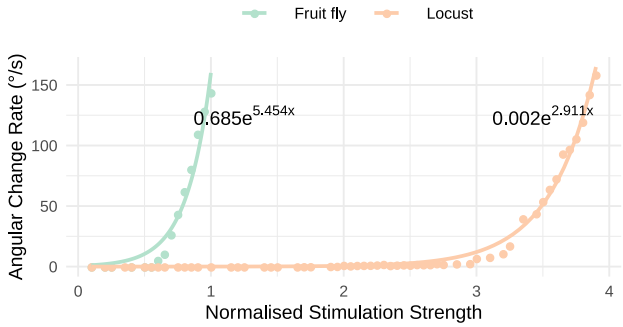

Figure 3.14: Response to uni-hemispheric stimulation. Response rate of change of the heading signal with uni-hemispheric stimulation of P-EN neurons. The angular rate of change increases exponentially with stimulation strength and does so most rapidly for the fruit fly circuit. The data points have been fit with the function $y = ae^{bx}$ and the parameters of the fitted curves are shown on the plot.

Continuous application of angular velocity input caused the heading signal to reach an edge of the PB and then wrap around and continue on the other edge. This behaviour is present in both models and is thus independent of the physical shape of the EB, that is, whether it forms a closed ring or possesses open ends. The wrapping around of the heading signal is required for the animals to track movements that involve turning around its body axis for more that 360° and is supported by the effective closed ring structure we found in both species.

3.3 DISCUSSION

The availability of tools for the study of insect brains at the single neuron level has opened the way to deciphering the neuronal organisation and principles of the underlying circuit's behaviour. However, even where there is progress towards a complete connectome, the lack of data on synaptic strengths, neurotransmitter identity, neuronal conductances, etc. leave many parameters of the circuit unspecified. Exploring these parameters via computational modelling can help to illuminate the functional significance of identified neural elements. We have applied this approach to gain greater insight into the nature of the heading encoding circuit in the insect central complex (CX), including the consequences of differences in circuit connectivity across two insect species.

3.3.0.1 *Overall conservation of structure and function*

We have focused on a subset of neurons in the PB and EB which have been hypothesised to operate as a ring attractor, with a 'bump' of neuronal activity moving across columns consistently with the changing heading direction of the animal. The neuronal projection patterns and columnar organisation differ between the two insect species we have analysed, the fruit fly and the locust. There are additional morphological columns in the PB of flies (9 vs. 8), resulting in a different number of functional units that could influence the symmetry of the underlying neural circuits. Also, the EB in the fruit fly forms a physical ring, while the homologous region in the locust is an open structure. Our analysis of the connectivity as a directed graph has revealed, surprisingly, that the circuits are nevertheless equivalent in their effective structure, forming a closed ring attractor in both species with an identical functional role for each neuron class. The preservation of this circuit across 400 million years of evolutionary divergence suggests that it is an essential, potentially fundamental, part of the insect brain.

It is worth noting that an essential part of the circuit, namely the functionally closed ring that we found in both species, is achieved with two different solutions. In the fruit fly, the torus-shaped EB provides an anatomical solution to the closure of the ring via overlapping projections from E-PG neurons innervating the innermost and outermost PB glomeruli. In contrast, in the locust the midline spanning output fibers of the E-PG neurons in the medial PB glomeruli serve this function in combination with a slightly different projection pattern that results in the P-EN neurons forming reciprocal connections back to E-PG neurons in the same octant. In this context, it is interesting to note that neither solution to this problem is possible for insects of a different order, the lepidoptera (moths and butterflies). These insects have an almost straight EB, their PB is split along the midline, and right-left connections between the two halves are realised by a neuropil-free fiber bundle (Heinze and Reppert, 2012; Adden et al., 2020). Neither midline crossing E-PG fibers within the PB, nor local connections around the ring of the EB are therefore morphologically possible, suggesting that a functional closure of the heading direction circuit is either not required or achieved via other means in these species. The notion that there are many solutions to the same problem is further highlighted by data from bumblebees showing the existence of a ninth E-PG neuron that connects the medialmost PB glomerulus to the outermost ipsilateral EB wedge, closing the ring in yet another way (personal observations, S.H.). Exploring these different solutions across many species could provide key insights into the evolution of this circuit under a multitude of evolutionary history constraints.

In combination, these findings underline that the large-scale anatomical differences at the level of neuropils and projection patterns do not necessarily affect the core functions of the circuit. Rather, the functional constraints appear significant enough that even in those parts of the circuit that clearly differ between species convergent solutions have evolved that solve similar problems, albeit in slightly different ways.

3.3.0.2 *Differences in dynamical response*

Surprisingly, more subtle differences in the morphology between the two species have significant effects on the dynamical response of the heading direction circuit. First, the shape of the dendritic arborizations of one type of CX neuron determines how quickly the model circuit tracks rotational movements. Second, a difference in the overlap of neuronal projections in the EB results in an extra feedback loop between the P-EN and E-PG neurons in the locust circuit that makes it more robust to synaptic noise.

We suggest that the effects of these differences are consistent with the behavioural ecology of the two species. On the one hand, the faster response of the ring attractor circuit in the fruit fly accommodates the fast body saccades that fruit flies are known to perform (Tammero and Dickinson, 2002; Fry et al., 2003). On the other hand, the locust is a migratory species, so its behaviour demands maintenance of a defined heading for a long period of time (Homberg, 2015; de Vries et al., 2017). This requirement for heading stability might have provided the selective pressure needed to drive the evolution of a more noise resilient head direction circuit.

3.3.1 *Assumptions and simplifications*

As any model, our circuits are necessarily condensed and simplified versions of the real circuits in the insect brain. In comparison to previous models, the work we present has been more precisely constrained by the latest anatomical evidence. We additionally constrained our models to use plausible values for the biophysical properties of neurons (membrane conductance and capacitance) as well as spiking rates (background activity) supported by electrophysiological evidence. Furthermore, in building our models we did not assume that the underlying circuits must be ring attractors, but rather asked and investigated whether, given the available connectivity data, they can be. This was especially the case for the locust model since our work represents the first model of this circuit to date. Nevertheless, it is important to outline those areas where our assumptions cannot be fully justified from the existing data and identify the potential consequences for the modelling results.

3.3.1.1 *Morphological Assumptions*

In our model of the fruit fly heading tracking circuit, we assumed a uniform distribution of dendrites across the Delta7 neurons. Imaging of these neurons suggests that there might be a subtle variation of the dendritic density along their length. However, it is unclear how this subtle variation might be related to synaptic density and efficacy. We, therefore, initially made the simplifying assumption that these neurons have uniform synaptic efficacy across the PB. However, we also explored the effect of varying the degree of synaptic uniformity, showing that there is a range of synaptic efficacy distributions that still can produce the fly-like rapidity in the circuit response.

In general, arborization trees of neurons in the CX can be very complex, as they are not only confined to specific slices, but also to one or several layers, especially within the EB. In *Drosophila*, the spiny terminal arbors of E-PG neurons extend to the width of single wedges in the EB, occupying both the posterior and medial layers. In contrast, P-EG and P-EN neurons arborize in tiles, hence innervating only the posterior surface volume of the EB (Wolff and Rubin, 2018). Therefore, we assume that presynaptic terminals of P-EG and P-EN neurons form synapses with E-PG postsynaptic terminals in the posterior layer of the EB. In locusts, the E-PG arborizations are more complex, as these cells innervate a single wedge of the anterior and medial EB layers, but extend at least twice this width to either side in the posterior layer that provides overlap with the P-EN neurons (Heinze and Homberg, 2008). Additionally, the wider fibres have a different morphological appearance. P-EG neurons in this species innervate all layers evenly. Although these detailed differences likely have consequences for connectivity, we simplified these arborizations to their most essential components, aiding the extraction of the core features. With the advance of comparative connectomics, these aspects will become accessible for investigation.

3.3.1.2 *Connectivity Assumptions*

Several assumptions were made while deriving the neuronal connectivity in our models. We assumed well delineated borders of synaptic domains, which is clearly not always the case. Especially in the EB, some overlapping of neighbouring synaptic domains due to stray terminals is to be expected (Wolff et al., 2015). The circumferential extent of arbors in wedges and tiles may affect the integrity of the resulting circuit and its properties. However, due to lack of adequate data about the extent of such overlap we cannot currently model this aspect in a sensible way.

Furthermore, neuronal connectivity was mostly inferred by co-location of neuronal arbors, that is, projection patterns. A functional connectivity study has reported that stimulation of E-PG neurons triggered significant responses to Delta7 neurons but

no columnar neurons (Franconville et al., 2018). However, as those authors note, the lack of response might be due to the limitations of the method used. Alternatively, such connections might be mediated by interneurons instead of being monosynaptic. Future work using electron microscopy data will elucidate which of the overlapping arborizations correspond to functional connections and allow us to augment our models.

3.3.1.3 *Functional Assumptions*

Further assumptions were made about neuronal polarity, type of synapses and synaptic efficacies. Lin et al. (2013) characterise the EB arbor of E-PG neurons in *Drosophila* as having both presynaptic and postsynaptic domains; however, Wolff et al. (2015) report that using anti-synaptotagamin is inconclusive for presynaptic terminals. In our models for both the fruit fly and the locust we thus assumed that E-PG neurons are purely postsynaptic in the EB, following the most parsimonious polarity estimate. Connectomics data from a recent preprint demonstrate that in *Drosophila* synapses exist that directly link Delta7 to E-PG neurons in the PB (Turner-Evans et al., 2019). These synapses are most likely inhibitory and would thus inhibit the distal portion of the ring and thus would not alter the location of the activity 'bump'. For simplicity and because they do not affect the functional layout of the circuit, these synapses were not included in our model.

Furthermore, the Delta7 neurons are assumed to have inhibitory effect on their postsynaptic neurons, as Kakaria and de Bivort (2017) proposed. However, there is evidence that Delta7 neurons make both inhibitory and excitatory synapses to other neurons (Franconville et al., 2018). Indeed, these cells were recently shown to be glutamatergic, enabling both inhibitory and excitatory effects on postsynaptic cells via different glutamate receptors (Turner-Evans et al., 2019). As the downstream neurons with demonstrated excitatory responses (P-FN neurons) are not part of our current model, we made the simplifying assumption that Delta7 neurons have exclusively inhibitory effect on their postsynaptic neurons, both in flies and locusts. It is also possible that there are other sources of inhibition in the circuit, for example mediated by the GABAergic ring neurons originating in the bulbs, as suggested by Green and Maimon (2018), or via GABAergic Gall-EB ring neurons (Turner-Evans et al., 2019). We do not explore this possibility in our current work.

We additionally assumed that the synaptic strengths of all synapses of each class are identical. This might not be the case in the actual animals, especially considering that one of the EB tiles (T1) is innervated by twice as many neurons as other tiles in fruit flies (Figure 3.3). Neurons innervating this tile might have reduced synaptic efficacy in order to maintain the radial symmetry of the circuit intact. Similarly, the synaptic

strengths of the neurons closing the ring in locusts would be expected to be different than those of other synapses if the ring does not have a functional 'seam'. Such a synaptic efficacy variation is suggested by the fact that the arborization density of E-PG neurons innervating the two medial PB glomeruli (G9 and G1) is not the same in both of them. There is certainly space for further exploration of the effect of synaptic efficacy in those segments of the ring in both species. Finally, synaptic strength variation might exist for the two Delta7 neurons that have presynaptic terminals in three glomeruli instead of two (Table 3.3).

3.3.1.4 *Biophysical Assumptions*

All types of neurons in our models were assumed to have the same nominal biophysical properties even though anatomical evidence has shown that their morphology, somata size and main neurite thickness differ (Heinze and Homberg, 2008). To relax this assumption, we explored the effect of heterogeneity in the biophysical properties of the neuronal population. We corroborated our conclusions using both rate-based and Leaky Integrate and Fire neurons with refractory period. This allowed us to highlight the significance of the neuronal connectivity on the circuit dynamics. The point spiking neuron model was sufficient for investigating the performance characteristics, spike timing dynamics and potential spike synchronisation effects in the ring attractors when exposed to neuronal noise, but clearly is highly abstracted in comparison to real neurons. However, we lack most of the necessary detail to constrain more complex neural models. One caveat is that intrinsic properties of neurons could provide short-term memory that would radically alter the circuit response. It is not possible to explore this possibility with the models we have used, but we can conclude that such properties do not appear to be necessary for generating basic ring attractor dynamics. Furthermore, it will be interesting to study how differences in the biophysical properties of neurons between the two species might be affecting performance. We are not exploring this possibility here.

3.3.2 *Comparison to 'canonical' ring attractor models*

In our work, we compared the hypothetical heading tracking circuit of two evolutionary distant species. We went beyond mere simulation of neuronal projection data by analysing and deriving the effective underlying circuit structure of the two ring attractors. Our analysis and derivation of the complete effective neuronal circuits revealed not only differences in dynamics but also the construction principles of these circuits. This approach allowed us to identify elements that differ in several ways from

the 'canonical' ring attractor described in earlier theoretical models (e.g. Amari (1977); Skaggs et al. (1995); Zhang (1996)).

For example, the circuit found in the two insect species combines two functionalities in the P-EN neurons that are typically assigned to separate neural populations in computational models of ring attractors. Such computational models use one set of neurons to provide the lateral excitation to nearest neighbours and a different set of neurons that receive angular velocity input to drive the left-right rotation of the heading signal. In the insect circuit, the P-EN cells are part of the lateral excitation circuit, providing excitation to their two nearest neighbours, but they also receive angular velocity input. This difference is suggestive of a more efficient use of neuronal resources than the typical computational models of ring attractors. Another novel element we found in the insect ring attractors is the presence of local feedback loops within each octant of the circuit structure (P-EG to E-PG and P-EN to E-PG). Both of these feedback loops increase the tolerance of the ring attractors to noise.

3.3.3 *Hypotheses regarding circuit differences*

Another unique aspect of our modelling work is the comparison of related, but not identical, circuits found in two species. Indeed, using computational modelling allows us to investigate 'hybrid' circuits, combining features of each, in order to try to understand the functional significance of each observed difference independently. Nevertheless, some differences between these circuits are not explained by the current model, and may require additional work to fully explicate.

One question is what is the role, if any, of the ninth PB glomeruli found so far only in *Drosophila*? In particular, the existence of the innermost glomeruli that are not innervated by the P-EN neurons seems perplexing. The same signals from tile 1 of the EB are sent to both ends of each hemisphere of the PB (glomeruli 1 and 9) and from there action potentials propagate along the Delta7 neurons along the PB length. Our speculation is that this may be a mechanism to reduce the distance and time these signals have to travel to cover the full PB, that is, the maximum distance any signal must travel is only half of the distance it would need to propagate from one end of the PB to the other as in other species, such as the locust. If this is the case, it would constitute one more specialisation in *Drosophila* that reduces the response time of the ring attractor. It therefore seems that several specialisations have been orchestrated in minimising the response delays in fruit flies. Testing this idea would require multi-compartmental models to capture the action potential transmission time along neurites; as argued above, this may be contingent upon first obtaining detailed biophysical characterisation of the Delta7 neurons.

Another remaining question is what is the role of the closed ring-shaped EB in *D. melanogaster*. One possibility is that such a closed ring topology would allow local reciprocal connections between P-EN and E-PG neurons all around the EB ring, as reported in (Turner-Evans et al., 2019). This would allow direct propagation of signals between these neurons within the EB instead of requiring them to travel via the PB, as in the current model, again increasing the speed with which the heading direction can be tracked and allowing smoother transition between neighbouring tiles. Note that such direct reciprocal connections within the EB can only span the full ring with a closed ring anatomy and would not be possible between the two ends of the EB in the locust. To investigate the potential effect of such hypothetical reciprocal connections within the EB, further studies are required. Possibly blocking signal transmission via the PB to isolate functional connectivity within the EB would allow comparison of signal transmission time measurements within the EB versus via the PB. Such measurements would determine how different and hence significant those two pathways might be in the ring attractor performance.

A further hypothesis relates to the evolutionary lineage of these two features in the *Drosophila* CX. It will be of interest to study whether the ring shaped EB appeared before or after the appearance of the ninth glomeruli. One possibility is that the EB evolved into a ring shape after the appearance of the ninth glomeruli in the PB, allowing connections from one common tile to both glomeruli 1 and 9 and hence providing such a common driving signal. Alternatively, a pre-existing ring-shaped EB might have allowed the evolution of usable ninth glomeruli that resulted in faster propagation. Similarly, the P-EN to E-PG recurrency found only in the locust might be an acquired adaptation of the locust that increases robustness to noise, or an ancestral feature that has been lost in fruit flies.

Comparison of different species could potentially elucidate such questions. We would expect individual species to have a selective subset of the specialisations we found, endowing them with brain circuits supporting the behavioural repertoire suiting their ecological niche. It will, therefore, be informative to analyse the effective heading direction circuit of other species, spanning evolutionary history, in order to get insights into how such adaptations relate to and accommodate behaviour. Our results emphasise the importance of comparative studies if we are to derive general principles about neuronal processing, even in systems that appear highly conserved such as the CX head direction circuit in insects. Many of the circuit properties observed in *Drosophila* appear to reflect specific evolutionary adaptations related to tracking rapid flight manoeuvres. Despite the many strengths of *Drosophila* as an experimental model, it therefore remains important to ground conclusions about the insect brain in comparison with other species.

3.4 METHODS AND MATERIALS

3.4.1 *Neuron model*

Our models used the source code of Kakaria and de Bivort (2017) as a starting point. We used Leaky Integrate and Fire neuron models with refractory period (Stein, 1967). The membrane potential of each neuron was modelled by the differential equation

$$\frac{dV_i}{dt} = \frac{1}{C_m}\left(\frac{V_0 - V_i}{R_m} + I_i + \sum_{j=1}^{N} M_{j,i} I_j\right) \tag{3.2}$$

where V_i is the membrane potential of neuron i, V_0 the resting potential, R_m the membrane resistance, C_m the membrane capacitance, I_i the external input current of neuron i, $M_{j,i}$ the network connectivity matrix, I_j the output current of each neuron in the circuit and N is the number of neurons.

The model parameter values including membrane resistance, capacitance, resting potential, undershoot potential and postsynaptic current magnitude (I_{PSC}) were set to the same values as used by Kakaria and de Bivort (2017). These values are consistent with evidence from measurements in *D. melanogaster* and other species. The membrane capacitance C_m is set to 2 nF and the membrane resistance R_m to 10 MΩ for all neurons, assuming a surface area of 10^{-3} cm^2 (Gouwens and Wilson, 2009). The resting potential V_0 is set to -52 mV for all neurons (Rohrbough and Broadie, 2002; Sheeba et al., 2008). The action potential threshold is -45 mV (Gouwens and Wilson, 2009). When the membrane potential reaches the threshold voltage an action potential template is inserted in the recorded time series. No other impulses occur during this period operating in effect as a refractory period. The action potential template is defined as (Kakaria and de Bivort, 2017):

$$V(t) = \begin{cases} V_{thr} + (V_{max} - V_{thr})\dfrac{\mathcal{N}\left(\frac{t_{tp}}{2}, \left(\frac{t_{AP}}{2}\right)^2\right) - \alpha_1}{\beta_1}, & \text{if } 0 \le t < \frac{t_{AP}}{2} \\ V_{min} + (V_{max} - V_{min})\dfrac{\sin\left(\left(t - \frac{t_{AP}}{2}\right)\frac{2\pi}{t_{AP}} + \frac{\pi}{2}\right) + \gamma_1}{\delta_1}, & \text{if } \frac{t_{AP}}{2} \le t \le t_{AP} \end{cases} \tag{3.3}$$

where V_{max} is the peak voltage set to 20 mV (Rohrbough and Broadie, 2002). V_{min} is the action potential undershoot voltage, set to -72 mV (Nagel et al., 2015). t_{AP} is the duration of the action potential set to 2 ms (Gouwens and Wilson, 2009; Gaudry et al., 2012). $\mathcal{N}(\mu, \sigma^2)$ is a Gaussian function with a mean μ and standard deviation σ. α_1, β_1, γ_1, and δ_1 are normalisation parameters for scaling the range of the Gaussian and the sinusoidal to 0 to 1.

The firing of an action potential also adds a postsynaptic current template to the current time series. The postsynaptic current template is defined as

$$I(t) = \begin{cases} I_{PSC}\frac{\sin\left(\frac{t\pi}{2}-\frac{\pi}{2}\right)+\alpha_2}{\beta_2}, & \text{if } 0 \leq t < 2\,\text{ms} \\ I_{PSC}\frac{2^{-(t-2)/t_{PSC}}+\gamma_2}{\delta_2}, & \text{if } 2\,\text{ms} \leq t \leq 2\,\text{ms} + 7t_{PSC} \end{cases} \tag{3.4}$$

where $I_{PSC} = 5\,\text{nA}$ (Gaudry et al., 2012). Excitatory and inhibitory postsynaptic currents are assumed to have the same magnitude but opposite signs. $t_{PSC} = 5\,\text{ms}$ is the half-life of the postsynaptic current decay (Gaudry et al., 2012). α_2, β_2, γ_2, and δ_2 are normalisation constants so that the range of the sinusoidal and exponential terms is 0 to 1. The postsynaptic current traces have duration $2\,\text{ms} + 7t_{PSC}$, that is 2 ms of rise time plus $7t_{PSC}$ of decay time. The simulation was implemented using Euler's method with a simulation time step of $10^{-4}s$. Our simulation code is derived from the source code published by Kakaria and de Bivort (2017). All simulations were performed using MATLAB (The MathWorks Inc, Natick, MA) and all the source code is available at `https://github.com/johnpi/eLife_Pisokas_Heinze_Webb_2019` (copy archived at `https://github.com/elifesciences-publications/eLife_Pisokas_Heinze_Webb_2019`). For data analysis we used MATLAB, python, and R scripts.

3.4.2 *Neuronal projections and connectivity*

We modelled and compared the hypothetical ring attractor circuits of the fruit fly *D. melanogaster* and the desert locust *S. gregaria*. The connectivity of the circuits has been inferred mostly from anatomical data derived using light microscopy, with overlapping neuronal terminals assumed to form synapses between them (Wolff and Rubin, 2018; Wolff et al., 2015; Heinze and Homberg, 2007, 2008; Pfeiffer and Homberg, 2014).

Our models include the E-PG, P-EG, P-EN and Delta7 neurons. Note that, in fruit flies, P-EG refers to the updated set of neurons innervating all PB glomeruli as reported in Wolff and Rubin (2018) (PBG1–9.s-EBt.b-D/V GA.b). In this paper, E-PG refers to the E-PG (PBG1–8.b-EBw.s-D/V GA.b) and the complimentary E-PG_T (PBG9.b-EB.P.s-GA-t.b) combined (Wolff et al., 2015; Wolff and Rubin, 2018). Therefore, E-PG neurons are innervating all PB glomeruli in both species. Delta7 refers to PB18.s-GxΔ7Gy.b and PB18.s-9i1i8c.b neurons combined (Wolff et al., 2015; Wolff and Rubin, 2018). Table 3.3 shows the nomenclature correspondence in detail.

These neurons innervate two of the central complex neuropils, the protocerebral bridge (PB) and the ellipsoid body (EB). Ellipsoid body is the name used for this structure in the fruit fly *D. melanogaster*, while in the locust *S. gregaria* the equivalent

Table 3.3: Neuronal nomenclature. The names used for the homologous neurons differ between *Drosophila* and other species. The first column shows the name used in this paper to refer to each group of neurons. The other three columns provide the names used in the literature.

Model	*Drosophila*		Locust
Neuron name	Consensus name	Systematic name (Wolff et al., 2018)	Name
E-PG	E-PG and E-PG$_T$	PBG1–8.b-EBw.s-D/V GA.b and PBG9.b-EB.P.s-GA-t.b	CL1a
P-EN	P-EN	PBG2-9.s-EBt.b-NO1.b	CL2
P-EG	P-EG	PBG1–9.s-EBt.b-D/V GA.b	CL1b
Delta7	Delta7 or Δ7	PB18.s-GxΔ7Gy.b and PB18.s-9i1i8c.b	TB1

structure is referred to as lower division of the central body (CBL). To aid comparisons with previous models and for general simplification, we use the term EB for both species. The PB is a moustache shaped structure consisting of 16 or 18 glomeruli, depending on the species. In the fruit fly *D. melanogaster*, the EB has a torus shape consisting of eight tiles. Each tile is further broken down in two wedges. In the locust *S. gregaria*, the EB (CBL) is a linear structure, open at the edges, consisting of eight columns. Each column has two subsections similar to the wedges found in *D. melanogaster*.

For both *D. melanogaster* and *S. gregaria*, the synaptic domains of each of the E-PG, P-EN and P-EG neurons are confined to one glomerulus of the PB, with the exception of the locust E-PG neurons that cross-innervate the two medial glomeruli (Figures 3.3 and 3.4). In the EB, the synaptic domains of E-PG neurons are constrained in single wedges (half tiles) while the synaptic domains of P-EN and P-EG neurons extend to whole tiles (Wolff et al., 2015). Furthermore, E-PG neurons innervate wedges filling the posterior and medial shells of the EB while P-EG neurons innervate whole tiles filling only the posterior shell of the EB (Wolff et al., 2015). Our model assumes that their overlap in the posterior shell implies functional connectivity.

In our models, the E-PG, P-EG and P-EN neurons are assumed to produce excitatory effect on their postsynaptic neurons while Delta7 neurons are assumed to provide the inhibition, as Kakaria and de Bivort (2017) proposed. The projection patterns of the aforementioned neurons were mapped to one connectivity matrix for each species (Supplementary Figure 3.17). Supplementary Figure 3.17A shows the connectivity matrix of the *D. melanogaster* fruit fly model, Supplementary Figure 3.17B the connectivity matrix of the *S. gregaria* desert locust model.

The most salient difference between the two matrices is the connectivity pattern of the Delta7 neurons (lower right part of Supplementary Figures 3.17A and 3.17B). In *D.*

melanogaster, the Delta7 neurons receive synapses uniformly across the PB glomeruli, while in the locust *S. gregaria* the Delta7 neurons have synaptic domains focused in specific glomeruli. We analysed the effect of this difference in detail in the Results section. Another major difference apparent in the connectivity matrices is the existence of 18 glomeruli in the PB of *D. melanogaster* but 16 in *S. gregaria*.

We modelled each PB glomerulus, as being innervated by one neuron of each class (E-PG, P-EG, P-EN) even though in reality there are several instances of each one. This was done in order to simplify the computational demands of the simulations.

The locust inhibition pattern has been modelled as the summation of two Gaussian functions that approximate the synaptic density across the PB glomeruli, as derived from estimates of dendritic density along the PB in dye-filled Delta7 neurons. The standard deviation (σ) of the Gaussian functions was set to the value 0.8 as the nearest approximation to the visually determined synaptic domain width. To calculate the synaptic strength of each synapse we used the expression

$$w(i) = W\frac{1}{\sigma\sqrt{2\pi}}e^{-\frac{1}{2}\left(\frac{\frac{i-1}{n}2\pi-\mu}{\sigma}\right)^2} \tag{3.5}$$

where W is a scaling factor specifying the maximum synaptic strength across the PB, i is the glomerulus number as shown in Figure 3.15, n is the number of glomeruli in each hemisphere, $\mu = \pi$, and σ is the standard deviation parameter specifying the width of the Gaussian function used. σ is the parameter estimated by visual inspection of light microscopy data. W is the parameter selected by the optimisation process.

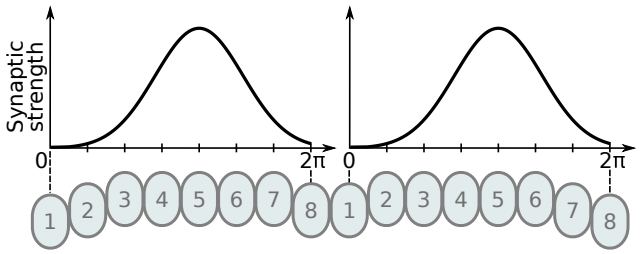

Figure 3.15: Illustration of Gaussian distribution of synaptic strengths. The Gaussian distribution of synaptic strengths along synapses located in the PB glomeruli. The synaptic strengths along the PB are illustrated for one Delta7 neuron. The example illustrates the distribution for eight glomeruli, the same method is used for the hybrid-species model using nine glomeruli instead.

It is worth noting that in all our simulations we use the full connectivity matrices derived from neuronal projection data and not the effective circuits described in the section Results.

3.4.3 *Stimuli*

Two types of input stimuli were used for the experiments: heading and angular velocity. The heading stimulus was provided as incoming spiking activity directly to the E-PG neurons, corresponding to input from Ring neurons (Young and Armstrong, 2010) (called TL neurons in locusts (Vitzthum et al., 2002)). The position of a visual cue, angle of light polarisation (Heinze and Homberg, 2007) or retinotopic landmark position (Seelig and Jayaraman, 2015) around the animal, was mapped to higher firing rates supplied to E-PG neurons at the corresponding location of the EB. The stimulus followed spatially a von Mises distribution with mean the azimuth of the stimulus and full width at half maximum (FWHM) of approximately 90° (Figure 3.16). The spatial distribution of the stimulus strength was derived using Equation 3.6.

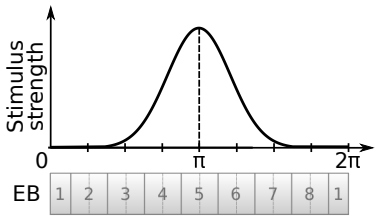

Figure 3.16: Illustration of von Mises distributed stimulus. The curve demonstrates the relative intensity of the stimulus supplied to neurons innervating each EB tile. In this illustration the stimulus is centred at tile 5.

$$
\begin{aligned}
f(\mu, x) &= \frac{e^{\kappa \cos(a(x)-\mu)}}{2\pi I_0(\kappa)}, \\
I_0(\kappa) &= \sum_{i=0}^{\infty} \frac{\kappa^{2i}}{2^{2i}(i!)^2}, \\
a(x) &= \frac{\pi}{4}(x-1)
\end{aligned}
\tag{3.6}
$$

where $\mu \in [0, 2\pi]$ is the stimulus centre location parameter, $x = \{1, 2, \ldots, 8\}$ is the EB tile numerical index and $\kappa = \frac{3}{4}\pi$ is the shape parameter. The values returned by $f(\mu, x)$ are converted to corresponding spiking activity levels. To do this, we sampled from a Poisson distribution. The minimum value is mapped to the background activity level and the maximum to the peak level of activity. We assumed that the background activity follows a Poisson distribution with a mean background action potential rate of 5 impulses/s. The peak impulse firing rate of the stimulus signal was equal to the peak spiking rate of the activity 'bump' across the E-PG neuron population under steady state conditions, in order to obtain comparable measurements across species.

The second type of stimulus, angular velocity stimulus, consisted of spikes which were directly supplied to all P-EN neurons in one hemisphere of the PB, corresponding to the direction of rotation (clockwise versus counter-clockwise). The peak impulse rate of the injected spike trains was equal to the peak rate of the steady state activity 'bump' across the P-EN neurons. This was done in order to allow for direct comparisons between species.

3.4.4 *Free parameters*

The free parameters of our models are the synaptic efficacies. The efficacies of synapses connecting each class of neurons are assumed to be identical, e.g., all P-EN to E-PG synapses have the same strength. Therefore, we have one free parameter for each synaptic class. Furthermore, we reduced the computational complexity of optimising the synaptic strengths by making the synaptic strength between some classes of neurons identical. The synaptic strengths of E-PG to P-EN and P-EG are identical as are the synaptic strengths of Delta7 to P-EN and P-EG. This is the minimum set of synaptic strengths that results in working ring attractors. We assumed that all synapses are excitatory apart from the synapses with Delta7 neurons on the presynaptic side, which were assumed to be inhibitory, as Kakaria and de Bivort (2017) proposed. The synaptic strength was modelled as the number of I_{PSC} unit equivalents flowing to the postsynaptic neuron per action potential.

Although our models are constrained by anatomical evidence, existing biological studies do not specify synaptic weights or connectivity. Based on the goal that each of the circuits should yield a functional ring attractor, an optimisation algorithm was used to search for synaptic strength combinations that resulted in working ring attractors. Both simulated annealing and particle swarm optimisation algorithms were used (Matlab Optimization Toolbox 'simulannealbnd' and 'particleswarm' functions); the first one converges quicker while the second one covers the search space more thoroughly. We constrained the acceptable solutions to those that produced an activity 'bump' with full width at half maximum (FWHM) of approximately 90° since this is the width that has been observed in fruit flies (Kim et al., 2017).

The objective function used to optimise the synaptic strengths w_i was:

$$
\begin{aligned}
\underset{\mathbf{w}}{\text{argmin}} \quad & 4(\epsilon_{H1}(\mathbf{w}) + \epsilon_{H2}(\mathbf{w})) + \epsilon_{W1}(\mathbf{w}) + \epsilon_{W2}(\mathbf{w}) + Np_0(\mathbf{w}) \\
\text{s. t.} \quad & \epsilon_{H1}(\mathbf{w}) = \frac{|H_d(t_1) - H_a(\mathbf{w}, t_1)|}{360^\circ} \\
& \epsilon_{H2}(\mathbf{w}) = \frac{|H_d(t_2) - H_a(\mathbf{w}, t_2)|}{360^\circ} \\
& \epsilon_{W1}(\mathbf{w}) = \frac{|90^\circ - W_a(\mathbf{w}, t_1)|}{360^\circ} \\
& \epsilon_{W2}(\mathbf{w}) = \frac{|90^\circ - W_a(\mathbf{w}, t_2)|}{360^\circ} \\
& p_0(\mathbf{w}) = \frac{1}{N}\sum_{i=1}^{N}(e^{-|w_i|})^2 \\
& 0 \leq w_1 \leq 100 \\
& 0 \leq w_2 \leq 100 \\
& 0 \leq w_3 \leq 100 \\
& -100 \leq w_4 \leq 0 \\
& -100 \leq w_5 \leq 0
\end{aligned}
\tag{3.7}
$$

Where ϵ_{H1}, ϵ_{H2}, ϵ_{W1} and ϵ_{W2} are the error factors measured as deviations from the desired values. p_0 is used to penalise synaptic strengths being too close to zero. N is the number of synaptic strengths w_i. $H_d(t)$ is the desired activity 'bump' heading at time t, while $H_a(\mathbf{w}, t)$ is the actual measured activity 'bump' heading at time t given a model with synaptic strengths $\mathbf{w}$. $W_a(\mathbf{w}, t)$ is the actual measured width of the activity 'bump' at time t (measured as the full width at half maximum). The constraints in Equation 3.7 specify that the synapses with Delta7 neurons at their presynaptic side are inhibitory (negative) and all others are excitatory (positive). Synaptic weights were initialised with values -0.01 or 0.01 depending on whether the negative only or positive only constraint was applied. During optimisation the spiking models were used to run the simulations and search the space of synaptic strengths. The synaptic strength sets that resulted from multiple runs were manually tested to verify the results. The objective function was used to optimise the synaptic strengths separately for each of the models: the fruit fly, the locust, and the hybrid-species model.

3.4.5 *Sensitivity Analysis and Parameter Noise*

For the sensitivity analysis, white Gaussian noise was added to the membrane parameters of neurons (conductance and capacitance) as well as to the synaptic efficacies, using the formula

$$v_i = v_{nominal} + \frac{x}{100} v_{nominal} \epsilon, \quad \epsilon \sim \mathcal{N}(\mu, \sigma^2) \tag{3.8}$$

where v_i is the resulting noisy value of the parameter with $i = \{1, 2, \ldots, M\}$ and M being the number of parameters. $v_{nominal}$ is the nominal value of the parameter, $x \in [0, 100]$ is the percentage of noise to be added to the nominal value, ϵ is a random variable sampled from the Gaussian distribution with $\mu = 0$ and $\sigma^2 = 1$. When noise was added to the conductance and capacitance of neurons the resulting values were clipped to a minimum of 0 because conductance and capacitance values cannot be negative. For measuring the tolerance to inter-hemispheric synaptic asymmetry we altered the P-EN to E-PG synapses in one hemisphere by different amounts in the range -100% to 100%.

The number of successful trials was counted in each condition. The criterion for a successful trial was that the activity 'bump' transitioned from an initial stimulus-driven heading to a second stimulus-driven heading with an error of less that $\pm 45^\circ$ and subsequently the second heading was maintained for at least 3 s. The criterion used for judging jump versus gradual transition of the heading signal was that for the transition to be considered a jump the intervening neurons between the origin and end location must not become maximally active during the transition.

3.5 ACKNOWLEDGEMENTS

The authors thank Matthias Hennig and Michael Rule for their invaluable comments.

3.6 ADDITIONAL INFORMATION

3.6.1 *Funding*

Table 3.4

Funder	Grant reference number	Author
University of Edinburgh	Graduate Student Fellowship	Ioannis Pisokas
H2020 European Research Council	Grant agreement no. 714599	Stanley Heinze

The funders had no role in study design, data collection and interpretation, or the decision to submit the work for publication.

3.6.2 *Author Contributions*

Ioannis Pisokas: Conceptualization, Software, Formal analysis, Validation, Investigation, Visualization, Methodology, Writing - original draft, Writing - review and editing; Stanley Heinze: Conceptualization, Supervision, Funding acquisition, Validation, Visualization, Writing - review and editing; Barbara Webb: Conceptualization, Resources, Supervision, Funding acquisition, Writing - review and editing.

3.6.3 *Author ORCIDs*

Ioannis Pisokas https://orcid.org/0000-0001-7426-3207
Stanley Heinze https://orcid.org/0000-0002-8145-3348

3.6.4 *Decision Letter and Author Response*

Decision letter https://doi.org/10.7554/eLife.53985.sa1
Author response https://doi.org/10.7554/eLife.53985.sa2

3.6.5 *Data Availability*

All source scripts for producing the data as well as for generating Figures 3.6A, 3.6B, 3.7, 3.8, 3.9, 3.10, 3.11, 3.12, 3.14 and Tables 3.1 and 3.2 are located at https://github.com/johnpi/eLife_Pisokas_Heinze_Webb_2019 (copy archived at https://github.com/elifesciences-publications/eLife_Pisokas_Heinze_Webb_2019).

3.7 SUPPLEMENTAL INFORMATION

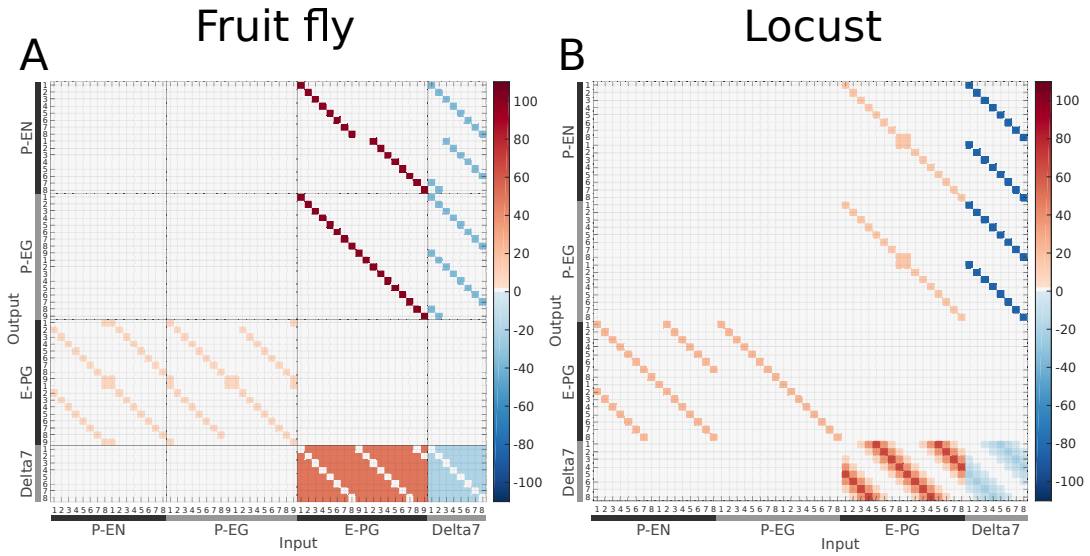

Figure 3.17: Connectivity matrices of the two species. The connectivity matrices derived by the exact neuronal projections of the fruit fly (*Drosophila melanogaster*) and the desert locust (*Schistocerca gregaria*), respectively. The difference in the distribution of Delta7 neuron synaptic domains is evident at the lower right part of the images. Synaptic strength is denoted by colour in units of postsynaptic current equivalents as described in Methods and Materials.

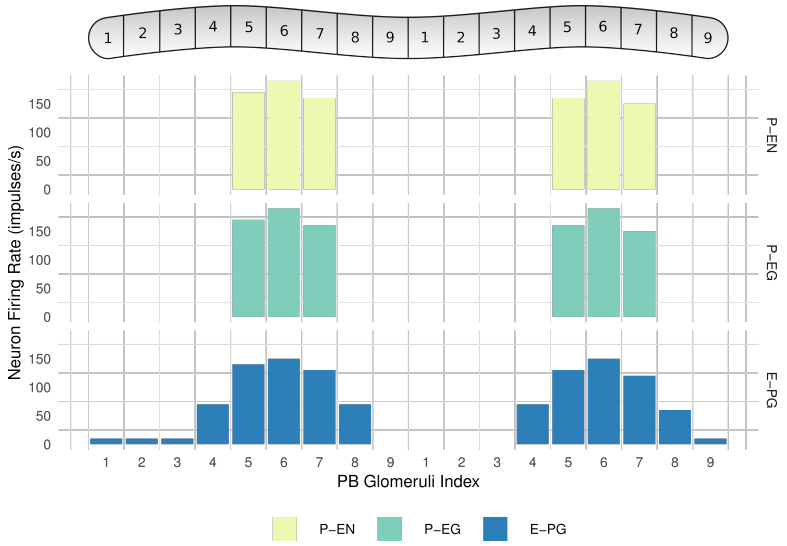

Figure 3.18: Neuronal activity across PB glomeruli. The neuronal activity of P-EN, P-EG and E-PG neurons innervating the glomeruli of the PB for the simulated model of the fruit fly. The activity 'bump' is centred around identically numbered glomeruli on the two hemispheres.

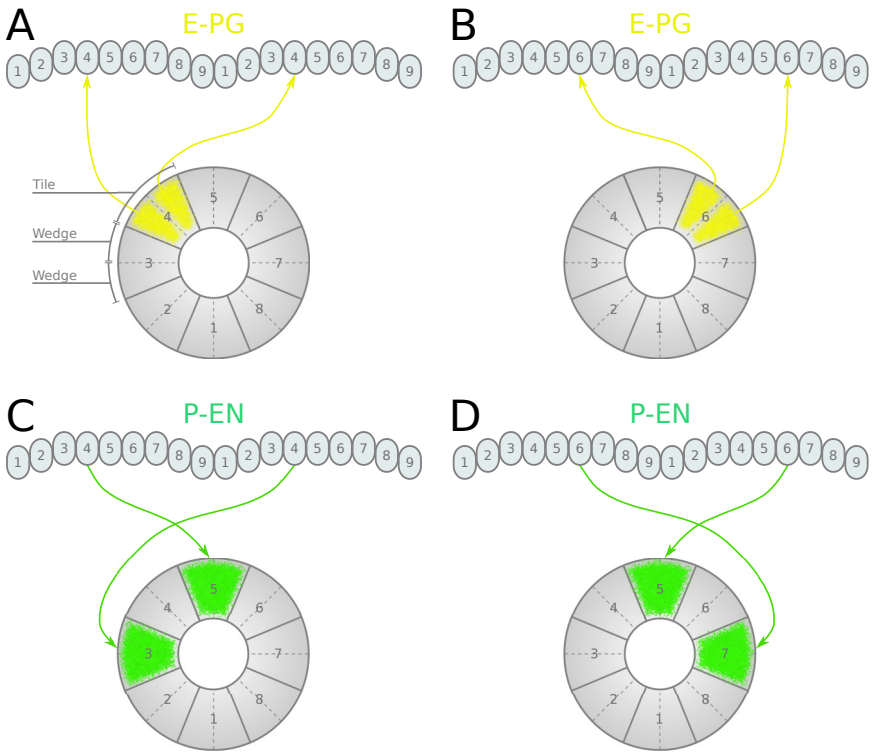

Figure 3.19: Neuronal projections in the fruit fly. (**A**, **B**) Examples of the projection patterns of E-PG neurons (combined E-PG and E-PG$_T$, see Table 3.3). (**C**, **D**) Examples of P-EN neurons with their synaptic domains and projection patterns (see main text for detailed description).

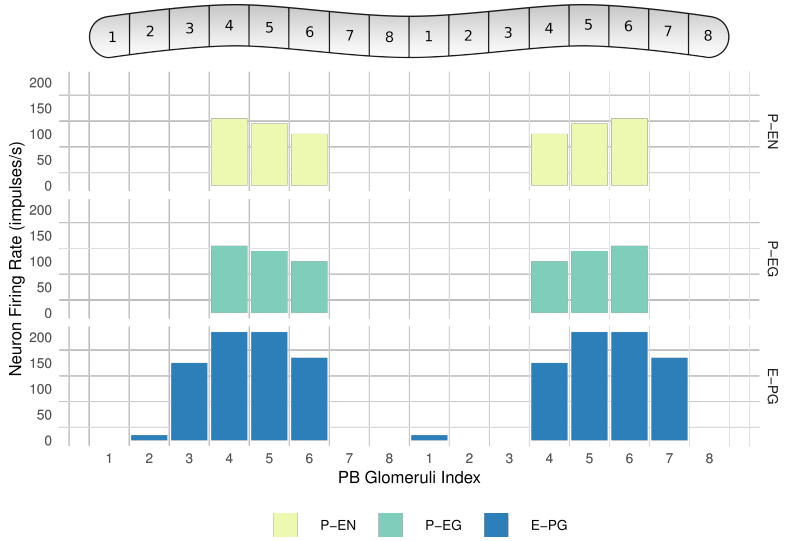

Figure 3.20: Neuronal activity across PB glomeruli. The neuronal activity of P-EN, P-EG and E-PG neurons innervating the glomeruli of the PB for the simulated model of the locust. The activity 'bump' is centred around identically numbered glomeruli on the two hemispheres.

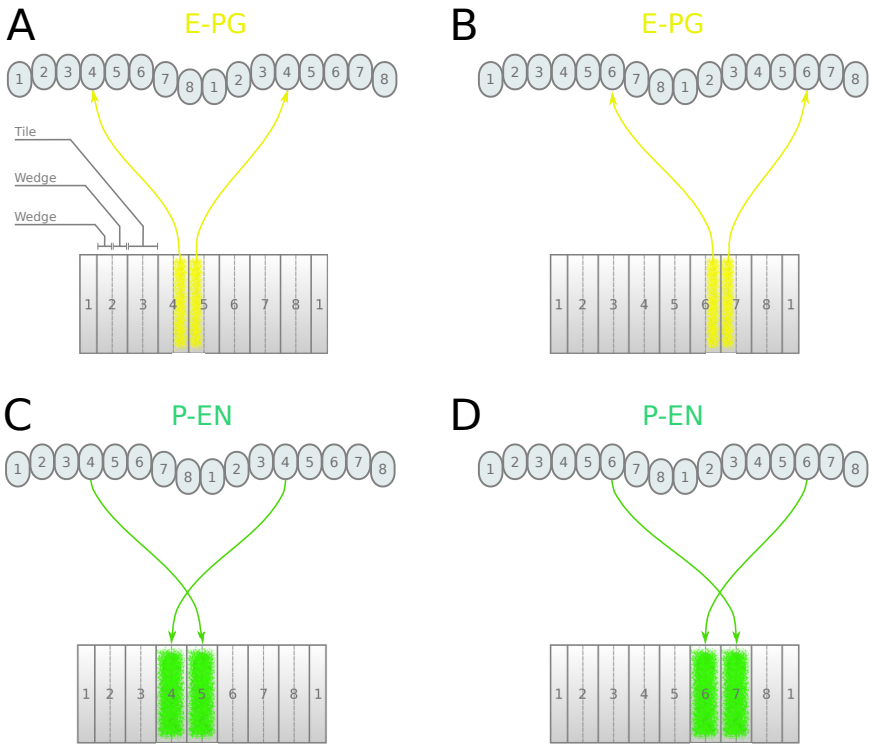

Figure 3.21: Neuronal projections in the locust. Examples of the projection patterns of E-PG (**A**, **B**) and P-EN (**C**, **D**) neurons in the locust. The anatomy and projection patterns differ from those in the fruit fly (see main text for detailed description).

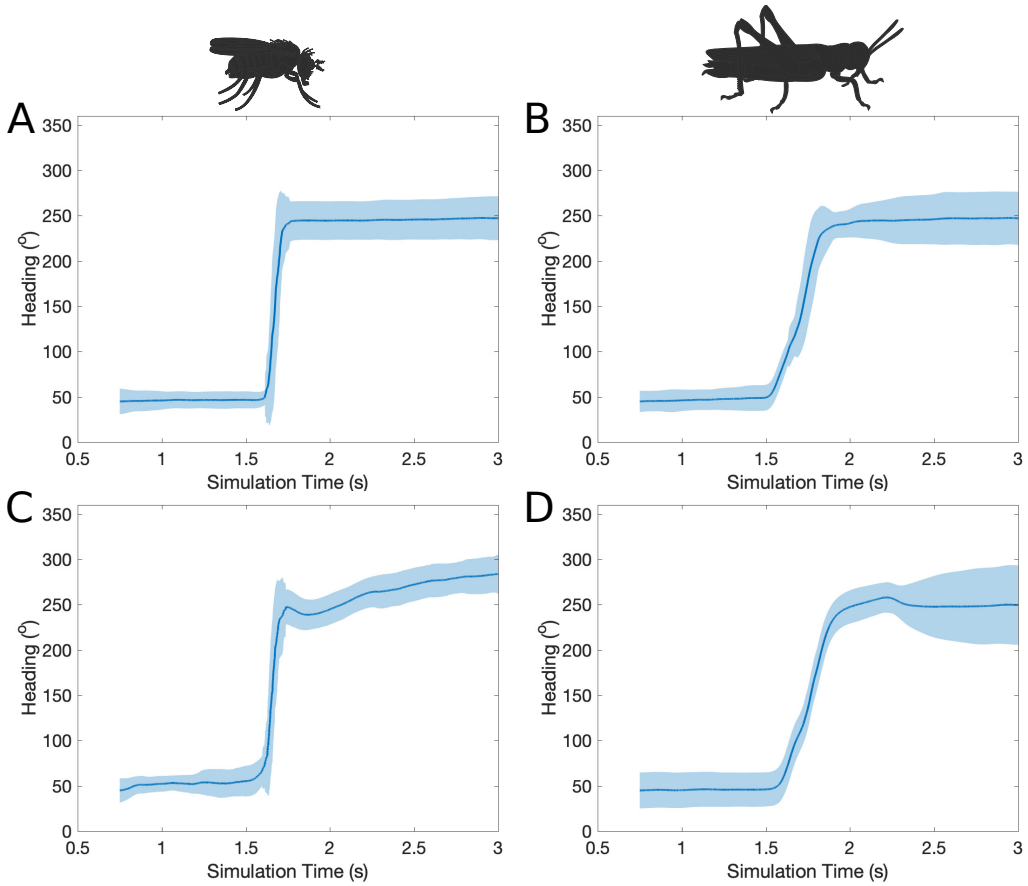

Figure 3.22: Response of spiking and rate-based models to step change of heading. The mean activity 'bump' heading and corresponding standard deviation for the fruit fly and the locust models across time when stimulated with a step change of heading by 180° (80 trials each). In **A** and **B** using spiking neuron models; while in **C** and **D** using rate-based neuron models. The activity 'bump' moves gradually to the new heading azimuth in the locust models (**B**, **D**) while it moves instantaneously in the fruit fly models (**A**, **C**). Note that in **A** and **C** the transition slope does not appear exactly vertical (instantaneous) because it is the mean of multiple trials with the transition for each trial occurring with a small time lag in respect to the others.

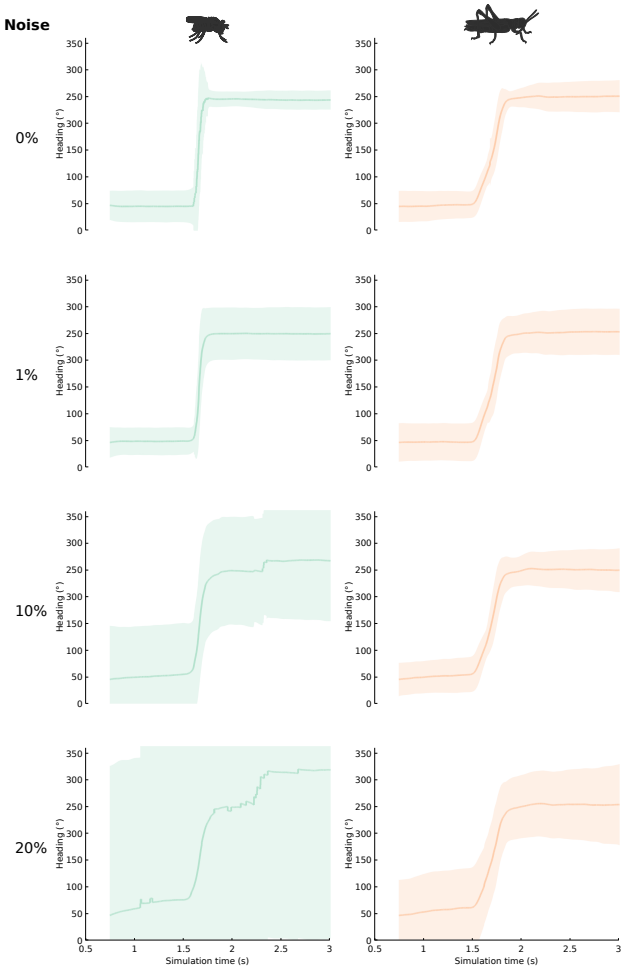

Figure 3.23: Effect of cell membrane parameter heterogeneity to transition regime. The difference in the heading signal transition is present at different amounts of heterogeneity in neuron membrane parameters. As neuronal parameters deviate from their nominal values, from top to bottom, the stability of the heading signal deteriorates. The noise added to each membrane property (conductance and capacitance) was chosen from a normally distributed pseudorandom generator with sigma values in the range from 0 to the nominal value of the parameter and the resulting values were clipped to 0 so they are never negative.

BIBLIOGRAPHY

Adden, A., Wibrand, S., Pfeiffer, K., Warrant, E., and Heinze, S. (2020). The brain of a nocturnal migratory insect, the Australian bogong moth. *Journal of Comparative Neurology*, (January):1942–1963.

Amari, S.-i. (1977). Dynamics of pattern formation in lateral-inhibition type neural fields. *Biological Cybernetics*, 27(2):77–87.

Beetz, M. J., el Jundi, B., Heinze, S., and Homberg, U. (2015). Topographic organization and possible function of the posterior optic tubercles in the brain of the desert locust *Schistocerca gregaria*. *Journal of Comparative Neurology*, 523(11):1589–1607.

Blair, H. T. and Sharp, P. E. (1995). Anticipatory head direction signals in anterior thalamus: evidence for a thalamocortical circuit that integrates angular head motion to compute head direction. *Journal of Neuroscience*, 15(9):6260–6270.

Bockhorst, T. and Homberg, U. (2015). Amplitude and dynamics of polarization-plane signaling in the central complex of the locust brain. *Journal of Neurophysiology*, 113(9):3291–3311.

Brody, C. D., Romo, R., and Kepecs, A. (2003). Basic mechanisms for graded persistent activity: Discrete attractors, continuous attractors, and dynamic representations. *Current Opinion in Neurobiology*, 13(2):204–211.

Cope, A. J., Sabo, C., Vasilaki, E., Barron, A. B., and Marshall, J. A. R. (2017). A computational model of the integration of landmarks and motion in the insect central complex. *PLoS ONE*, 12(2):e0172325.

Dacke, M., Nilsson, D.-E., Scholtz, C. H., Byrne, M., and Warrant, E. J. (2003). Insect orientation to polarized moonlight. *Nature*, 424(6944):33–33.

Darwin, C. (1873). Origin of certain instincts. *Nature*, 7(179):417–418.

de Vries, L., Pfeiffer, K., Trebels, B., Adden, A. K., Green, K., Warrant, E., and Heinze, S. (2017). Comparison of navigation-related brain regions in migratory versus non-migratory noctuid moths. *Frontiers in Behavioral Neuroscience*, 11:158.

el Jundi, B., Heinze, S., Lenschow, C., Kurylas, A., Rohlfing, T., and Homberg, U. (2010). The locust standard brain: A 3d standard of the central complex as a platform for neural network analysis. *Frontiers in Systems Neuroscience*, 3(FEB):21.

el Jundi, B., Pfeiffer, K., Heinze, S., and Homberg, U. (2014). Integration of polarization and chromatic cues in the insect sky compass. *Journal of Comparative Physiology A*, 200(6):575–589.

el Jundi, B., Warrant, E. J., Pfeiffer, K., and Dacke, M. (2018). Neuroarchitecture of the dung beetle central complex. *Journal of Comparative Neurology*, 526(16):2612–2630.

Franconville, R., Beron, C., and Jayaraman, V. (2018). Building a functional connectome of the *Drosophila* central complex. *eLife*, 7.

Fry, S. N., Sayaman, R., and Dickinson, M. H. (2003). The aerodynamics of free-flight maneuvers in *Drosophila*. *Science*, 300(5618):495–498.

Gaudry, Q., Hong, E. J., Kain, J., de Bivort, B. L., and Wilson, R. I. (2012). Asymmetric neurotransmitter release enables rapid odour lateralization in *Drosophila*. *Nature*, 493(7432):424–428.

Giraldo, Y. M., Leitch, K. J., Ros, I. G., Warren, T. L., Weir, P. T., and Dickinson, M. H. (2018). Sun navigation requires compass neurons in *Drosophila*. *Current Biology*, 28(17):2845–2852.e4.

Goodridge, J. P., Dudchenko, P. A., Worboys, K. A., Golob, E. J., and Taube, J. S. (1998). Cue control and head direction cells. *Behavioral Neuroscience*, 112(4):749–761.

Goodridge, J. P. and Touretzky, D. S. (2000). Modeling attractor deformation in the rodent head-direction system. *Journal of Neurophysiology*, 83(6):3402–3410.

Gouwens, N. W. and Wilson, R. I. (2009). Signal propagation in *Drosophila* central neurons. *Journal of Neuroscience*, 29(19):6239–6249.

Green, J., Adachi, A., Shah, K. K., Hirokawa, J. D., Magani, P. S., and Maimon, G. (2017). A neural circuit architecture for angular integration in *Drosophila*. *Nature*, 546(7656):101–106.

Green, J. and Maimon, G. (2018). Building a heading signal from anatomically defined neuron types in the *Drosophila* central complex. *Current Opinion in Neurobiology*, 52:156–164.

Heinze, S., Florman, J., Asokaraj, S., El Jundi, B., and Reppert, S. M. (2013). Anatomical basis of sun compass navigation II: The neuronal composition of the central complex of the monarch butterfly. *Journal of Comparative Neurology*, 521(2):267–298.

Heinze, S., Gotthardt, S., and Homberg, U. (2009). Transformation of polarized light information in the central complex of the locust. *Journal of neuroscience*, 29(38):11783–93.

Heinze, S. and Homberg, U. (2007). Maplike representation of celestial e-vector orientations in the brain of an insect. *Science*, 315(5814):995–997.

Heinze, S. and Homberg, U. (2008). Neuroarchitecture of the central complex of the desert locust: Intrinsic and columnar neurons. *Journal of Comparative Neurology*, 511(4):454–478.

Heinze, S. and Homberg, U. (2009). Linking the input to the output: new sets of neurons complement the polarization vision network in the locust central complex. *Journal of neuroscience*, 29(15):4911–21.

Heinze, S. and Reppert, S. M. (2012). Anatomical basis of sun compass navigation I: The general layout of the monarch butterfly brain. *Journal of Comparative Neurology*, 520(8):1599–1628.

Homberg, U. (2004). In search of the sky compass in the insect brain. *Naturwissenschaften*, 91(5):199–208.

Homberg, U. (2015). Sky compass orientation in desert locusts—evidence from field and laboratory studies. *Frontiers in Behavioral Neuroscience*, 9:346.

Homberg, U., Heinze, S., Pfeiffer, K., Kinoshita, M., and El Jundi, B. (2011). Central neural coding of sky polarization in insects. *Philosophical Transactions of the Royal Society B: Biological Sciences*, 366(1565):680–687.

Kakaria, K. S. and de Bivort, B. L. (2017). Ring attractor dynamics emerge from a spiking model of the entire protocerebral bridge. *Frontiers in Behavioral Neuroscience*,

11:8.

Kim, S. S., Rouault, H., Druckmann, S., and Jayaraman, V. (2017). Ring attractor dynamics in the *Drosophila* central brain. *Science*, 356(6340):849–853.

Lin, C.-Y., Chuang, C.-C., Hua, T.-E., Chen, C.-C., Dickson, B. J., Greenspan, R. J., and Chiang, A.-S. (2013). A comprehensive wiring diagram of the protocerebral bridge for visual information processing in the *Drosophila* brain. *Cell Reports*, 3(5):1739–1753.

Mittelstaedt, H. (1985). Analytical cybernetics of spider navigation. In Barth, F. G., editor, *Neurobiology of Arachnids*, pages 298–316. Springer Berlin Heidelberg.

Mouritsen, H. and Frost, B. J. (2002). Virtual migration in tethered flying monarch butterflies reveals their orientation mechanisms. *Proceedings of the National Academy of Sciences of the United States of America*, 99(15):10162–6.

Müller, M. and Wehner, R. (1988). Path integration in desert ants, *Cataglyphis fortis*. *Proceedings of the National Academy of Sciences*, 85(14):5287–5290.

Nagel, K. I., Hong, E. J., and Wilson, R. I. (2015). Synaptic and circuit mechanisms promoting broadband transmission of olfactory stimulus dynamics. *Nature Neuroscience*, 18(1):56–65.

Neuser, K., Triphan, T., Mronz, M., Poeck, B., and Strauss, R. (2008). Analysis of a spatial orientation memory in *Drosophila*. *Nature*, 453(7199):1244–1247.

Ofstad, T. A., Zuker, C. S., and Reiser, M. B. (2011). Visual place learning in *Drosophila melanogaster*. *Nature*, 474(7350):204–209.

Pegel, U., Pfeiffer, K., and Homberg, U. (2018). Integration of celestial compass cues in the central complex of the locust brain. *Journal of Experimental Biology*, 221(2):jeb171207.

Pegel, U., Pfeiffer, K., Zittrell, F., Scholtyssek, C., and Homberg, U. (2019). Two compasses in the central complex of the locust brain. *Journal of Neuroscience*, 39(16):3070–3080.

Pfeiffer, K. and Homberg, U. (2014). Organization and functional roles of the central complex in the insect brain. *Annual Review of Entomology*, 59(1):165–184.

Redish, A. D., Elga, A. N., and Touretzky, D. S. (1996). A coupled attractor model of the rodent head direction system. *Network: Computation in Neural Systems*, 7(4):671–685.

Rohrbough, J. and Broadie, K. (2002). Electrophysiological analysis of synaptic transmission in central neurons of *Drosophila* larvae. *Journal of Neurophysiology*, 88(2):847–860.

Seelig, J. D. and Jayaraman, V. (2015). Neural dynamics for landmark orientation and angular path integration. *Nature*, 521(7551):186–191.

Sharp, P. E., Blair, H. T., and Cho, J. (2001). The anatomical and computational basis of the rat head-direction cell signal. *Trends in Neurosciences*, 24(5):289–294.

Sheeba, V., Gu, H., Sharma, V. K., O'Dowd, D. K., and Holmes, T. C. (2008). Circadian- and light-dependent regulation of resting membrane potential and spontaneous action potential firing of *Drosophila* circadian pacemaker neurons. *Journal of Neurophysiology*, 99(2):976–988.

Skaggs, W. E., Knierim, J. J., Kudrimoti, H. S., and McNaughton, B. L. (1995). A model of the neural basis of the rat's sense of direction. *Advances in neural information processing systems*, 7(1984):173–180.

Stackman, R. W. and Taube, J. S. (1998). Firing properties of rat lateral mammillary single units: head direction, head pitch, and angular head velocity. *Journal of neuroscience*, 18(21):9020–37.

Stein, R. B. B. (1967). Some models of neuronal variability. *Biophysical Journal*, 7(1):37–68.

Stone, T., Webb, B., Adden, A., Weddig, N. B., Honkanen, A., Templin, R., Wcislo, W., Scimeca, L., Warrant, E., and Heinze, S. (2017). An anatomically constrained model for path integration in the bee brain. *Current Biology*, 27(20):3069–3085.

Stratton, P., Wyeth, G., and Wiles, J. (2010). Calibration of the head direction network: A role for symmetric angular head velocity cells. *Journal of Computational Neuroscience*, 28(3):527–538.

Su, T. S., Lee, W. J., Huang, Y. C., Wang, C. T., and Lo, C. C. (2017). Coupled symmetric and asymmetric circuits underlying spatial orientation in fruit flies. *Nature Communications*, 8(1):1–15.

Tammero, L. F. and Dickinson, M. H. (2002). The influence of visual landscape on the free flight behavior of the fruit fly *Drosophila melanogaster*. *The Journal of experimental biology*, 205(Pt 3):327–43.

Taube, J. S. and Bassett, J. P. (2003). Persistent neural activity in head direction cells. *Cerebral Cortex*, 13(11):1162–1172.

Taube, J. S., Muller, R. U., and Ranck, J. B. (1990). Head-direction cells recorded from the postsubiculum in freely moving rats. I. Description and quantitative analysis. *Journal of Neuroscience*, 10(2):420–435.

Triphan, T., Poeck, B., Neuser, K., and Strauss, R. (2010). Visual targeting of motor actions in climbing *Drosophila*. *Current Biology*, 20(7):663–668.

Turner-Evans, D., Wegener, S., Rouault, H., Franconville, R., Wolff, T., Seelig, J. D., Druckmann, S., and Jayaraman, V. (2017). Angular velocity integration in a fly heading circuit. *eLife*, 6:2112–2126.

Turner-Evans, D. B., Jensen, K., Ali, S., Paterson, T., Sheridan, A., Ray, R. P., Lauritzen, S., Bock, D., and Jayaraman, V. (2019). The neuroanatomical ultrastructure and function of a biological ring attractor. *bioarxiv*.

Vitzthum, H. and Homberg, U. (1998). Immunocytochemical demonstration of locustatachykinin-related peptides in the central complex of the locust brain. *Journal of Comparative Neurology*, 390(4):455–469.

Vitzthum, H., Müller, M., and Homberg, U. (2002). Neurons of the central complex of the locust *Schistocerca gregaria* are sensitive to polarized light. *Journal of Neuroscience*, 22(3):1114–1125.

von Frisch, K. (1967). *The dance language and orientation of bees*. Harvard University Press.

von Hadeln, J., Hensgen, R., Bockhorst, T., Rosner, R., Heidasch, R., Pegel, U., Quintero Pérez, M., and Homberg, U. (2020). Neuroarchitecture of the central complex of the desert locust: Tangential neurons. *Journal of Comparative Neurology*, 528(6):906–934.

Williams, J. L. D. (1975). Anatomical studies of the insect central nervous system: A ground-plan of the midbrain and an introduction to the central complex in the locust, *Schistocerca gregaria* (orthoptera). *Journal of Zoology*, 176(1):67–86.

Wolff, T., Iyer, N. A., and Rubin, G. M. (2015). Neuroarchitecture and neuroanatomy of the *Drosophila* central complex: A GAL4-based dissection of protocerebral bridge neurons and circuits. *Journal of Comparative Neurology*, 523(7):997–1037.

Wolff, T. and Rubin, G. M. (2018). Neuroarchitecture of the *Drosophila* central complex: A catalog of nodulus and asymmetrical body neurons and a revision of the protocerebral bridge catalog. *Journal of Comparative Neurology*, 526(16):2585–2611.

Young, J. M. and Armstrong, J. D. (2010). Structure of the adult central complex in *Drosophila*: Organization of distinct neuronal subsets. *Journal of Comparative Neurology*, 518(9):1500–1524.

Zhang, K. (1996). Representation of spatial orientation by the intrinsic dynamics of the head-direction cell ensemble: a theory. *Journal of Neuroscience*, 16(6):2112–2126.

Part II

HOME VECTOR MEMORY

For integrating velocity vectors over time, a temporal integration mechanism is required. Part ii of this thesis is concerned with this aspect of path integration; what is the neuronal substrate that integrates velocity into a home vector memory? This part consists of three studies approaching this question with different methods.

Chapter 4 contains a review of neural integration models that have been proposed in the literature and discusses their appropriateness for the home vector memory.

Chapter 5 compares behavioural data with computational models and agent simulations to test the hypothesis that the substrate of the home vector memory is a bump attractor network, and concludes that the predictions of the bump attractor hypothesis contradict animal behaviour.

Chapter 6 consists of behavioural experiments combined with computational modelling and agent simulations that investigate the nature of the memory employed by the path integration system. It reveals that the distance component of the home vector is disrupted by cold-induced anaesthesia but the direction component survives.

Chapter 4 was authored by myself with some reviewing and editing contributed by Matthias Hennig, Barbara Webb, and Stanley Heinze.

Chapter 5 is under review for publication as of May 2022 (Pisokas and Hennig, 2022). The paper was co-authored by myself and Matthias Hennig. As the lead author, I was responsible for the conceptualisation, modelling, analysis, visualisations, methodology, writing of the original draft, reviewing, and editing.

Chapter 6 was published in the journal Current Biology in 2022 (Pisokas et al., 2022). The paper was co-authored by myself, Wolfgang Rössler, Barbara Webb, Jochen Zeil, and Ajay Narendra. As the lead author, I was responsible for the conceptualisation, field experiments design and execution, modelling, analysis, validation, visualisations, methodology, writing of the original draft, reviewing, and editing. The field experiments were performed independently by two teams, one led by myself and the other by Ajay Narendra, Wolfgang Rössler, and Jochen Zeil. Most of the field data used in Pisokas et al. (2022) and Chapter 6 are from the second team. The spelling used in Chapter 6 is the American English spelling as published in Current Biology.

Pisokas, I. and Hennig, M. (2022). Can the insect path integration memory be a bump attractor? *In review*.

Pisokas, I., Rössler, W., Webb, B., Zeil, J., and Narendra, A. (2022). Anesthesia disrupts distance, but not direction, of path integration memory. *Current Biology*, 32(2):445–452.

4

INTEGRATORS IN THE BRAIN

4.1 INTRODUCTION

In the broadest sense, memory is the maintenance of an internal state that persists beyond the duration of the triggering event. Commonly, a memory is thought of as having a static value, but for certain tasks, a value in memory needs to be updated by accumulating sensory information over time. Such a gradually accumulated memory value is equivalent to calculating the integral of the input over time, commonly referred to as temporal integration. An integrator composed of neurons is known as a 'neural integrator'. Neural integrators are believed to be involved in various brain systems and processes, such as keeping the eyes' location fixed (Fukushima and Kaneko, 1995; Seung, 1996; Arnold and Robinson, 1997; Aksay et al., 2007; Joshua and Lisberger, 2015), tracking the head direction (Taube et al., 1990a,b; Skaggs et al., 1995; Zhang, 1996; Redish et al., 1996; Goodridge and Touretzky, 2000; Boucheny et al., 2005), temporal prediction (Durstewitz, 2003; Durstewitz and Deco, 2008), decision making (Huk and Shadlen, 2005; Cain and Shea-Brown, 2012), and path integration (Vickerstaff and Di Paolo, 2005; Haferlach et al., 2007; Kim and Lee, 2011; Goldschmidt et al., 2015; Webb and Wystrach, 2016; Stone et al., 2017; Goldschmidt et al., 2017; Samsonovich and McNaughton, 1997; Conklin and Eliasmith, 2005; McNaughton et al., 2006; Burak and Fiete, 2009).

Depending on the task and the brain faculty involved, the integrated value must be maintained in memory for mere seconds or for much longer periods. For instance, the oculomotor system that maintains the eye position fixed between eye saccades operates in the order of a few hundreds of milliseconds, while path integrating desert ants that accumulate a memory of the distance travelled away from their nest, need to maintain this memory until they need it to return to their dwelling several hours later (Ziegler and Wehner, 1997; Cheng et al., 2005; Heinze et al., 2018; Knaden, 2019). This wide range of time scales over which neural integrators operate in brains suggests the existence of a variety of task-specific neuronal solutions and has led to the development of various neural integrator models, each with different characteristics.

In this review, we discuss the different families of computational models that have been proposed for neural integrators. To this end, we classify neural integrator models according to the value encoding they utilise. The first type of neural integrator encodes

the integrated value as a graded magnitude of neural activity (Figure 4.1a). The second type uses positional encoding, with the integrated value being related to the location of the most active neurons in a neuronal population (Figure 4.1b). The third type uses recruitment-based population coding, with the number of active units encoding the integrated quantity (Figure 4.1c). Finally, we report on the limitations and stability characteristics of the different neural integrator models that have been proposed and identify opportunities for new research.

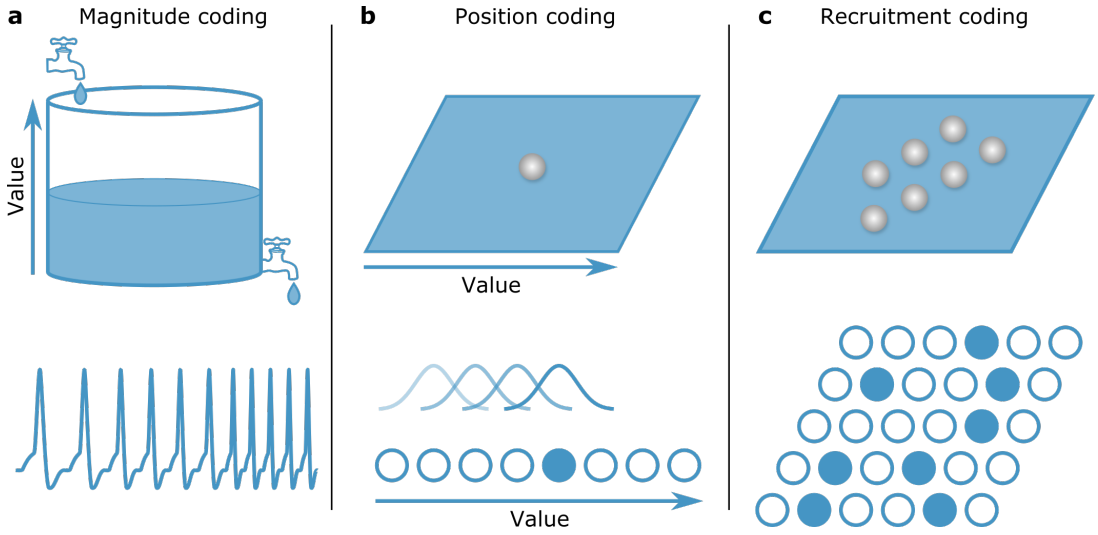

Figure 4.1: Three strategies for encoding an integrated value in memory. The top of each panel depicts a metaphor of the value encoding method while the bottom an exemplar neuronal implementation. (**a**) Encoding as the magnitude of a quantity, e.g. the liquid amount in a tank or the spike rate of a neuron. (**b**) Encoding as the spatial position of an entity, e.g. the position of the active neuron in a neuronal population. (**c**) Encoding as the number of present or active entities, e.g. the number of active neurons in a population.

4.2 GRADED MAGNITUDE ENCODING

An intuitive way to encode an integrated quantity is in the graded magnitude of neuronal activity. The magnitude of neuronal activity has been found to be related to the integral of angular velocity in the oculomotor system (Robinson, 1972), the animal's spatial location during path integration in mice (Tennant et al., 2021), and the accumulation of evidence during decision making (Huk and Shadlen, 2005; Cain and Shea-Brown, 2012). The types of models utilising graded magnitude encoding will be described in the following paragraphs.

4.2.1 *Single-neuron integrators*

Single neurons can be used as integrators of their synaptic input currents over time. In this case, the integral of the input currents is encoded as the somatic membrane potential. In the absence of synaptic input, the membrane potential of a neuron returns to a 'resting potential'[1] over time, a characteristic behaviour of leaky integrators (Box 1 in Supplemental information, Figure 4.8). However, due to the limited integration ability of a typical neuron (time constants up to a few tens or so milliseconds), its membrane potential decays quickly; thus, any integrated state value can be maintained only for a short time period. This period is often insufficient for relevant behavioural time scales. A simple method to increase neural time constants is to introduce positive feedback through recurrent synaptic connections or specific conductances.

4.2.2 *Recurrent neural networks with positive feedback*

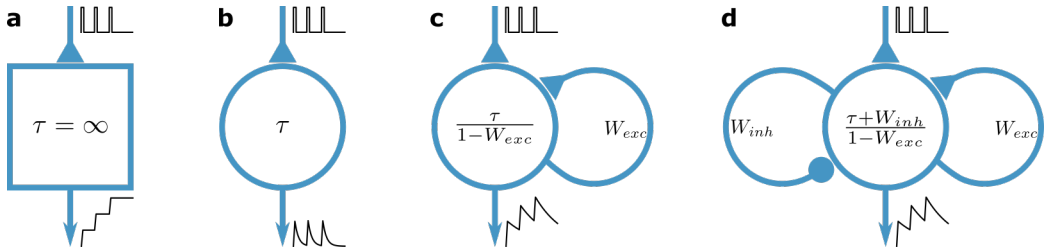

Figure 4.2: Neuronal time constants can be extended by forming recurrent neural networks. Feedback can be used to create a system with a time constant larger than the time constants of its components. (**a**) An ideal integrator has an infinite time constant. (**b**) A single neuron can be used as a neural integrator of stimuli. (**c**) A population of neurons with positive feedback can exhibit a time constant larger than the individual neurons. (**d**) A combination of positive with negative feedback can produce effective negative-derivative feedback counteracting fast deviations from the current neuronal activity state. Here τ is the membrane time constant, typically in the order of tens of milliseconds, and W are the weights associated with the recurrent connections.

Populations of neurons with recurrent connections that form positive feedback loops can self-sustain reverberating neural activity and exhibit time constants larger than the time constants of the individual constituent neurons and synapses (Figures 4.2a–4.2c). The positive feedback counteracts the leakage of the constituent neurons by feeding back to them a portion of their output in order to maintain the neural state (Figure 4.2c). If the amount of feedback is set to be equal to the neuronal leakage currents, we could achieve indefinite maintenance of the neuronal state. This situation is known as a system with a gain equal to one.

1 The resting potential of a neuron is the potential at which its membrane returns in the absence of input.

However, in practice, neurons are noisy, and their physiological parameters are heterogeneous and subject to fluctuations due to neuromodulatory inputs, state of the organism, ambient temperature, etc. With a gain precisely tuned to one, even small fluctuations of the neuronal parameters from their ideal values can increase the gain and cause self-amplification of neural activity that would lead to loss of the stored information. To avoid this situation, the feedback gain must be less than one, allowing a tolerance margin for fluctuations. The closer to one the gain is, the smaller the effective leakage and the longer the effective system time constant would be. Practically, the maximum plausible system time constant is limited by how close to one the gain can be set without risking exceeding a gain of one.

Positive feedback can be implemented in neural networks using either mutual excitatory synapses (Kamath and Keller, 1976; Seung, 1996; Seung et al., 2000) or mutual inhibitory synapses between neurons, which result in effective positive feedback through regulated disinhibition (Cannon et al., 1983; Cannon and Robinson, 1985). The average spike rate of such a neuronal population can be used to encode the integral of the input signal over time.

However, one outstanding issue with any mechanism utilising reverberating electrical activity is the relatively short time scales of persistence they can attain because of their sensitivity to parameter fine-tuning and variability. For example, Cannon et al. (1983) and Seung (1996) found that achieving a time constant of 20 s with a positive-feedback-based neural integrator composed of neurons with a typical membrane time constant ($\tau = 5$ ms) requires the network parameters to remain within 0.025% of their nominal values[2]. This is an unrealistic expectation in practice because neuronal parameters are significantly more variable (Gouwens et al., 2019). To achieve a time constant larger than 20 s, a gain even closer to one would be required; thus, the system will be even less tolerant to fluctuations of parameters.

Increasing the number of neurons in a recurrent network might alleviate the effect of a small portion of the neuronal population deviating from the ideal parameter values by averaging parameter fluctuations out (Cannon and Robinson, 1985; Seung, 1996). However, the required increase in the number of neurons may be unrealistic when considering the available neuronal resources of the animal (Pisokas and Hennig, 2022).

2 The tolerance of these models to parameter variation is a function of the ratio of the neuronal time constant (5 ms) over the neural integrator system time constant (20 s); thus, 5 ms/20 s=0.025%.

4.2.3 *Balanced recurrent neural networks*

Another class of neural networks are the 'balanced networks'. These typically consist of two neuronal populations, one population forming excitatory synapses and the other inhibitory synapses with each other (Figure 4.2d) (Vreeswijk and Sompolinsky, 1996). The average spike rate of these neural networks is determined by the balancing effect between the excitatory and inhibitory population activities and can be used to encode the integral of an input stimulus that drives the excitatory population (Shaham and Burak, 2017).

An attempt to improve upon networks with exclusively positive feedback used balanced networks with slow excitatory and fast inhibitory synaptic conductances, in effect combining positive with negative-derivative feedback (Lim and Goldman, 2013). In this model, positive feedback was used again to increase the system time constant, while the difference between the response times of the excitatory and inhibitory synapses generated a negative derivative error feedback signal that counteracts fast changes in the system's state (Lim and Goldman, 2013). This negative derivative feedback emulates how viscous substances, such as honey, resist fast changes more than slow changes. However, that study did not present a significant improvement in the system's state stability and similarly to other positive-feedback-based models, increasing the system's time constant beyond a few seconds requires unrealistically precise tuning of the synaptic weights.

4.2.4 *Feedforward neuron chains*

An alternative to positive feedback is to use chains of feedforward connected neurons embedded in a stable recurrent network (Goldman, 2009). Due to the low-pass frequency filtering provided by the neurons, the activity propagates to each neuron in the chain with a delay, and thus contributes to the output at different times (Figure 4.3). In this way, a summed output activity may be sustained for longer time periods than the time constant of the recurrent part of the network would allow. This type of network has been shown to maintain activity for time scales in the order of a few seconds and has been proposed as a model for short-lived integration in working memory (Goldman, 2009).

The advantage of feedforward networks is that, unlike positive feedback networks, they do not amplify the effect of parameter deviations from ideal values. For this reason, they are not as sensitive to neuronal parameter deviations. However, the disadvantage of feedforward networks is that the effective network time constant increases only linearly with the number of neurons. Thus, a considerable number of

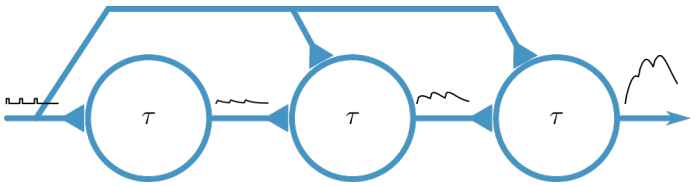

Figure 4.3: Time constants can be extended using chains of neurons. Delaying neural activity propagation through a chain of neurons can be used to prolong neural activity.

neurons would be required for maintaining the neural activity for a few seconds if neurons with a typical time constant are used.

4.2.5 *Neurons exhibiting graded persistent activity*

We mentioned earlier that unicellular integrators are constrained by the small membrane and synaptic time constants. Here, we describe an exotic cell type, the principal neurons found in layer V of the entorhinal cortex (EC) and the lateral nucleus of the lateral amygdala (LA) of mammals. These neurons can generate action potentials with a constant frequency for prolonged periods of time after the stimulus has been removed (Egorov et al., 2002, 2006). These single-neuron oscillators are not dependent on reverberating neural activity around recurrent neural circuits. The action potentials frequency can be controllably increased or decreased in a graded manner by providing appropriate synaptic input to the cell, which effectively functions as a single-neuron integrator that encodes the integral of its synaptic inputs as its spike rate (Egorov et al., 2002, 2006; Fransén et al., 2006).

Depending on the stimulus strength and duration, these principal neurons have been shown to maintain their spike rate for several tens of seconds, and when their spike rate is saturated, they can maintain it for more than ten minutes (Egorov et al., 2002; Fransén et al., 2006). Various membrane channels and metabotropic pathways are involved, but the exact biochemical mechanism is not yet well understood (Egorov et al., 2019).

The potential for maintaining any frequency within a range has been demonstrated (Fransén et al., 2006), but more work needs to be done to ascertain the resolution, repeatability, and stability of these persistent spike rates. Furthermore, the persistent activity phenomenon has been demonstrated only under specific and questionably realistic *in vitro* conditions (high levels of muscarine, see Egorov et al. 2002). It remains uncertain whether these neurons can exhibit the same phenomenon *in vivo*.

4.2.6 *Summary*

Mechanisms utilising reverberating neuronal activity are sensitive to parameter tuning and can practically maintain their state only for short time periods (a few seconds at most). Homeostatic and other regulatory processes could potentially be used to dynamically regulate the biophysical parameters to alleviate deviations from their nominal values and keep the system gain within desired bounds (Robinson, 1989; Arnold and Robinson, 1997; Lim and Goldman, 2013). However, there is little evidence that these processes can produce the precise tuning required to counteract the effects of parameter fluctuations precisely and quickly enough. It appears that adding another layer of control infrastructure to solve the tuning problem delegates it but does not solve it and unavoidably increases the complexity of the neuronal circuit. In animals with a limited number of neurons, such as insects, the assumption that additional neuronal resources might solve the stability problem may render seemingly simple mechanisms to be infeasible in practice (Chapter 5 and Pisokas and Hennig 2022).

As mentioned, neural implementations of integrators based on positive feedback obey the dynamics of leaky integrators (Box 1 in Supplemental information). When a system with leaky integrator dynamics receives no input, its state dissipates to zero over time, following an exponential progression (Figure 4.9, Box 1 in Supplemental information). This rapid dissipation of state is not amenable to the persistence of an integrated value over time. Recurrent networks that include feedforward neuron chains that prolong activity maintenance are not as sensitive to parameter deviations but require a considerable number of neurons because the activity's duration increases linearly with the number of neurons. These considerations show that practical implementations of neural integrators based on recurrent or feedforward neural networks are limited to attaining system time constants in the order of a few seconds, with the maintenance of their state for longer periods being unrealistic. Self-sustained activity through specific membrane conductances has been reported in neurons in the entorhinal cortex that can maintain their activity for several tens of seconds and do not suffer from these problems. Yet this phenomenon has only been observed *in vitro* under physiologically unrealistic conditions (high muscarine concentration) and has, so far, not been demonstrated to contribute to activity in neural integrators found in brains. Therefore, at this point, this mechanism is not a viable candidate for neural integration, and further experimental work may be required to understand its role.

4.3 POSITIONAL VALUE ENCODING

Another way to encode an integrated quantity is in the location of neural activity across a population of neurons. The canonical examples are the locus of maximal neural activity in the mammalian head direction system, which is related to the integral of angular velocity (Skaggs et al., 1995; Zhang, 1996; Redish et al., 1996; Goodridge and Touretzky, 2000; Stringer et al., 2002b; Xie et al., 2002a; Taube and Bassett, 2003; Song, 2005), and the locus of activity in the grid and place cell populations, which is related to the integral of translational velocity in path integrating animals (McNaughton et al., 1996; Samsonovich and McNaughton, 1997; Conklin and Eliasmith, 2005; McNaughton et al., 2006; Burak and Fiete, 2009). Neural network models that can maintain such a localised activity have been demonstrated with a class of networks known as 'bump attractors'.

4.3.1 *Continuous Bump Attractors*

Bump attractors are neuronal networks that maintain a localised increase of neuronal activity (referred to as an 'activity bump') across a population of neurons arranged (topologically if not anatomically) in a manifold, for instance, a line, plane, or torus (Amari, 1977; Amit, 1989; Xie et al., 2002b; Brody et al., 2003; Wu and Amari, 2005; Eliasmith, 2005; Conklin and Eliasmith, 2005). The location of the activity bump across the population of neurons encodes the system's state; this is a positional encoding of the state (Figure 4.4).

In these networks, the activity bump is established by the synaptic connectivity pattern. Typically, in models, the neurons are placed one next to the other, and each neuron excites its nearest neighbours while it inhibits neurons further away (Figure 4.4b). This dependence of the synaptic strength and polarity on the spatial proximity of neurons is not required, but it is a useful conceptualisation of how such a structured synaptic pattern might emerge.

The bump's location in an attractor network can be imposed by injecting current to a specific neuron or shifted from its current location by making the bump's shape temporarily asymmetric by providing appropriate external input. The effect of such input that shifts the bump's location can be thought of as temporarily causing an inclination in the energy landscape of the network so that the system's state (activity bump location) moves downhill (Figure 4.5b). If the bump's shift is proportional to the magnitude and duration of the input stimulus, then the bump's accumulated shift corresponds to the integral of the input signal over time (Skaggs et al., 1995; Conklin and Eliasmith, 2005). For this reason, bump attractors have been used as models

of neuronal systems that integrate signals. For instance, the head direction system which integrates angular velocity signals into the animal's heading (Skaggs et al., 1995; Zhang, 1996; Redish et al., 1996; Goodridge and Touretzky, 2000; Stringer et al., 2002b; Xie et al., 2002a; Taube and Bassett, 2003; Song, 2005) and the path integration system which integrates translational velocity signals into the spatial position of the animal (McNaughton et al., 1996; Samsonovich and McNaughton, 1997; Conklin and Eliasmith, 2005; McNaughton et al., 2006; Burak and Fiete, 2009).

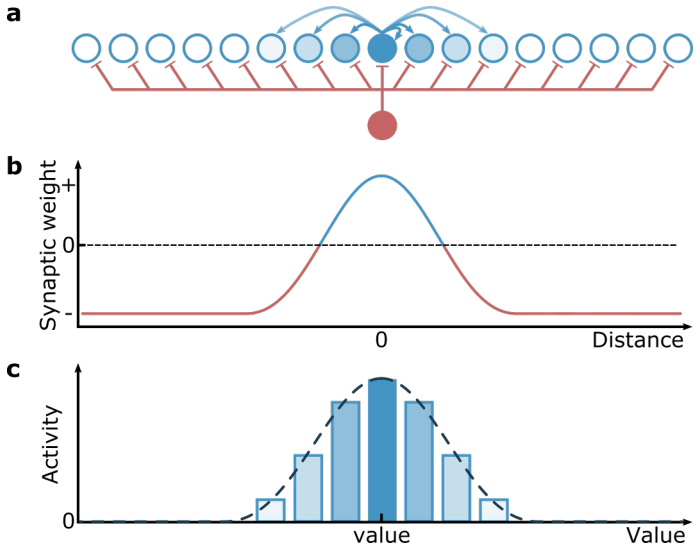

Figure 4.4: Positional encoding of integrated value using bump attractors. (**a**) Example of a bump attractor network that utilises lateral excitation, and global inhibition proportional to the average activity of all neurons. The excitatory synaptic connections of one neuron are shown as arrows and the global inhibition connections as lines ending with bars. (**b**) The effective synaptic weights of each neuron follow a Gaussian distribution pattern, with synaptic weights decreasing with the distance of the post-synaptic from the presynaptic neuron. (**c**) The population activity forms a bump. The horizontal position of the bump's centre encodes the system's state. In this illustration, the peak of the activity bump is centred on the single most active neuron, but this need not be always the case.

In the limit of an infinite number of neurons, such a neural network becomes a continuous bump attractor because the bump of activity can settle at any point along the attractor manifold, and it takes an arbitrarily small perturbation to move the bump to another point along the manifold (Brody et al., 2003; Wu and Amari, 2005).

In the absence of noise, if no stimulus is provided, the activity bump will remain in place (Figure 4.5a). However, two types of noise may be present in bump attractor networks: one is systematic noise due to structural deviation from nominal values, for instance, imperfect tuning of the biophysical parameters of the neurons and synapses, and the other is stochastic noise, for instance, due to random ion-channel activity and fluctuations in the physiological state of the organism (Mainen and

Seinowski, 1995; Mainen and Sejnowski, 1996). Both of these types of noise result in the imperfect integration of input signals. Systematic noise results in breaking the continuous attractor into a number of individual point attractors and causes a systematic (biased) drift of the activity bump towards these point attractors (Dayan and Abbott, 2005). Stochastic noise results in diffusion (random, unbiased movement) of the bump's location, akin to Brownian motion (Compte et al., 2000; Burak and Fiete, 2012). Diffusion affects the encoded value because the bump's location stochastically moves away from its initial location over time (Compte et al., 2000; Burak and Fiete, 2012). The variance of the bump's expected location increases at a constant rate over time due to diffusion (Compte et al., 2000; Burak and Fiete, 2012).

4.3.2 *Real Bump Attractors are Discrete*

In reality, a network with an infinite number of neurons is a mathematical construct useful for the analytical study of such systems. Practical implementations of bump attractor networks consist of a finite number of neurons; thus, the attractor manifold is not continuous but consists of a finite number of point attractors (Figure 4.5c). This results in a discrete approximation of the continuous attractor manifold. However, with a large enough number of neurons, these point attractors can be so close together that the input required for moving the bump from one stable point attractor (stable state) to another is smaller than the intrinsic stochastic noise present in the network. In this case, the system dynamics approximate a continuum of point attractors and are typically treated as a continuous attractor.

As the number of neurons in the bump attractor is reduced, the effects of discretisation become significant, and the individual point attractors are manifested as wells in the system energy manifold (Figure 4.5c). This ragged system energy manifold allows the activity bump to be stably maintained only at the bottom of the energy wells. The depth of the wells can be adjusted with the appropriate selection of synaptic weights, effectively introducing hysteresis in the system's state transition. Due to hysteresis, the activity bump would move over the well's lip to a neighbouring well only when the noise and stimulus exceed a threshold (Koulakov et al., 2002). Therefore, the system's state sensitivity to stochastic noise is reduced (Koulakov et al., 2002; Brody et al., 2003). However, stimuli causing only a slight tilt of the energy manifold would not move the system's state (activity bump location) over the current well's lip, so these stimuli would not be integrated, leading to error accumulation (Figure 4.5e).

Despite the improved robustness to noise exhibited by discrete bump attractors, stochastic noise causes diffusion in the bump's location in both continuous and discrete bump attractors. The diffusion rate is inversely proportional to the number

of neurons in the network and their time constants (Burak and Fiete, 2012). For this reason, increasing the number of neurons or their time constants would reduce the diffusion rate. However, this should be seen in the context of each organism since the necessary numbers for the desired diffusion rate (determined by the stability requirements) might be unrealistically large for the neuronal resources of a particular organism (Pisokas and Hennig, 2022).

The discussion here has been limited to one-dimensional attractors, but attractors have been extended to more dimensions forming planar or toroidal manifolds that support the concurrent representation of two spatial variables (Taylor, 1999; Stringer et al., 2002a; Conklin and Eliasmith, 2005; McNaughton et al., 2006; Gardner et al., 2021).

4.3.3 *Summary*

A bump attractor is a feedback-based integrator with specific connectivity that significantly slows down the loss of the stored information compared to the exponential decay in leaky integrators. However, bump attractors are also sensitive to the tuning of parameters and to noise (Wu and Amari, 2005), with requirements thought to be biologically unrealistic when used to model systems operating in time scales of several tens of seconds, such as the oculomotor system (Seung et al., 2000; Brody et al., 2003). Several attempts have been made to improve the stability of bump attractor networks in the context of spatial memory and path integration by introducing time-averaged adaptation of synaptic weights (Wu and Amari, 2005), utilising control theory in the design process (Eliasmith, 2005; Conklin and Eliasmith, 2005), or employing homeostatic mechanisms, either cellular or synaptic, to alleviate the sensitivity to parameter variation (Renart et al., 2003). However, as discussed earlier, homeostatic mechanisms require additional assumptions about the system and demand additional neuronal resources that might be unrealistic in the context of the studied animal. Again, a seemingly simple solution, in reality, might require a much more complex supporting neuronal circuit to achieve the desired performance characteristics (Pisokas and Hennig, 2022).

Discrete bump attractors sacrifice resolution to offer improved system state stability. The improved state stability can be achieved with the appropriate selection of hysteresis imposing energy barriers between states that are not exceeded by the present noise level (Figure 4.5c). The resolution of value representation depends on the number of neuronal units used in the bump attractor network. These two aspects, resolution and state stability, are both concomitant to the available neuronal resources; hence a trade-off must be found.

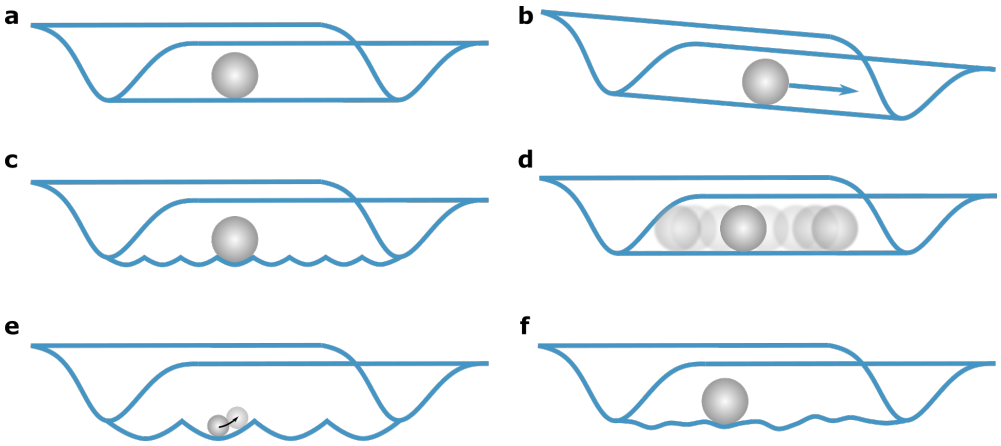

Figure 4.5: Conceptual depiction of attractor manifolds. The valley represents a function of the system's energy (Lyapunov function) at every possible system state, and the ball represents the current system state. (**a**) A line attractor is a one-dimensional continuous attractor. In a continuous line attractor, the system's state is stable at every point along the valley's basin since all points are equal to the minimum system energy value. If the system is perfectly tuned, as indicated here, the system's state (represented with a ball) will remain in place. However, in the presence of noise in the system, the state will drift randomly since there are no restorative forces preventing the state from moving along the valley. This state drift is equally likely to be towards the left or right (random walk). (**b**) An imperfectly tuned system might result in a non-level basin, causing the state (ball position) to shift downhill towards lower system energy states. The attractor basin may be non-level due to structural connectivity weights bias or may become inclined due to an input stimulus; in both cases, the non-level basin will result in a drift of the system's state. (**c**) Real neural bump attractors have a finite number of neurons approximating the continuous attractor manifold with a set of multiple point attractors located one next to the other. A finite number of wells result in an uneven and ragged manifold. For changing the system's state (ball position), enough energy is required to move it over the lip between two wells. Therefore, such a ragged manifold endows the system's state with reduced sensitivity to noise, both intrinsic system noise and noise present in stimulus signals. (**d**) Neuronal noise causes the system's state (ball location) to diffuse following Brownian motion dynamics, with the error in the system's state (variance) increasing at a constant rate over time (Burak and Fiete, 2012). (**e**) Small input signal pulses may not be integrated by discrete bump attractors. If an input event is so small that the system's state is not pushed over the transition threshold (well's lip), the state will return to the nearest stable state. Such input events will not be integrated, and integration errors will be accumulated over time. (**f**) Illustration of the effect of structural noise (synaptic and neuronal heterogeneity) on the system's state (ball location). Structural noise would cause the system's state to drift towards the locally lowest energy state resulting in systematic state drift and reduced encoding resolution.

4.4 RECRUITMENT BASED ENCODING

Heterogeneity and noise are prominent in biological systems. As we saw, reducing the resolution of representation can be traded off for increased stability of the system's

state, and as we will see, parameter variability can be utilised as a feature rather than fought as an enemy. Along these lines, a third class of models utilises collections of bistable elements to encode a system's state. A bistable element has two stable states (e.g. an ON and an OFF state), and the transition from one stable state to the other requires an input stimulus that exceeds a given threshold (Figure 4.6a). In a bistable element, we can create a hysteresis loop using two different transition thresholds, one for each transition direction (thresholds $\vartheta 1$ and $\vartheta 2$ in Figure 4.6a). The margin between the two thresholds endows a bistable unit with tolerance to noise. Because of this tolerance, the maintenance of its state is not sensitive to the precise fine-tuning of parameters.

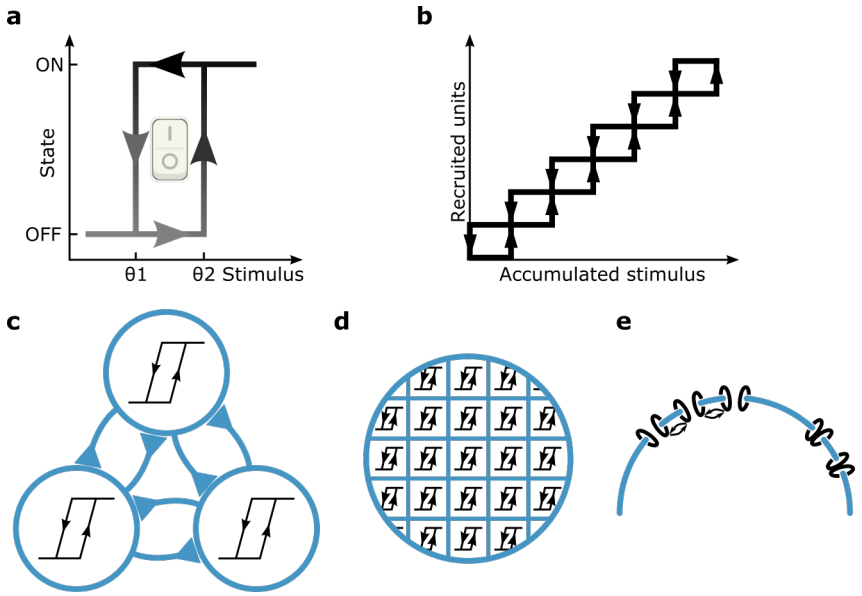

Figure 4.6: Recruitment of bistable units as integration substrate. When multiple units that exhibit bistability with different transition thresholds are interconnected, they can function as a gradually activating or deactivating population that encodes the integral of the input signal. (**a**) Bistability can be the result of hysteresis in state transition. The stimulus must exceed a minimum threshold ($\vartheta 2$) for the system state to transition from one stable state (OFF) to the other (ON). This is akin to a light switch that requires a minimum force to transition from one state to the other. For transitioning in the reverse direction (from the ON state to the OFF state), the stimulus must be adequately reduced to be lower than a different threshold ($\vartheta 1$). Stimuli between $\vartheta 1$ and $\vartheta 2$ do not cause changes in the system's state. (**b**) The accumulative effect of a population of bistable elements can be used to create a multi-stable system (a system that exhibits multiple stable states). (**c**) Hysteresis can be the result of intercellular feedback. Groups of interconnected neurons can function as a bistable unit (shown as a blue circle), and when interconnected such bistable units can function as a multi-stable system. (**d** and **e**) Bistability can emerge at the sub-cellular level through intracellular biochemical interactions. Examples are (**d**) interactions among sub-cellular compartments and (**e**) metabotropic interactions among voltage-sensitive ion channels.

Utilising a population of bistable units activated or deactivated one after the other, we can obtain a graded increase or decrease in the number of active units. Suppose the activation or deactivation of the bistable units is controlled by the intensity and duration of an input signal (Figure 4.6b). In that case, the number of active units at any instant will encode the integral of the input signal over time (Koulakov et al., 2002; Goldman et al., 2003; Nikitchenko and Koulakov, 2008). For bistable units to become active successively as the input signal is integrated, models have used bistable units with different activation thresholds, spanning the range of interest (e.g. Koulakov et al., 2002). The activation thresholds of the units may be systematically or randomly distributed. Randomly distributed thresholds may result from the population's diversity in biophysical parameter values, thus exploiting biophysical variation. For bistable units to become activated successively, in addition to their different thresholds, the input of each unit is typically the sum of the external input signal and the current states of all other units (e.g. Figure 4.6c). Initially, only the bistable units with the lowest threshold get activated by input. As more bistable units become active, the total input to each inactive unit gets closer to its threshold, and eventually, it exceeds it, and the unit gets activated. The gradual recruitment (activation) of bistable units can encode the integrated value in the number of active units (Koulakov et al., 2002; Goldman et al., 2003; Nikitchenko and Koulakov, 2008). The same mechanism and sequence of events may be applied for the gradual deactivation of the bistable units.

4.4.1 *Bistability in neuron groups*

Various substrates exhibiting bistability have been explored for recruitment-based encoding. Clusters of neurons with recurrent connections providing positive feedback to each other can self-sustain their neural activity and resist change, thus functioning as bistable units (Rosen, 1972; Koulakov et al., 2002; Goldman et al., 2003; Nikitchenko and Koulakov, 2008). In this case, the feedback gain within the neuron cluster can be arbitrarily larger than one. In practice, it is set to a high enough value so that the state maintenance is insensitive to neuronal parameter fluctuations and noise. Once each bistable unit (neuron cluster) transitions into the active state, it remains in that state. For the gradual activation of the bistable units, the clusters are interconnected via a second layer of recurrent connections (Figure 4.6c). Each neuron cluster receives both the input signal and inputs through connections from the other clusters. The second layer of connections provides all units with input proportional to the number of active units, gradually bringing the input of more units near their transition threshold as the number of active units increases (Figure 4.6b) (Koulakov et al., 2002; Goldman et al.,

2003; Nikitchenko and Koulakov, 2008). Note that this second layer of connections does not require precise fine-tuning either (Koulakov et al., 2002).

4.4.2 *NMDA receptor bistability*

As an alternative to bistable clusters of neurons, the negative resistance region of the voltage-current relation of NMDA receptors has been exploited to produce bistability at the neuron level (Koulakov et al., 2002). While the NMDA receptors are blocked by Mg^{2+} ions, they are not conductive. Once synaptic input increases the membrane potential sufficiently to unblock NMDA receptors from Mg^{2+} ions, the receptors get into a stable high conductance state and remain in it until the membrane potential decreases below the Mg^{2+} unblocking threshold and attracts Mg^{2+} ions again. This difference between blocking and unblocking potentials results in hysteresis in the conductance state transition and bistability at the neuron level.

Each neuron is assumed to have a different membrane leak conductance; hence a different amount of synaptic input is required for its bistable transition. The neurons are interconnected with mutual recurrent connections, so each neuron receives input proportional to the number of active neurons in the population. This total input brings each neuron to the bistable regime at a different moment due to their different leak currents. As the stimulus duration and intensity increase, the neuronal membrane potentials increase and more neurons transition to the high conductance state, encoding the amount of accumulated stimulus in the number of active neurons (Koulakov et al., 2002).[3]

4.4.3 *Dendritic bistability*

Other models have exploited bistability at the sub-cellular level. One such model speculated that bistability due to hysteresis in the dendritic response of neurons could be the basis for integrating presynaptic stimuli (Goldman et al., 2003). In this model, the more the dendritic branches that transition to an active state due to synaptic input, the higher the somatic membrane potential and the neuron firing rate are. However, no biologically plausible mechanism for dendritic bistability was proposed (Teramae and Fukai, 2005).

3 The authors report a 20% tolerance to NMDA receptor channel conductance fluctuation without compromising the integrator function.

4.4.4 *Ca^{2+} wavefronts*

Work following from dendritic bistability speculated on the role of calcium, proposing that calcium (Ca^{2+}) concentration wavefronts, formed in dendritic tree segments depending on synaptic input, may result in high calcium concentration and low concentration sub-segments in each dendritic segment[4] (Loewenstein and Sompolinsky, 2003). The contribution of each dendritic segment to the membrane potential and neuronal spike rate depends on the portion of its length that has a high concentration of calcium. However, this model has been criticised for its lack of biological plausibility due to its sensitivity to variations in calcium concentration, tonic calcium fluxes through membrane ion channels, as well as calcium store inactivation and desensitisation effects (Fransen, 2008).

4.4.5 *Non-linear Ca^{2+} – IP_3 interaction*

The aforementioned graded persistent activity phenomenon, observed in principal neurons in layer V of the entorhinal cortex (Section 4.2.5), has been modelled using the non-linear interaction of Ca^{2+} release from intracellular stores and IP_3 activation to create compartmentalised bistability within single neurons (Teramae and Fukai, 2005). For this model to work, the relative isolation of the sub-cellular bistable compartments is required, which requires a low Ca^{2+} diffusion between them. This isolation requirement limits the number of possible compartments and the attainable encoding resolution (Teramae and Fukai, 2005).

4.4.6 *Cooperative channel opening*

The cooperative opening of cell membrane ion channels was proposed as an alternative process that may provide graded persistent activity in cells (Pfeiffer et al., 2020). In this model, membrane ion channels are organised in clusters with spatially restricted interaction between the channels. The probability of an ion channel transitioning to the open state is a function of the membrane potential and the number of already open ion channels in the same cluster. This mechanism provides local positive feedback within ion-channel clusters so that the clusters operate as bistable units, gradually opening and contributing to the graded persistent activity of the neuron (Pfeiffer et al., 2020). Once channels in a cluster are opened, they remain open due to hysteresis, and additional input stimuli open even more clusters. The use of the cumulative

4 This model does not depend on bistability but rather on reaction-diffusion dynamics, but since it is mostly related to recruitment based encoding, it is included in this section.

stochastic opening of bistable ion-channel clusters is similar to the model proposed by Koulakov et al. (2002), but in this case, instead of the bistability being a property of NMDA channels, it is an emergent property of groups of interacting ion channels. Such cooperative opening of clustered voltage-dependent L-type calcium channels ($Ca_V1.3_S$) has been reported in hippocampal cells (Moreno et al., 2016). Once open, these channels allow the entrance of calcium into the cell and, therefore, a change in the intracellular calcium concentration that increases the neuron's membrane potential and spike rate. The increase in the membrane potential makes voltage-gated ion channels in other clusters more likely to open, providing a mechanism similar to the second layer of synaptic connections used in models utilising neuron clusters.

4.4.7 *Intrinsic neuronal excitability*

Synaptic input can modulate the intrinsic excitability of neurons (Armano et al., 2000; Paz et al., 2009; Mahon and Charpier, 2012; Debanne et al., 2019). Consecutive synaptic input events can cumulatively increase neuronal excitability. This phenomenon could be potentially exploited to encode the integral of the input signal over time, but further work is needed to explore the temporal stability characteristics of intrinsic excitability.

4.4.8 *Functional bistability of proteins*

Proteins may also exhibit bistability in their functional state (Lisman and Goldring, 1988). The feasibility of protein bistability as a mechanism for the integration of input stimuli has been explored by Lisman and Goldring (1988). The accumulative switching of proteins to their active functional state, due to synaptic input, could encode the integral of the input signal. A protein of interest that exhibits functional bistability is CaMKII. Once phosphorylated, CaMKII remains in the active state through autophosphorylation-based positive feedback.

4.4.9 *Summary*

Recruitment-based neural integrators can provide a discrete encoding of an integrated signal. They provide improved stability due to their insensitivity to parameter variations and noise because a minimum energy amount is required for a state change. Therefore they sacrifice encoding resolution to gain improved stability against noise. The encoding resolution depends on the number of bistable units utilised and the distribution of their thresholds in the integration interval. However, in the case of

bistability at the neuronal population level, the representation resolution is limited by the number of neurons. In the case of bistability at the protein, receptor, or molecule level, this resolution can be potentially high due to the large number of such bistable units that can fit in the volume of even a single cell or synapse.

When not provided with inputs, a system based on the recruitment of bistable units may potentially maintain its state indefinitely if the noise does not exceed the state transition thresholds of the units. Whether the bistable units lose their state over time and the dynamics of such state loss depend on the particular implementation substrate utilised.

Recruitment of bistable units is the most promising mechanism for integrating input signals when stability is required over long periods of time, but encoding resolution can be sacrificed. However, as already mentioned, when using sub-cellular level bistability, the resolution can still be so high that resolution would not be practically a concern.

4.5 DECODING

For an integrator to be useful, it is essential that we have a method for decoding its state into a usable format. The appropriate decoded format would depend on the specific use case. For the purposes of this review, I will consider the example of requiring a spike rate encoding as the decoded output. In the case of systems encoding the integral of their inputs as the magnitude of neuronal activity (spike rate), the integrated value is already in the desired form and can be readout directly. If the integrated value is stored in a positional encoding, it may be used directly as a population vector code (Stone et al., 2017), or a decoding step would be required to convert it into a spike rate. This decoding can be achieved by calculating a weighted sum of the individual neurons' activities to produce a spike rate corresponding to the encoded value (Figure 4.7a). This is similar to the way we decode our familiar decimal numeral system. Finally, if the integrated value is stored in a recruitment-based encoding system, to convert the number of active units into a spike rate, a summation of all the bistable elements' states with equal weighting can be used (Figure 4.7b). In the specific case of sub-cellular recruitment-based mechanisms, this summation is provided through the additive contribution of ionic currents to the membrane potential. Therefore, the resulting spike rate can be directly readout without the need for a layer of synaptic connections for its decoding.

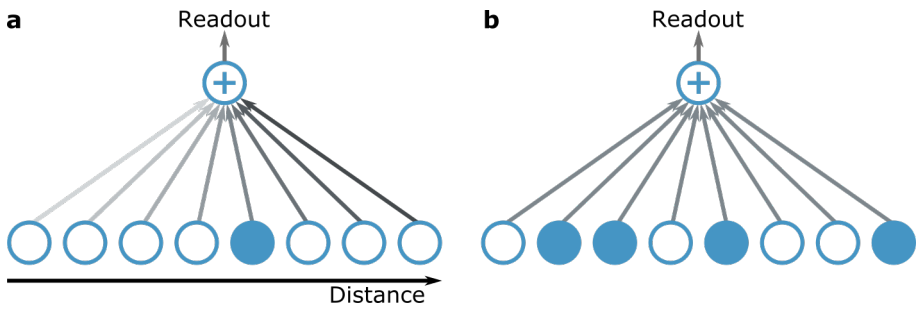

Figure 4.7: Decoding of the encoded value. (**a**) Positional encoding: For decoding a positional encoding, the neuronal outputs may be summed with each neuron contributing with a different significance (synaptic weight) to the final result, depending on its position in the population. (**b**) Recruitment-based encoding: For decoding a recruitment-based encoding, the neuron position does not matter; each neuron has an equal contribution significance to the result; this can be seen as a count of votes.

4.6 DISCUSSION

Temporal integration of input signals may occur in a wide range of task-dependent time scales, and a variety of potential neural substrates and models have been proposed. Each type of neural integrator has different properties rendering it appropriate for some situations but not others. Furthermore, the variety of neural integrator performance characteristics found in animals suggests that task-dependent solutions to neural integration may have evolved.

Animals have a finite number of neurons (especially invertebrates), and neurons have significant intrinsic parameter diversity (Gouwens et al., 2019), yet many animals are capable of reliable behaviour. A trade-off between encoding resolution, stability, and required resources must be achieved for a solution adequate for animal survival. The available resources might be allocated for increased stability, increased resolution, or other functional aspects facilitating the organism's survivability.

Typical models focus on either fast-updating memory systems that are also characterised by rapid value degradation or on memory systems that can maintain their state for long periods of time but require multiple stimulus presentations to be updated. However, there is a range of brain functions that require a memory capable of continuous and fast updating in conjunction with long persistence of the encoded state. In particular, path integrating insects, as will be discussed in Chapters 5 and 6, exhibit quick updating of their home vector memory as well as memory state persistence of several hours. Their home vector memory needs to gradually accumulate input, be updated quickly, maintain its state for several hours, be quickly reset when the animal returns to its nest, and be reusable throughout the animals' lifetime. Current models of neural integrators do not satisfy this combination of requirements.

In the preceding sections, I reviewed existing neural integration models. Neural integrators, maintaining their state as the spike rate of reverberating activity through feedback loops, can be updated quickly but are prone to significant state drift. This significant drift allows state maintenance only for short periods, which is insufficient for the insect home vector memory that may last several hours (Ziegler and Wehner, 1997; Cheng et al., 2005).

Attractor networks can also be updated quickly and potentially can be made stable enough through strong feedback connections that shape the state manifold appropriately. However, as discussed in Pisokas and Hennig (2022) and Chapter 5, the resource requirements and degradation dynamics of attractor networks do not match the available resources and homing performance of path integrating insects.

On the other hand, integrators based on collections of bistable units can be potentially updated quickly and can maintain their state for significant periods of time. The degradation dynamics of such integrators depend on the particular implementation substrate, but they may resemble the homing performance degradation observed in path integrating insects.

In conclusion, currently, no concrete model has been presented that can satisfy all the requirements of the neural integrator that is the basis of insect path integration memory. In the subsequent chapters, I investigate this memory in an attempt to decipher its underlying neural mechanism.

4.7 SUPPLEMENTAL INFORMATION

Box 1: Leaky Integrators

Leaky integrator dynamics resemble the physical metaphor of a leaky tank that is gradually filled with water (Figure 4.8a). At any moment in time, the amount of water in the tank is the accumulated incoming water minus the amount of leaked water. Systems with such dynamics are called leaky integrators, and their dynamics are mathematically described by

$$\frac{dv(t)}{dt} = \frac{1}{\tau}(-v(t) + i(t)) \qquad (4.1)$$

where $v(t)$ is the accumulated value, $i(t)$ is the input value, and τ is the decay time constant. The time constant determines how fast the stored value decays (Figure 4.8b). A constant percentage of the instantaneous value is subtracted per time unit, resulting in the characteristic exponential decay rate due to leakage, given by

$$Leakage = e^{-t/\tau} \qquad (4.2)$$

and the instantaneous value $v(t)$ at any moment in time is

$$v(t) = ke^{-t/\tau} + v_0 \qquad (4.3)$$

where v_0 determines the stable state value reached when no input is provided (i.e. the resting potential of a neuron), and k is a constant scaling factor for $v(t)$.

Leaky integrators can be implemented using various substrates, e.g. hydraulic, pneumatic, or neuronal. In neuronal integrators, we can utilise the membrane potential or the spike rate of a stimulated neuron to encode the accumulated stimuli.

The membrane potential and spike rate of neurons decay and gradually return to their base values due to electric charges leaking through the membrane.

A major problem with systems exhibiting leaky integrator dynamics is the rapid (exponential) value decay (Figure 4.8b). The time constant of the leaky integrator determines how fast an integrated value decays (Figures 4.9a and 4.9b).

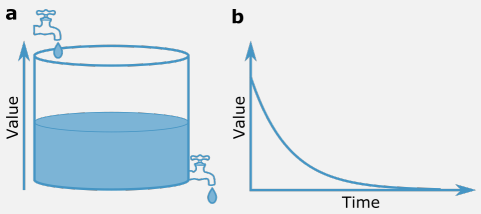

Figure 4.8: Leaky integrator dynamics. (**a**) The archetypical example of a leaky integrator is a leaky water tank. (**b**) In systems exhibiting leaky integrator dynamics, the stored quantity decays exponentially with time.

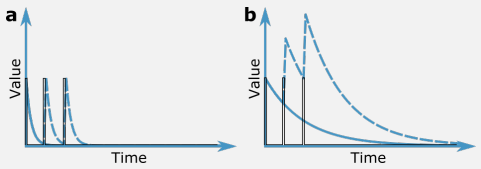

Figure 4.9: The time constant of the leaky integrator determines how fast an integrated value decays to the base value. The time constant may be (**a**) smaller or (**b**) larger than the inter-stimulus interval. If the leaky integrator's time constant is significantly larger than the inter-stimulus interval, it approximates an integrator accumulating input stimulus pulses (**b**).

BIBLIOGRAPHY

Aksay, E., Olasagasti, I., Mensh, B. D., Baker, R., Goldman, M. S., and Tank, D. W. (2007). Functional dissection of circuitry in a neural integrator. *Nature Neuroscience*, 10(4):494–504.

Amari, S.-i. (1977). Dynamics of pattern formation in lateral-inhibition type neural fields. *Biological Cybernetics*, 27(2):77–87.

Amit, D. J. (1989). *Modeling brain function: the world of attractor neural networks*. Cambridge University Press.

Armano, S., Rossi, P., Taglietti, V., and D'Angelo, E. (2000). Long-term potentiation of intrinsic excitability at the mossy fiber-granule cell synapse of rat cerebellum. *Journal of Neuroscience*, 20(14):5208–5216.

Arnold, D. B. and Robinson, D. A. (1997). The oculomotor integrator: testing of a neural network model. *Experimental Brain Research*, 113(1):57–74.

Boucheny, C., Brunel, N., and Arleo, A. (2005). A continuous attractor network model without recurrent excitation: Maintenance and integration in the head direction cell system. *Journal of Computational Neuroscience*, 18(2):205–227.

Brody, C. D., Romo, R., and Kepecs, A. (2003). Basic mechanisms for graded persistent activity: Discrete attractors, continuous attractors, and dynamic representations. *Current Opinion in Neurobiology*, 13(2):204–211.

Burak, Y. and Fiete, I. R. (2009). Accurate path integration in continuous attractor network models of grid cells. *PLoS Computational Biology*, 5(2):e1000291.

Burak, Y. and Fiete, I. R. (2012). Fundamental limits on persistent activity in networks of noisy neurons. *Proceedings of the National Academy of Sciences*, 109(43):17645–17650.

Cain, N. and Shea-Brown, E. (2012). Computational models of decision making: Integration, stability, and noise. *Current Opinion in Neurobiology*, 22(6):1047–1053.

Cannon, S. C. and Robinson, D. A. (1985). An improved neural-network model for the neural integrator of the oculomotor system: more realistic neuron behavior. *Biological cybernetics*, 53(2):93–108.

Cannon, S. C., Robinson, D. A., and Shamma, S. (1983). A proposed neural network for the integrator of the oculomotor system. *Biological Cybernetics*, 49(2):127–136.

Cheng, K., Narendra, A., and Wehner, R. (2005). Behavioral ecology of odometric memories in desert ants: Acquisition, retention, and integration. *Behavioral Ecology*, 17(2):227–235.

Compte, A., Brunel, N., Goldman-Rakic, P. S., and Wang, X.-J. (2000). Synaptic mechanisms and network dynamics underlying spatial working memory in a cortical network model. *Cerebral Cortex*, 10(9):910–923.

Conklin, J. and Eliasmith, C. (2005). A controlled attractor network model of path integration in the rat. *Journal of Computational Neuroscience*, 18(2):183–203.

Dayan, P. and Abbott, L. F. (2005). *Theoretical neuroscience: computational and mathematical modeling of neural systems*. MIT press.

Debanne, D., Inglebert, Y., and Russier, M. (2019). Plasticity of intrinsic neuronal excitability. *Current opinion in neurobiology*, 54:73–82.

Durstewitz, D. (2003). Self-organizing neural integrator predicts interval times through climbing activity. *Journal of Neuroscience*, 23(12):5342–5353.

Durstewitz, D. and Deco, G. (2008). Computational significance of transient dynamics in cortical networks. *European Journal of Neuroscience*, 27(1):217–227.

Egorov, A. V., Hamam, B. N., Fransén, E., Hasselmo, M. E., and Alonso, A. A. (2002). Graded persistent activity in entorhinal cortex neurons. *Nature*, 420(6912):173–178.

Egorov, A. V., Schumacher, D., Medert, R., Birnbaumer, L., Freichel, M., and Draguhn, A. (2019). TRPC channels are not required for graded persistent activity in entorhinal cortex neurons. *Hippocampus*, 29(11):1038–1048.

Egorov, A. V., Unsicker, K., and von Bohlen Und Halbach, O. (2006). Muscarinic control of graded persistent activity in lateral amygdala neurons. *European Journal of Neuroscience*, 24(11):3183–3194.

Eliasmith, C. (2005). A unified approach to building and controlling spiking attractor networks. *Neural Computation*, 17(6):1276–1314.

Fransen, E. (2008). *Mechanisms of Graded Persistent Activity: Implications for Epilepsy*. Elsevier B.V., first edit edition.

Fransén, E., Tahvildari, B., Egorov, A. V., Hasselmo, M. E., and Alonso, A. A. (2006). Mechanism of graded persistent cellular activity of entorhinal cortex layer V neurons. *Neuron*, 49(5):735–746.

Fukushima, K. and Kaneko, C. R. S. (1995). Vestibular integrators in the oculomotor system. *Neuroscience Research*, 22(3):249–258.

Gardner, R. J., Hermansen, E., Pachitariu, M., Burak, Y., Baas, N. A., Dunn, B. A., Moser, M.-B., and Moser, E. I. (2021). Toroidal topology of population activity in grid cells. *bioRxiv*.

Goldman, M. S. (2009). Memory without feedback in a neural network. *Neuron*, 61(4):621–634.

Goldman, M. S., Levine, J. H., Major, G., Tank, D. W., and Seung, H. S. (2003). Robust persistent neural activity in a model integrator with multiple hysteretic dendrites per neuron. *Cerebral Cortex*, 13(11):1185–1195.

Goldschmidt, D., Dasgupta, S., Wörgötter, F., and Manoonpong, P. (2015). A neural path integration mechanism for adaptive vector navigation in autonomous agents. In *Proceedings of the International Joint Conference on Neural Networks (IJCNN)*, pages 1–8.

Goldschmidt, D., Manoonpong, P., and Dasgupta, S. (2017). A neurocomputational model of goal-directed navigation in insect-inspired artificial agents. *Frontiers in Neurorobotics*, 11:1–17.

Goodridge, J. P. and Touretzky, D. S. (2000). Modeling attractor deformation in the rodent head-direction system. *Journal of Neurophysiology*, 83(6):3402–3410.

Gouwens, N. W., Sorensen, S. A., Berg, J., Lee, C., Jarsky, T., et al. (2019). Classification of electrophysiological and morphological neuron types in the mouse visual cortex.

Nature Neuroscience, 22(7):1182–1195. Characterisation of neuronal diversity in mice. Characterises diversity of electrophysiology and morphology.

Haferlach, T., Wessnitzer, J., Mangan, M., and Webb, B. (2007). Evolving a neural model of insect path integration. *Adaptive Behavior*, 15(3):273–287.

Heinze, S., Narendra, A., and Cheung, A. (2018). Principles of insect path integration. *Current Biology*, 28(17):R1043–R1058.

Huk, A. C. and Shadlen, M. N. (2005). Neural activity in macaque parietal cortex reflects temporal integration of visual motion signals during perceptual decision making. *Journal of Neuroscience*, 25(45):10420–10436.

Joshua, M. and Lisberger, S. G. (2015). A tale of two species: Neural integration in zebrafish and monkeys. *Neuroscience*, 296:80–91.

Kamath, B. Y. and Keller, E. L. (1976). A neurological integrator for the oculomotor control system. *Mathematical Biosciences*, 30(3-4):341–352.

Kim, D. and Lee, J. (2011). Path integration mechanism with coarse coding of neurons. *Neural Processing Letters*, 34(3):277–291.

Knaden, M. (2019). Learning and processing of navigational cues in the desert ant. *Current Opinion in Neurobiology*, 54(2):140–145.

Koulakov, A. A., Raghavachari, S., Kepecs, A., and Lisman, J. E. (2002). Model for a robust neural integrator. *Nature Neuroscience*, 5(8):775–782.

Lim, S. and Goldman, M. S. (2013). Balanced cortical microcircuitry for maintaining information in working memory. *Nature Neuroscience*, 16(9):1306–1314.

Lisman, J. E. and Goldring, M. A. (1988). Feasibility of long-term storage of graded information by the Ca2+/calmodulin-dependent protein kinase molecules of the postsynaptic density. *Proceedings of the National Academy of Sciences*, 85(14):5320–5324.

Loewenstein, Y. and Sompolinsky, H. (2003). Temporal integration by calcium dynamics in a model neuron. *Nature Neuroscience*, 6(9):961–967.

Mahon, S. and Charpier, S. (2012). Bidirectional plasticity of intrinsic excitability controls sensory inputs efficiency in layer 5 barrel cortex neurons in vivo. *Journal of Neuroscience*, 32(33):11377–11389.

Mainen, Z. F. and Seinowski, T. J. (1995). Reliability of spike timing in neocortical neurons. *Science*, 268(5216):1503–1506.

Mainen, Z. F. and Sejnowski, T. J. (1996). Influence of dendritic structure on firing pattern in model neocortical neurons. *Nature*, 382(6589):363–366.

McNaughton, B. L., Barnes, C., Gerrard, J. L., Gothard, K., Jung, M. W., Knierim, J. J., Kudrimoti, H., Qin, Y., Skaggs, W. E., Suster, M., and Weaver, K. L. (1996). Deciphering the hippocampal polyglot: the hippocampus as a path integration system. *Journal of experimental biology*, 199(1):173–185.

McNaughton, B. L., Battaglia, F. P., Jensen, O., Moser, E. I., and Moser, M.-B. (2006). Path integration and the neural basis of the 'cognitive map'. *Nature Reviews Neuroscience*, 7(8):663–678.

Moreno, C. M., Dixon, R. E., Tajada, S., Yuan, C., Opitz-Araya, X., Binder, M. D., and Santana, L. F. (2016). Ca2+ entry into neurons is facilitated by cooperative gating of clustered Cav1.3 channels. *eLife*, 5.

Nikitchenko, M. and Koulakov, A. (2008). Neural integrator: A sandpile model. *Neural Computation*, 20(10):2379–2417.

Paz, J. T., Mahon, S., Tiret, P., Genet, S., Delord, B., and Charpier, S. (2009). Multiple forms of activity-dependent intrinsic plasticity in layer v cortical neurones in vivo. *Journal of Physiology*, 587(13):3189–3205.

Pfeiffer, P., Egorov, A. V., Lorenz, F., Schleimer, J.-h., Draguhn, A., and Schreiber, S. (2020). Clusters of cooperative ion channels enable a membrane-potential-based mechanism for short-term memory. *eLife*, 9:1–27.

Pisokas, I. and Hennig, M. (2022). Can the insect path integration memory be a bump attractor? *In review*.

Redish, A. D., Elga, A. N., and Touretzky, D. S. (1996). A coupled attractor model of the rodent head direction system. *Network: Computation in Neural Systems*, 7(4):671–685.

Renart, A., Song, P., and Wang, X.-J. (2003). Robust spatial working memory through homeostatic synaptic scaling in heterogeneous cortical networks. *Neuron*, 38(3):473–485.

Robinson, D. (1989). Integrating with neurons. *Annual Review of Neuroscience*, 12(1):33–45.

Robinson, D. A. (1972). Eye movements evoked by collicular stimulation in the alert monkey. *Vision research*, 12(11):1795–1808.

Rosen, M. J. (1972). A theoretical neural integrator. *IEEE Transactions on Biomedical Engineering*, BME-19(5):362–367.

Samsonovich, A. and McNaughton, B. L. (1997). Path integration and cognitive mapping in a continuous attractor neural network model. *Journal of Neuroscience*, 17(15):5900–5920.

Seung, H. S. (1996). How the brain keeps the eyes still. *Proceedings of the National Academy of Sciences of the United States of America*, 93(23):13339–44.

Seung, H. S., Lee, D. D., Reis, B. Y., and Tank, D. W. (2000). Stability of the memory of eye position in a recurrent network of conductance-based model neurons. *Neuron*, 26(1):259–271.

Shaham, N. and Burak, Y. (2017). Slow diffusive dynamics in a chaotic balanced neural network. *PLoS Computational Biology*, 13(5):1–26.

Skaggs, W. E., Knierim, J. J., Kudrimoti, H. S., and McNaughton, B. L. (1995). A model of the neural basis of the rat's sense of direction. *Advances in neural information processing systems*, 7(1984):173–180.

Song, P. (2005). Angular path integration by moving "hill of activity": A spiking neuron model without recurrent excitation of the head-direction system. *Journal of Neuroscience*, 25(4):1002–1014.

Stone, T., Webb, B., Adden, A., Weddig, N. B., Honkanen, A., Templin, R., Wcislo, W., Scimeca, L., Warrant, E., and Heinze, S. (2017). An anatomically constrained model for path integration in the bee brain. *Current Biology*, 27(20):3069–3085.

Stringer, S. M., Rolls, E. T., Trappenberg, T. P., and Araujo, I. E. T. d. (2002a). Self-organizing continuous attractor networks and path integration: Two-dimensional models of place cells. *Network: Computation in Neural Systems*, 13(4):429–446.

Stringer, S. M., Trappenberg, T. P., Rolls, E. T., and Araujo, I. E. T. D. (2002b). Self-organizing continuous attractor networks and path integration: One-dimensional models of head direction cells. *Network: Computation in Neural Systems*, 13(2):217–242.

Taube, J. S. and Bassett, J. P. (2003). Persistent neural activity in head direction cells. *Cerebral Cortex*, 13(11):1162–1172.

Taube, J. S., Muller, R. U., and Ranck, J. B. (1990a). Head-direction cells recorded from the postsubiculum in freely moving rats. I. Description and quantitative analysis. *Journal of Neuroscience*, 10(2):420–435.

Taube, J. S., Muller, R. U., and Ranck, J. B. (1990b). Head-direction cells recorded from the postsubiculum in freely moving rats. II. Effects of environmental manipulations. *Journal of Neuroscience*, 10(2):436–447.

Taylor, J. G. (1999). Neural 'bubble' dynamics in two dimensions: foundations. *Biological Cybernetics*, 80(6):393–409.

Tennant, S. A., Hawes, I., Clark, H., Tam, W. K., Hua, J., Yang, W., Gerlei, K., Wood, E. R., and Nolan, M. F. (2021). Analogue representation of a spatial memory by ramp-like neural activity in retrohippocampal cortex. *bioRxiv*.

Teramae, J. N. and Fukai, T. (2005). A cellular mechanism for graded persistent activity in a model neuron and its implications in working memory. *Journal of Computational Neuroscience*, 18(1):105–121.

Vickerstaff, R. J. and Di Paolo, E. A. (2005). Evolving neural models of path integration. *Journal of Experimental Biology*, 208(17):3349–3366.

Vreeswijk, C. V. and Sompolinsky, H. (1996). Chaos in neuronal networks with balanced excitatory and inhibitory activity. *Science*, 274(5293):1724–1726.

Webb, B. and Wystrach, A. (2016). Neural mechanisms of insect navigation. *Current Opinion in Insect Science*, 15:27–39.

Wu, S. and Amari, S. I. (2005). Computing with continuous attractors: Stability and online aspects. *Neural Computation*, 17(10):2215–2239.

Xie, X., Hahnloser, R. H. R., and Seung, H. S. (2002a). Double-ring network model of the head-direction system. *Physical Review E*, 66(4):041902.

Xie, X., Hahnloser, R. H. R., and Seung, H. S. (2002b). Selectively grouping neurons in recurrent networks of lateral inhibition. *Neural Computation*, 14(11):2627–2646.

Zhang, K. (1996). Representation of spatial orientation by the intrinsic dynamics of the head-direction cell ensemble: a theory. *Journal of Neuroscience*, 16(6):2112–2126.

Ziegler, P. E. and Wehner, R. (1997). Time-courses of memory decay in vector-based and landmark-based systems of navigation in desert ants, *Cataglyphis fortis*. *Journal of Comparative Physiology A*, 181(1):13–20.

5

IS THE ANT PATH INTEGRATION MEMORY A BUMP ATTRACTOR?

Many animal species are able to return to their nest after a foraging excursion without using familiar visual cues to guide them. They accomplish this by using a navigation competence known as path integration, which is vital in environments that do not have prominent visual features. To perform path integration, an animal maintains a running estimate of the distance and direction to its origin as it moves. This distance and direction estimate needs to be maintained in memory until the animal uses it to return to its nest. However, the neural substrate of this memory remains uncertain. A common hypothesis is that the information is maintained in a bump attractor's state. We test the bump attractor hypothesis and find that its predictions are inconsistent with the path integration behaviour of ants, thus highlighting the need for alternative models of path integration memory.

5.1 INTRODUCTION

When a foraging ant of the species *Cataglyphis fortis*, inhabiting the Saharan desert, embarks in search of food, it typically follows a circuitous path. However, once it finds a food item, it readily returns to its nest, travelling along a straight path, even though there are no visual cues to guide it along its trip (Müller and Wehner, 1988; Collett, 2019; Menzel and Muller, 1996). The animal achieves this by maintaining a running estimate of the direction and distance to a starting location, using a navigational competence known as 'path integration' or 'dead-reckoning' (Darwin, 1873; von Frisch, 1967; Mittelstaedt, 1985; Müller and Wehner, 1988). This estimate is known as the 'home vector'[1] (Collett, 2019) and is updated continuously as the animal moves (Müller and Wehner, 1988; Menzel and Muller, 1996; Heinze et al., 2018; Collett, 2019).

To update its home vector, the insect has to have access to two pieces of information at every instant in time, its current heading and an estimate of the distance[2] it travels.

1 The home vector is a conceptual vector with a direction parallel to the line connecting the animal's current location with its nest and length corresponding to the current distance of the animal from its nest.

2 The distance or the speed can be used for the calculation since the integral of speed over time gives the distance travelled.

These displacement estimates are accumulated continuously updating the home vector as the animal travels (Heinze et al., 2018; Collett, 2019). This procedure is similar to that employed by sea navigators in the past who used a magnetic compass to gauge their heading and vector addition to track their position on a map.

Path integration has been described in several species, including desert ants of the genus *Cataglyphis*, the honey bee *Apis mellifera*, the sweat bee *Megalopta genalis*, the fruit fly *Drosophila melanogaster*, as well as in rodents (Müller and Wehner, 1988; Collett, 2019; Menzel and Muller, 1996; Heinze and Homberg, 2007; Heinze et al., 2013; Stone et al., 2017; Kim and Dickinson, 2017; McNaughton et al., 2006). The spatial scale of path integration varies between species. For instance, fruit flies (*Drosophila melanogaster*) employ path integration for returning to a previously visited drop of sugar a few centimetres away (Kim and Dickinson, 2017), while other insect species use path integration to return to their nest over much larger distances, for instance, hundreds of meters in the case of the desert ant *Cataglyphis fortis*, or several kilometres in the case of the honey bee *Apis mellifera* (Sommer and Wehner, 2004; Cheng et al., 2005; Huber and Knaden, 2015; von Frisch, 1967).

At the end of its excursion, a path integrating animal can return to its nest by travelling in the direction and for the distance indicated by its accumulated home vector memory (Müller and Wehner, 1988; Menzel and Muller, 1996; Collett, 2019). To do this, the animal needs to be able to maintain its home vector in memory for the duration of its excursion, even if it is interrupted and prohibited from returning to its nest for several hours (Ziegler and Wehner, 1997; Cheng et al., 2005). Therefore, a memory mechanism that can be updated quickly and maintain its state long enough is required (Pisokas et al., 2022). However, the substrate of the employed memory remains unknown.

Most path integration models leave the memory substrate unspecified, while some authors have suggested that the home vector memory might be maintained through reverberating neural activity and more specifically, in a bump attractor network (McNaughton et al., 1996; Samsonovich and McNaughton, 1997; Conklin and Eliasmith, 2005; McNaughton et al., 2006; Burak and Fiete, 2009; Vickerstaff and Di Paolo, 2005; Haferlach et al., 2007; Kim and Lee, 2011; Goldschmidt et al., 2015; Webb and Wystrach, 2016; Stone et al., 2017; Goldschmidt et al., 2017).

Bump attractors are recurrent neural networks that maintain a localised peak of neural activity. A bump attractor can be used to encode an agent's spatial position as the location of the peak of neural activity ('activity bump') in the network (Figure 5.1A). If we imagine that the neurons of the bump attractor are organised topologically (if not spatially) on a line, the higher the represented spatial value, the further along the

line the most active neurons will be located (Figure 5.1A). This constitutes a positional encoding of value along a line of neurons.

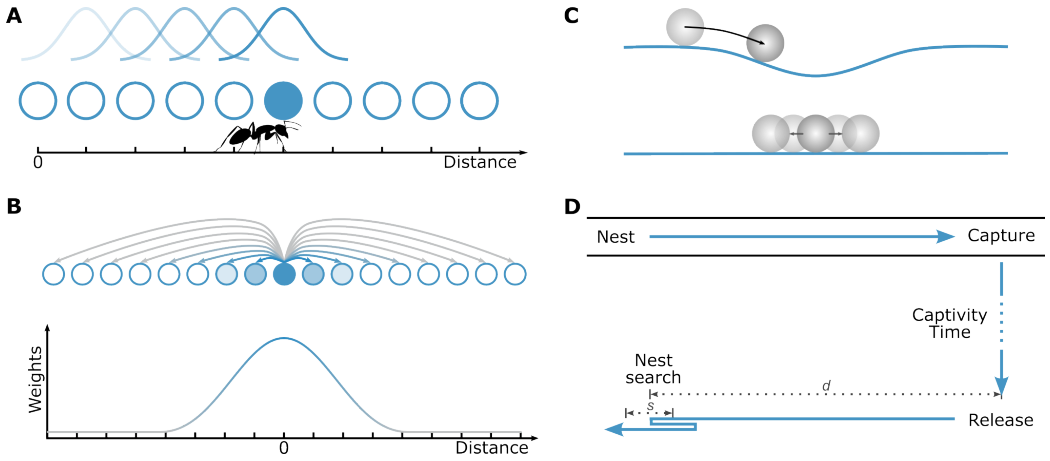

Figure 5.1: Bump attractor networks as spatial location memory. (**A**) The state of a bump attractor is encoded in the position of the most active neuron in the network. In a bump attractor that integrates an animal's velocity, the location of the activity bump would encode the spatial position of the animal. (**B**) In a bump attractor network, the synaptic connectivity weights pattern results in the formation of one activity bump. The synaptic weights of one exemplar neuron are shown; the same synaptic pattern is repeated for all neurons. The synaptic connections (arrows) are colour-coded by their strength, with blue denoting excitatory synapses and grey inhibitory synapses. The synaptic strength is a function of the distance from the emanating neuron. (**C**) Inhomogeneities in the biophysical and synaptic properties of the network cause a systematic drift in the bump's location (top of panel), while neuronal noise causes an unbiased stochastic drift of the bump's location (bottom of panel). (**D**) For measuring the homing accuracy of path integration, ants were captured once they reached a feeder, held in captivity for different amounts of time, and then released in a remote unfamiliar location (Ziegler and Wehner, 1997). Upon release, ants that had not been kept in prolonged captivity would typically run towards their expected nest location, not finding it since they were displaced, and would perform a focused search for the entrance of their nest. The distance (d) at which ants start searching for their nest is a measure of the memorised home vector distance. The spread of this distance (s) over trials is a measure of the homing distance error or dispersion.

In bump attractor networks, the activity bump is maintained through specific synaptic connectivity with short-range excitation and long-range inhibition (Gerstner et al., 2014, see Figure 5.1B). The dynamics of the neuronal activities are described by the coupled set of differential equations

$$\tau \frac{d\mathbf{a}(t)}{dt} = -\mathbf{a}(t) + f\left[\mathbf{W}\mathbf{a}(t) + \mathbf{u}(t)\right]$$

where τ is the neuronal time constant, $\mathbf{a}$ is the neuronal activities vector, $f[\cdot]$ is the neuronal activation function, $\mathbf{W}$ is the weight matrix stipulating a local lateral

excitation profile between neurons and global inhibition (section 5.4.2 in Materials and Methods), and $\mathbf{u}(t)$ is the vector of external inputs to the attractor network.

The location of the activity bump can be changed by an external input that moves the bump towards a particular direction. With appropriate connectivity, the amount of the bump's movement along the neural network can be proportional to the integral of the input stimulus over time (Skaggs et al., 1995). In this case, bump attractor networks can be used as neural integrators that encode the integral of the input signal as the location of the activity bump along the network.

Bump attractor networks have been used to model systems that gradually accumulate velocity signals, such as angular velocity for tracking the head direction of rodents (Zhang, 1996; Redish et al., 1996; Goodridge and Touretzky, 2000; Boucheny et al., 2005) or translational velocity in path integration models of rodent place and grid cells to track the spatial position of the animal (McNaughton et al., 1996; Samsonovich and McNaughton, 1997; Conklin and Eliasmith, 2005; Burak and Fiete, 2009).

In insects, the computations pertaining to path integration are believed to occur in the central complex (CX), a brain structure conserved among insect species (Heinze et al., 2013; Pfeiffer and Homberg, 2014; Seelig and Jayaraman, 2015; Weir and Dickinson, 2015; Heinze, 2015; Turner-Evans and Jayaraman, 2016; el Jundi et al., 2018; Franconville et al., 2018). Neurons that encode the animal's heading and speed have been identified in the central complex (Heinze and Homberg, 2007; Homberg et al., 2011; Seelig and Jayaraman, 2015; Green et al., 2017; Stone et al., 2017) and its characteristic columnar structure and regular projection patterns have been hypothesised to provide a plausible substrate for the required path integration computations (Stone et al., 2017).

The existence of the necessary anatomical connectivity for the formation of a bump attractor has been demonstrated in the head direction circuit of insects (Seelig and Jayaraman, 2015; Kim et al., 2017; Turner-Evans et al., 2017; Kakaria and de Bivort, 2017; Green et al., 2017; Su et al., 2017; Green and Maimon, 2018; Pisokas et al., 2020; Turner-Evans et al., 2020), but no direct connectomic evidence of bump attractor synaptic structure for encoding translational displacement has been identified in the underlying neural substrate.

Current bump attractor models exhibit limited state stability over time (Brody et al., 2003), while insects can maintain the memory of their home vector for hours (Ziegler and Wehner, 1997). This is an important discrepancy and it is, therefore, imperative to investigate whether bump attractors are an ecologically plausible underlying memory mechanism for path integration. To address this question, we compare the dynamics of bump attractors with those of the home vector memory of the desert ant *Cataglyphis fortis*. If the ants' memory mechanism is indeed a bump attractor network, the state

dynamics of such a network should be consistent with the behaviour dynamics of the ants.

5.2 RESULTS

5.2.1 *Homing accuracy*

The way the homing accuracy of an animal degrades over time could provide crucial information about its spatial memory characteristics. The state of a bump attractor is subject to two phenomena: systematic and stochastic drift. The systematic drift is due to inhomogeneities in the network parameters, while the stochastic drift is due to neuronal noise. Both of these would affect the bump's location (Figure 5.1C). In bump attractors, when no input signal is provided, stochastic neuronal noise causes the activity bump's location to stochastically drift over time (Compte et al., 2000; Burak and Fiete, 2012). Due to the stochastic drift, the bump increasingly deviates from its original location resulting in increased dispersion over time (Figure 5.2A). Therefore, if the ant's home vector memory were based on a bump attractor network, we would expect an increase in the animal's home vector memory error and accordingly a deterioration in its homing distance accuracy over time.

Two studies have attempted to quantify how the homing accuracy of path integrating ants (*Cataglyphis fortis*) degrades with time (Ziegler and Wehner, 1997; Cheng et al., 2005). The *Cataglyphis fortis* ants are endemic in the salt pans of Tunisia and Algeria, where the skyline is flat, providing no prominent visual cues the animals can use for navigation, so the ants are known to resort to path integration for their navigation (Müller and Wehner, 1988). Therefore, this ant species is a suitable candidate for studying path integration in isolation from other navigational competencies. In the aforementioned studies, the ants were captured once reaching a feeder, away from their nest, and were kept confined in a dark box for different amounts of time before being released at an unfamiliar location. Once released, these ants typically run towards their expected nest location (Figure 5.1D). The authors measured the distance the ants ran before they started searching for their nest's entrance.

Even though the typical foraging excursion of a *Cataglyphis fortis* ant in its natural habitat lasts no more than one hour, Ziegler and Wehner (1997) found that the ants maintained their home vector memory for several hours, a finding that was confirmed by Cheng et al. (2005) in a similar experiment. We analysed the data reported by these authors and observed that the homing distance error (defined here as the squared median absolute deviation, a measure of dispersion) increases with a constant rate over captivity time (Figure 5.2B). In bump attractors, stochastic drift causes a constant

increase in the bump's expected location variance over time (Compte et al., 2000; Burak and Fiete, 2012). Similarly with the variance, the squared median absolute deviation of the bump's expected location would grow linearly with time, as seen in Figure 5.2A. This is in agreement with the linear relationship between captivity time and squared median absolute deviation seen in the ants (Figure 5.2B). However, more aspects of the animal behaviour should coincide with the predictions of the bump attractor hypothesis for it to be a plausible memory substrate.

5.2.2 *Required number of neurons*

In principle, a bump attractor could reproduce the linear increase of homing distance error over time (Figure 5.2A). However, the homing distance error of the *Cataglyphis fortis* ants increases at a rate of $0.343\,\mathrm{m}^2/\mathrm{h}$ (Figure 5.2B), which is three orders of magnitude slower than the bump attractor simulations in Figure 5.2A. In bump attractor networks, the dispersion (squared median absolute deviation) of the bump's expected location depends on the number of neurons in the network (Figure 5.2A). Thus the question arises, how many neurons are required to reproduce the dispersion rate observed in the ant behaviour experiments?

The required number of neurons, N, is inversely proportional to the desired dispersion rate $\mathcal{D} \propto 1/N$ (Compte et al., 2000; Burak and Fiete, 2012). However, the exact number of neurons depends on the assumptions about the circuit structure and the biophysical properties of the neurons. We, therefore, provide an indicative solution for a bump attractor implementation with physiologically plausible neuronal parameters (see Materials and Methods). The result should be seen as an indication of order of magnitude and not as a specific number of required neurons. We varied the size of the simulated bump attractor network and used the above relation to extrapolate from the simulation results to larger networks, estimating the size of the network required to reproduce the experimentally measured dispersion rate of the ants (Figure 5.2D, dashed line). We found that a bump attractor network of at least 6 million neuronal units is required ($6.2 \times 10^6 \pm 2.3 \times 10^6$ neurons, mean $\pm$ std) for exhibiting a dispersion rate comparable with that observed in the ants' behaviour ($0.343\,\mathrm{m}^2/\mathrm{h}$). In reality, each neuronal unit in a bump attractor might consist of several neurons, and the circuit would require additional neuronal resources for controlling the bump's shift in response to input signals as well as a population of inhibitory neurons. This means that the actual number of neurons required for the bump attractor circuit would be a multiple of 6 million.

In insects, the home vector memory has been speculated to lie in the upper central body (CBU, also known as the fan-shaped body) of the central complex (Stone et al.,

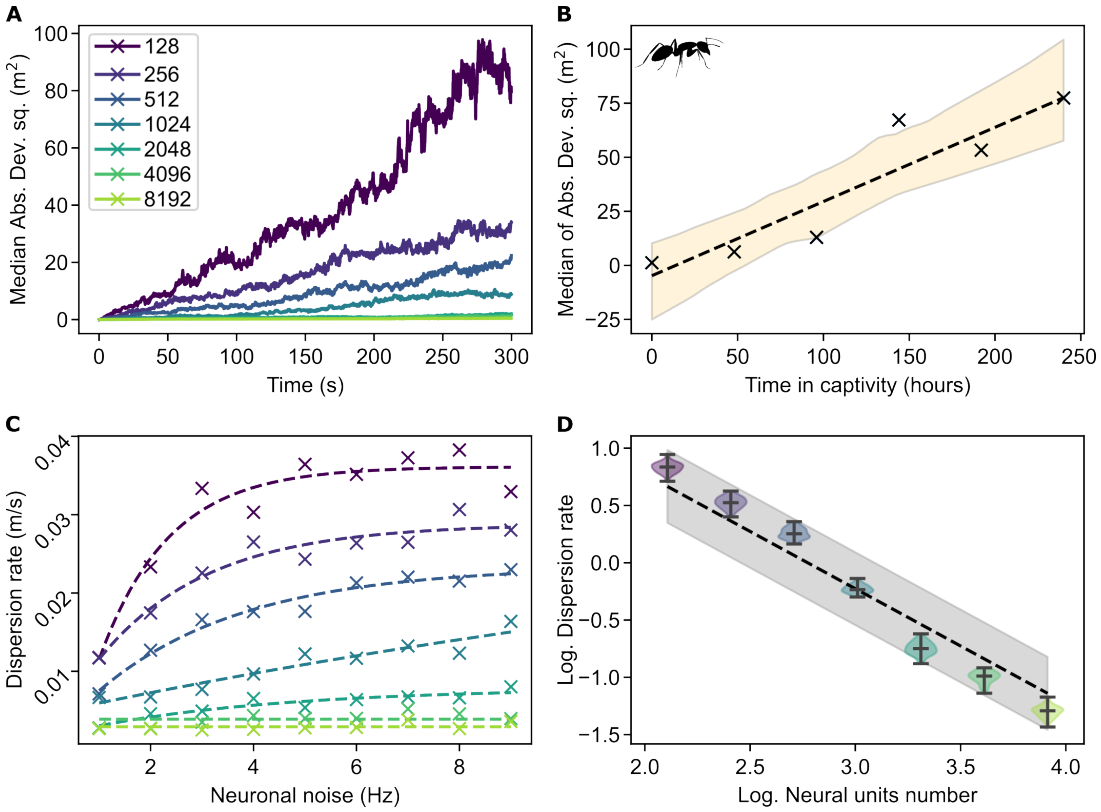

Figure 5.2: Path integration error increase over time. (**A**) Simulation results of the error (dispersion, measured as squared median absolute deviation) in the attractor's activity bump location over time for networks of different sizes (300 trials for each condition). Since a homogeneous neuronal population was used, the error increase was due to neuronal noise. The error increases linearly with time. An increased number of neuronal units in the bump attractor network results in a reduced error increase rate. (**B**) The ants' homing distance error increases linearly with captivity duration (Data from Ziegler and Wehner 1997). The line $y = ax + b$ was fitted to the data with parameters $a = (0.343 \pm 0.088)\,\mathrm{m}^2/\mathrm{h}$ and $b = (-4.784 \pm 12.122)\,\mathrm{m}^2$ (mean $\pm$ std, R^2=0.85), showing that the homing distance error (dispersion) increased at a rate of $0.343\,\mathrm{m}^2/\mathrm{h}$. The 95% confidence intervals for the linear regression fits are indicated by the shaded zone. (**C**) Error increase rate (dispersion rate, measured as median absolute deviation per second) in the activity bump's location for different attractor network sizes. The colours signify the numbers of neurons used in the simulations (as in **A**). (**D**) The required number of neurons is inversely proportional to the dispersion rate ($\mathcal{D} \propto 1/N$). The function (dashed line) $y = -x + b$ was regressed to the logarithm of the dispersion rate vs. the logarithm of the neurons number with parameter $b = 2.77 \pm 0.02$ (mean $\pm$ std, R^2=0.95). The 95% confidence intervals for the dispersion rate are indicated by the shaded zone. Extrapolation to dispersion rate $0.343\,\mathrm{m}^2/\mathrm{h}$ gives a minimal required network size of around 6 million neuronal units ($6.2 \times 10^6 \pm 2.3 \times 10^6$ neuronal units, mean $\pm$ std).

2017; Collett, 2019). The exact number of neurons in the ant's brain is not known, but the comparable central complex of *Drosophila melanogaster* is estimated to have no more than 5,000 neurons, while the whole brain is estimated to have 200,000 neurons

(Raji and Potter, 2021; Hulse et al., 2021). Current models and neuroanatomical evidence suggest the existence of 8 or 16 independent distance integrators, one for each represented cardinal direction (Stone et al., 2017), and independent distance integrators might exist for path integrating based on optical flow and stride counting self-movement estimation, further increasing the required number of neurons (Collett, 2019). Therefore, the insect brain does not have enough neurons to accommodate a memory circuit that requires so many neurons to reproduce the homing distance error rate (dispersion rate) observed in the animals.

5.2.3 *Required neuronal time constant*

In the previous section, we assumed that neurons have a typical membrane and synaptic time constant (see section 5.4.2 in Materials and Methods). However, the bump's dispersion rate also depends on the neuronal time constant and decreases as the time constant increases, $\mathcal{D} \propto \frac{1}{\tau^2}$ (Burak and Fiete, 2012, see Figure 5.3). If we assume a network of a plausible size, i.e. a few hundreds of neurons (256 neuronal units were used in the simulations), we find that we would need a neuronal membrane time constant of around 16 h (16 h $\pm$ 8 h, mean $\pm$ std), to achieve a bump attractor with a dispersion rate of approximately 0.343 m^2/h. This is beyond the time constants range of typical neurons.

5.2.4 *Neurons with a long time constant*

One way to increase the time constant of neurons is to replace each neuron with a recurrent neural circuit with positive feedback (Cannon et al., 1983; Seung, 1996). Such recurrent networks may exhibit time constants higher than those of their constituent neurons, however, at the expense of an even larger number of neurons.

On the other hand, principal neurons in layer V of the entorhinal cortex (EC) and the lateral nucleus of the lateral amygdala (LA), are able to generate graded persistent activity that is sustained at a constant frequency for prolonged periods of time (Egorov et al., 2002, 2006). These single-neuron oscillators are not dependent on reverberating activity in recurrent circuits, and their spike rate can be gradually increased or decreased with appropriate synaptic input (Egorov et al., 2002; Fransén et al., 2006).

This graded persistent activity mechanism depends on a non-specific calcium-sensitive cationic current and introduces dynamics operating at a time scale that is many times larger than the time constants of the neuronal membrane and synapses. We, therefore, replaced the neurons in our bump attractor model with a model of

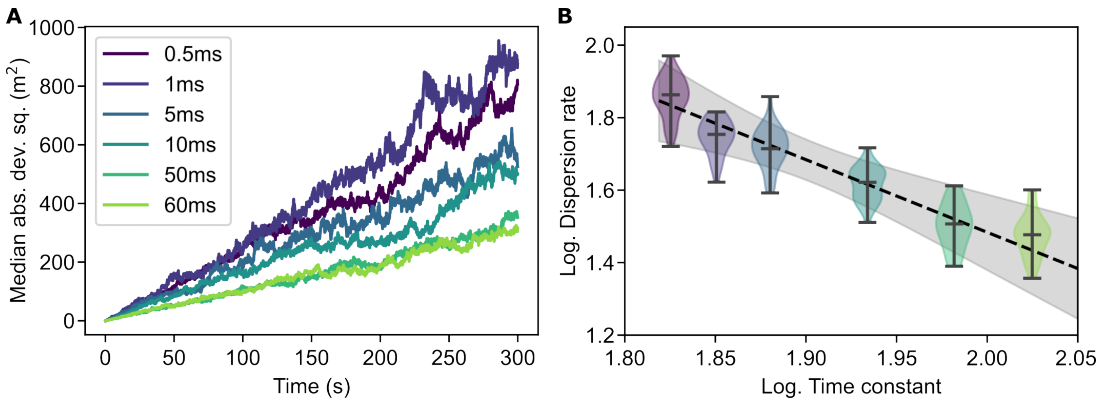

Figure 5.3: Effect of time constant on error increase. (**A**) Simulation results show the error (dispersion, measured as squared median absolute deviation) in the bump's location over time for different neuronal membrane time constants (300 trials for each condition). Higher time constants result in lower error increase rates. A network of 256 neuronal units was used for the simulations. Note the higher error increase rate than in Figure 5.2A due to the use of higher Poisson neuronal noise for the attractor network to sustain a bump at higher neuronal time constants (1400 impulses/s Poisson noise). As the time constant is varied towards lower and higher values, its effect is progressively reduced until the model breaks. (**B**) Dependence of error increase rate (dispersion rate, measured as squared median absolute deviation per second) on the neuronal membrane time constant for the simulation data in **A**. The function $\mathcal{D} = a/(\tau + b)^2$ was regressed to the dispersion rate $\mathcal{D}$ vs. the time constant τ simulation data with parameters $a = (0.31 \pm 0.03)\,\mathrm{m^2\,s}$ and $b = (66 \pm 4)\,\mathrm{ms}$ (mean $\pm$ std, R^2=0.82). In panel **B**, the logarithm of $\mathcal{D}$ vs. the logarithm of $\tau + b$ are depicted. The shaded zone indicates the 95% confidence intervals for the model fits. Extrapolation to the desired dispersion rate, $0.343\,\mathrm{m^2/h}$ (Figure 5.2B), resulted in a minimum required neuronal time constant of 16 h (16 h $\pm$ 8 h, mean $\pm$ std).

these neurons to investigate whether the prolonged activity phenomenon would result in more stable bump attractor dynamics. Indeed this replacement resulted in a significantly lower bump location dispersion rate (Figure 5.4), making such a bump attractor network model seem to be a plausible solution even in the face of the limited number of neurons in an insect's brain. If such neurons exist in insect brains, the required homing distance error increase rate (rate of increase in the homing distance dispersion) of $0.343\,\mathrm{m^2/h}$ could be achievable even with as few as 256 neuronal units. However, so far, graded persistent activity has only been reported in mammalian cells *in vitro* under very specific non-physiological conditions, and it is uncertain whether it is expressed under realistic physiological *in vivo* conditions.

5.2.5 *Homing distance decay regime*

Even though we have shown that the desired dispersion rate could be achieved with neurons exhibiting persistent graded activity, there is an additional aspect of the

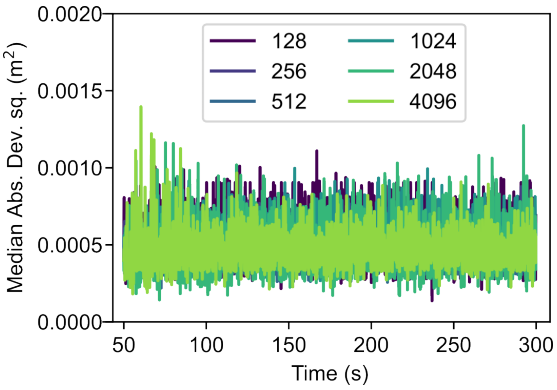

Figure 5.4: Bump attractor error increase using neurons with a persistent non-specific cation conductance. Simulation results show the error in the activity bump's location over time for networks of different sizes. A homogeneous neuronal population was used. In these experiments the dispersion of the bump's location is significantly smaller than in Figures 5.2A and 5.3A.

ants' distance memory dynamics that we should consider. In bump attractors, the bump may drift isotropically and equally likely towards higher and lower values (Figure 5.5A). Therefore, another prediction of the bump attractor hypothesis is that the increase of the animal's homing distance error due to memory drift would be equally likely to result in longer or shorter homing distances than the actual distance to the nest. On the contrary, the homing distance of the ants systematically and monotonically decreases with time (Figure 5.5B). This is a fundamental difference between ant behaviour and the predicted state loss of bump attractors, rendering the vanilla bump attractor hypothesis an insufficient explanation of the observed animal behaviour.

It is, however, conceivable that the monotonic decay of the homing distance over time might be due to a systematic bias in the bump attractor network. This systematic bias could be caused by a structural bias in the synaptic weights that would shift the activity bump in one direction over time. We, therefore, tested the effect of introducing bias to the synaptic weights of the bump attractor by replacing the Gaussian synaptic profile (Figure 5.1B) with a skewed Gaussian synaptic profile (see section 5.4.2 in Materials and Methods). This manipulation resulted in systematically biased drift in the bump's location; however, the activity bump moved at a constant rate (Figures 5.5C and 5.5D) that cannot account for the accelerating decay rate seen in ants (Figure 5.5B). This suggests that a different process causes homing distance degradation in the animals.

Altering the synaptic bias to produce the accelerating decay regime observed in the animals would require the biased synaptic profile to change depending on the homing distance. Such dynamic adaptation of the synaptic weights seems unrealistic

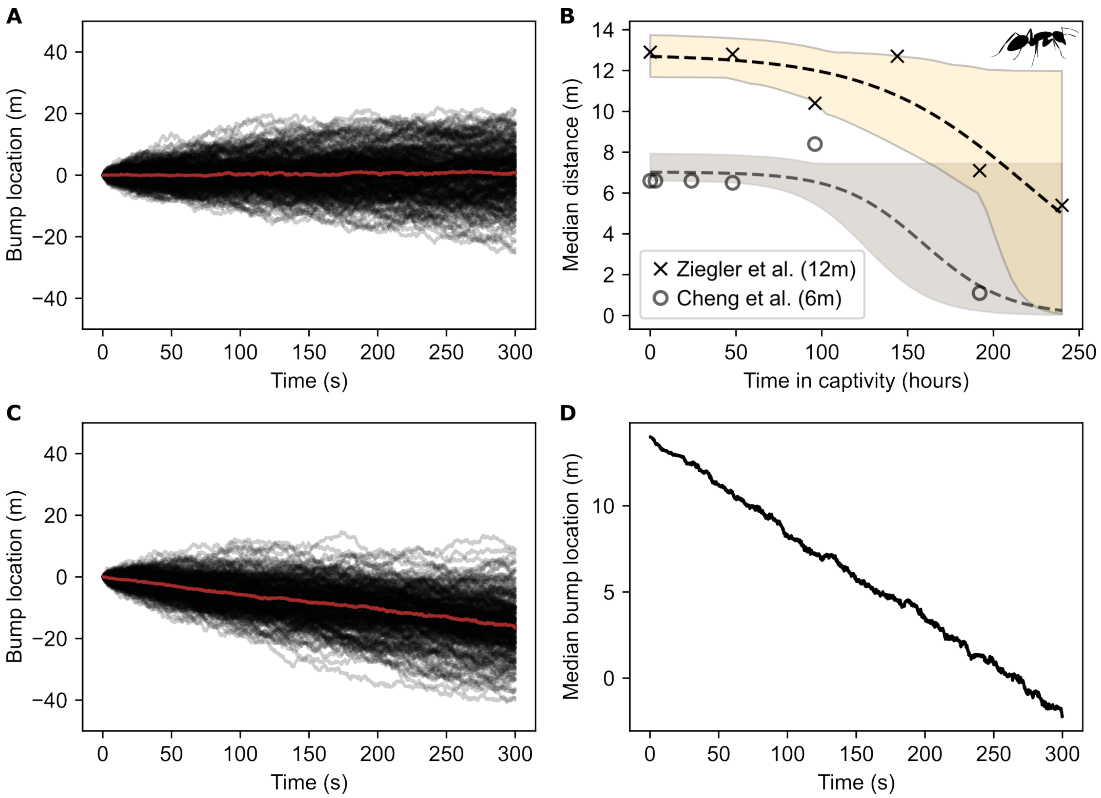

Figure 5.5: Loss of state value over time. (**A**) Dispersion in the bump attractor's state over time for 200 simulation trials starting from the same initial state of the bump attractor. The initial bump location disperses over time due to stochastic neuronal noise. During individual trials, the bump is equally likely to move towards higher or lower values. The median across trials is shown in red. (**B**) The homing distance of ants monotonically decays with captivity time. Data points in black x's are from Ziegler and Wehner (1997), while data points in grey o's are from Cheng et al. (2005). The actual distance between nest and capture point is 12 m in Ziegler and Wehner (1997) and 6 m in Cheng et al. (2005). The inverse logistic function $y = K/(1 + \frac{N_l}{K-N_l}e^{rt})$ was regressed to the data points, where t is the captivity time in hours and the regressed parameter values are $K = (12.800 \pm 0.761)$ m, $N_l = 0.099 \pm 0.580$, and $r = 0.022 \pm 0.035$ (mean $\pm$ std, R^2=0.85) for Ziegler and Wehner (1997) and $K = (7.000 \pm 0.357)$ m, $N_l = 0.010 \pm 0.006$, and $r = 0.041 \pm 0.018$ (mean $\pm$ std, R^2=0.86) for Cheng et al. (2005). The shaded regions indicate the 95% confidence intervals for the function fits. (**C**) Effect of systematic anisotropy in the synaptic weights of the bump attractor. Anisotropy was introduced by changing the synaptic strength pattern from Gaussian to skewed Gaussian with parameter a=-0.0005, resulting in a constant bump drift rate. Data of 200 simulation trials are shown (the median across trials is shown in red). The bump location changes because of the combination of systematic drift due to the structural bias and stochastic drift due to neuronal noise. (**D**) Median bump location of the data shown in **C** with the starting value set to 15 m for comparison with **B**. Unlike the ants, the bump's mean location drifts with a constant rate.

and would require an additional neuronal apparatus to manage it, raising the number of needed neurons once more.

5.2.6 *Effect of bump dispersion on agent homing*

In animals, memory does not exist in isolation but in the context of behaving agents. We, therefore, investigated the bump attractor memory model as part of a simulated agent. This allowed us to compare the agent's behaviour with that of the animals and investigate alternative memory degradation models. After travelling away from its origin (nest), the agent was held in 'captivity' for different waiting times, and then released for returning to its nest.

Theoretical analysis, neuroanatomical evidence, and modelling work indicate that the insect home vector is stored as a Cartesian vectorial representation with individual memory units storing the coordinate values along each cardinal axis (see Figure 5.6; Cheung and Vickerstaff, 2010; Vickerstaff and Cheung, 2010; Wittmann and Schwegler, 1995; Kim and Hallam, 2000; Vickerstaff and Di Paolo, 2005; Haferlach et al., 2007; Stone et al., 2017; Wolff and Rubin, 2018; Hulse and Jayaraman, 2020; Pisokas et al., 2022). Modelling has shown that the columnar organisation of the central complex provides a neural basis for potentially encoding and storing the coordinate values along eight columns of neurons, with each column corresponding to a cardinal axis (Haferlach et al., 2007; Stone et al., 2017). In this model, the eight memory values form a sinusoidal pattern with its amplitude encoding the distance the agent has travelled away from its origin and the location of the minimal memory value (column) corresponding to the direction the agent has mostly travelled away from its origin (Figure 5.6C) (Hartmann and Wehner, 1995; Haferlach et al., 2007; Stone et al., 2017). When a homing agent returns to its origin, the sinusoid's amplitude approaches zero and does not provide the agent with a direction to move towards. As a result, the homing agent moves in loops around the current location, resembling the search pattern observed in ants (Stone et al., 2017).

In our model, each memory unit consists of a bump attractor encoding the agent's displacement in the corresponding cardinal direction. We assumed that the bump attractors consist of neurons with a large enough time constant, resulting in a homing distance error increase rate comparable to that observed in ants ($0.343\,m^2/h$, see section 5.4.6 in Materials and Methods). During the waiting time period the bump attractors accumulated error at that rate. Then the agent was 'released' to return to its starting point (nest). As expected, the dispersion of the homing distance increased with the waiting time (Figure 5.7Ai, and 5.7Aii). However, the median homing distance of the agent across trials did not significantly change with waiting time which is contrary to the monotonic decay observed in the animals (Figure 5.7Aii). Clearly, the animal's memory follows dissipation dynamics that do not match the state degradation dynamics of bump attractor networks.

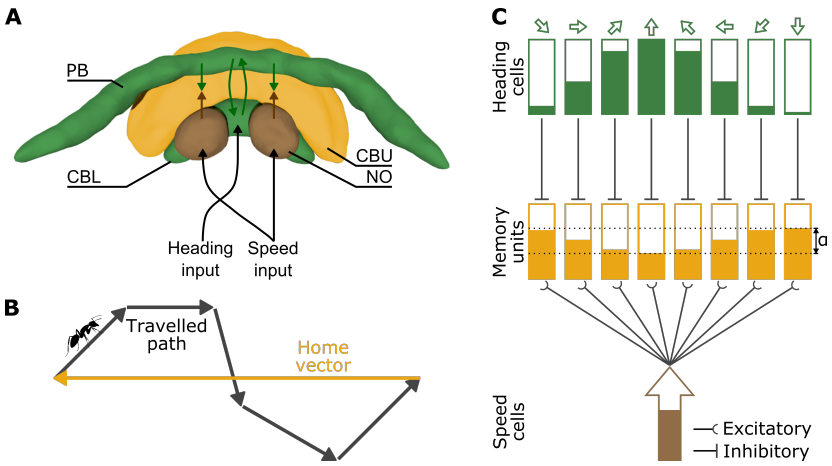

Figure 5.6: A Cartesian home vector encoding model of insect path integration. (**A**) The anatomy of the central complex and the main neuronal signal pathways involved in path integration. The brain structures — protocerebral bridge (PB), upper central body (CBU, also fan-shaped body), lower central body (CBL, also ellipsoid body), and noduli (NO) — are colour coded to match the conceptual drawing in **C**. The compartment and arrow colours indicate the type of identified signals (heading and speed) and their convergence in the CBU, where the path integration memory is hypothesised to reside (Stone et al., 2017). Image adapted from the `insectbraindb.org`. This pseudo-colour image of the ant *Cataglyphis nodus* was created with original data from Habenstein et al. (2020). (**B**) Illustration of example outbound path and corresponding accumulated home vector. (**C**) Conceptual depiction of the path integration model with each of the eight columns encoding one of the cardinal directions in a Cartesian coordinate system (Stone et al., 2017). Rectangular boxes represent neuronal ensembles and shaded portions the activity level or stored value. The inputs are the current insect heading (population coding with eight cardinal directions around the animal, i.e. E-PG neurons Wolff and Rubin 2018) and the current insect speed (encoded as the spike rate of TN neurons Stone et al. 2017). Both the heading and speed neurons drive the eight speed integrating 'memory units'. The inhibitory heading signals mask the speed signal, so the lower the heading neuron activity, the more the speed signal is integrated by the corresponding memory unit. The memory unit values form a sinusoidal pattern encoding the distance from the origin in its amplitude (α) and the direction to the origin in the horizontal location of the minimum.

We next investigated the agent homing performance when using an alternative memory degradation model. In this alternative model, the memory decayed over time following the logistic function observed in ants (Figure 5.5B), instead of the diffusive stochastic degradation produced by the bump attractor memory model. With this memory decay model the homing distance decreased monotonically as expected, but its dispersion remained constant (see the violin plots in Figure 5.7Bii), instead of increasing with the waiting time (as in Figure 5.7Aii). In addition, the directional accuracy was not compatible with ant performance (Figure 5.7Biv). Therefore, the pure logistic memory decay is not a sufficient model of the animal memory degradation.

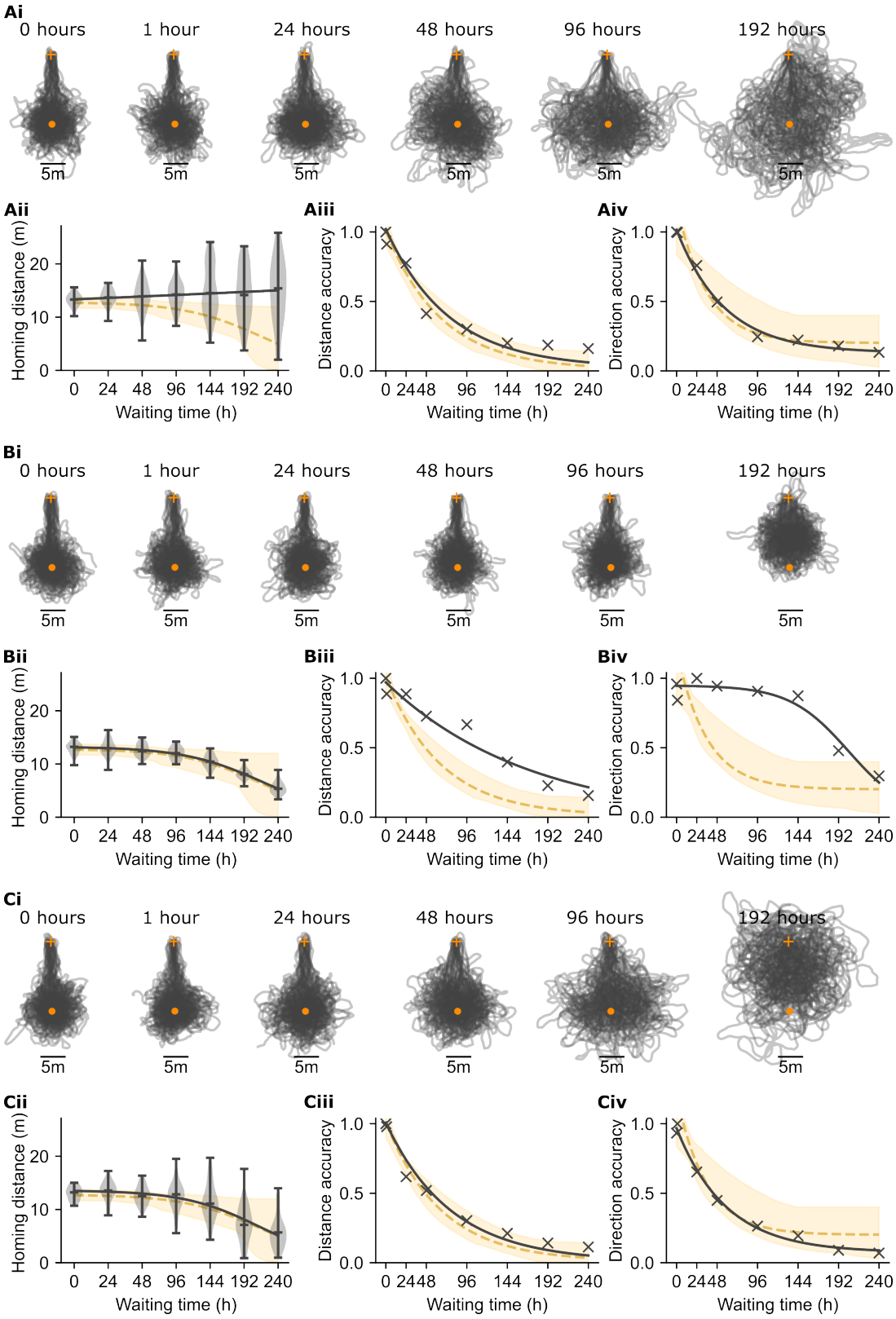

Figure 5.7: Comparisons of simulated agent homing to ant homing performance. Panels **A**, **B**, and **C** show the results obtained with three memory degradation models:

Figure 5.7 (cont.): (**A**) bump attractors exhibiting diffusive stochastic memory degradation; (**B**) time-dependent logistic memory decay (with parameters $K = 1$, $N_l = 0.02$, $r = 0.018$, see section 5.4.6.2 in Materials and Methods), and (**C**) the combined effect of time-dependent logistic decay and stochastic diffusive memory degradation (with parameters $K = 1$, $N_l = 0.021$, $r = 0.021$, and dispersion rate $\mathcal{D} = 0.0065$, see section 5.4.6.3 in Materials and Methods). (**i**) Paths of an agent that was kept stationary (waiting) for different amounts of time before being released for homing. During the waiting time, the memory state accumulated error according to one of the three models (**A**, **B**, **C**). Then the agent is released to return to its origin as indicated by its home vector memory. The release location is indicated with an orange cross and the nest location with an orange disc. Once the agent reaches the location indicated by its memory, it searches following a looping trajectory resulting in the blob of overlapping paths centered at the expected home location. (**ii**) The homing distance (distance between the release point and the geometric centre of the search) as a function of the waiting time (the bars of the violin plots show the median, minimum and maximum). The black solid curve shows the regressed logistic function to the simulation data. The yellow dashed line shows the regressed logistic function to the ant homing distance data and the yellow shaded region indicates the 95% confidence intervals of the function fits as in Figure 5.5B. (**iii**) The homing distance accuracy as a function of the waiting time (the ordinate shows MAD^{-1} in m^{-1} units). The exponential function (yellow dashed curve) $y = e^{(bx)} + c$ was regressed to the ant homing data from Ziegler and Wehner (1997) with parameters $b = -0.015\,\text{h}^{-1}$, and $c = 0.009\,\text{m}^{-1}$. The yellow shaded region indicates the 95% confidence intervals for the function fits. The crosses (x's) mark the medians of model simulation results and the black curve the exponential function regressed to the simulation data points with parameters $b = -0.013$, $c = 0.020$ (R^2=0.94) for model **A**, $b = -0.006$, $c = -0.030$ (R^2=0.95) for model **B**, and $b = -0.013$, $c = 0.008$ (R^2=0.97) for model **C**. (**iv**) The homing direction accuracy as a function of the waiting time (the ordinate shows σ^{-1} in degree^{-1} units). The exponential function (yellow dashed curve) $y = e^{(bx)} + c$ was regressed to the ant data from Ziegler and Wehner (1997) with parameters $b = -0.028\,\text{h}^{-1}$, and $c = 0.201\text{degree}^{-1}$. The yellow shaded region indicates the 95% confidence intervals of the function fits. The crosses (x's) mark the model simulation medians and the black curve is the exponential function regressed to the simulation data points with parameters $b = -0.018$, $c = 0.130$ (R^2=0.99) for model **A**, no parameters were found for model **B** (the curve shown in panel **Biv** is the logistic function with parameters $K = 0.948$, $N_l = 0.003$, $r = 0.028$, resulting in R^2=0.94), and $b = -0.017$, $c = 0.073$ (R^2=0.99) for model **C**.

Finally, we tested a hybrid model, combining the logistic memory decay with diffusive stochastic state loss. With this hybrid model the agent's homing behaviour indeed resembled that of the ants (Figure 5.7C). The homing distance decayed with the waiting time, the dispersion increased, while both the distance and direction accuracy were within the confidence intervals of animal behaviour (Figures 5.7Cii–iv). Therefore, the hybrid model was the only one that reproduced all the measures of ant homing behaviour.

5.3 DISCUSSION

We investigated the plausibility of the bump attractor model as the mechanism underlying path integration memory in ants. To this end, we compared the temporal dynamics of the path integration memory of *Cataglyphis fortis* ants with those of bump attractors encoding the agent's displacement in respect to its starting point. We tested the bump attractor hypothesis with respect to the temporal dynamics of increase in the homing distance error, the number of required neurons, and the required neuronal time constants.

The bump attractor hypothesis predicts that the error in the ants' homing distance would increase as a function of the time intervening before release. This is indeed the case in *Cataglyphis fortis* ants. The bump attractor hypothesis also predicts that the bump attractor network must consist of a considerable number of neurons or of neurons with adequately high time constants to be stable enough at the ecologically relevant time scale. However, the corporeal reality of the insect brain renders this last prediction inadmissible since it neither contains enough neurons nor are they known to have the high time constants required. But even in the case that these conditions are satisfied by a yet unobserved physiological property substantially increasing the neuronal time constant, we showed that the state value drift dynamics predicted by the bump attractor hypothesis do not match the observed dynamics of the animal's homing distance. All our attempts to coax the bump attractor into reproducing the animal homing distance dynamics have failed. We then investigated alternative models of memory degradation and found that the underlying memory mechanism must be subject to the combined effect of logistic decay and diffusive stochastic noise to reproduce behaviour resembling that of the animals.

In the present work, we assumed that the homing distance degradation in ants is due to a degradation in the animal's home vector memory. It is not inconceivable that other factors might be involved in the observed behaviour, such as the motivational state of the animals. However, there was no evidence of such an effect in the experiments since the animals continued searching for their nest, indicating that they were motivated to return to it. We also assumed a linear relationship between memory and homing distance. This relationship might be more complex and further research combining behavioural with physiological observations might be required to elucidate its exact nature.

A further consideration is that the biophysical parameters used in our models are based on measurements performed on neurons *in vitro*, typically at room temperatures. The desert ants, *Cataglyphis fortis*, are active at much higher temperatures which unavoidably affect the biophysical properties of their neurons. At higher temperatures,

Table 5.1: Ant and bump attractor dynamics comparison.

Parameter	Ants	Bump Attractor
Distance degradation type	Monotonic	Random walk
Quickly resettable to zero state	Yes	Yes
Given $\mathcal{D} = 0.343\,\mathrm{m}^2/\mathrm{h}$:		
Number of neurons	thousands	millions
Time constant	<1 s	>8 h

the membrane ion-channels become faster (Frankenhaeuser and Moore, 1963; Tang et al., 2010), their conductance increases (Volgushev et al., 2000), and the synaptic transmission is faster (Postlethwaite et al., 2007). The structural properties of the membrane are also affected, resulting in decreased capacitance and time constant (Volgushev et al., 2000), while the neuronal channel noise level also decreases (Faisal et al., 2005, 2008). The exact effect of the higher temperature on the neurons is complex and further investigation is needed. However, the magnitude and polarity of the effects of temperature seem unlikely to result in a significant coordinated improvement of the bump attractor's stability.

Despite our attempts to address every one of the model's limitations, the bump attractor hypothesis failed to withstand all our tests. The model is limited both in the duration of state maintenance and the dynamics of state degradation. We illustrated, however, that a memory degradation model combining the diffusive state degradation with a monotonic state decay following the logistic function can reproduce the animal homing behaviour. Our work casts doubt on the bump attractor memory hypothesis and rekindles the quest for the memory substrate of path integration. The presented findings provide important bounds to the memory degradation dynamics and therefore the range of plausible biophysical processes that could underlie the path integration memory.

5.4 MATERIALS AND METHODS

5.4.1 *Data extraction and processing*

The ant behaviour data were extracted from Ziegler and Wehner (1997) and Cheng et al. (2005). The extracted data points as well as the data produced from simulations in this paper were fitted using the curve_fit function of SciPy's optimize Python package with curve parametrisation as described in Figures 5.2, 5.3, 5.5, and 5.7. The slopes of

the curves in Figures 5.2A and 5.3A were calculated with linear regression on the data points.

The rate of increase in the variance of the bump's expected location is inversely proportional to the number of neurons in the attractor network N (Burak and Fiete, 2012). Therefore, the rate of increase of MAD^2 (squared median absolute deviation) would also be inversely proportional to the number of neurons N. We use MAD^2 per time unit as the measure of dispersion rate, $\mathcal{D}$, in $\mathrm{m}^2\,\mathrm{s}^{-1}$ units. To extrapolate from the simulation-derived data points to higher values of N, in Figure 5.2D, we used linear regression to the logarithm transformed data points

$$\mathcal{D} \propto \frac{1}{N} \Rightarrow$$
$$\log \mathcal{D} = -\log N + \mathrm{const}$$

where $\mathcal{D}$ is the dispersion rate measured as squared median absolute deviation per second in $\mathrm{m}^2\,\mathrm{s}^{-1}$ units.

Theoretical work suggests that the rate of increase in the variance of the bump's expected location is bounded from below by a function inversely proportional to τ_{total}^2, where τ_{total} is the sum of the time constants in the attractor network (Burak and Fiete, 2012). In Figure 5.3B, the function $\mathcal{D} = a/(\tau + b)^2$ was regressed to the dispersion rate $\mathcal{D}$ vs. the membrane time constant τ used in the simulations.

The confidence intervals in Figures 5.2B, 5.2D, 5.3B, 5.5B, and 5.7 were estimated using bootstrapping.

5.4.2 *Bump attractor network model*

The bump attractor network model implementation used in our experiments was derived from the code of Gerstner et al. (2014). Our source code is available at `https://github.com/johnpi/Pisokas_Hennig_2022_Attractor_Based_Memory`. To avoid the effect of boundary conditions at the edges of a line attractor, we used a ring attractor network topology and we made sure our experiments were confined to activity bump shifts smaller than $\pm 180°$. In this way, for the purposes of our experiments the topology of the circuit was indistinguishable from an actual line attractor.

The bump attractor network model used in the experiments had uniform global inhibition and structured lateral excitatory synapses with efficacies that followed a Gaussian profile. The skewed Gaussian formulation described below was used for determining the synaptic efficacies and allowed us to choose between Gaussian and skewed Gaussian profiles. The excitatory synaptic efficacies $w(x_i, x_j)$ were therefore

determined by the following formulation. Let $\phi(x)$ denote the Gaussian probability density function

$$\phi(x) = \frac{1}{\sigma\sqrt{2\pi}} e^{-\frac{1}{2}(\frac{x}{\sigma})^2}$$

where $\sigma^2 = 20$ is the variance (width) of the Gaussian profile. Let $\Phi(x)$ denote the cumulative distribution function of the Gaussian

$$\Phi(x) = \int_{-\infty}^{x} \phi(y)\, dy = \frac{1}{2}\left[1 + \text{erf}\left(\frac{x}{\sigma\sqrt{2}}\right)\right]$$

where $erf(\cdot)$ is the error function. Then the probability density function of the skewed Gaussian and thus the synaptic weights are given by

$$w(x_i, x_j) = 2\phi(x_i - x_j)\Phi(\alpha(x_i - x_j))$$

where α is the skewness factor, with $\alpha = 0$ resulting in the Gaussian probability density function. In the case of simulations with systematically biased bump drift we used $\alpha = -0.0005$ (Figure 5.5). x_i and x_j are the positions of the presynaptic and postsynaptic neurons, respectively, and $w(x_i, x_j) \in [-1, 1]$ is the synaptic connection weight from neuron x_i to neuron x_j. The values of x_i and x_j are periodic integers in the range $[0, N-1]$, where N is the number of excitatory neuronal units in the circuit and the difference $x_i - x_j$ is calculated by modulo N subtraction, as in Brody et al. (2003). The values of $w(x_i, x_j)$ determined the synaptic efficacy profile of the excitatory synapses while the inhibitory synapses had uniform efficacy.

The encoded distance values were in the range [0, 100]. This interval was mapped to the excitatory neurons around the ring attractor. Each of the excitatory neurons around the ring attractor was tuned to a distance value in the series $k\frac{100}{N}$, for $k \in 0, 1, 2, \ldots, N-1$. The bump's location was decoded as a population vector for the purposes of the analysis presented here.

5.4.3 *Neuron model*

We used two neuronal models in our experiments. The first one, the base model, utilised leaky integrate and fire neurons with AMPA, NMDA and $GABA_A$ receptor channels. The inclusion of NMDA receptors endows the network with regular activity, since a network with only AMPA and $GABA_A$ receptors produces synchronous spiking activity (Compte et al., 2000).

The second neuron model, utilised the neurotransmitter receptors of the first model and in addition mACh receptors that metabotropically opened clusters of cooperative

non-specific cation channels that provided the graded persistent spiking observed in the entorhinal cortex layer V neurons (Egorov et al., 2002, 2006).

The model parameter values were set to values consistent with evidence from measurements in *D. melanogaster* and other species when available (Gouwens and Wilson, 2009; Rohrbough and Broadie, 2002; Sheeba et al., 2008). The intrinsic neuronal properties for the excitatory neurons of the base model were set to a membrane capacitance $C_m = 2\,\text{nF}$, leak conductance $g_L = 100\,\text{nS}$, reversal potential $E_L = -70\,\text{mV}$, threshold potential $V_{th} = -50\,\text{mV}$, reset potential $V_{res} = -60\,\text{mV}$, and absolute refractory period $\tau_{ref} = 2\,\text{ms}$. For the inhibitory neurons of the base model the corresponding values were $C_m = 2\,\text{nF}$, $g_L = 200\,\text{nS}$, $E_L = -70\,\text{mV}$, $V_{th} = -50\,\text{mV}$, $V_{res} = -60\,\text{mV}$, and $\tau_{ref} = 1\,\text{ms}$.

In the second model, the intrinsic neuronal properties for the excitatory neurons with the non-specific cation conductance were set to a membrane capacitance $C_m = 2\,\text{nF}$, leak conductance $g_L = 2\,\text{nS}$, reversal potential $E_L = -63\,\text{mV}$, threshold potential $V_{th} = 10\,\text{mV}$, reset potential $V_{res} = -60\,\text{mV}$, and absolute refractory period $\tau_{ref} = 3\,\text{ms}$. For the inhibitory neurons of the second model the values were $C_m = 2\,\text{nF}$, $g_L = 2\,\text{nS}$, $E_L = -63\,\text{mV}$, $V_{th} = 10\,\text{mV}$, $V_{res} = -60\,\text{mV}$, and $\tau_{ref} = 2\,\text{ms}$.

For modifying the membrane time constant of the neurons the membrane capacitance was adjusted accordingly using the equation

$$C_m = \tau_m * g_L$$

where τ_m is the desired time constant. The external input that set the initial bump location was provided by neurons forming synaptic connections with the excitatory neurons that were mediated by AMPA receptors, as in Compte et al. (2000). The maximum conductance of the AMPA receptor channels for the excitatory cells was $G_{ext,E} = 3.1\,\text{nS}$ and for the inhibitory cells $G_{ext,I} = 2.38\,\text{nS}$.

Postsynaptic currents were modelled as

$$I_{post} = s g_{syn}(V_m - E_{syn})$$

where s is the gating variable, g_{syn} the synaptic conductance, V_m the membrane potential, and E_{syn} the synaptic reversal potential (set to 0 mV for AMPA, NMDA, and mACh receptor channels and to $-70\,\text{mV}$ for GABA_A ones). The gating variables were modelled as in Compte et al. (2000). The decay time constants of the gating variables were set to 2 ms for AMPA, 10 ms for GABA_A, 65 ms for NMDA, and 5 ms for mACh receptor channels.

The non-specific cation channels were modelled as clusters of cooperatively opening channels (Pfeiffer et al., 2020). The cluster opening kinetics were governed by

$$\frac{dO_{coop}}{dt} = \frac{\alpha_o}{\tau_{coop}} s_{mACh} G_{EE} - \frac{\beta_o}{\tau_{coop}} s_{GABA} G_{IE}$$

where $\alpha_o = 1 \times 10^{13}$ and $\beta_o = 5 \times 10^{13}$ are the opening and closing rate factors, respectively. $\tau_{coop} = 100\,\text{s}$ is the average cluster transition time constant. s_{mACh} and s_{GABA} are the channel gating variables. G_{EE} and G_{IE} are synaptic conductances described in Table 5.2. The number of open clusters, O_{coop}, was clipped to the range [0, 100]. The total cluster current was

$$I_{cluster} = G_{coop} O_{coop} (V_m - E_{coop})$$

where $G_{coop} = 7\,\text{nS}$ derived from the value used in Pfeiffer et al. (2020) and manually adjusted to obtain a functioning neuron model for the range of O_{coop} values. The synaptic conductances between neurons i and j were modelled as

$$g_{syn,ij} = w(x_i, x_j) G_{syn}$$

The synaptic conductances G_{syn} mediated by the AMPA, NMDA, GABA_A, and mACh receptor channels were determined by following the procedure outlined in Brody et al. (2003) to obtain the formation of a stable activity bump. Subsequently, starting with the hand tuned values, the dual_annealing optimiser from SciPy's optimize package was utilised to optimise the synaptic conductances using the objective function

$$
\begin{aligned}
\underset{\mathbf{G}}{\text{argmin}} \quad & \epsilon_H(\mathbf{G}) + 5\epsilon_W(\mathbf{G}) + \epsilon_{A1}(\mathbf{G}) + \epsilon_{A2}(\mathbf{G}) + 2\epsilon_S(\mathbf{G}) + W_{\text{diff}}(\mathbf{G}) \\
\text{s. t.} \quad & \epsilon_H(\mathbf{G}) = \frac{|H_d(t_1) - H_a(\mathbf{G}, t_1)|}{360^\circ} + \frac{|H_d(t_2) - H_a(\mathbf{G}, t_2)|}{360^\circ} \\
& \epsilon_W(\mathbf{G}) = \frac{|55^\circ - W_a(\mathbf{G}, t_1)|}{360^\circ} + \frac{|55^\circ - W_a(\mathbf{G}, t_2)|}{360^\circ} \\
& \epsilon_{A1}(\mathbf{G}) = \frac{1}{1 + (A_{max}(\mathbf{G}, t_1, \Delta t) - A_{min}(\mathbf{G}, t_1, \Delta t))} \\
& \epsilon_{A2}(\mathbf{G}) = \frac{1}{1 + (A_{max}(\mathbf{G}, t_2, \Delta t) - A_{min}(\mathbf{G}, t_2, \Delta t))} \\
& \epsilon_S(\mathbf{G}) = \frac{1}{1 + S(\mathbf{G}, t_2, \Delta t)} \\
& W_{\text{diff}}(\mathbf{G}) = \frac{|W_a(\mathbf{G}, t_1) - W_a(\mathbf{G}, t_2)|}{360^\circ} \\
& 0 \leq G_{II} \leq 0.01 \\
& 0 \leq G_{IE} \leq 10 \\
& 0 \leq G_{EE} \leq 10 \\
& 0 \leq G_{EI} \leq 10
\end{aligned}
\tag{5.1}
$$

Where ϵ_H and ϵ_W are error factors measured as deviations from the desired values. ϵ_{A1}, ϵ_{A2}, ϵ_S, and W_{diff} are factors penalising undesirable network behaviour. $H_d(t)$ is the desired activity 'bump' heading at time t, while $H_a(\mathbf{G}, t)$ is the actual measured activity 'bump' heading at time t given a model with synaptic channel efficacies $\mathbf{G}$. $W_a(\mathbf{G}, t)$ is the actual measured width of the activity 'bump' at time t (measured as the full width at half maximum). $A_{max}(\mathbf{G}, t, \Delta t)$ and $A_{min}(\mathbf{G}, t, \Delta t)$ are the maximum and minimum neuron spike rates across all excitatory neurons in the attractor network with channel conductances $\mathbf{G}$, measured for a duration Δt starting at time t. $S(\mathbf{G}, t, \Delta t) \in [0, 1]$ is the proportion of the inhibitory neurons in the attractor network that have a spike rate greater than 30 impulses/s, measured for a duration Δt starting at time t. t_1 and t_2 are sampling times located near the beginning and the end of the simulation, respectively. $\epsilon_H(\mathbf{G})$ penalises deviation of the activity bump's location from the desired location. $\epsilon_W(\mathbf{G})$ penalises deviation of the activity bump width from the desired value of 55°. $\epsilon_{A1}(\mathbf{G})$ and $\epsilon_{A2}(\mathbf{G})$ reward the formation of a bump with larger amplitude. $\epsilon_S(\mathbf{G})$ rewards increased spike rate activity across the inhibitory neuron population to avoid these neurons being completely silenced. $W_{\text{diff}}(\mathbf{G})$ penalises changes in the bump's width between the beginning and the end of the simulation thus promoting sustenance of an activity bump. $\mathbf{G}$ is the vector $[G_{II}, G_{IE}, G_{EE}, G_{EI}]$. G_{II}, G_{IE}, G_{EE}, and G_{EI} are the synaptic conductances as described in Table 5.2. These were optimised separately for the base model and the model that included the non-specific cation

Table 5.2: Synaptic conductances.

Conductance variable	Corresponding synapse and receptors
G_{II}	From inhibitory to inhibitory neurons ($GABA_A$)
G_{IE}	From inhibitory to excitatory neurons ($GABA_A$)
G_{EE}	From excitatory to excitatory neurons (NMDA and mACh)
G_{EI}	From excitatory to inhibitory neurons (NMDA and AMPA)

conductances. For the base model the values were G_{II} = 0.3584 nS, G_{IE} = 0.4676 nS, G_{EE} = 0.133 35 nS, and G_{EI} = 0.122 64 nS for networks with 2048 neurons. The conductances were scaled according to the number of neurons used as in Brody et al. (2003). For the model that included the non-specific cation conductances the values were G_{II} = 0.0001 nS, G_{IE} = 0.005 nS, G_{EE} = 0.11 nS, G_{EI} = 1.339 624 49 nS, and the additional G_{coop} = 7.0 nS for networks with 2048 neurons. The constraint $0 \leq G_{coop} \leq 10$ was added to the constraints of Equation 5.1 when optimising for the last case.

5.4.4 *Neuronal noise*

All neurons receive excitatory input modelled as uncorrelated Poisson spike trains with average spike rate as specified in the appropriate sections of the text. The neuronal noise used in Figures 5.2A, 5.2C, 5.2D, 5.4, 5.5A, 5.5C, and 5.5D was modelled as Poisson noise with an average spike rate 5 impulses/s. This noise level was chosen because the attractor's state dispersion rate reaches a plateau beyond Poisson neuronal noise with an average spike rate of 4 impulses/s (Figure 5.2C). Furthermore, this is a plausible spike rate near the lower end of background activity rates measured in neurons of the central complex (Heinze and Homberg, 2007, 2009). For Figure 5.3, the Poisson neuronal noise was set to an average spike rate 1400 impulses/s to allow networks with higher neuronal time constants to sustain a bump of activity.

5.4.5 *Agent simulations*

The agent simulations were based on the anatomically constrained model of Stone et al. (2017). The source code of the original work was modified and extended as described below and it is available at `https://github.com/johnpi/Pisokas_Hennig_2022_Attractor_Based_Memory`. The neurons were modelled as rate-based perceptrons with a sigmoid activation function. Independent Gaussian noise with $\mu = 0$ and $\sigma^2 = 0.01$ was added to the activation of each neuron and the resulting values were clipped to the interval $[0, 1]$.

To reproduce agent paths resembling those of ants we added motor noise that is parametric to the home vector length, as in Pisokas et al. (2022). This motor noise was modelled as a Gaussian noise factor applied to the steering commands of the agent

$$steering = steering\_command \cdot \epsilon \tag{5.2}$$

where *steering_command* is the steering command generated by the path integration model in homing mode, *steering* is the actual agent steering, and $\epsilon \sim \mathcal{N}(\mu, \sigma^2)$ is a random variable sampled from the Gaussian distribution with $\mu = 1$ and σ set to the motor noise level (Equation 5.3). The motor noise level was modelled as a decaying exponential function of the memory amplitude, as in Pisokas et al. (2022).

$$Motor\ noise = \frac{y_{max}}{e^{s_m \cdot a_m}} \tag{5.3}$$

where y_{max} is the maximum motor noise level (corresponding to zero vector ant paths), and s_m is the slope of the exponential function. The memory amplitude a_m was defined as the difference between the maximum and minimum value along the sinusoidal pattern of memory unit values (Pisokas et al., 2022).

The translational velocity of the simulated agents during homing was iteratively updated using the formula

$$v(t) = \begin{cases} v(t-1) + a\Delta t - \mu_f v(t-1), & \text{if } |steering| \leq 20^\circ \\ v(t) = 0, & \text{if } |steering| > 20^\circ \end{cases} \tag{5.4}$$

where $v(t)$ is the agent's velocity at time step t, $a = 0.08\,\mathrm{m/s^2}$ is an acceleration constant, Δt is the simulated time step duration, and $\mu_f = 0.15$ is a friction constant. The velocity was reset to $0\,\mathrm{m/s}$ whenever the agent performed a turn larger than 20° simulating a stop on turning as observed in ants (Pisokas et al., 2022).

We performed a grid search following the procedure outlined in Pisokas et al. (2022) to find the combination of maximum motor noise level ($y_{max} = 7$) and slope ($s_m = 9$) of the decaying exponential that produces simulated paths that resemble the paths of both zero vector ants (zero memory amplitude) and full vector ants.

The inputs to the path integration model were the allocentric orientation of the agent and the speed of the agent's motion (Figure 5.6, see also Stone et al. 2017). Visual cues were not used in either the outbound or the homing part of the simulations; path integration was the sole navigation method utilised. The simulations had two stages, an outbound trip and a homing trip. For generating the outbound trip, the agent begun from a designated nest location and moved following a path generated by a filtered (smoothed) noise process, as previously described by Stone et al. (2017),

until it reached a designated food location. Outbound agent simulations that did not result in the agent reaching the designated food location after 1500 simulation steps were disregarded. During the outbound trip, a home vector was accumulated that was encoded as the states of the eight memory units. Subsequently, an intervening waiting period was simulated during which stochastic memory state drift occurred, and then the simulation proceeded with the agent release in homing mode. The simulated homing paths were cut at 3000 steps from release allowing a sufficiently long observation period of the search behaviour to estimate the centre of search.

5.4.6 *Agent memory degradation model*

5.4.6.1 *Diffusive stochastic degradation model*

In the agent behaviour simulations, for computational efficiency, the bump attractor memory dynamics were modeled with stochastic state diffusion. Therefore, the states of the memory units were updated by

$$mem_{post} = mem_{pre} + b \tag{5.5}$$

where mem_{pre} is the memory at the moment the agent was captured, mem_{post} the memory at the moment the agent was released, and

$$b \sim \mathcal{N}(\mu, \sigma^2) \tag{5.6}$$

There were eight such memory unit variables one for each cardinal direction (Figure 5.6C). We set $\mu = 0$ and σ to appropriate values corresponding to the effect of stochastic bump location drift for the different waiting periods. We set $\sigma = \sqrt{t_w}D$, with t_w being the waiting period in hours and D determining the memory state dispersion rate. We experimentally determined that $D = 28.8$ produces the nearest approximation to the error increase rate observed in ant behaviour (dispersion rate $\mathcal{D} = 0.343\,\mathrm{m}^2/\mathrm{h}$).

5.4.6.2 *Logistic decay model*

For the logistic decay memory model, instead of using the diffusive stochastic degradation model, the memory values were multiplied by a time-dependent factor

$$l = \frac{K}{1 + (\frac{N_l}{K - N_l})e^{rt_w}}$$

where t_w is the waiting time in hours, $K = 1$ sets the maximum value of l to 1, while $N_l = 0.02$ and $r = 0.018$ were determined using grid search to get the logistic function's shape that minimizes the mean squared error between the agent homing distance and the ant homing distance over waiting time (Figure 5.5B). Note that these logistic function parameter values are different from the ones in Figure 5.5B because for the agent model, we regressed the logistic function to the normalised ant homing distance data (distance normalised to a maximum value of 1) so that l is in the interval [0,1]. The memory values were multiplied by the time-dependent factor l before release

$$mem_{post} = mem_{pre} \times l$$

5.4.6.3 *Hybrid logistic decay and diffusive degradation model*

In the hybrid memory degradation model both the time-dependent logistic decay and diffusive stochastic degradation were applied on the memory values before release

$$mem_{post} = mem_{pre} \times l + b$$

In this case the parameter values were $K = 1$, $N_l = 0.021$, and $r = 0.021$, while the dispersion rate determining factor was $D = 0.0065$. These parameter values were determined using grid search to minimize the sum of the mean squared errors between the agent simulation and the ant behaviour data for homing distance, homing distance error, homing distance accuracy, and homing direction accuracy.

5.5 ACKNOWLEDGEMENTS

We would like to thank Barbara Webb for early discussion of the ideas developed in this paper and her comments on the draft. We would also like to thank Eve Marder and Stanley Heinze for early discussion of this work. Part of this work was funded by the Principal's Career Development Scholarship, University of Edinburgh.

BIBLIOGRAPHY

Boucheny, C., Brunel, N., and Arleo, A. (2005). A continuous attractor network model without recurrent excitation: Maintenance and integration in the head direction cell system. *Journal of Computational Neuroscience*, 18(2):205–227.

Brody, C. D., Romo, R., and Kepecs, A. (2003). Basic mechanisms for graded persistent activity: Discrete attractors, continuous attractors, and dynamic representations. *Current Opinion in Neurobiology*, 13(2):204–211.

Burak, Y. and Fiete, I. R. (2009). Accurate path integration in continuous attractor network models of grid cells. *PLoS Computational Biology*, 5(2):e1000291.

Burak, Y. and Fiete, I. R. (2012). Fundamental limits on persistent activity in networks of noisy neurons. *Proceedings of the National Academy of Sciences*, 109(43):17645–17650.

Cannon, S. C., Robinson, D. A., and Shamma, S. (1983). A proposed neural network for the integrator of the oculomotor system. *Biological Cybernetics*, 49(2):127–136.

Cheng, K., Narendra, A., and Wehner, R. (2005). Behavioral ecology of odometric memories in desert ants: Acquisition, retention, and integration. *Behavioral Ecology*, 17(2):227–235.

Cheung, A. and Vickerstaff, R. (2010). Finding the way with a noisy brain. *PLoS Computational Biology*, 6(11):e1000992.

Collett, T. S. (2019). Path integration: how details of the honeybee waggle dance and the foraging strategies of desert ants might help in understanding its mechanisms. *Journal of Experimental Biology*, 222(11):jeb205187.

Compte, A., Brunel, N., Goldman-Rakic, P. S., and Wang, X.-J. (2000). Synaptic mechanisms and network dynamics underlying spatial working memory in a cortical network model. *Cerebral Cortex*, 10(9):910–923.

Conklin, J. and Eliasmith, C. (2005). A controlled attractor network model of path integration in the rat. *Journal of Computational Neuroscience*, 18(2):183–203.

Darwin, C. (1873). Origin of certain instincts. *Nature*, 7(179):417–418.

Egorov, A. V., Hamam, B. N., Fransén, E., Hasselmo, M. E., and Alonso, A. A. (2002). Graded persistent activity in entorhinal cortex neurons. *Nature*, 420(6912):173–178.

Egorov, A. V., Unsicker, K., and von Bohlen Und Halbach, O. (2006). Muscarinic control of graded persistent activity in lateral amygdala neurons. *European Journal of Neuroscience*, 24(11):3183–3194.

el Jundi, B., Warrant, E. J., Pfeiffer, K., and Dacke, M. (2018). Neuroarchitecture of the dung beetle central complex. *Journal of Comparative Neurology*, 526(16):2612–2630.

Faisal, A. A., Selen, L. P. J., and Wolpert, D. M. (2008). Noise in the nervous system. *Nature Reviews Neuroscience*, 9(4):292–303.

Faisal, A. A., White, J. A., and Laughlin, S. B. (2005). Ion-channel noise places limits on the miniaturization of the brain's wiring. *Current Biology*, 15(12):1143–1149.

Franconville, R., Beron, C., and Jayaraman, V. (2018). Building a functional connectome of the *Drosophila* central complex. *eLife*, 7.

Frankenhaeuser, B. and Moore, L. E. (1963). The effect of temperature on the sodium and potassium permeability changes in myelinated nerve fibres of *Xenopus laevis*. *The Journal of Physiology*, 169(2):431–437.

Fransén, E., Tahvildari, B., Egorov, A. V., Hasselmo, M. E., and Alonso, A. A. (2006). Mechanism of graded persistent cellular activity of entorhinal cortex layer V neurons. *Neuron*, 49(5):735–746.

Gerstner, W., Kistler, W. M., Naud, R., and Paninski, L. (2014). *Neuronal dynamics: From single neurons to networks and models of cognition*. Cambridge University Press.

Goldschmidt, D., Dasgupta, S., Wörgötter, F., and Manoonpong, P. (2015). A neural path integration mechanism for adaptive vector navigation in autonomous agents. In *Proceedings of the International Joint Conference on Neural Networks (IJCNN)*, pages 1–8.

Goldschmidt, D., Manoonpong, P., and Dasgupta, S. (2017). A neurocomputational model of goal-directed navigation in insect-inspired artificial agents. *Frontiers in Neurorobotics*, 11:1–17.

Goodridge, J. P. and Touretzky, D. S. (2000). Modeling attractor deformation in the rodent head-direction system. *Journal of Neurophysiology*, 83(6):3402–3410.

Gouwens, N. W. and Wilson, R. I. (2009). Signal propagation in *Drosophila* central neurons. *Journal of Neuroscience*, 29(19):6239–6249.

Green, J., Adachi, A., Shah, K. K., Hirokawa, J. D., Magani, P. S., and Maimon, G. (2017). A neural circuit architecture for angular integration in *Drosophila*. *Nature*, 546(7656):101–106.

Green, J. and Maimon, G. (2018). Building a heading signal from anatomically defined neuron types in the *Drosophila* central complex. *Current Opinion in Neurobiology*, 52:156–164.

Habenstein, J., Amini, E., Grübel, K., el Jundi, B., and Rössler, W. (2020). The brain of *Cataglyphis* ants: Neuronal organization and visual projections. *Journal of Comparative Neurology*, 528(18):3479–3506.

Haferlach, T., Wessnitzer, J., Mangan, M., and Webb, B. (2007). Evolving a neural model of insect path integration. *Adaptive Behavior*, 15(3):273–287.

Hartmann, G. and Wehner, R. (1995). The ant's path integration system: a neural architecture. *Biological Cybernetics*, 73(6):483–497.

Heinze, S. (2015). Neuroethology: Unweaving the senses of direction. *Current Biology*, 25(21):R1034–R1037.

Heinze, S., Florman, J., Asokaraj, S., El Jundi, B., and Reppert, S. M. (2013). Anatomical basis of sun compass navigation II: The neuronal composition of the central complex of the monarch butterfly. *Journal of Comparative Neurology*, 521(2):267–298.

Heinze, S. and Homberg, U. (2007). Maplike representation of celestial e-vector orientations in the brain of an insect. *Science*, 315(5814):995–997.

Heinze, S. and Homberg, U. (2009). Linking the input to the output: new sets of neurons complement the polarization vision network in the locust central complex. *Journal of neuroscience*, 29(15):4911–21.

Heinze, S., Narendra, A., and Cheung, A. (2018). Principles of insect path integration. *Current Biology*, 28(17):R1043–R1058.

Homberg, U., Heinze, S., Pfeiffer, K., Kinoshita, M., and El Jundi, B. (2011). Central neural coding of sky polarization in insects. *Philosophical Transactions of the Royal Society B: Biological Sciences*, 366(1565):680–687.

Huber, R. and Knaden, M. (2015). Egocentric and geocentric navigation during extremely long foraging paths of desert ants. *Journal of Comparative Physiology A: Neuroethology, Sensory, Neural, and Behavioral Physiology*, 201(6):609–616.

Hulse, B. K., Haberkern, H., Franconville, R., Turner-Evans, D. B., Takemura, S.-y., Wolff, T., Noorman, M., Dreher, M., Dan, C., Parekh, R., et al. (2021). A connectome of the drosophila central complex reveals network motifs suitable for flexible navigation and context-dependent action selection. *eLife*, 10:e66039.

Hulse, B. K. and Jayaraman, V. (2020). Mechanisms underlying the neural computation of head direction. *Annual Review of Neuroscience*, 43:31–54.

Kakaria, K. S. and de Bivort, B. L. (2017). Ring attractor dynamics emerge from a spiking model of the entire protocerebral bridge. *Frontiers in Behavioral Neuroscience*, 11:8.

Kim, D. and Hallam, J. C. T. (2000). Neural network approach to path integration for homing navigation. In Meyer, A., Berthoz, A., Floreano, D., Roitblat, H., and Wilson, S. W., editors, *From Animals to Animats 6*, pages 228–235. MIT Press.

Kim, D. and Lee, J. (2011). Path integration mechanism with coarse coding of neurons. *Neural Processing Letters*, 34(3):277–291.

Kim, I. S. and Dickinson, M. H. (2017). Idiothetic path integration in the fruit fly *Drosophila melanogaster*. *Current Biology*, 27(15):2227–2238.

Kim, S. S., Rouault, H., Druckmann, S., and Jayaraman, V. (2017). Ring attractor dynamics in the *Drosophila* central brain. *Science*, 356(6340):849–853.

McNaughton, B. L., Barnes, C., Gerrard, J. L., Gothard, K., Jung, M. W., Knierim, J. J., Kudrimoti, H., Qin, Y., Skaggs, W. E., Suster, M., and Weaver, K. L. (1996). Deciphering the hippocampal polyglot: the hippocampus as a path integration system. *The Journal of experimental biology*, 199(1):173–185.

McNaughton, B. L., Battaglia, F. P., Jensen, O., Moser, E. I., and Moser, M.-B. (2006). Path integration and the neural basis of the 'cognitive map'. *Nature Reviews Neuroscience*, 7(8):663–678.

Menzel, R. and Muller, U. (1996). Learning and memory in honeybees: From behavior to neural substrates. *Annual Review of Neuroscience*, 19:379–404.

Mittelstaedt, H. (1985). Analytical cybernetics of spider navigation. In Barth, F. G., editor, *Neurobiology of Arachnids*, pages 298–316. Springer Berlin Heidelberg.

Müller, M. and Wehner, R. (1988). Path integration in desert ants, *Cataglyphis fortis*. *Proceedings of the National Academy of Sciences*, 85(14):5287–5290.

Pfeiffer, K. and Homberg, U. (2014). Organization and functional roles of the central complex in the insect brain. *Annual Review of Entomology*, 59(1):165–184.

Pfeiffer, P., Egorov, A. V., Lorenz, F., Schleimer, J.-h., Draguhn, A., and Schreiber, S. (2020). Clusters of cooperative ion channels enable a membrane-potential-based mechanism for short-term memory. *eLife*, 9:1–27.

Pisokas, I., Heinze, S., and Webb, B. (2020). The head direction circuit of two insect species. *eLife*, 9:e53985.

Pisokas, I., Rössler, W., Webb, B., Zeil, J., and Narendra, A. (2022). Anesthesia disrupts distance, but not direction, of path integration memory. *Current Biology*, 32(2):445–452.

Postlethwaite, M., Hennig, M. H., Steinert, J. R., Graham, B. P., and Forsythe, I. D. (2007). Acceleration of AMPA receptor kinetics underlies temperature-dependent changes in synaptic strength at the rat calyx of Held. *The Journal of Physiology*, 579(1):69–84.

Raji, J. I. and Potter, C. J. (2021). The number of neurons in *Drosophila* and mosquito brains. *PLoS ONE*, 16(5):e0250381.

Redish, A. D., Elga, A. N., and Touretzky, D. S. (1996). A coupled attractor model of the rodent head direction system. *Network: Computation in Neural Systems*, 7(4):671–685.

Rohrbough, J. and Broadie, K. (2002). Electrophysiological analysis of synaptic transmission in central neurons of *Drosophila* larvae. *Journal of Neurophysiology*, 88(2):847–860.

Samsonovich, A. and McNaughton, B. L. (1997). Path integration and cognitive mapping in a continuous attractor neural network model. *Journal of Neuroscience*, 17(15):5900–5920.

Seelig, J. D. and Jayaraman, V. (2015). Neural dynamics for landmark orientation and angular path integration. *Nature*, 521(7551):186–191.

Seung, H. S. (1996). How the brain keeps the eyes still. *Proceedings of the National Academy of Sciences of the United States of America*, 93(23):13339–44.

Sheeba, V., Gu, H., Sharma, V. K., O'Dowd, D. K., and Holmes, T. C. (2008). Circadian- and light-dependent regulation of resting membrane potential and spontaneous action potential firing of *Drosophila* circadian pacemaker neurons. *Journal of Neurophysiology*, 99(2):976–988.

Skaggs, W. E., Knierim, J. J., Kudrimoti, H. S., and McNaughton, B. L. (1995). A model of the neural basis of the rat's sense of direction. *Advances in neural information processing systems*, 7(1984):173–180.

Sommer, S. and Wehner, R. (2004). The ant's estimation of distance travelled: experiments with desert ants, *Cataglyphis fortis*. *Journal of Comparative Physiology A*, 190(1):1–6.

Stone, T., Webb, B., Adden, A., Weddig, N. B., Honkanen, A., Templin, R., Wcislo, W., Scimeca, L., Warrant, E., and Heinze, S. (2017). An anatomically constrained model for path integration in the bee brain. *Current Biology*, 27(20):3069–3085.

Su, T. S., Lee, W. J., Huang, Y. C., Wang, C. T., and Lo, C. C. (2017). Coupled symmetric and asymmetric circuits underlying spatial orientation in fruit flies. *Nature Communications*, 8(1):1–15.

Tang, L. S., Goeritz, M. L., Caplan, J. S., Taylor, A. L., Fisek, M., and Marder, E. (2010). Precise temperature compensation of phase in a rhythmic motor pattern. *PLoS Biology*, 8(8):e1000469.

Turner-Evans, D., Wegener, S., Rouault, H., Franconville, R., Wolff, T., Seelig, J. D., Druckmann, S., and Jayaraman, V. (2017). Angular velocity integration in a fly heading circuit. *eLife*, 6:2112–2126.

Turner-Evans, D. B. and Jayaraman, V. (2016). The insect central complex. *Current Biology*, 26(11):R453–R457.

Turner-Evans, D. B., Jensen, K. T., Ali, S., Paterson, T., Sheridan, A., Ray, R. P., Wolff, T., Lauritzen, J. S., Rubin, G. M., Bock, D. D., and Jayaraman, V. (2020). The neuroanatomical ultrastructure and function of a biological ring attractor. *Neuron*, 108(1):145–163.

Vickerstaff, R. J. and Cheung, A. (2010). Which coordinate system for modelling path integration? *Journal of Theoretical Biology*, 263(2):242–261.

Vickerstaff, R. J. and Di Paolo, E. A. (2005). Evolving neural models of path integration. *Journal of Experimental Biology*, 208(17):3349–3366.

Volgushev, M., Vidyasagar, T. R., Chistiakova, M., and Eysel, U. T. (2000). Synaptic transmission in the neocortex during reversible cooling. *Neuroscience*, 98(1):9–22.

von Frisch, K. (1967). *The dance language and orientation of bees*. Harvard University Press.

Webb, B. and Wystrach, A. (2016). Neural mechanisms of insect navigation. *Current Opinion in Insect Science*, 15:27–39.

Weir, P. T. and Dickinson, M. H. (2015). Functional divisions for visual processing in the central brain of flying *Drosophila*. *Proceedings of the National Academy of Sciences of the United States of America*, 112(40):E5523–E5532.

Wittmann, T. and Schwegler, H. (1995). Path integration — a network model. *Biological Cybernetics*, 73(6):569–575.

Wolff, T. and Rubin, G. M. (2018). Neuroarchitecture of the *Drosophila* central complex: A catalog of nodulus and asymmetrical body neurons and a revision of the protocerebral bridge catalog. *Journal of Comparative Neurology*, 526(16):2585–2611.

Zhang, K. (1996). Representation of spatial orientation by the intrinsic dynamics of the head-direction cell ensemble: a theory. *Journal of Neuroscience*, 16(6):2112–2126.

Ziegler, P. E. and Wehner, R. (1997). Time-courses of memory decay in vector-based and landmark-based systems of navigation in desert ants, *Cataglyphis fortis*. *Journal of Comparative Physiology A*, 181(1):13–20.

6

ANAESTHESIA DISRUPTS DISTANCE, BUT NOT DIRECTION, OF PATH INTEGRATION MEMORY

6.1 SUMMARY

Solitary foraging insects, such as ants, maintain an estimate of the direction and distance to their starting location as they move away from it, in a process known as path integration. This estimate, commonly known as the 'home vector', is updated continuously as the ant moves (Müller and Wehner, 1988; Menzel and Muller, 1996; Heinze et al., 2018; Collett, 2019) and is reset as soon as it enters its nest (Knaden and Wehner, 2005), yet ants prevented from returning to their nest can still use their home vector when released several hours later (Ziegler and Wehner, 1997; Cheng et al., 2005). This conjunction of fast update and long persistence of the home vector memory does not directly map to existing accounts of short-, mid-, and long-term memory (Giurfa and Sandoz, 2012; Müller, 2013; Menzel, 1999; Menzel and Muller, 1996; Dezazzo and Tully, 1995; Tully et al., 1994); hence, the substrate of this memory remains unknown. Chill-coma anaesthesia (Ebadi et al., 1980; Xia et al., 1998; Overgaard and MacMillan, 2016) has previously been shown to affect associative memory retention in fruit flies (Quinn and Dudai, 1976; Xia et al., 1998) and honeybees (Chen et al., 2014; Erber et al., 1980; Giurfa and Sandoz, 2012). We investigate the nature of path integration memory by anaesthetising ants after they have accumulated home vector information and testing if the memory persists on recovery. We show that after anaesthesia the memory of the distance ants have travelled is degraded, but the memory of the direction is retained. We also show that this is consistent with models of path integration that maintain the memory in a redundant Cartesian coordinate system and with the hypothesis that chill-coma produces a proportional reduction of the memory, rather than a subtractive reduction or increase of noise. The observed effect is not compatible with a memory based on recurrent circuit activity and points toward an activity-dependent molecular process as the basis of path integration memory.

6.2 RESULTS

6.2.1 *Cooling disrupts path integration memory*

In the absence of familiar terrestrial visual landmarks, ants rely on path integration for returning to their nest. The path integration memory is solely based on the information integrated during the latest foraging journey (Narendra et al., 2007) and is available to the ant when it attempts to return to its nest several hours later (Ziegler and Wehner, 1997). We sought to investigate the nature of the path integration memory using chill-coma anaesthesia (Ebadi et al., 1980; Xia et al., 1998; Overgaard and MacMillan, 2016). Chill-coma anaesthesia causes disruption of the ionic permeability of cellular membranes and loss of ion pump activity (MacMillan and Sinclair, 2011), resulting in depolarisation of membrane resting potential, reduction in action potential amplitude, and reduction in synaptic transmission (Weight and Erulkar, 1976; Erber et al., 1980; Burrows, 1989; MacMillan and Sinclair, 2011; Overgaard and MacMillan, 2016; Zhu and Cooper, 2018). We thus hypothesised that the effect of chill-coma anaesthesia on neural activity and synaptic transmission should disrupt any reverberating activity in recurrent circuitry, which has been hypothesised to underlie path integration memory in many models (Vickerstaff and Di Paolo, 2005; Haferlach et al., 2007; Kim and Lee, 2011; Goldschmidt et al., 2015; Webb and Wystrach, 2016; Stone et al., 2017; Goldschmidt et al., 2017; Samsonovich and McNaughton, 1997; Conklin and Eliasmith, 2005; McNaughton et al., 2006; Burak and Fiete, 2009).

We studied the Australian jack jumper ant *Myrmecia croslandi*. These ants establish distinct foraging corridors between their nest and a specific tree (Narendra et al., 2013a). We captured *Myrmecia croslandi* foragers 11 m away from their nest, as they were arriving at or descending from their foraging tree (referred to as 'full vector' ants to indicate that they had an intact home vector). The ants were given food, and half of them were anaesthetised by cooling to 0 °C for 30 min (chill-coma anaesthesia). Once the 'anaesthetised full vector' ants regained locomotion, we gave them sugar solution and prey, and released them individually in an unfamiliar location so that they could not use the visual surroundings to return to their nest. We also released full vector ants that were not anaesthetised but otherwise experienced the same handling; these ants should use their home vector to run toward their expected nest location. For comparison, we applied the same procedures (chill-coma anaesthesia, or equivalent handling without anaesthesia) to 'zero vector' ants, i.e., returning foragers collected at their nest. These ants would be expected to search for their nest around the release location (Wehner and Srinivasan, 1981; Müller and Wehner, 1994; Schultheiss et al., 2015, 2012).

Upon release at the unfamiliar location, non-anaesthetised full vector ants promptly ran directly toward the expected location of their nest (Figures 6.1A and 6.1B, first column). By contrast, anaesthetised full vector ants, upon recovery and release, perambulated more time within a 20 cm radius around the release point (Figures 6.1A and 6.1B, second column), had higher path sinuosity, and covered a smaller expected distance ($Emax_b$) than non-anaesthetised full vector ants (Figures 6.1C–6.1E and 6.1G; Mann–Whitney U test, $p < 0.05$; see also Figures 6.5A and 6.5B). This shows that anaesthetised ants were not able to utilise their home vector memory to walk back to their expected nest location.

To control for the possibility that this was due to impaired sensory or motor faculties, we also released anaesthetised full vector ants, after they recovered from anaesthesia, at a familiar place at the base of the tree where they had been captured. These anaesthesia-recovered ants readily walked straight back to their nest upon release, presumably using the familiar visual cues to navigate, illustrating that the observed effect was not due to impaired sensory or motor capacities caused by chill-coma anaesthesia (Figure 6.2). Furthermore, in comparable experiments done with *Cataglyphis velox*, we observed that anaesthetised full vector ants were able to path integrate newly travelled paths immediately after recovery from anaesthesia (see STAR Methods for details).

6.2.2 *Direction memory survives anaesthesia*

The heading directions of both non-anaesthetised full vector and anaesthetised full vector ants released at the unfamiliar location were not uniformly distributed (V-test for uniformity of circular data with expected homeward mean direction 100°; full vector ants, $n = 13$, $p < 0.001$; anaesthetised full vector ants, $n = 16$, $p < 0.001$). The mean heading angle of the anaesthetised full vector ants pointed toward the fictive nest location, as did the mean heading vector of the non-anaesthetised full vector ants (mean ± SD, 105° ± 72° and 97° ± 54°, respectively; Figure 6.1C, first and second column), and their difference was not statistically significant (Watson-Wheeler test, $p = 0.710$). The anaesthetised full vector ants walked, on average, a bit further from the release point toward the expected nest direction than the zero vector ants, although not as far as the full vector ants (Figures 6.1A and 6.5F). This tendency of anaesthetised full vector ants to walk toward their expected nest location implies that their home vector memory was not completely lost. Rather, information about the expected nest direction was preserved even though the spread of headings followed by the ants increased (Figure 6.1C).

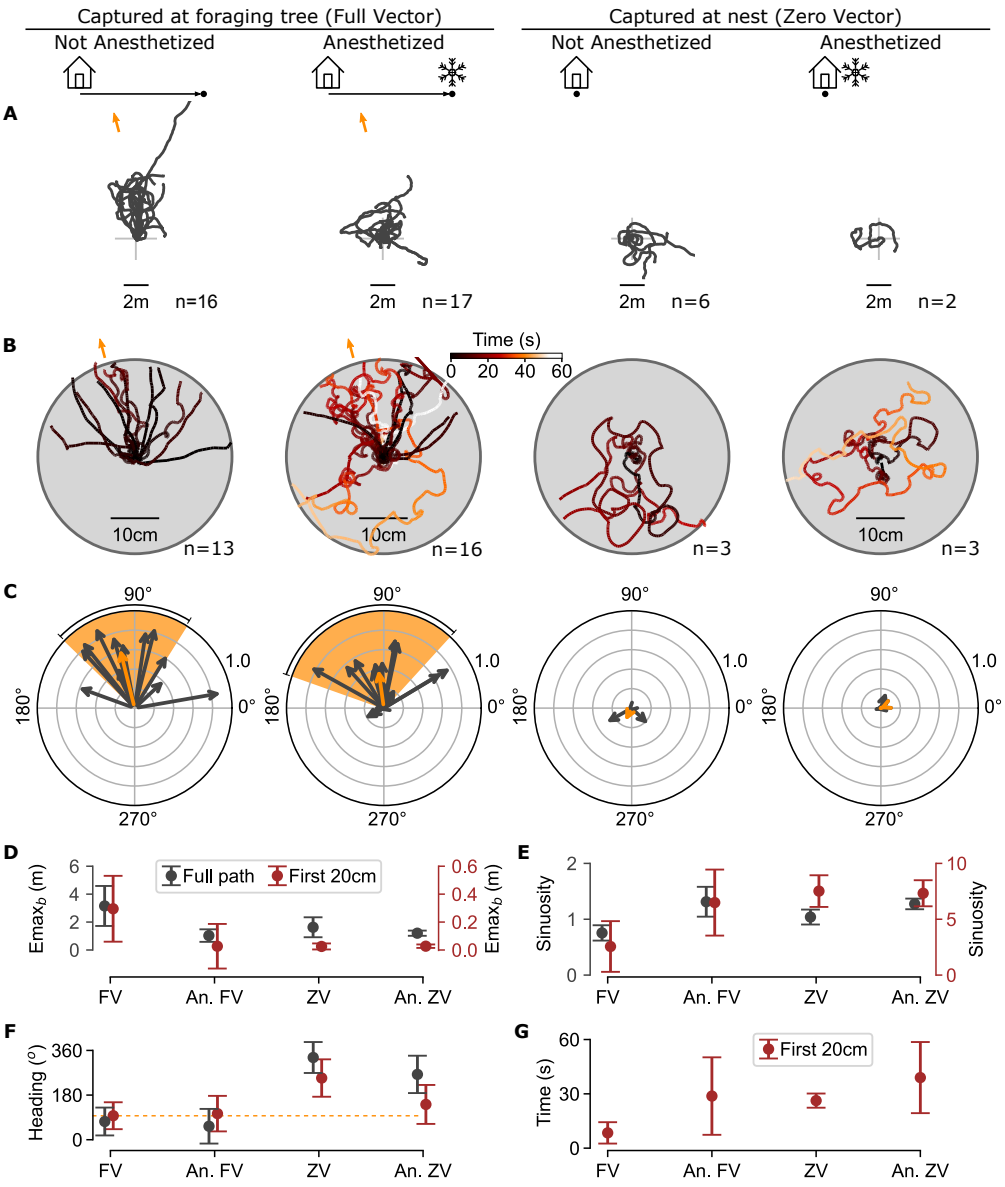

Figure 6.1: Paths of anaesthetised ants upon release differ in distance, but not direction. (**A**) Full paths marked with pins every 20 cm of trajectory length and subsequently traced using DGPS for the first 15 min after release or until ants started searching. Cross hairs indicate the release point and orange arrows the expected nest direction. *M. croslandi* typically follow their home vector only for half its length before searching for their nest (Narendra et al., 2013a). Sample sizes as shown (n = 16, n = 17, n = 6, and n = 2). (**B**) High-resolution camera recordings (25 fps) of the paths within a 20 cm radius from the release point, colour-coded by the time stamp. Orange arrows indicate the expected nest direction. Sample sizes as shown (n = 13, n = 16, n = 3, and n = 3). (**C**) Polar diagrams of the mean vector of each path (black) and the mean of mean vectors (orange). Sectors indicate the circular standard deviation of headings (shown only for the two conditions that are statistically significantly different from the uniform heading distribution). (**D**) Expected distance the ants moved away from

In contrast to anaesthetised full vector ants, zero vector ants (control ants captured at their nest) as expected exhibited no coherent general direction (Wehner and Srinivasan,

Figure 6.1 (cont.): the release point (calculated using the $Emax_b$ measure (Cheung et al., 2007)), shown for full vector (FV), anaesthetised full vector (An. FV), zero vector (ZV), and anaesthetised zero vector (An. ZV) ants. Bars show median ± SD, in black for trajectories in **A** and in red for those in **B**. (**E**) Median sinuosity of the paths. (**F**) Mean heading and circular standard deviation of the paths. The dashed orange line indicates the expected direction to the nest. (**G**) Time the ants took to reach a distance of 20 cm from the release point. See also Figure 6.5.

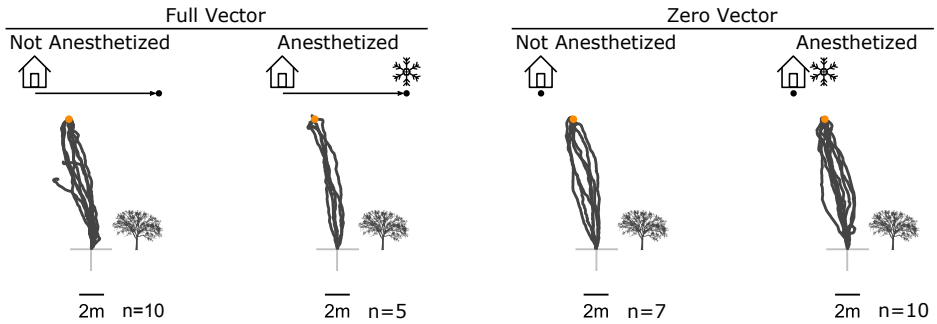

Figure 6.2: Regardless of condition, ants released at the familiar tree return to their nest successfully. *Myrmecia croslandi* ants released at a familiar place at the base of their foraging tree (cross hairs) head to their nest (orange disc) regardless of vector state or anaesthesia treatment.

1981; Müller and Wehner, 1994; Schultheiss et al., 2015, 2012) (Figure 6.1C, third and fourth column). This means that the preferred heading of anaesthetised full vector ants was not due to an inherent tendency of these ants to move toward a particular direction when they do not have path integration information. Further support that there were no attractive cues biasing the heading direction of the ants at the unfamiliar release location comes from the homing paths of full vector ants taken from different nests. As shown in Figures 6.5C and 6.5D, these ants travelled in different directions, according to their path integration state.

6.2.3 *Effects on distance and direction are consistent with Cartesian encoding of homing vector*

It might appear that the survival of direction, but not distance, memory in anaesthetised ants suggests that the two pieces of information are encoded by two independent memories with different sensitivity to the chill-coma manipulation. An obvious mechanism that would store the direction and distance components independently is a polar coordinate encoding of the home vector (Benhamou et al., 1990; Hartmann and Wehner, 1995). However, theoretical work has shown that a polar coordinate encoding would suffer from noise introduced during the position updating process while an allocentric Cartesian position representation is much more robust to such noise and

therefore the more likely encoding used by insects (Cheung and Vickerstaff, 2010; Vickerstaff and Cheung, 2010). Accordingly, several authors have proposed that the insect home vector is stored as a Cartesian vectorial representation with individual memory units storing the coordinate values along each corresponding cardinal axis (Wittmann and Schwegler, 1995; Kim and Hallam, 2000; Vickerstaff and Di Paolo, 2005; Haferlach et al., 2007; Stone et al., 2017) (Figure 6.3A).

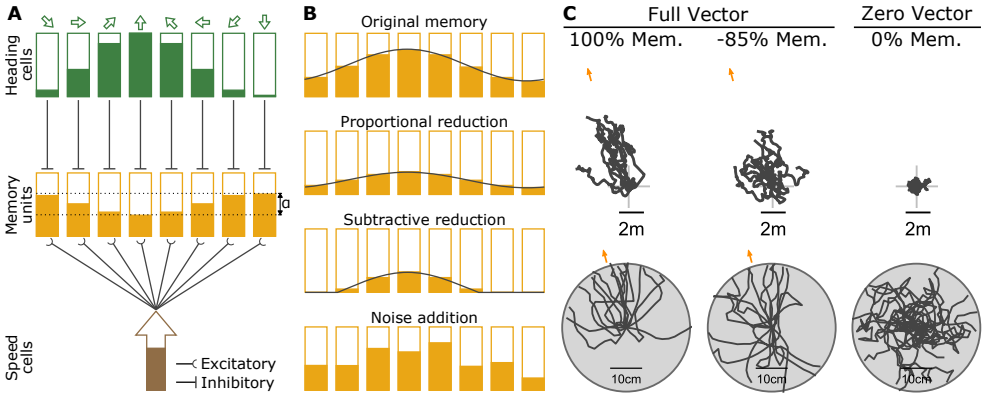

Figure 6.3: A Cartesian encoding model can reproduce the path characteristics of the ants. (**A**) Conceptual depiction of the path integration model with eight columns encoding each of the cardinal directions in a Cartesian coordinate system (Stone et al., 2017). Rectangular boxes represent cells and shaded portions the activity level or stored value. The inputs are the current insect heading (population coding with eight cardinal directions around the animal, i.e., E-PG neurons (Wolff and Rubin, 2018)) and the current insect speed (encoded as the spike rate of TN neurons (Stone et al., 2017)). Both the heading and speed neurons drive the eight speed integrating 'memory units'. The inhibitory heading signals mask the speed signal, so the lower the heading neuron activity, the more the speed signal is integrated by the corresponding memory unit. The memory unit values form a sinusoidal pattern encoding the distance from the origin in its amplitude (α) and the direction to the origin in the horizontal location of the minimum. (**B**) Illustration of different manipulations of the memory units: proportional manipulation reduces all eight memory values by a percentage from their initial values; subtractive manipulation reduces all memory values by a fixed amount; Gaussian noise addition stochastically changes each of the eight memory values. (**C**) Simulated agent paths upon release. Top: full paths. Bottom: paths within the first 20 cm from the release point. The first column shows paths of full vector agents, the second column full vector agents whose memory unit values have been reduced by 85% each, and the third column zero vector agents.

A Cartesian encoding is also supported by the existence of a columnar neural organisation in the central complex of the insect brain (Wolff and Rubin, 2018; Stone et al., 2017; Hulse and Jayaraman, 2020). Modelling has shown that this columnar organisation provides a neural basis for potentially storing the coordinate values along eight columns of neurons where each column represents a cardinal axis (Haferlach et al., 2007; Stone et al., 2017). In this scheme, the stored memory values in the eight columns form a sinusoidal pattern (Figure 6.3A). This encoding combines both pieces

of information as two aspects of the same memory, with the amplitude of the sinusoid encoding the distance the agent has travelled away from its origin and the location of the minimal memory value (column) corresponding to the direction the agent has mostly travelled away from its origin (Haferlach et al., 2007; Stone et al., 2017). When the agent is near its origin, the amplitude of the sinusoid is almost zero and does not provide a direction to move toward. As a result, a homing agent would move in a random pattern around the current location, resembling the search pattern observed in ants (Stone et al., 2017).

Since a reduced amplitude of the sinusoidal pattern of memory values would result in a less directed path, we hypothesised that chill-coma might be causing such a reduction of the memory values that results in the observed increased path sinuosity. Note that such a reduction should significantly affect the home vector length, which is encoded in the amplitude of the sinusoid, but could have less impact on the home vector direction, as this is encoded by the location of the minimum (Figure 6.3B). This would explain our observations that the anaesthetised ants preserve information about the home vector's direction, but the information about the distance they must walk to reach their nest is degraded.

6.2.4 *Proportional memory reduction best explains decline in homing ability*

We next investigated the kind of memory degradation effect that would reproduce the observed behaviour, assuming the Cartesian home vector encoding described in the previous section. We explored three types of memory manipulation: reduction proportional to each memory unit's value, reduction by subtraction of a fixed value from all memory units, and addition of noise to all memory units (Figure 6.3B).

Proportional reduction of memory unit values produced gradual degradation of the path characteristics as the amount of memory loss was increased. A memory reduction by around 85% of the original values produced the most similar path characteristics to those of the anaesthetised full vector ants (Figures 6.4A and 6.4D).

On the other hand, subtractive reduction of memory unit values caused an abrupt transition of the path characteristics as the amount of memory loss was increased (Figure 6.4B). Initially, no significant effect was produced on path characteristics; then, a steep deterioration was observed when the memory unit values lost their sinusoidal pattern because they started being clipped to the minimum of zero (Figure 6.3B). A second plateau was reached when the subtracted amount reduced all memory unit values to zero (Figure 6.4B). The amount of memory reduction required for the sinusoid to be clipped to zero depends on its initial amplitude, which depends on the distance the agent has travelled from its origin. However, the deterioration follows the

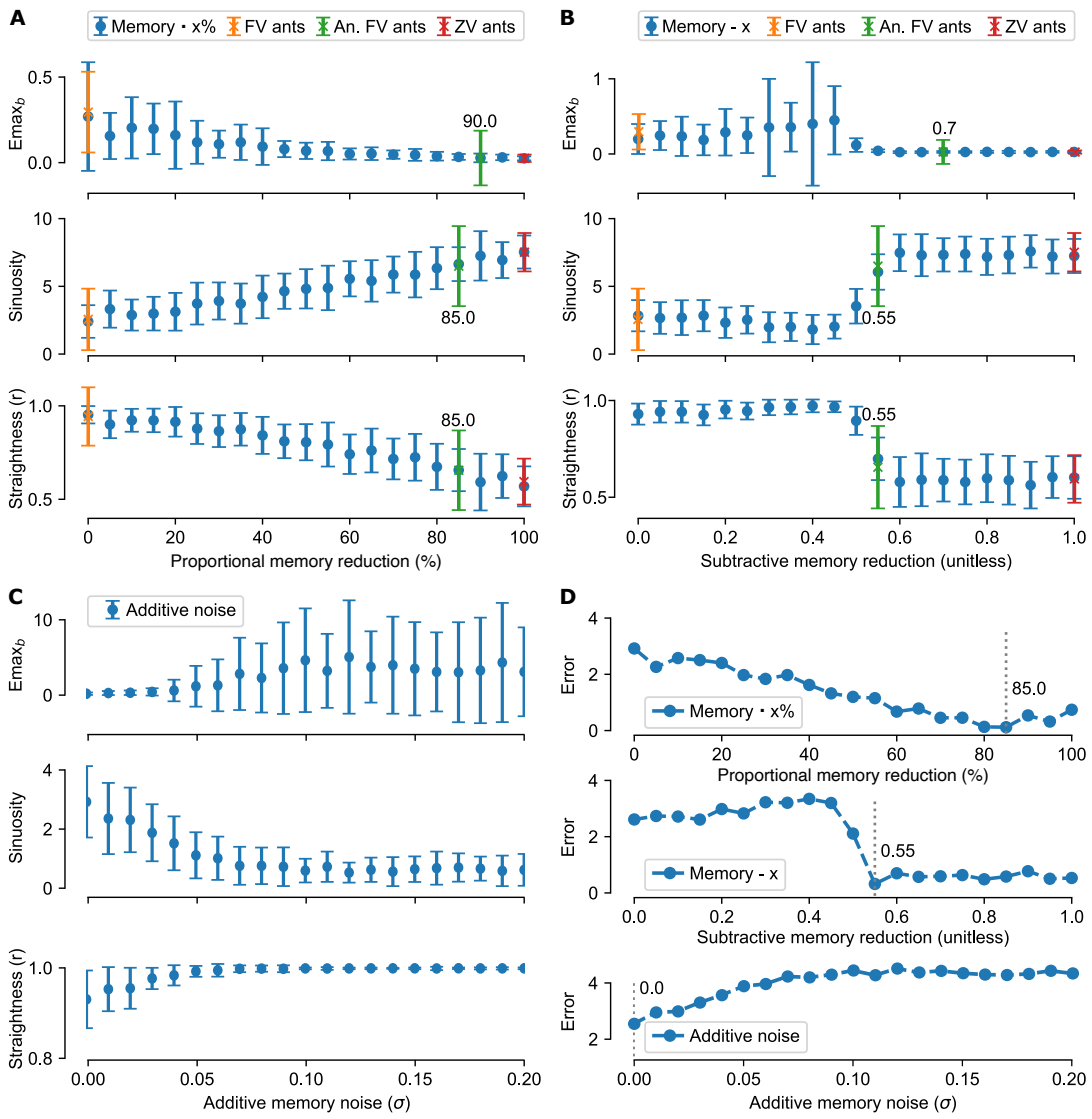

Figure 6.4: Effect of different memory manipulations on path characteristics. (**A–C**) Effect of the three different memory manipulations on simulated agent path characteristics ($Emax_b$, sinuosity, and mean vector length r as a measure of straightness). For each condition, 100 trials were simulated (bars show median ± SD). Ant path characteristic values are shown superimposed ('FV ants', 'An. FV ants', and 'ZV ants'). (**A**) Effect of proportional memory unit value reduction before simulated agent release for homing (Memory · x%). Proportional reduction causes gradual degradation of homing ability. An 80%–85% reduction results in the most similar path characteristics to anaesthetised full vector ants. (**B**) Effect of subtractive memory unit value reduction before simulated agent release for homing (Memory − x). Subtractive reduction results in sudden degradation of homing ability. (**C**) Effect of adding independent Gaussian noise on the memory unit values before simulated agent release for homing. Small noise levels do not affect homing, but once noise exceeds a threshold the agent veers in the wrong direction or overshoots the nest. This often results in straight paths toward random directions before turning again, and hence the path sinuosity drops while its straightness increases.

Figure 6.4 (cont.): This effect is the opposite of what we observe in the ant paths. (**D**) The overall path characteristics reproduction error for each of the three types of memory manipulation as the degree of reduction or noise is varied (calculated as the root mean squared error; see STAR Methods and Figure 6.6 for details). Vertical dotted grey lines indicate the memory manipulation that best matched the anaesthetised full vector ants' path characteristics. The proportional memory manipulation results in a better fit for a wider range of reduction values than the subtractive manipulation. See also Figure 6.6.

same pattern regardless of the exact initial amplitude. Our simulation results reveal that a precise amount of memory reduction is required in order to reproduce the path characteristics of anaesthetised ants when using the subtractive manipulation. This is because the required memory reduction lies on the steeply sloping region of path characteristics (Figures 6.4B and 6.4D). This is unlike proportional manipulation, which has a gradual slope and consequently a wider range of memory degradations that could reproduce path characteristics similar to those of anaesthetised full vector ants. If memory degradation occurs progressively with cooling duration as found by Erber et al. (1980), then it would be an unlikely serendipity that the ant cooling duration we used happened to match the precise amount of home vector deterioration required to reproduce the observed effect on path characteristics with the subtractive manipulation. On the other hand, our cooling duration is significantly longer than the ones used by Erber et al. (1980); the residual memory after prolonged cooling could be explained by the proportional state loss exhibited by leaky-integrator dynamics present in a wide range of physical processes that might underlie memory but would be difficult to explain in another way. We, therefore, consider a subtractive memory degradation to be a less plausible explanation of the observed behaviour.

We found that adding independent Gaussian noise to each memory unit's value before the simulated release of the agent did not produce an effect that would explain the ants' behaviour (Figure 6.4C). While the added noise remained low ($\sigma < 0.01$), no significant effect was observed in the homing path characteristics, but once noise exceeded the error tolerance of the memory, the agent veered straight in a noise-determined direction. This often resulted in straight paths toward random directions before the agent turned again. In effect, the overall measured path sinuosity dropped while the straightness increased as we increased the noise. This effect on path characteristics is the opposite of what we observed in the actual ant paths. Therefore, increased memory noise is not an adequate explanation of the effect of chill-coma.

6.3 DISCUSSION

We have used anaesthesia to investigate the type of memory employed for insect path integration. We found that even though ants have their home vector degraded when exposed to chill-coma anaesthesia, their paths maintain a statistically significant trend toward the correct homing direction. This suggests that the home vector memory is not completely lost. That is, the distance information is affected, but the direction remains. Interestingly, our findings resonate with the faster deterioration in homing distance accuracy than homing direction accuracy over time observed when ants are kept in captivity at ambient temperature (Ziegler and Wehner, 1997).

One possible interpretation of our results is that direction and distance are stored and maintained by different mechanisms in the insect brain. However, we showed that our results could be explained by a Cartesian encoding of the insect's position that combines both pieces of information as two aspects of the same memory, with the amplitude of the sinusoid encoding the distance and the location of the minimum encoding the direction. A proportional reduction of memory values resulted in smoother degradation of homing behaviour, which appears to be a better explanation than a subtractive memory reduction, which caused a sudden degradation of homing behaviour. Future experiments keeping the ants in chill-coma for different amounts of time would confirm whether the home vector memory is lost gradually with anaesthesia duration or abruptly.

In our experiments, we used behaviour as a proxy for elucidating what happens to memory. One might wonder whether the observed effect is due to a degraded ability to retrieve the memory rather than degradation of the memory itself. However, as we observed, the home vector direction of anaesthetised ants was not completely lost; these ants tended to move in the correct direction, which suggests that at least some of the home vector memory was still available and retrievable. Furthermore, in comparable experiments done on *Cataglyphis velox* ants, we observed that anaesthetised full vector ants regained their ability to path integrate newly travelled paths immediately after recovery from anaesthesia. This finding shows that the ants were able to both update and retrieve their home vector memory immediately after recovering from anaesthesia. This supports the conclusion that the cause of the observed behaviour is a degradation of the memory itself and not of the ability to retrieve it.

Previous models of path integration have speculated that the memory is maintained as reverberating activity in recurrent neural networks (Vickerstaff and Di Paolo, 2005; Haferlach et al., 2007; Kim and Lee, 2011; Goldschmidt et al., 2015; Webb and Wystrach, 2016; Stone et al., 2017; Goldschmidt et al., 2017). In the corresponding mammalian path integration literature in particular, it has been proposed that the memory is

maintained as the state of attractor networks (Samsonovich and McNaughton, 1997; Conklin and Eliasmith, 2005; McNaughton et al., 2006; Burak and Fiete, 2009). If the home vector memory were based on reverberating electrical activity, it would have been completely lost because ceasing electrical activity should interrupt the feedback loop that maintains the memory. On the other hand, if it were based on structural synaptic plasticity, it would have survived chill-coma. If, alternatively, the memory were maintained as a molecular concentration or process, we would have expected a smaller deterioration with cooling because molecular metabolism slows down with reduced temperature (Clarke and Fraser, 2004). The exact nature of the underlying memory remains elusive. Our working hypothesis is that it may be based on an activity-maintained molecular process such as neurotransmitter receptor mobility or synaptic facilitation, both of which involve CaMKII signalling pathways. Calcium influx can quickly induce an increase of CaMKII activity levels, which can be sustained for several hours through autophosphorylation, potentially enabling both quick change and long persistence of state (Lisman et al., 2012; Scholl et al., 2015). However, targeted pharmacological manipulations will be required for investigating these possibilities. It remains to be seen if the basis of the path integration memory is a variation of a known biophysical process or a yet undiscovered memory type specialised to the ecological needs of path integrating animals.

6.4 ACKNOWLEDGEMENTS

We would like to thank Chloé Raderschall, Franziska Schmitt, and Patrick Schultheiss for their support in carrying out behavioural experiments. We would also like to thank Michael Mangan for his invaluable advice and help with carrying out behavioural experiments. I.P. received funding from the University of Edinburgh and the Engineering and Physical Sciences Research Council (EP/M 008479/ 1), W.R. from DAAD Germany/Go8 Australia (Funding code: 56259154) and DFG (Ro1177/7-1), J.Z. and A.N. from the Australian Research Council (ARC) Centre of Excellence Scheme (CE0561903) and A.N. from an ARC Discovery Early Career Award (DE120100019).

6.4.1 *Author contributions*

All authors participated in the conceptual design of field experiments. I.P. participated in field experiments on *C. velox*, designed simulation experiments, did the modelling, implemented the code, analysed the data with input from B.W. and A.N., and wrote the first paper draft. All authors contributed to editing the paper. W.R., A.N., and J.Z.

participated in field experiments done on *Myrmecia* and discussions on experimental results and analyses.

6.4.2 *Declaration of interests*

The authors declare no competing interests.
Received: August 2, 2021
Revised: September 21, 2021
Accepted: November 15, 2021
Published: November 30, 2021

6.5 STAR METHODS

6.5.1 *Key Resources Table*

See Table 6.1.

6.5.2 *Resource Availability*

6.5.2.1 *Lead contact*

Further information and requests for resources and reagents should be directed to and will be fulfilled by the Lead Contact, Ioannis Pisokas.

6.5.2.2 *Materials availability*

This study did not generate any unique reagents.

6.5.2.3 *Data and code availability*

- Ant path data have been deposited at Zenodo and are publicly available as of the date of publication. DOIs are listed in the key resources table.
- All original code has been deposited at Zenodo and is publicly available as of the date of publication. DOIs are listed in the key resources table.
- Any additional information required to reanalyse the data reported in this paper is available from the lead contact upon request.

Table 6.1: Key Resources Table.

REAGENT or RESOURCE	SOURCE	IDENTIFIER
Deposited Data		
Raw and analysed data files	This paper	Zenodo: http://doi.org/10.5281/zenodo.5715964
Custom scripts for simulation and data processing	This paper	Zenodo: http://doi.org/10.5281/zenodo.5715964
Experimental Models: Organisms/Strains		
Myrmecia croslandi	Wild caught, Canberra, Australia	N/A
Cataglyphis velox	Wild caught, Seville, Spain	N/A
Software and Algorithms		
Python (3.7.9)	Python Software Foundation	https://www.python.org; RRID: SCR_008394
NumPy (1.16.6)	NumPy project community	https://numpy.org; RRID: SCR_008633
SciPy (1.2.3)	Virtanen et al. (2020)	https://scipy.org; RRID: SCR_008058
AstroPy (4.2.1)	Robitaille et al. (2013); Price-Whelan et al. (2018)	https://www.astropy.org; RRID: SCR_018148
MatPlotLib (3.3.3)	The Matplotlib development team	https://matplotlib.org; RRID: SCR_008624
R (4.0.3)	R Core Team	https://www.r-project.org; RRID: SCR_001905
trajr R library	McLean and Skowron Volponi (2018)	https://github.com/JimMcL/trajr
MATLAB (2020a)	Mathworks	http://www.mathworks.com; RRID: SCR_001622
MATLAB CircStats Toolbox (1.21.0.0)	Berens (2009)	https://github.com/circstat/circstat-matlab

6.5.3 *Experimental Model And Subject Details*

Animal experiments were performed with wild-type Australian jack jumper (*Myrmecia croslandi*) foragers (female) at ambient temperature in their natural environment.

6.5.4 *Method Details*

6.5.4.1 *Experimental protocol*

Australian jack jumper foragers, *Myrmecia croslandi* Taylor, were captured just outside their nest as they returned (zero vector ants) or at the base of their foraging tree 11 m south of their nest (full vector ants) in an urban park in Canberra, Australia (35°15.114′S, 149°9.555′E) in November and December 2013 and 2014. *M. croslandi* ants forage individually and there is no evidence for recruitment through trail pheromones or other interactions (Narendra et al., 2013a). The ants, once captured, were offered 10% sugar solution and insect prey, marked with paint, and randomly placed in experimental conditions. The experimental conditions were: captured at the nest ('zero vector'), captured at the foraging tree ('full vector'), captured at the nest and anaesthetised ('anaesthetised zero vector'), and captured at the foraging tree and anaesthetised ('anaesthetised full vector'). All ants were placed in individual foam-stoppered Perspex tubes (10 cm long, 4 cm wide) and kept in darkness for 40 minutes. For inducing anaesthesia, the ants in tubes were placed in melting ice (temperature 0 °C) for the first 30 minutes and then at ambient temperature for the remaining 10 minutes. Non-anaesthetised ants were kept at ambient temperature for the whole 40 minutes period. The ambient temperature during the experiments was 23 °C to 33 °C.

With preceding experiments, we established that as it has been reported in *Drosophila melanogaster*, the ants were immobilised soon after the tubes were immersed in the melting ice (Krashes and Waddell, 2008). We kept the ants in chill-coma for 30 minutes that far exceeds the required time in order to reduce the significance of variations between individuals. Similar to *Drosophila melanogaster*, ants regained mobility shortly after return to ambient temperature. We allowed them to acclimatise at ambient temperature for 10 minutes to ensure they had recovered from anaesthesia.

6.5.4.2 *Ant manipulation*

All ants were offered food (10% sugar solution and prey) and released individually at an adjacent sports field, 100 m east of their nest, an unfamiliar location which ants from this nest had never visited. When a familiar visual panorama is unavailable, *M. croslandi* ants resort to using path integration to return to their nest (Narendra et al., 2013a). The ants were transported individually in foam-stoppered Perspex tubes that were placed in black nylon sleeves. The ants were released at the centre of a 40 cm diameter wooden platform, raised 15 cm off the ground, and levelled using a spirit level. The Perspex tube with the ant fitted tightly in a circular hole at the centre of the

platform. The foam stopper was replaced with a piece of cardboard that had a hole of 5 mm in diameter for ants to exit the tube and reach the top of the platform.

We recorded the paths of the ants on the platform around the release point (20 cm radius) with a video camera at 25 frames per second, offering a high-resolution recording of movement. Once the ants left the platform, we marked the remainder of their paths with pins, carefully avoiding disturbing the ants, and subsequently recorded the pin trails using differential GPS (Narendra et al., 2013a,b). Released ants were caught again once 15 minutes had passed from release or once they started searching for their nest, in the case of full vector ants. Each ant's position over time was extracted from the video recording for the first 20 cm radius around the release point and from the differential GPS recording for the rest of the path.

6.5.4.3 *Ants can path integrate after anaesthesia*

A similar experimental procedure was followed with *Cataglyphis velox* Santschi ants in Seville, Spain, in June 2018. In these experiments, the ants were kept in darkness for 45 minutes. For the first 30 minutes, the anaesthetised ants were placed in melting ice and for the following 15 minutes at ambient temperature. The non-anaesthetised ants were kept at ambient temperature for the whole period. All ants were released individually at an unfamiliar location, where we had set up a 6 m $\times$ 8 m grid over a region that was previously cleared of vegetation. These paths were recorded by hand on graph paper. Similar to *M. croslandi*, *C. velox* ants are also solitary foragers. These ants also resort to using their path integrator in order to head toward their fictive nest when in an unfamiliar visual surrounding (Mangan and Webb, 2012).

An additional experiment was performed with these ants for testing whether they can path integrate immediately after chill-coma anaesthesia. We recaptured the full vector anaesthetised ants after their initial release at the unfamiliar location. They were then released individually next to the feeder within 6 minutes from the first release. In response, these ants promptly run to their nest, presumably navigating using the familiar views surrounding the area near their nest. We recaptured these ants just before entering their nest hole. We then released them once more individually at the unfamiliar location. Upon release, they run back toward the direction where the feeder would have been in respect to their nest (Figure 6.5E). This is what we would expect by a path integrating ant (Andel and Wehner, 2004). This last experiment illustrated that these ants had accumulated a new home vector as they walked from the feeder to their nest, and they used this new home vector to run in the direction of the feeder (their new origin) upon this last release. Since they were able to do this a few minutes after regaining locomotion, we conclude that the ants were capable of path integrating after recovery from anaesthesia.

Tested ants were not culled and were allowed to return to their nest but they were marked with paint so they were not tested again. These previously anaesthetised and tested ants were seen exiting their nest and foraging the following days (unpublished data). This fact also indicates that anaesthesia did not cause any observable long-term damage to their motivation and ability to forage.

6.5.4.4 *Model parameters*

Our model source code is based on previous work (Stone et al., 2017) that we extended. That original model (Stone et al., 2017) utilised a fixed noise level introduced as additive Gaussian noise on the neural activation functions, but that noise model does not reproduce the path characteristics of actual ants. We found that to reproduce the path characteristics of ants, additional motor noise that is parametric to the home vector length must be introduced. This motor noise was modelled as a Gaussian noise factor applied to the steering commands of the agent.

$$steering = steering\_command \cdot \epsilon \tag{6.1}$$

where *steering_command* is the steering command generated by the path integration model in homing mode, *steering* is the actual agent steering, and $\epsilon \sim \mathcal{N}(\mu, \sigma^2)$ is a random variable sampled from the Gaussian distribution with $\mu = 1$ and σ set to the motor noise level. The motor noise level was modelled as a decaying exponential function of the memory amplitude (Figure 6.7). The memory amplitude is defined as the difference between the maximum and minimum value along the sinusoidal pattern of memory unit values (Figure 6.7 inset).

$$Motor\ noise = \frac{y_{max}}{e^{s \cdot x}} \tag{6.2}$$

where x is the memory amplitude, y_{max} is the maximum motor noise level (corresponding to zero vector ant paths), and s is the slope of the exponential function.

The translational velocity of the simulated agents during homing was iteratively updated using the formula

$$v(t) = \begin{cases} v(t-1) + a\Delta t - \mu_f v(t-1), & \text{if } |steering| \leq 20^o \\ v(t) = 0, & \text{if } |steering| > 20^o \end{cases} \tag{6.3}$$

where $v(t)$ is the agent's velocity at time step t, $a = 0.08\,\mathrm{m/s^2}$ is an acceleration constant, Δt is the simulated time step duration, and $\mu_f = 0.15$ is a friction constant. The velocity was reset to $0\,\mathrm{m/s}$ whenever the agent performed a turn larger than 20° because we observed in the video recordings that ants typically slowed down to a

stand-still when performing such turns (data not shown). This formulation produced a speed profile approximating the speed dynamics of the recorded ants.

We set the neural activation function noise to $\sigma = 0.01$ and used grid search to find the combination of maximum motor noise level (y_{max}) and slope (s) of the decaying exponential that produces simulated paths with similar characteristics to ant paths ($Emax_b$, sinuosity, and resultant vector length) of both zero vector (zero memory amplitude) and full vector ants. The deviation from the required path characteristics values for the search space of parameters (maximum motor noise and exponential function slope, Equation 6.2) is shown in Figure 6.8. The combination of maximum motor noise $y_{max} = 7$ and exponential function slope $s = 9$ resulted in the best match to the ant path characteristics (full vector and zero vector ant paths) and was used in the simulations.

The simulated homing paths were cut at 600 steps, resulting in the closest approximation to the recording cut off points of the ant data (15 minutes from release or until ants started searching for their nest).

6.5.4.5 *Simulated memory manipulation*

The simulations had two stages, an outbound trip and a homing trip. For generating the outbound trip, the agent started from a designated nest location and moved following a path generated by a filtered (smoothed) noise process, as previously described (Stone et al., 2017), until it reached a designated food location. Outbound agent simulations that did not result in the agent reaching the designated food location after 1500 simulation steps were disregarded. During the outbound trip, a home vector was accumulated. Subsequently, the accumulated home vector memory was manipulated, and the simulation continued (simulated release) in homing mode. In the work presented here, we compared the homing path characteristics with those of the ants.

The memory was manipulated in three different ways before the simulated agent release: proportional value reduction, subtractive value reduction, or addition of independent Gaussian noise. In the case of the Gaussian noise, each memory unit's value was modified by adding a value drawn from the Gaussian distribution $\mathcal{N}(0, \sigma)$.

In neither the outbound nor the homing part of the simulations, we used visual landmark cues; thus, path integration was the sole navigation mechanism used. The inputs to the path integration model were the allocentric orientation of the agent and the speed of the agent's motion (Figure 6.3A).

6.5.5 *Quantification And Statistical Analysis*

6.5.5.1 *Statistical analysis*

The ant paths were discretised at 10 cm steps for the full path recordings (recorded using DGPS) and 2 cm steps for the first 20 cm radius from the release point (recorded at 25 frames per second using a camera). The same discretisation step lengths were used for the simulated agent paths after scaling the paths by multiplying their spatial coordinates by 0.03. We quantified the path characteristics using the path sinuosity (Benhamou, 2004), the mean vector length r (Batschelet, 1981), and $Emax_b$ (Cheung et al., 2007). For the analysis of the path characteristics, we used the trajr R library (McLean and Skowron Volponi, 2018). For the statistical analysis, we used the Python SciPy and Astropy libraries when possible, and the MATLAB CircStats toolbox for double-checking results and when no equivalent function existed in the Python libraries.

The $Emax_b$ index of path straightness is a measure of the maximum expected displacement of the animals from the release point, with larger values indicating straighter paths (Cheung et al., 2007). For Figure 6.5F the values were calculated with the compass direction set to 100° (heading to the expected nest location in respect to the release point). For all other cases the values were calculated without assuming directed walks.

Statistics are reported in the results and the figure legends when appropriate. Sample sizes were not estimated in advance, and the number of animals in each condition (n) is shown in the corresponding figures and figure legends. Animals were randomly assigned to experimental groups. We used the non-parametric Mann–Whitney U test for distribution equality, the V-test for circular uniformity, and the non-parametric Watson-Wheeler test for circular means difference. The p values are reported for all the statistical significance tests. All bar plots show median±SD unless stated otherwise.

6.5.5.2 *Model match to data calculation*

For producing each of the error plots in Figure 6.4D, we first calculated the differences (errors) of the anaesthetised ants' median $Emax_b$, sinuosity, and straightness (mean vector length r) values from the corresponding median values of 100 simulations for each memory manipulation type (proportional, subtractive, additive noise) and magnitude (Figure 6.6 top three rows). Then for each memory manipulation type and magnitude, the root mean squared error of the three corresponding error values was calculated (Figure 6.6 bottom row).

6.6 SUPPLEMENTAL INFORMATION

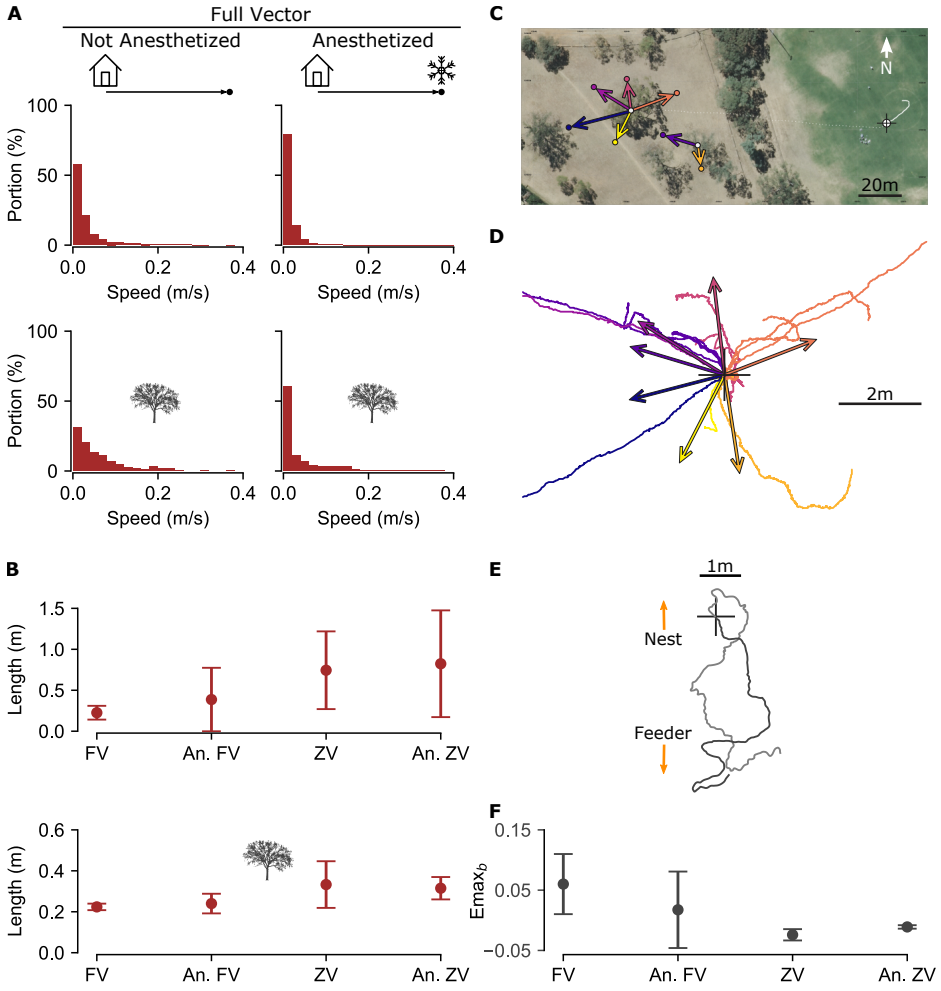

Figure 6.5: Speed, path length, and behavioural controls. Related to Figure 6.1. (**A**) Histograms of speed distribution of *Myrmecia croslandi* ants released at an unfamiliar place (top row, same data as in Figure 6.1B) or at the familiar tree (bottom row). The speed was calculated at 40 ms intervals along the paths within a 20 cm radius from the release point. The total height of the bars in each histogram is 100%. Ants released at the familiar location moved faster. Anaesthetised ants paused more and tended to move slower than non-anaesthetised ones. (**B**) Path lengths of *M. croslandi* ants released at an unfamiliar place (top plot; same data as in Figure 6.1B; FV n=13, An. FV n=16, ZV n=3, An. ZV n=3) and at the familiar tree (bottom plot; FV n=8, An. FV n=7, ZV n=6, An. ZV n=9). The path lengths were calculated within a 20 cm radius from the release point until the ants exited this area (bars show median ± SD). The path lengths of non-anaesthetised ants within the 20 cm radius from the release point were smaller. The difference between conditions was larger for ants released at the unfamiliar location. This is possibly because at the familiar location the visual surroundings provided contextual information about the nest's location.

Figure 6.5 (cont.): (**C**–**D**) *M. croslandi* foragers from multiple nests rely on path integration when displaced to an unfamiliar location. Data reproduced with permission from Narendra et al. (2013a). (**C**) *M. croslandi* forager ants from seven different nests were captured when they arrived at the base of their respective foraging tree (two white circles in the aerial photo). Each nest is indicated with a circle of different colour, and nest-specific coloured arrows point from the capture point (white circles) to the true nest location (coloured circles). Once captured, ants were transferred (dotted white line) in dark vials and released at an unfamiliar location (white circle with cross hairs on the right end of the aerial photo). An example path of a released ant is shown with the white trace. (**D**) Paths of the full vector ants upon release at the unfamiliar place (n = 12). All ants were released individually at the same location, indicated with the cross hairs. Path colours correspond to each ant's nest of origin, and coloured arrows indicate the expected direction to each nest. Colours correspond to the colours in panel (**C**). (**E**) Ants can path integrate upon recovery from anaesthesia. Anaesthetised full vector *Cataglyphis velox* ants released after they navigated from a familiar place to their nest using visual navigation had accumulated a new 'home' vector pointing them away from their nest. Two example paths are shown. Cross hairs indicate the release point, and arrows the direction to the nest and the feeder. (**F**) $Emax_b$ as a measure of how far *M. croslandi* foragers advance in the fictive nest direction when released at the unfamiliar site ($Emax_b$ was calculated with an expected compass direction of 100° as described in STAR Methods; medians±SD; same paths as in Figure 6.1A; sample sizes n=16, n=17, n=6, and n=2; An. FV statistically significantly different from FV and ZV, Mann–Whitney U test $p<0.05$).

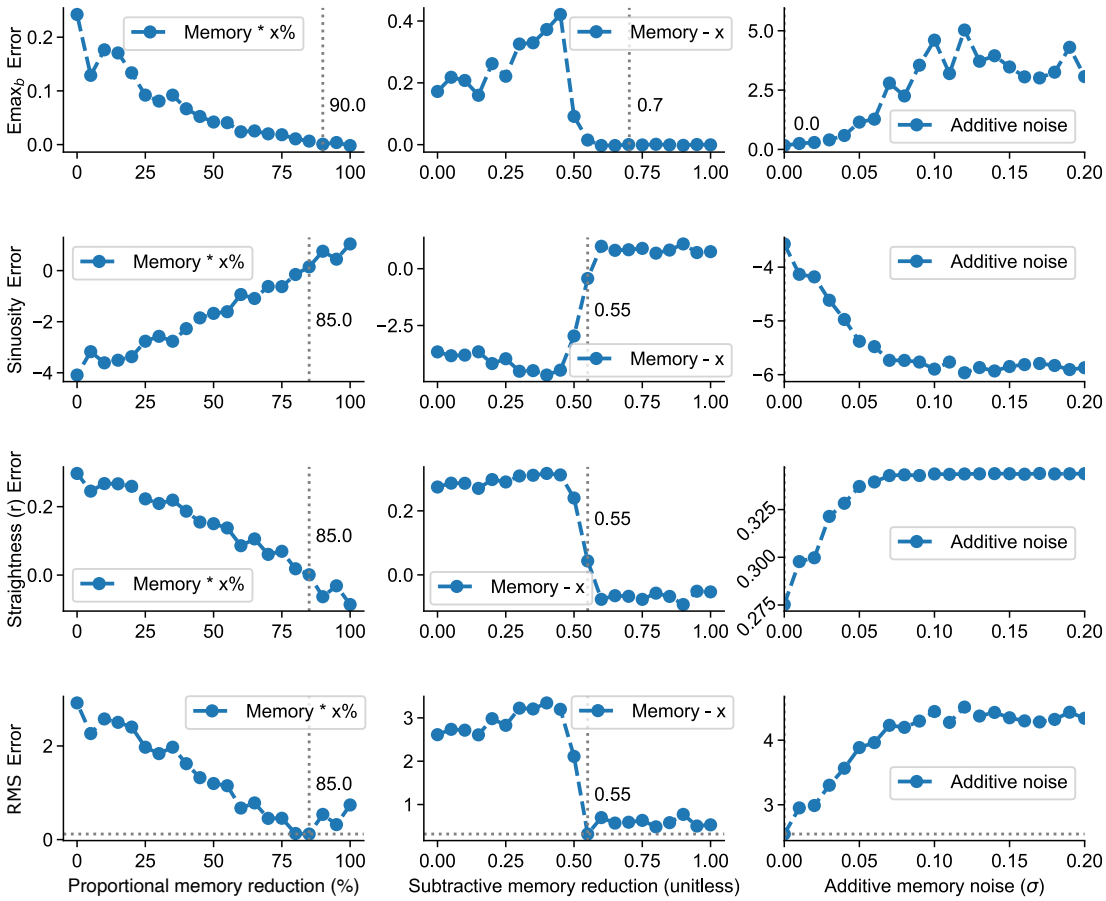

Figure 6.6: Differences in path characteristics between simulated and anaesthetised ants. Related to Figure 6.4. Differences between the simulated path characteristics and the anaesthetised full vector ants' path characteristics for the different types and amounts of memory manipulation. The overall error (bottom row of panels) for each memory manipulation type and amount was calculated as the root mean squared error of the corresponding Emax$_b$, sinuosity, and straightness (mean vector length r) errors. The dotted vertical grey lines indicate the memory manipulation amount that resulted in the smallest absolute difference from the anaesthetised full vector ants' path characteristics.

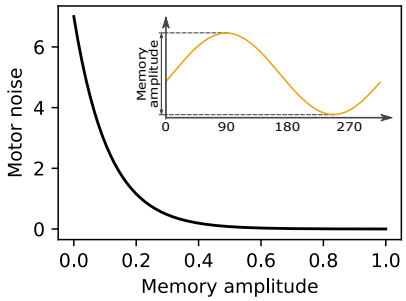

Figure 6.7: Motor noise model. Related to STAR Methods. The motor noise was parameterised as a function of the memory amplitude.

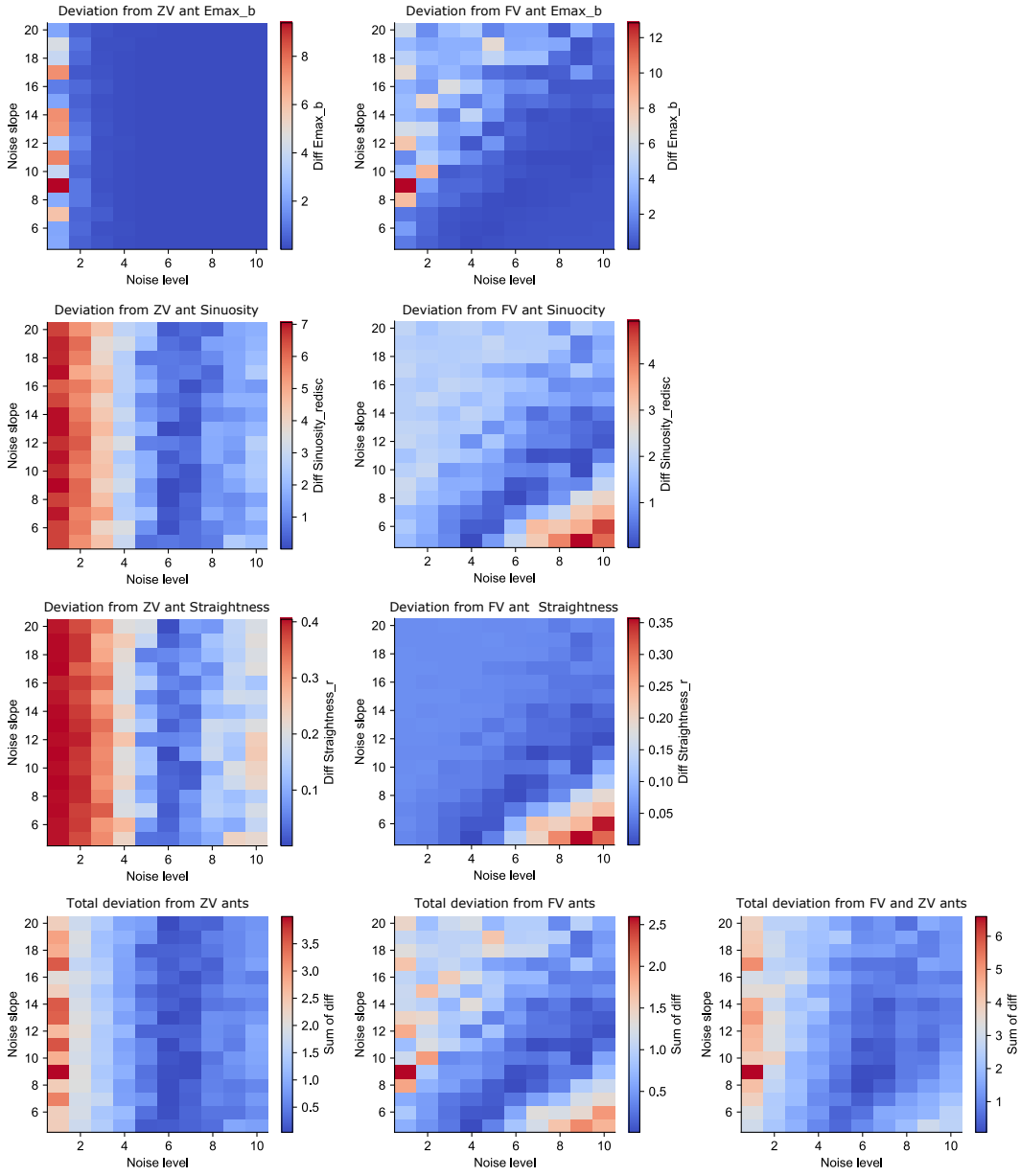

Figure 6.8: Parameters optimisation grid search. Related to STAR Methods. Grid search for the minimum deviation from zero vector (ZV) and full vector (FV) ant path characteristics. The optimum maximum motor noise (y_{max}) and noise function slope (s) are those resulting in the minimum deviation from the ants' path characteristics (dark blue). A larger range of values than the depicted was searched; the figure only shows the search space segment where the best matching combinations were found.

BIBLIOGRAPHY

Andel, D. and Wehner, R. (2004). Path integration in desert ants, *Cataglyphis*: How to make a homing ant run away from home. *Proceedings of the Royal Society B: Biological Sciences*, 271(1547):1485–1489.

Batschelet, E. (1981). *Circular statistics in biology*. New York: Academic Press.

Benhamou, S. (2004). How to reliably estimate the tortuosity of an animal's path: Straightness, sinuosity, or fractal dimension? *Journal of Theoretical Biology*, 229(2):209–220.

Benhamou, S., Sauvé, J.-P., and Bovet, P. (1990). Spatial memory in large scale movements: Efficiency and limitation of the egocentric coding process. *Journal of Theoretical Biology*, 145(1):1–12.

Berens, P. (2009). CircStat: A MATLAB toolbox for circular statistics. *Journal of Statistical Software*, 31(10).

Burak, Y. and Fiete, I. R. (2009). Accurate path integration in continuous attractor network models of grid cells. *PLoS Computational Biology*, 5(2):e1000291.

Burrows, M. (1989). Effects of temperature on a central synapse between identified motor neurons in the locust. *Journal of Comparative Physiology A*, 165(5):687–695.

Chen, Y.-M., Fu, Y., He, J., and Wang, J.-H. (2014). Effects of cold narcosis on memory acquisition, consolidation and retrieval in honeybees (*Apis mellifera*). *Zoological Research*, 35(2):118–123.

Cheng, K., Narendra, A., and Wehner, R. (2005). Behavioral ecology of odometric memories in desert ants: Acquisition, retention, and integration. *Behavioral Ecology*, 17(2):227–235.

Cheung, A. and Vickerstaff, R. (2010). Finding the way with a noisy brain. *PLoS Computational Biology*, 6(11):e1000992.

Cheung, A., Zhang, S., Stricker, C., and Srinivasan, M. V. (2007). Animal navigation: The difficulty of moving in a straight line. *Biological Cybernetics*, 97(1):47–61.

Clarke, A. and Fraser, K. P. P. (2004). Why does metabolism scale with temperature? *Functional Ecology*, 18(2):243–251.

Collett, T. S. (2019). Path integration: how details of the honeybee waggle dance and the foraging strategies of desert ants might help in understanding its mechanisms. *Journal of Experimental Biology*, 222(11):jeb205187.

Conklin, J. and Eliasmith, C. (2005). A controlled attractor network model of path integration in the rat. *Journal of Computational Neuroscience*, 18(2):183–203.

Dezazzo, J. and Tully, T. (1995). Dissection of memory formation: from behavioral pharmacology to molecular genetics. *Trends in Neurosciences*, 18(5):212–218.

Ebadi, R., Gary, N. E., and Lorenzen, K. (1980). Effects of carbon dioxide and low temperature narcosis on honey bees, *Apis mellifera*. *Environmental Entomology*, 9(1):144–150.

Erber, J., Masuhr, T., and Menzel, R. (1980). Localization of short-term memory in the brain of the bee, *Apis mellifera*. *Physiological Entomology*, 5(4):343–358.

Giurfa, M. and Sandoz, J. C. (2012). Invertebrate learning and memory: Fifty years of olfactory conditioning of the proboscis extension response in honeybees. *Learning and Memory*, 19(2):54–66.

Goldschmidt, D., Dasgupta, S., Wörgötter, F., and Manoonpong, P. (2015). A neural path integration mechanism for adaptive vector navigation in autonomous agents. In *Proceedings of the International Joint Conference on Neural Networks (IJCNN)*, pages 1–8.

Goldschmidt, D., Manoonpong, P., and Dasgupta, S. (2017). A neurocomputational model of goal-directed navigation in insect-inspired artificial agents. *Frontiers in Neurorobotics*, 11:1–17.

Haferlach, T., Wessnitzer, J., Mangan, M., and Webb, B. (2007). Evolving a neural model of insect path integration. *Adaptive Behavior*, 15(3):273–287.

Hartmann, G. and Wehner, R. (1995). The ant's path integration system: a neural architecture. *Biological Cybernetics*, 73(6):483–497.

Heinze, S., Narendra, A., and Cheung, A. (2018). Principles of insect path integration. *Current Biology*, 28(17):R1043–R1058.

Hulse, B. K. and Jayaraman, V. (2020). Mechanisms underlying the neural computation of head direction. *Annual Review of Neuroscience*, 43:31–54.

Kim, D. and Hallam, J. C. T. (2000). Neural network approach to path integration for homing navigation. In Meyer, A., Berthoz, A., Floreano, D., Roitblat, H., and Wilson, S. W., editors, *From Animals to Animats 6*, pages 228–235. MIT Press.

Kim, D. and Lee, J. (2011). Path integration mechanism with coarse coding of neurons. *Neural Processing Letters*, 34(3):277–291.

Knaden, M. and Wehner, R. (2005). Ant navigation: resetting the path integrator. *Journal of Experimental Biology*, 209(1):26–31.

Krashes, M. J. and Waddell, S. (2008). Rapid consolidation to a radish and protein synthesis-dependent long-term memory after single-session appetitive olfactory conditioning in *Drosophila*. *Journal of Neuroscience*, 28(12):3103–3113.

Lisman, J., Yasuda, R., and Raghavachari, S. (2012). Mechanisms of CaMKII action in long-term potentiation. *Nature Reviews Neuroscience*, 13(3):169–182.

MacMillan, H. A. and Sinclair, B. J. (2011). Mechanisms underlying insect chill-coma. *Journal of Insect Physiology*, 57(1):12–20.

Mangan, M. and Webb, B. (2012). Spontaneous formation of multiple routes in individual desert ants (*Cataglyphis velox*). *Behavioral Ecology*, 23(5):944–954.

McLean, D. J. and Skowron Volponi, M. A. (2018). trajr: An R package for characterisation of animal trajectories. *Ethology*, 124(6):440–448.

McNaughton, B. L., Battaglia, F. P., Jensen, O., Moser, E. I., and Moser, M.-B. (2006). Path integration and the neural basis of the 'cognitive map'. *Nature Reviews Neuroscience*, 7(8):663–678.

Menzel, R. (1999). Memory dynamics in the honeybee. *Journal of Comparative Physiology A*, 185(4):323–340.

Menzel, R. and Muller, U. (1996). Learning and memory in honeybees: From behavior to neural substrates. *Annual Review of Neuroscience*, 19:379–404.

Müller, M. and Wehner, R. (1988). Path integration in desert ants, *Cataglyphis fortis*. *Proceedings of the National Academy of Sciences*, 85(14):5287–5290.

Müller, M. and Wehner, R. (1994). The hidden spiral: systematic search and path integration in desert ants, *Cataglyphis fortis*. *Journal of Comparative Physiology A*, 175(5):525–530.

Müller, U. (2013). Chapter 31 - Memory phases and signaling cascades in honeybees. In Menzel, R. and Benjamin, P. R., editors, *Handbook of Behavioral Neuroscience*, volume 22, pages 433–441. Elsevier.

Narendra, A., Cheng, K., and Wehner, R. (2007). Acquiring, retaining and integrating memories of the outbound distance in the Australian desert ant *Melophorus bagoti*. *Journal of Experimental Biology*, 210(4):570–577.

Narendra, A., Gourmaud, S., and Zeil, J. (2013a). Mapping the navigational knowledge of individually foraging ants, *Myrmecia croslandi*. *Proceedings of the Royal Society B: Biological Sciences*, 280(1765):20130683.

Narendra, A., Reid, S. F., and Raderschall, C. A. (2013b). Navigational efficiency of nocturnal *Myrmecia* ants suffers at low light levels. *PLoS ONE*, 8(3):e58801.

Overgaard, J. and MacMillan, H. A. (2016). The integrative physiology of insect chill tolerance. *Annual Review of Physiology*, 79(1):187–208.

Price-Whelan, A. M., Sipőcz, B. M., Günther, H. M., Lim, P. L., et al. (2018). The Astropy project: Building an open-science project and status of the v2.0 core package. *The Astronomical Journal*, 156(3):123.

Quinn, W. G. and Dudai, Y. (1976). Memory phases in *Drosophila*. *Nature*, 262(5569):576–577.

Robitaille, T. P., Tollerud, E. J., Greenfield, P., Droettboom, M., et al. (2013). Astropy: A community Python package for astronomy. *Astronomy and Astrophysics*, 558:1–9.

Samsonovich, A. and McNaughton, B. L. (1997). Path integration and cognitive mapping in a continuous attractor neural network model. *Journal of Neuroscience*, 17(15):5900–5920.

Scholl, C., Kübert, N., Muenz, T. S., and Rössler, W. (2015). CaMKII knockdown affects both early and late phases of olfactory long-term memory in the honeybee. *Journal of Experimental Biology*, 218(23):3788–3796.

Schultheiss, P., Cheng, K., and Reynolds, A. M. (2015). Searching behavior in social hymenoptera. *Learning and Motivation*, 50:59–67.

Schultheiss, P., Wystrach, A., Legge, E. L. G., and Cheng, K. (2012). Information content of visual scenes influences systematic search of desert ants. *Journal of Experimental Biology*, 216(4):742–749.

Stone, T., Webb, B., Adden, A., Weddig, N. B., Honkanen, A., Templin, R., Wcislo, W., Scimeca, L., Warrant, E., and Heinze, S. (2017). An anatomically constrained model for path integration in the bee brain. *Current Biology*, 27(20):3069–3085.

Tully, T., Preat, T., Boynton, S. C., and Vecchio, M. D. (1994). Genetic dissection of consolidated memory in *Drosophila*. *Cell*, 79(1):35–47.

Vickerstaff, R. J. and Cheung, A. (2010). Which coordinate system for modelling path integration? *Journal of Theoretical Biology*, 263(2):242–261.

Vickerstaff, R. J. and Di Paolo, E. A. (2005). Evolving neural models of path integration. *Journal of Experimental Biology*, 208(17):3349–3366.

Virtanen, P., Gommers, R., Oliphant, T. E., Haberland, M., Reddy, T., et al. (2020). SciPy 1.0: fundamental algorithms for scientific computing in Python. *Nature methods*, 17(3):261–272.

Webb, B. and Wystrach, A. (2016). Neural mechanisms of insect navigation. *Current Opinion in Insect Science*, 15:27–39.

Wehner, R. and Srinivasan, M. V. (1981). Searching behaviour of desert ants, genus *Cataglyphis* (formicidae, hymenoptera). *Journal of Comparative Physiology A*, 142(3):315–338.

Weight, F. F. and Erulkar, S. D. (1976). Synaptic transmission and effects of temperature at the squid giant synapse. *Nature*, 261:720–722.

Wittmann, T. and Schwegler, H. (1995). Path integration — a network model. *Biological Cybernetics*, 73(6):569–575.

Wolff, T. and Rubin, G. M. (2018). Neuroarchitecture of the *Drosophila* central complex: A catalog of nodulus and asymmetrical body neurons and a revision of the protocerebral bridge catalog. *Journal of Comparative Neurology*, 526(16):2585–2611.

Xia, S. Z., Feng, C. H., and Guo, A. K. (1998). Temporary amnesia induced by cold anesthesia and hypoxia in *Drosophila*. *Physiology and Behavior*, 65(4-5):617–623.

Zhu, Y. C. and Cooper, R. L. (2018). Cold exposure effects on cardiac function and synaptic transmission at the neuromuscular junction in invertebrates. *International Journal of Zoological Research*, 14(2):49–60.

Ziegler, P. E. and Wehner, R. (1997). Time-courses of memory decay in vector-based and landmark-based systems of navigation in desert ants, *Cataglyphis fortis*. *Journal of Comparative Physiology A*, 181(1):13–20.

7

GENERAL DISCUSSION

The motivation for the research presented in this thesis was to investigate the neural substrate of path integration in some of the best navigators known on Earth, insects. Throughout the studies in this thesis, I used a combination of computational neuroscience and biorobotics techniques together with behavioural experiments as well as neuroanatomical and electrophysiological data to investigate the path integration system of insects. This combination of techniques enabled several new insights into the head direction circuit and the path integration memory substrate of insects.

7.1 CONTRIBUTIONS

In Chapter 3, I used existing neuroanatomical data to derive the effective neuronal circuits of the head direction tracking system of two insect species, the fruit fly *Drosophila melanogaster* and the locust *Schistocerca gregaria*. I discovered that the homologous neuronal circuits share a similar fundamental structure despite the significant anatomical differences between the two species.

However, I also demonstrated that subtle differences in neuronal morphology could significantly affect circuit performance. Such morphological differences between the two species enable the fruit fly circuit to respond faster to heading changes and the locust circuit to maintain a more stable heading signal.

The identified differences in the response characteristics of the circuits are consistent with the behavioural ecology of the two species. On the one hand, the faster response of the ring attractor circuit in the fruit fly can accommodate the fast flight manoeuvres that fruit flies are known to perform (Tammero and Dickinson, 2002; Fry et al., 2003). On the other hand, the locust is a migratory species, so its behaviour could benefit from the maintenance of a defined heading for long periods of time (Homberg, 2015; de Vries et al., 2017).

I also discovered that a functionally closed-ring circuit structure is obtained with two different solutions in the two studied species. In the fruit fly, the torus-shaped ellipsoid body (EB) provides an anatomical solution to forming a closed ring. By contrast, the ring is closed in the locust by the midline spanning output fibres of the E-PG neurons in the medial protocerebral bridge (PB) glomeruli.

In Chapter 4, I composed a comprehensive literature review of neural integration models, and I discussed the appropriateness of these models for the insect home vector memory. This chapter functions as a foundation for the studies included in this thesis but also provides a general map of the neural integrator research landscape.

In Chapter 5, I tested the often voiced hypothesis that the path integration memory in insects is a bump attractor type of recurrent network. I found that the predictions of this hypothesis — which stems from rodent path integration research — are inconsistent with the path integration behaviour of *Cataglyphis fortis*.

In Chapter 6, I further investigated the type of home vector memory employed in ants by using cold-induced anaesthesia. This is the first time anaesthesia has been used for testing insect navigation memory. I found that the distance component of the home vector memory is disrupted by cooling, but the direction component is preserved.

Furthermore, I argued that these findings are consistent with the direction and distance components of path integration memory being maintained in shared memory instead of two different types of memory that are differently affected by cooling. These results pose valuable constraints on the range of plausible underlying memory substrates.

Beyond answering specific research questions, this thesis also provides important methodological insights that could be applied across computational neuroscience. I used reverse engineering techniques to derive the effective neuronal circuits of two insect species (Pisokas, 2021; Pisokas et al., 2020). This derivation allowed the circuit-level comparison of the homologous neuronal circuits found in the two species. Such comparative studies in neuroscience are valuable not only for identifying what differs but also for deriving general principles about neuronal computation.

I investigated the role of each difference by creating computational models of 'hybrid' circuits, selectively combining features found in the two species, to isolate and understand the functional significance of each observed difference independently. This methodology can also be applied in reverse to predict what the expected brain circuitry might be in species for which we have less physiological detail but more behavioural data, for instance, ants. Such an approach will advise neurophysiologists on what the expected circuit features might be and help them focus their research efforts.

Furthermore, the use of robot agent simulations enabled the testing of hypotheses both at the level of neural circuits and behaviour. For example, simulating the hypothetical effects that cooling might have on memory allowed me to observe the produced agent behaviour and, in turn, to formulate further hypotheses and predictions about the memory substrate of the animals. Similarly, hypotheses about how

the behavioural capabilities of each species might relate to adaptations in the head tracking circuit guided experiments that revealed differences in circuit performance. The observed differences in circuit dynamics guided the selective swapping of parts of the circuit with the corresponding parts of another species, creating 'hybrid' species models; this constitutes a synthetic approach to neuroscience.

As more detail about neurophysiology becomes available and modelling techniques improve, studies making surgically targeted interventions swapping simulated circuits and testing their implications using agents can accelerate brain research. Such interventions and testing would have been impossible in animals, but a combination of computational neuroscience and robotics makes them feasible.

7.2 LIMITATIONS

As detailed in Chapter 3, I used neuronal projection data to infer functional connectivity for deriving the head direction tracking circuit in the fruit fly and the locust. Of course, observed neuronal projections do not necessarily imply functional connectivity; however, electron microscopy data published after the publication of Pisokas et al. (2020) confirmed most of the assumed connectivity with some differences that do not invalidate the model but would require its adaptation in future work (Turner-Evans et al., 2020; Hulse et al., 2021).

The research presented in Chapter 5 investigated numerous modifications of the basic bump attractor model in an attempt to invalidate the finding that bump attractor dynamics are incompatible with animal path integration behaviour. Of course, it is impossible to test all possible variations of a model; however, all the alternatives we tested had fundamental discrepancies when compared with behavioural evidence.

In the behavioural experiments presented in Chapter 6, the ant behaviour was used as a proxy for elucidating the effect of anaesthesia on memory. Several experimental controls were used to ensure that the behavioural observations were not confounded with additional non-memory related effects that the anaesthesia might have on the animals.

It is also unknown what is the relationship between memory and exhibited homing behaviour. We assumed a proportional relationship between the distance value encoded in memory and the homing distance exhibited by the animals.

A further consideration is whether the animals utilise two different memories, one short-term memory and another longer-term memory. In that scenario, a running estimate of the home vector would be maintained in short-term memory and transferred to a longer-term memory periodically or when the insect is motivated to store it for a longer duration. Such an arrangement might allow both fast updating and long

persistence of the home vector memory in a way compatible with current accounts of memory types (short, mid, and long-term memory). However, such a hypothesis predicts that a temporal change in homing distance and error would be produced during the transition period between memory types, as manifested in experiments of memory consolidation phases in other experimental paradigms (e.g. Giurfa and Sandoz, 2012). Such a transitionary change has not been observed in the literature (e.g. Ziegler and Wehner, 1997; Cheng et al., 2005). However, explicitly testing this hypothesis is beyond the scope of this thesis.

Moreover, the research presented in this thesis used point neuron models that are sufficient for answering the questions posed. However, multi-compartmental neuron models and biochemical models would be needed for future research that would investigate some of the questions that will be raised in the next section.

7.3 FUTURE WORK

The work presented in this thesis raises several specific questions about the neuronal circuits involved in path integration. Ongoing and planned research projects outlined in the sequel will attempt to address some of these questions.

Ongoing research is investigating what is the role, if any, of the ninth glomerulus in each PB hemisphere found so far only in *Drosophila*. The same signals from tile 1 of the EB are sent to both ends of each hemisphere of the PB (glomeruli 1 and 9) and from there action potentials propagate along the PB length. I hypothesise that this may be a mechanism to reduce the distance and thus the time these signals have to propagate to reach all glomeruli of the PB. If this is the case, it will constitute one more specialisation in *Drosophila* that reduces the response time of the ring attractor circuit.

Another remaining question regards the role of the torus-shaped EB in *D. melanogaster*. One possibility is that such closed-ring anatomy allows local reciprocal connections between P-EN and E-PG neurons around the whole EB ring, which is compatible with electron microscopy data reported in Turner-Evans et al. (2020) after this hypothesis was proposed by Pisokas et al. (2020). This would enable direct propagation of signals between these neurons within the EB instead of requiring them to travel via the PB, as in the current model, again increasing the speed with which the heading direction can be tracked and possibly allowing a smoother transition between neighbouring tiles. However, such direct reciprocal connections within the EB can only span the full ring with closed ring anatomy and would not be possible between the two ends of the EB in the locust.

Further research is needed to investigate the finding that the closed-ring structure of the circuit is obtained in different ways in the two species studied in this thesis. Investigating the homologous circuits of other species would reveal if even more solutions have evolved to close the ring.

It also remains to be seen if individual species have a selective subset of the specialisations reported in this thesis, endowing them with brain circuits specialised for the behavioural repertoire suiting their ecological niche or whether generic solutions have evolved. Therefore, it will be important to analyse the effective head-direction circuit of other species and make comparisons. This could generate insights into the adaptations of this circuit under different evolutionary histories and selective pressures, and into how adaptations relate to behaviour and accommodate it.

The finding that the predictions of the bump attractor hypothesis are contradicted by behavioural evidence from *Cataglyphis fortis* has implications not only limited to insect path integration; it also raises questions regarding the corresponding hypothesis in mammal path integration. Research in rodent navigation typically uses limited small scale environments. More extensive behavioural paradigms might investigate the path integration memory dynamics in rodents and compare them to the predictions of the bump attractor hypothesis. Recent research on bats navigating in large scale environments might provide insights into the stability, accuracy, and dynamics of their path integration memory that will be valuable in future studies.

More research is also needed to elucidate the nature of the home vector memory employed during insect path integration. The model used in Chapter 6 predicts that a proportional reduction of memory values would result in a smoother degradation of homing behaviour. Future experiments keeping the ants in chill-coma for different periods of time would reveal whether the home vector memory is lost gradually with anaesthesia duration or abruptly. Combined with modelling, such experiments could provide more insights into the underlying memory mechanism and eventually lead to concrete hypotheses about the specific neurons that participate in the elusive neural integrator.

Based on the findings of Chapters 4, 5, and 6, the author's working hypothesis is that the home vector memory might be based on an activity-maintained molecular process such as neurotransmitter receptor mobility or synaptic facilitation, both of which involve CaMKII signalling pathways. Calcium influx can quickly induce an increase in CaMKII activity levels, which can be sustained for several hours through autophosphorylation, potentially enabling both quick change and long persistence of memory (Lisman et al., 2012; Scholl et al., 2015). Targeted pharmacological manipulations in combination with computational modelling will be required to investigate these possibilities. Ongoing research on modelling the biochemical pathways of syn-

aptic facilitation has already shown that they can function as an integrator capable of fast enough updating and exhibiting persistence of its state for several hours. This line of research will reveal whether the basis of the path integration memory is a variation of a known biophysical process or a yet undiscovered memory type specialised to the ecological needs of path integrating insects.

7.4 CLOSING REMARKS

The combination of computational modelling, behavioural experiments, biorobotics techniques as well as neuroanatomical and electrophysiological data to investigate the path integration system of insects has been invaluable throughout this thesis. This approach enabled numerous insights into the head direction circuit and the memory employed by the path integration system.

It is perhaps questionable whether robotics can benefit from the findings about the path integration system of the insects as much as the path integration research reported in this thesis benefited from robot agent simulations. There are already solutions to many robot navigation problems taking advantage of knowledge and technologies developed originally to assist human navigation (e.g. maps, GPS, automotive navigation systems). However, path integration (dead reckoning) is used as a component of more advanced robot navigation techniques (e.g. SLAM). In addition, navigating using path integration would be advantageous where the aforementioned assistive navigation technologies are not available, for example, in indoor environments or planetary exploration.

Insects exhibit a variety of behaviours solving complex tasks while their brains are smaller and simpler than those of mammals, rendering them more accessible for studies. The assumption among many in the scientific community is that studying simpler brains will reveal neuronal principles shared by more complex brains. However, insect physiology has several features not shared with other classes of animals (Niven and Farris, 2012), so it remains to be seen to what extent neuronal principles are shared. Finally, performing computation with minimal resources is a common feature of insects and contemporary neuromorphic systems (Niven, 2016). Studying how insect brains solve computation problems could provide inspiration for the design of improved neuromorphic solutions.

BIBLIOGRAPHY

Cheng, K., Narendra, A., and Wehner, R. (2005). Behavioral ecology of odometric memories in desert ants: Acquisition, retention, and integration. *Behavioral Ecology*, 17(2):227–235.

de Vries, L., Pfeiffer, K., Trebels, B., Adden, A. K., Green, K., Warrant, E., and Heinze, S. (2017). Comparison of navigation-related brain regions in migratory versus non-migratory noctuid moths. *Frontiers in Behavioral Neuroscience*, 11:158.

Fry, S. N., Sayaman, R., and Dickinson, M. H. (2003). The aerodynamics of free-flight maneuvers in *Drosophila*. *Science*, 300(5618):495–498.

Giurfa, M. and Sandoz, J. C. (2012). Invertebrate learning and memory: Fifty years of olfactory conditioning of the proboscis extension response in honeybees. *Learning and Memory*, 19(2):54–66.

Homberg, U. (2015). Sky compass orientation in desert locusts—evidence from field and laboratory studies. *Frontiers in Behavioral Neuroscience*, 9:346.

Hulse, B. K., Haberkern, H., Franconville, R., Turner-Evans, D. B., Takemura, S.-y., Wolff, T., Noorman, M., Dreher, M., Dan, C., Parekh, R., et al. (2021). A connectome of the drosophila central complex reveals network motifs suitable for flexible navigation and context-dependent action selection. *eLife*, 10:e66039.

Lisman, J., Yasuda, R., and Raghavachari, S. (2012). Mechanisms of CaMKII action in long-term potentiation. *Nature Reviews Neuroscience*, 13(3):169–182.

Niven, J. and Farris, S. (2012). Miniaturization of nervous systems and neurons. *Current Biology*, 22(9):R323–R329.

Niven, J. E. (2016). Neuronal energy consumption: biophysics, efficiency and evolution. *Current Opinion in Neurobiology*, 41:129–135. Microcircuit computation and evolution.

Pisokas, I. (2021). Reverse engineering and robotics as tools for analyzing neural circuits. *Frontiers in Neurorobotics*, 14:122.

Pisokas, I., Heinze, S., and Webb, B. (2020). The head direction circuit of two insect species. *eLife*, 9:e53985.

Scholl, C., Kübert, N., Muenz, T. S., and Rössler, W. (2015). CaMKII knockdown affects both early and late phases of olfactory long-term memory in the honeybee. *Journal of Experimental Biology*, 218(23):3788–3796.

Tammero, L. F. and Dickinson, M. H. (2002). The influence of visual landscape on the free flight behavior of the fruit fly *Drosophila melanogaster*. *The Journal of experimental biology*, 205(Pt 3):327–43.

Turner-Evans, D. B., Jensen, K. T., Ali, S., Paterson, T., Sheridan, A., Ray, R. P., Wolff, T., Lauritzen, J. S., Rubin, G. M., Bock, D. D., and Jayaraman, V. (2020). The neuroanatomical ultrastructure and function of a biological ring attractor. *Neuron*, 108(1):145–163.

Ziegler, P. E. and Wehner, R. (1997). Time-courses of memory decay in vector-based and landmark-based systems of navigation in desert ants, *Cataglyphis fortis*. *Journal of Comparative Physiology A*, 181(1):13–20.

The bibliography of individual chapters can be found on pages 25, 12, 83, 115, 147, and 174.